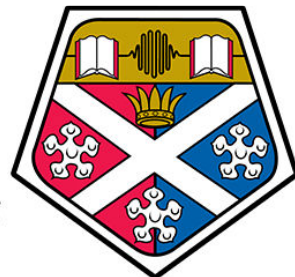


UNIVERSITY OF STRATHCLYDE

Department of Physics

**Development of thermally efficient,  
ultrathin, diamond-based  $\mu$ LED neural  
implants for versatile optogenetics**

Antoine Boudet



University of  
**Strathclyde**  
**Glasgow**

A thesis presented in fulfilment of the requirements  
for the degree of Doctor of Philosophy

2019

# Copyright Statement

This thesis is the result of the author's original research. It has been composed by the author and has not been previously submitted for examination which has led to the award of a degree. The copyright of this thesis belongs to the author under the terms of the United Kingdom Copyright Acts as qualified by University of Strathclyde Regulation 3.50. Due acknowledgement must always be made of the use of any material contained in, or derived from, this thesis.

Glasgow, 01/04/2019

A handwritten signature in dark ink, appearing to read 'Antoine BouDET', written over a solid horizontal line.

**Antoine BOUDET**

# Frontispiece

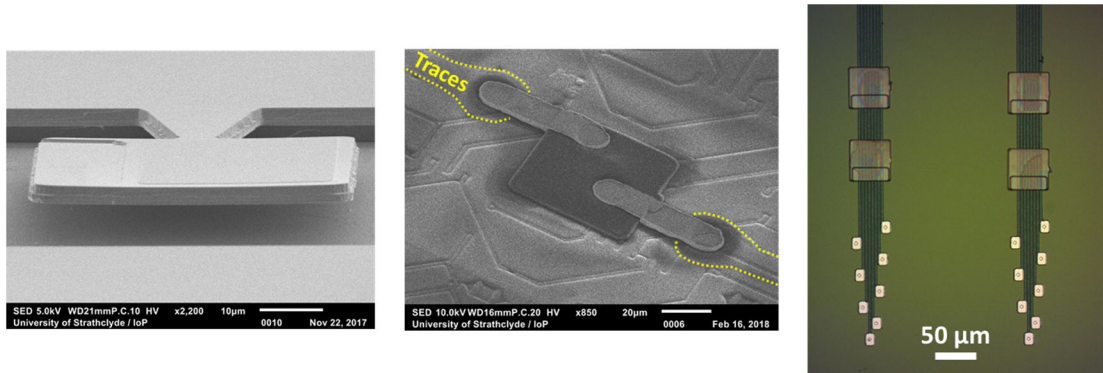


Figure I: AllnGaN  $\mu\text{LED}$ s linked to their native substrate by breakable anchors, ready for pickup (left), printed and contacted onto a CMOS chip (middle), and transferred onto a Neuronexus probe structure by advanced picodroplet adhesive printing (right)

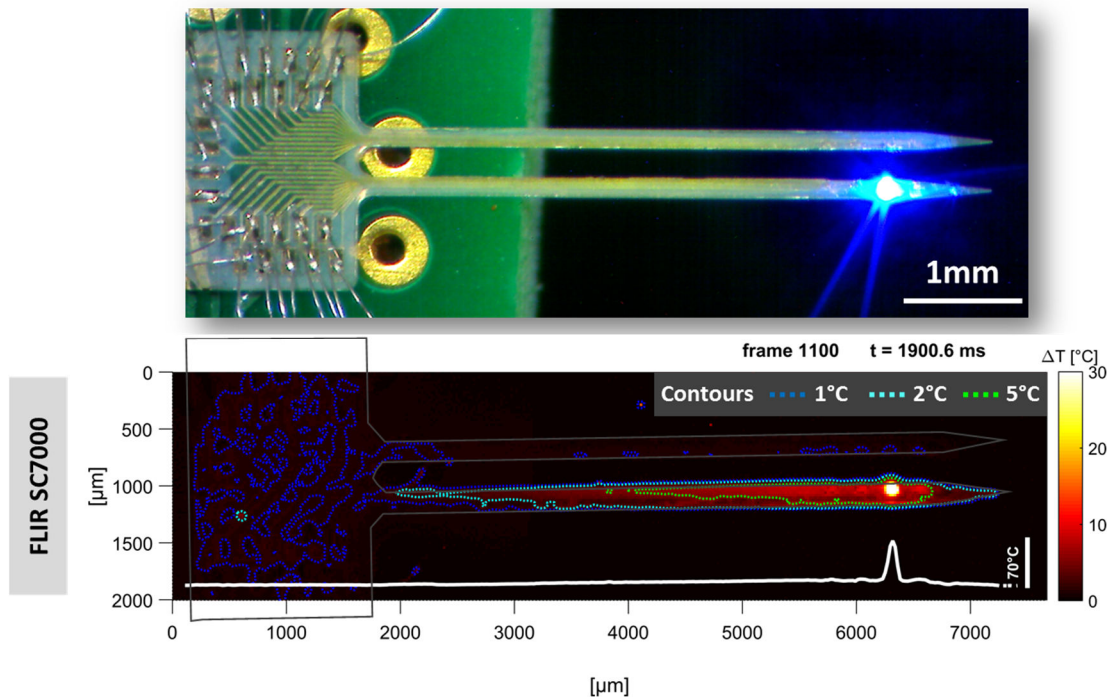


Figure II: Double-shank diamond optrode wirebonded on PCB, with LED n° R3 operated at high irradiance ( $> 200 \text{ mW} \cdot \text{mm}^{-2}$ ) and 50% duty cycle (top) and infrared thermal imaging of the same, showing the corresponding heat distribution on the probe in air.

# Abstract

Optogenetics helps revolutionise the study of neural networks by allowing localised, genetically targeted, millisecond-timescale optical stimulations of neurons. Optogenetic implants embedded with LED sources hold great potential for experimental neuroscience, as they dispense with external optical coupling and enable site-specific light delivery to deep-brain regions.

Although this technology has attracted firm interest in recent years, a long-standing question is whether these devices can attain optical powers or pulse rates suited for high-illumination protocols or circuit-level stimulation (e.g  $P > 50\text{mW}\cdot\text{mm}^2$ ), while keeping average or peak Joule heating of tissue within commonly accepted “safe” boundaries (e.g  $< 1^\circ\text{C}$  increase). Typical LED substrates are restricted by their thermal and optical properties, and heterogeneously integrated devices have thus far suffered from poor optical output or exceedingly invasive footprints resulting from design or manufacturing trade-offs. As a result, none of the LED-based implant demonstrated in the literature has ever been shown to safely output high optical power while exhibiting dimensions comparable to more mature guided-light devices (e.g width  $\sim < 100\mu\text{m}$ ).

This work presents novel diamond-based LED optrodes which, for the first time, simultaneously demonstrate minimal invasiveness, optical performance and outstanding thermal efficiency. The devices harness the superior thermal conductivity, corrosion resistance and increasing availability of synthetic diamond which make it a promising candidate for the next generation of hybrid bioimplants. Our single-crystal diamond optrodes have penetrating shanks, each integrating 4 transfer-printed AlInGan  $\mu\text{LEDs}$  ( $50\times 50\mu\text{m}^2$ ,  $\lambda = 455\text{nm}$ ) and 8 electrodes. As key milestones, specific techniques were developed for **a)** the processing of ultrathin diamond membranes, **b)** the optimised manufacturing of high-efficiency transfer-printing LEDs (EQE  $> 4\%$  at irradiance  $I_{\text{LED}} = 100\text{mW}\cdot\text{mm}^{-2}$ ) and **c)** their reliable transfer onto highly textured substrates, yielding an advanced printing method via adhesive picodroplets.

For the first time, the probe dimensions (shank  $L \times W \times T = 5.5\text{mm} \times 150\mu\text{m} \times 25\mu\text{m}$ ) and large irradiance range (up to  $\sim 300\text{mW}/\text{mm}^2$  per LED at 3mA driving current) approach those of state-of-the-art monolithic Silicon-based optrodes, with a thermal performance improved by more than an order of magnitude. This is predicted to allow a uniquely wide set of optogenetic protocols including extended/high-power optical pulses at high duty cycles, capable of stimulating thousands of neurons while keeping peak tissue temperature increase below  $1^\circ\text{C}$ . Process scalability on commercial wafers is demonstrated on a polycrystalline diamond membrane (20mm diameter,  $50\mu\text{m}$  thickness), opening the way for novel, inexpensive diamond-based tools for neurophotonics and biomedical applications.

# Table of contents

<i>Table of contents</i> .....	<i>i</i>
<i>List of figures and tables</i> .....	<i>v</i>
<i>Acronyms and abbreviations</i> .....	<i>ix</i>
<b>Introduction</b> .....	<b>1</b>
<b>Chapter 1</b> .....	<b>5</b>
1.1    A brief introduction on the brain and neurons.....	5
1.1.1    Organisation of the brain .....	5
1.1.2    Neuron and action potentials .....	6
1.1.3    Current devices for neural electrophysiology.....	8
1.2    Optogenetics and guided light implants.....	9
1.2.1    Optogenetics : concept, development and applications .....	10
1.2.2    Technologies for intra-cranial light delivery by extraneous sources .....	11
1.3    In situ light emitters : LED-based neural implants.....	14
1.3.1    Light emitting diodes and $\mu$ LEDs.....	14
1.3.2    LED-based implantable probes for optogenetics.....	20
1.3.3    Thermal challenges of implanted $\mu$ LED emitters.....	22
1.4    Synthetic diamond and diamond-based devices .....	23
1.5    Targets for the present work – implant specifications .....	25
1.6    Summary .....	27
1.7    References.....	28
<b>Chapter 2</b> .....	<b>39</b>
2.1    Pattern definition by photolithography.....	39
2.1.1    Film application.....	39
2.1.2    PR exposure .....	40
2.1.3    PR development.....	41
2.2    Material deposition.....	43
2.2.1    Physical vapor deposition (PVD) of metallic films.....	43
2.2.2    Metal film annealing .....	44
2.2.3    Chemical vapor deposition (CVD) of dielectric films.....	44

2.3	Material etching.....	46
2.3.1	Dry etching.....	46
2.3.2	Wet etching.....	48
2.4	Analysis and characterisation techniques.....	50
2.4.1	Thin film thickness measurement by ellipsometry.....	51
2.4.2	Surface topography by stylus and optical profiling .....	52
2.4.3	Scanning electron microscopy (SEM).....	53
2.5	Micro-transfer printing .....	54
2.5.1	Context and introduction.....	54
2.5.2	Mechanics of transfer-printing .....	55
2.5.3	Transfer-printing at Strathclyde.....	57
2.6	Conclusion.....	59
2.7	<i>References</i> .....	60
<b>Chapter 3</b>	.....	<b>65</b>
3.1	Introduction .....	65
3.2	Optimised fabrication for high-efficiency, top emitting 50x50 $\mu\text{m}^2$ LEDs for micro transfer-printing.....	66
3.2.1	Previous work and limitations .....	66
3.2.2	Electro-optical performance requirements for $\mu\text{LEDs}$ in this work .....	66
3.2.3	Optimisation of manufacturing process .....	67
3.2.4	Fabrication process : GaN-based $\mu\text{LEDs}$ for transfer printing .....	70
3.2.5	LED performance.....	74
3.2.6	LED curvature .....	76
3.3	Development of a strategy for advanced integration .....	77
3.3.1	Specific challenges for transfer-printing in this project.....	77
3.3.2	Fundamental limitations to fully adhesiveless printing : VDW forces.....	80
3.3.3	$\mu\text{LED}$ transfer on textured substrates : picodroplet adhesive printing .....	83
3.3.4	Parylene-based contacting strategy.....	86
3.4	Demonstrator : $\mu\text{LED}$ printing on CMOS chip .....	88
3.4.1	Context and motivation .....	88
3.4.2	Concept of a $\mu\text{LED}$ -on-CMOS demonstrator.....	88
3.4.3	Integration process flow .....	88

3.4.4	Results.....	90
3.4.5	Conclusion regarding demonstrator.....	93
3.5	Conclusion.....	93
3.6	<i>References</i> .....	94
<b>Chapter 4</b>	.....	<b>99</b>
4.1	Introduction .....	99
4.2	Design of hybrid diamond optrodes .....	100
4.2.1	Demand from the neuroscience community.....	100
4.2.2	Inherent advantages and limitations of synthetic diamond substrates .....	102
4.2.3	Prototype design.....	103
4.3	Optrode development and specific challenges.....	105
4.3.1	Starting material : ultrathin diamond membranes.....	105
4.3.2	Ultrathin membrane handling .....	106
4.3.3	Challenges to photolithography and processing .....	106
4.3.4	Process development and identification of failure modes.....	108
4.4	Fabrication process : Diamond-based optrodes .....	111
4.5	Probe singulation and final device.....	122
4.5.1	Deep diamond etch with Aluminium hard masking .....	122
4.5.2	Final fabricated device .....	123
4.6	Conclusion.....	125
4.7	<i>References</i> .....	126
<b>Chapter 5</b>	.....	<b>129</b>
5.1	Introduction .....	129
5.2	Modelling tools for optical and thermal analysis.....	130
5.2.1	Simulation of light propagation <i>in vivo</i> .....	130
5.2.2	FEM simulation of device and tissue heating .....	133
5.2.3	Contribution of radiative heating to tissue temperature increase.....	135
5.3	Device characterisation.....	138
5.3.1	Electro-optical characterisation and expected output in tissue.....	138
5.3.2	Thermal characterisation, simulation accuracy and predictions in tissue... ..	141
5.4	Prediction of optrode-induced heating in brain tissue.....	146
5.5	Conclusion.....	150



5.6	References.....	151
<b>Chapter 6</b>	.....	<b>154</b>
6.1	Introduction .....	154
6.2	Diamond optrode outcome and adjustments .....	155
6.2.1	Versatile fabrication techniques and diamond optrodes .....	155
6.2.2	Parallel fabrication of silicon-based devices for experimental comparison .....	155
6.2.3	Improvement of bioinsulation layer .....	156
6.3	Direct next steps : upcoming prototype iteration .....	159
6.3.1	Silicon carbide based insulation layer.....	159
6.3.2	Use of diamond optrode <i>in vivo</i> .....	160
6.3.3	<i>In vivo</i> temperature measurements .....	161
6.3.4	Multicolour diamond optrodes.....	163
6.4	Future work.....	163
6.4.1	Upscaled fabrication process for mid-volume fabrication .....	163
6.4.2	Hybridisation of existing, commercially available devices.....	165
6.4.3	Wireless optrodes .....	166
6.4.4	Multifunctional devices and electronics on chip .....	166
6.4.5	Probe arrays and 3D stacking.....	167
6.5	Conclusion.....	167
6.6	References.....	168
<b>Conclusion</b>	.....	<b>176</b>
<b>APPENDICES</b> .....		
	APPENDIX A1 : DEPOSITION & ETCH RECIPES.....	178
	APPENDIX A2 : PHOTOMASKS.....	189
	APPENDIX A3 : $\mu$ TP STAMP FABRICATION .....	190
	APPENDIX A4 : PARYLENE-C ADHESION TESTS .....	191
	APPENDIX A5 : COMPARISON OF INTEGRATED $\mu$ LED PERFORMANCE.....	193
	APPENDIX A6 : ESTIMATION OF $\mu$ LED CURVATURE : NEWTON RINGS ANALYSIS .....	195
	APPENDIX A7 : INTAN RHS2116 CHIP .....	202
	APPENDIX A8 : PHOTODETECTOR CORRECTION FACTOR.....	204
	APPENDIX A9 : MODELLED TISSUE $\Delta T$ , $I = 2\text{MA}$ .....	205
<b>Acknowledgements</b>	.....	<b>206</b>
<b>Contributions</b>	.....	<b>207</b>

# List of figures and tables

## Introduction

<i>Figure 0.1 : Historical tools and current global efforts in brain research</i> .....	2
---	---

## Chapter 1

<i>Figure 1.1 Schematics of a) the human neocortex b) a neuronal membrane, c) an example neuron, and d) an action potential</i> .....	7
<i>Figure 1.2 : Three influential technologies currently used for neural recordings in mammals</i> .	8
<i>Figure 1.3 : Step-by-step description of an optogenetic experiment with “first-generation” optical fibre light delivery. Modified from [53].</i> .....	10
<i>Figure 1.4 : Schematic of some main types of optogenetic tools (taken from [72]).</i> .....	11
<i>Figure 1.5 : Guided light delivery technologies for deep optogenetics</i> .....	12
<i>Figure 1.6 : a) Semiconductors of interest for LEDs, b) illustration of the development of commercially produced LEDs over 3 decades</i> .....	14
<i>Figure 1.7 : a) Schematised semiconductors band structures, b) Schematics of an unbiased pn junction and c) free carrier distribution in a homojunction (top) and a heterojunction (bottom)</i> .....	16
<i>Figure 1.8 : Bandgap energy vs lattice constant <math>a_0</math> of III-nitride materials at room temperature</i> .....	18
<i>Figure 1.9 : Characteristics of 6-inch GaN-on-Si LED wafers grown by Plessey semiconductors, similar to the material used in this work for <math>\mu</math>LED fabrication</i> .....	19
<i>Figure 1.10 : LED-based optogenetic implants</i> .....	21
<i>Figure 1.11 : Some characteristics of CVD diamond</i> .....	23
<i>Figure 1.12 : Previous neural probes based on CVD diamond (polycrystalline)</i> .....	25

## Chapter 2

<i>Figure 2.1 : Schematic of photolithography steps</i> .....	40
<i>Figure 2.2 : Main microfabrication tools in the Institute of Photonics cleanroom used in this work</i> ...	42
<i>Figure 2.3 : Schematics of PVD techniques</i> .....	43
<i>Figure 2.4 : Dielectrics deposition by CVD</i> .....	45
<i>Figure 2.5 : Etching anisotropy influence on pattern transfer</i> .....	46
<i>Figure 2.6 : Dry etching tools</i> .....	47
<i>Figure 2.7 : Heated KOH etching can etch 3D structures in silicon</i> .....	50
<i>Figure 2.8 : Analysis and characterisation tools used in this work</i> .....	51
<i>Figure 2.9 : Multi-tool inspection of an imperfect device uniquely allows complete characterisation and understanding of failure modes</i> .....	54

Figure 2.10 : Summary of the generic technique of micro-transfer printing now used both in academic research and for industrial production..... 56

Figure 2.11 : Transfer-printing setup used in this work ..... 58

### Chapter 3

Figure 3.1 : Previous TP- $\mu$ LEDs demonstrated at Strathclyde (100x100 $\mu$ m<sup>2</sup>, Pd spreading layers).... 66

Figure 3.2 : Silicon underetch duration for various sizes of GaN membranes..... 67

Figure 3.3 : Optimised TP- $\mu$ LEDs electro-optical performance & comparison to previous IoP work.... 74

Figure 3.4 : Inbuilt stress in the epilayers induces significant bowing in the released  $\mu$ LEDs ..... 76

Figure 3.5 : Elementary heat transfer model of a LED heat source (50mW pulse for 1s in air ambient, geometry in inset), printed on a substrate with thermal conductivity  $k_{\text{substrate}}$  with help of an intermediary adhesive layer of varying thickness and thermal conductivity  $k_{\text{adhesive}}$  ..... 78

Figure 3.6 : The process of capillary bonding ..... 80

Figure 3.7 : van der Waals (VDW) forces can vary by orders of magnitudes depending on body separation and geometries ..... 82

Figure 3.8 : Relative importance of stamp/LED to LED/substate attraction during approach of a flat, smooth receiver substrate in VDW-dominated regime, for a fully relaxed stamp holding the LED by 4 low-area microtip..... 83

Figure 3.9 : Schematics and micrographs of a full PA printing cycle (50x50 $\mu$ m<sup>2</sup> LED printed on a very textured area of a patterned diamond membrane) ..... 84

Figure 3.10 : SEM scans of  $\mu$ LEDs printed at various PSA droplet volumes post 2hrs heating, 150°C . 85

Figure 3.11 : PA printing allows LED release with high bonding strength on a variety of surfaces .... 86

Figure 3.12 : Contacting strategy used in this work to address printed  $\mu$ LEDs ..... 87

Figure 3.13 : Integration of a  $\mu$ LED on a commercial CMOS chip by picodroplet adhesive printing ... 90

Figure 3.14 : LED-on-CMOS operation induces distinct electrical transients in recording channels .... 91

### Chapter 4

Figure 4.1 : Principle of a diamond optrode ..... 100

Figure 4.2 : Generic concept for the diamond optrode in this work ..... 102

Figure 4.3 : Schematic layout of the probes over the actual diamond samples..... 103

Figure 4.4 : Diamond samples used in this work ..... 105

Figure 4.5 : Handling of ultrathin, freestanding diamond membranes via carrier wafers..... 106

Figure 4.6 : Comparison of photolithography on prototype, standard GaN-on-Si sample (top row) and ultrathin diamond membrane (bottom row)..... 108

Figure 4.7 : Testbed samples for process development..... 109

Figure 4.8 : Diamond oxygen etch (ICP#1 **DIA\_ARO2**) with an Aluminium hard mask..... 123

Figure 4.9 : Final fabricated devices (sample SC4) and comparison to previous diamond probes..... 124

## Chapter 5

<i>Figure 5.1 : Monte-Carlo modelling of light propagation in tissue</i> .....	131
<i>Figure 5.2 : MC model is robust against medium uncertainty</i> .....	132
<i>Figure 5.3 : Finite element model of heat transfer between probe and tissue using COMSOL</i> .....	134
<i>Figure 5.4 : Initial parametric studies highlight the benefits of diamond's superior thermal properties. The model is run for different probe materials, keeping all other parameters constant</i> .....	135
<i>Figure 5.5 : Magnitude of tissue radiative heating by a 50<math>\mu</math>m-diameter <math>\mu</math>LED emitter at <math>\lambda = 470</math>nm. Model adapted from Stujenske et al. [26], and run with high reported absorption coefficient for cortical tissue (<math>\mu_a = 1.06 \text{ mm}^{-1}</math> [15]) as a "worst-case scenario"</i> .....	137
<i>Figure 5.6 : Electrical and optical characterisation of a diamond probe (sample SC4, double-shank device)</i> .....	139
<i>Figure 5.7 : Calibration of FLIRSC7000 IR measurements</i> .....	142
<i>Figure 5.8 : Comparison between experimental and modelled values of temperature increase <math>\Delta T_{LED}</math> at <math>\mu</math>LED, in air, during operation</i> .....	143
<i>Figure 5.9: Full-probe temperature maps during LED R2 operation at 2 mA (~11 mW electrical power), at the peak of <b>a</b>) a single 50ms pulse, <b>b</b>) a single 100ms pulse and <b>c</b>) a continuous pulsed stimulation (100ms, 5Hz; steady-state pulse peak)</i> .....	145
<i>Figure 5.10 : Simulated spatial and temporal spread of temperature change in surrounding brain tissue during <math>\mu</math>LED pulsed operation at various pulse width and frequencies, given here for an LED current of <math>I = 1</math>mA (~4.7mW electrical power, ~115mW.mm<sup>-2</sup> irradiance at LED)</i> .....	148
<i>Figure 5.11 : Simulated LED operation in tissue allows comparison between the tissue volume experiencing potentially detrimental heating and that irradiated above a given optogenetically relevant threshold.</i> .....	149

## Chapter 6

<i>Figure 6.1 : Same geometry silicon-based probes were fabricated for direct comparison with diamond optrodes but samples were destroyed during externally sourced separation process</i> .....	156
<i>Figure 6.2 : Final devices exhibit significant parylene-C delamination at the probe shank tip</i> .....	157
<i>Figure 6.3 : Simulated optical transmittance into tissue of bioinsulating SiC-parylene stacks as a function of layer thicknesses. Data calculated using the transfer matrix method (TMM)</i> .....	160
<i>Figure 6.4 : Design and prototype of resistive temperature sensor directly integrated on optrode</i> ..	152
<i>Figure 6.5 : Scalability is achievable via use of large-area polycrystalline (PC) diamond wafers</i> .....	164
<i>Figure 6.6 : 50x50 <math>\mu\text{m}^2</math> <math>\mu</math>LEDs printed on a commercial NeuroNexus 4" wafer as a proof of concept for integration with existing medium-volume technology</i> .....	165

## Appendices – Tables and figures

<i>Table A1.1 : Photoresists used in this work.</i> .....	178
<i>Table A1.2.a : Dielectrics deposition recipes (SiO<sub>2</sub>, Parylene C)</i> .....	178
<i>Table A1.2.b : Metal deposition parameters (sputtering, e-beam)</i> .....	179
<i>Table A1.3 : Annealing recipes (Ni/Au, Pd)</i> .....	180
<i>Table A1.4 : Wet etch rates for etchants used in this work</i> .....	181
<i>Table A1.5.a : ICP etching recipes (GaN, Al, Diamond)</i> .....	183
<i>Table A1.5.b : RIE etching recipes (SiO<sub>2</sub>, Parylene-C, Si, Au, Ti, Pd, Ni/Au)</i> .....	185
<i>Table A1.6 : Matrix and “barrel” photoresist ashing recipes</i> .....	188
<i>Figure A2.1 : Photomasks designed and used in this work</i> .....	189
<i>Figure A3.1 : Fabrication of micro-transfer printing stamps</i> .....	190
<i>Figure A4.1 : Protocol for parylene-on-glass adhesion test</i> .....	191
<i>Figure A4.2 : Result of parylene-on-glass adhesion test, array #2</i> .....	191
<i>Figure A4.3 : Collated results of parylene-on-glass adhesion test</i> .....	192
<i>Table A5 : Extended comparison of this work’s <math>\mu</math>LED performance to previously published work on GaN-based integrated <math>\mu</math>LEDs</i> .....	193
<i>Figure A6.1 : Reconstruction of <math>\mu</math>LED curvature by analysis of Newton rings</i> .....	195
<i>Figure A7.1 : Diagram of INTAN RHS2116 CMOS chip</i> .....	202
<i>Figure A7.2 : Sideview of wirebonds from PCB to INTAN chip</i> .....	203
<i>Figure A8.1 : Graph of the calculated light power received at a photodiode as a function of distance and angle to a Lambertian point emitter</i> .....	204
<i>Figure A9.1 : Simulated spatial and temporal spread of temperature change in surrounding brain tissue during <math>\mu</math>LED pulsed operation at various pulse width and frequencies, given here for an LED current of <math>I = 2\text{mA}</math> (1mA curves given in fig. 5.11)</i> .....	205

# Acronyms and abbreviations

$\Delta x$	Scan distance	[m]
$\Delta z$	Height difference	[m]
$\lambda$	Wavelength	[m]
$\mu_a$	Absorption coefficient	[m <sup>-1</sup> ]
$\mu_s$	Scattering coefficient	[m <sup>-1</sup> ]
$\rho$	Density	[kg.m <sup>-3</sup> ]
$\sigma$	Electrical conductivity	[S.m <sup>-1</sup> ]
$\tau$	Decay time constant	[s]
<b>C</b>	Heat capacity	[J.kg <sup>-1</sup> .K <sup>-1</sup> ]
<b>c</b>	Speed of light ( $\sim 2.998.10^8$ )	[m.s <sup>-1</sup> ]
<b>e</b>	Elementary charge ( $\sim 1.602.10^{-19}$ )	[C]
$E_c$	Conduction band energy	[eV]
$E_F$	Fermi energy level	[eV]
$E_g$	Bandgap energy	[eV]
$E_{K^+}$	Equilibrium potential for potassium ions	[V]
$E_{Na^+}$	Equilibrium potential for sodium ions	[V]
$E_v$	Valence band energy	[eV]
<b>EQE</b>	External quantum efficiency	[%]
<b>F</b>	Frequency	[s <sup>-1</sup> ]
<b>h</b>	Planck's constant ( $\sim 6.626.10^{-34}$ )	[m <sup>2</sup> .kg <sup>-1</sup> .s <sup>-1</sup> ]
<b>I</b>	Current	[A]
$I_{LED}$	LED irradiance	[W.m <sup>-2</sup> ]
<b>J</b>	Current density	[A.m <sup>-2</sup> ]

<b>k</b>	Boltzmann constant ( $\sim 1.381 \cdot 10^{-23}$ )	$[m^2 \cdot kg \cdot s^{-2} \cdot K^{-1}]$
<b><math>\kappa</math></b>	Thermal conductivity	$[W \cdot m^{-1} \cdot K^{-1}]$
<b><math>P_{el}</math></b>	Electrical power	[W]
<b>Q</b>	Volumetric heat source	$[W \cdot m^{-3}]$
<b>R</b>	Radius of curvature	[m]
<b>R</b>	Resistance	$[\Omega]$
<b>T</b>	Temperature	[K]
<b><math>T_0</math></b>	Initial temperature	[K]
<b>t</b>	Time	[s]
<b><math>t_f</math></b>	Film thickness	[m]
<b><math>t_{sub}</math></b>	Substrate thickness	[m]
<b>V</b>	Voltage	[V]
<b><math>V_{irradiated}</math></b>	Volume of tissue irradiated over a threshold of $1mW \cdot mm^{-2}$	$[m^3]$
<b><math>V_{hot}</math></b>	Volume of tissue heated above a threshold of $0.5^\circ C$ or $1^\circ C$	$[m^3]$
<b><math>V_m</math></b>	Membrane potential	[V]
<b><math>\Delta E</math></b>	Activation energy	$[J \cdot mol^{-1}]$
<b>“</b>	Inch (2.54 cm)	
<b><math>\mu LED</math></b>	Micro-sized light emitting diode	
<b><math>\mu TP</math></b>	Micro transfer printing	
<b>AAV</b>	Adeno-associated virus	
<b>AC</b>	Alternating current	
<b>ALD</b>	Atomic layer deposition	
<b>AlGaAs</b>	Aluminium gallium arsenide	
<b>AlGaInP</b>	Aluminium gallium indium phosphide	
<b>ATP</b>	Adenosine triphosphate	
<b>Au</b>	Gold	

<b>BOE</b>	Buffered oxide etch
<b>CCD</b>	Charge-coupled device
<b>ChR2</b>	Channelrhodopsin 2
<b>CMOS</b>	Complementary metal-oxide semiconductor
<b>CMP</b>	Chemical mechanical polishing
<b>CNS</b>	Central Nervous System
<b>Cr</b>	Chromium
<b>CSD</b>	Current source density
<b>CVD</b>	Chemical vapour deposition
<b>DAC</b>	Digital to analog converter
<b>DC</b>	Direct current
<b>DRIE</b>	Deep reactive ion etching
<b>E-beam</b>	Electron beam
<b>EBL</b>	Electron blocking layer
<b>eV</b>	Electronvolt ( $\sim 1.602 \cdot 10^{-19}$ J)
<b>FEM/FEA</b>	Finite element method / Finite element analysis
<b>FIB</b>	Focussed ion beam
<b>fMRI</b>	Functional magnetic resonance imaging
<b>FWHM</b>	Full Width at Half Maximum
<b>k</b>	Refractive index (imaginary part)
<b>GABA</b>	Gamma-aminobutyric acid
<b>GaN</b>	Gallium nitride
<b>GaP</b>	Gallium phosphide
<b>HCl</b>	Hydrochloric acid
<b>HDMS</b>	Hexamethyldisilazane
<b>HF</b>	Hydrofluoric acid
<b>Hz</b>	Hertz ( $s^{-1}$ )



<b>IC</b>	Integrated circuit
<b>ICP RIE</b>	Inductively coupled plasma reactive ion etching
<b>InGaN</b>	Indium Gallium Nitride
<b>IoP</b>	Institute of Photonics of the University of Strathclyde
<b>IPA</b>	Isopropanol
<b>IV</b>	Current-voltage (curve/characteristics)
<b>KOH</b>	Potassium hydroxide
<b>LED</b>	Light-emitting diode
<b>LFP</b>	Local field potential
<b>LI</b>	Light-current (curve/characteristics)
<b>Li-Fi</b>	Light fidelity
<b>LTO</b>	Low-temperature oxide
<b>MOVPE</b>	Metalorganic vapour phase epitaxy
<b>MQW</b>	Multiple quantum wells
<b>n</b>	Refractive index (real part)
<b>N<sub>2</sub></b>	Nitrogen
<b>NpHR</b>	Halorhodopsin
<b>O<sub>2</sub></b>	Oxygen
<b>Pd</b>	Palladium
<b>PDMS</b>	Polydimethylsiloxane
<b>PECVD</b>	Plasma-enhanced chemical vapour deposition
<b>pL</b>	Picolitre (10 <sup>-12</sup> L)
<b>PA printing</b>	Picodroplet adhesive printing
<b>PR</b>	Photoresist
<b>Pt</b>	Platinum
<b>PVD</b>	Physical vapour deposition

<b>PSS</b>	Patterned sapphire substrate
<b>PW</b>	Pulse width
<b>PWM</b>	Pulse width modulation
<b>RF</b>	Radio frequency
<b>RIE</b>	Reactive ion etching
<b>rpm</b>	Revolutions per minute
<b>SEM</b>	Scanning electron microscope
<b>sccm</b>	Standard cubic centimetres per minute
<b>Si</b>	Silicon
<b>SiC</b>	Silicon carbide
<b>SiO<sub>x</sub>N<sub>y</sub></b>	Silicon oxynitride
<b>SIPBS</b>	Strathclyde Institute of Pharmacy and Biomedical Sciences
<b>SNF</b>	Stanford Nanofabrication Facility
<b>SOI</b>	Silicon-on-insulator
<b>Ti</b>	Titanium
<b>TP-μLED</b>	Micro-sized light-emitting diode specifically designed for transfer printing
<b>Torr</b>	Torr (~ 133.3 Pa)
<b>VDW</b>	Van der Waals
<b>VSD</b>	Voltage-sensitive dye

# Introduction

With its ~100 billion interconnected neurons at the source of our thoughts, emotions, perceptions, actions, memories, and even this doctoral work, the human brain may be the most sophisticated system ever researched. It presents a scientific challenge surpassing even the space race or the genome project in scope and complexity ([1], [2]). Furthering brain research is key to fight major healthcare battles such as neurodegenerative diseases, which affect nearly a million people in the UK alone, at a cost of over ~£26 billion to the national economy [3]. Alongside biologists and neuroscientists, physicists and engineers have already proven instrumental to progress on that path.

## 1.1 Motivation

Modern neuroscience emerged in the late 19<sup>th</sup> century with Camillo Golgi's discovery of neuronal architecture by cell staining and the foundational work of Santiago Ramón y Cajal on neuron arborisation and connectivity [4]. Its progress ever since has been tied to advances in technology (figure 1, left). The use of micro-electrodes in the 1930s revealed the neuron as an electrical unit, while concurring breakthroughs in microscopy and functional imaging techniques revealed multiscale brain anatomy and connectivity in unprecedented detail, from submicron dendritic structures to inter-regional networks. More recently, the advent of high-resolution perturbation techniques such as optogenetics have allowed unprecedented functional studies of neural networks, although the interpretation of causality experiments remains a subject of debate [5].

Neuroscience is at a turning point, with researchers now able to “envision a comprehensive understanding of the brain in action” [6]. Countries worldwide are taking stock and since 2013 are massively investing in large-scale initiatives, ushering in the era of “Global Neuroscience” [7], with differing approaches (figure 1, right).

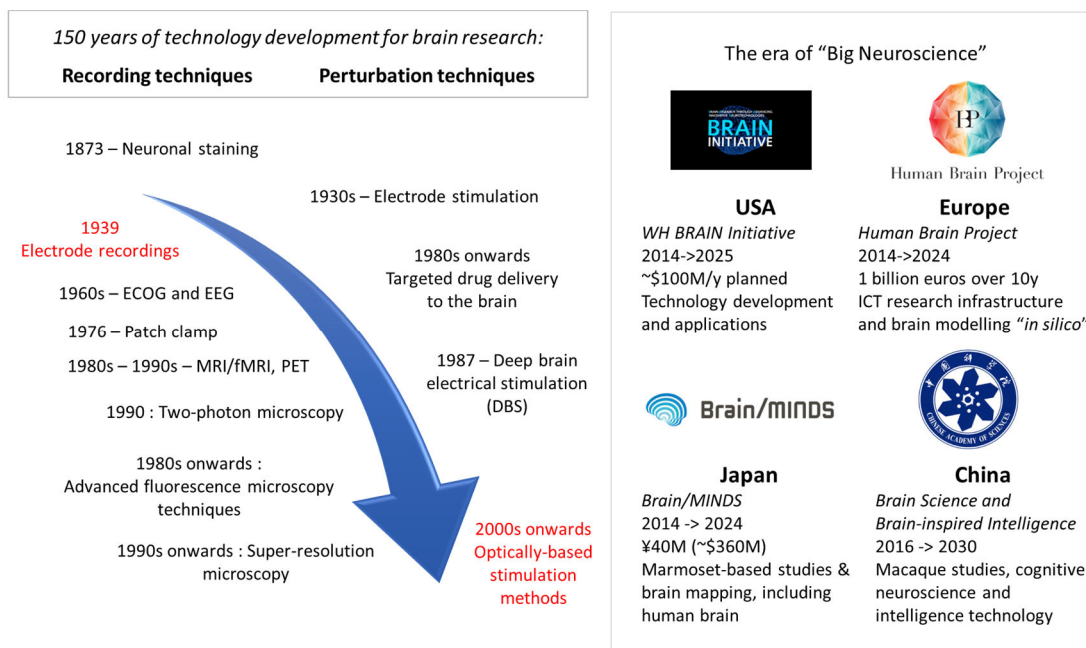


Figure 1 : Historical tools and current global efforts in brain research. **(left)** Much of today’s knowledge of the brain was enabled through 150+ years of technological development, bringing tools to analyse, record and influence neural anatomy and activity. **(right)** Since the 2010s, large-scale global efforts are transforming neuroscience, and bring ever larger investments into technological solutions.

This work aims to contribute to the international effort towards new tools for brain science. The development of technologies permitting simultaneous full control and readout of neuronal populations, notably through optogenetics, is recognised by leaders in the field as a key milestone for understanding neural circuits [6]. While LED-based implants show high promise for multisite, precise and scalable optical stimulation of neurons, their development has raised substantial challenges in microfabrication and for device heat dissipation. High irradiance LED probes suitable for acute *in vivo* optogenetics have never been shown, leaving a gap in the neuroscientists’ toolkit which creates a bottleneck for the development of novel optogenetic studies and protocols. Seeking to bridge that gap, this work reports on the design, fabrication and testing of the first diamond-based optrode for optogenetics, incorporating GaN-based microsized light-emitting diodes and electrodes. The device, demonstrating state-of-the-art optical performance, a minimal footprint, and the highest thermal efficiency reported to date for comparable probes, is expected to open new paths for optogenetic experiments relying on high optical power or long irradiance times.

## 1.2 Thesis outline

**Chapter 1** of this thesis is devoted to a quick overview of important contextual elements, including the neuronal structure, current neural probe technologies, and the LEDs and diamond material used in this work. **Chapter 2** details the microfabrication techniques used throughout this work. **Chapter 3** introduces micro-sized LED optimised fabrication and transfer to novel substrates. Highly efficient  $50 \times 50 \mu\text{m}^2$ , free-standing GaN-based  $\mu\text{LEDs}$  with irradiances up to  $>300 \text{mW} \cdot \text{mm}^{-2}$  are developed. A specific printing method is created to reliably transfer these on unusual substrates including CMOS chips, textured glass and patterned diamond, as a key milestone towards our final hybrid device.

**Chapter 4** explains the design, challenges and fabrication of the first diamond-based optrode for optogenetics. The first diamond optrodes in single- and double-shank configuration, with dimensions comparable to the best silicon-based devices and up to 8  $\mu\text{LEDs}$  and 16 electrodes, are demonstrated. **Chapter 5** focuses on the electro-optical and thermal characterisation of the devices. The probes are capable of reaching high optical powers suitable for optogenetic stimulation of large brain volumes (up to  $\sim 1 \text{mm}^3$  for each LED) while thermally outperforming similar silicon-based devices by an order of magnitude, thanks to ms-timescale heat extraction along the probe shank. **Chapter 6** examines directions and ideas for short- to long-term future work, and overall conclusions are drawn in **chapter 7**.

### 1.3 References

- [1] S. Ackerman, N. Academy, S. Isbn, T. Pdf, N. A. Press, N. A. Press, N. Academy, N. Academy, and N. A. Press, *Discovering the Brain (Foreword)*. 1992.
- [2] P. G. Allen and F. S. Collins, "Towards the Final Frontier : the Human Brain," *Wall Street Journal*, 08-Apr-2013.
- [3] Alzheimer's Society, "Dementia UK: Second edition - Overview," pp. 1–62, 2014.
- [4] E. R. Kandel, J. H. Schwartz, T. M. Jessell, S. A. Siegelbaum, and A. J. Hudspeth, *Principles of Neural Science, Fifth Edition*, vol. 3. 2014.
- [5] S. B. Wolff and B. P. Ölveczky, "The promise and perils of causal circuit manipulations," *Curr. Opin. Neurobiol.*, vol. 49, pp. 84–94, Apr. 2018.
- [6] B. W. Group, "Brain 2025," p. 146, 2014.
- [7] K. Brose, "Global Neuroscience," *Neuron*, vol. 92, no. 3, pp. 557–558, 2016.

# Chapter 1

## Background

This PhD thesis presents the development of novel tools designed to extend the possibilities of optogenetic studies in neuroscience. The devices and related fabrication techniques created in this work were inspired by, and hopefully will contribute to, the fast-growing outputs of a decades-long, worldwide effort towards neural implants capable of interfacing with the brain and untangle the secrets of its information processing.

**Section 1.1** provides an introduction on neural organisation, electrical signalling in the brain and briefly reviews the main types of devices currently used by neuroscientists for passively recording neural signals *in vivo*. **Section 1.2** introduces the technique known as optogenetics, and key technologies based on guided light currently used to deliver optical stimulation beyond scattering depth in the animal cortex. **Section 1.3** focuses on neural implants embedded with deep-implanted microscale light-emitting diodes, on which this work is based. **Section 1.4** considers aspects of synthetic diamond, used as a substrate for our device.

### 1.1 A brief introduction on the brain and neurons

#### 1.1.1 Organisation of the brain

The human brain contains ~86 billion highly specialised signalling nerve cells (neurons), interconnected by  $\sim 10^{15}$  electrochemical terminals called synapses, and classified into at least a thousand different types [1, p. 22]. Neurons form the basic units responsible for information signalling and processing, and are surrounded by an even larger number of glial cells, whose supporting role is still being investigated.

Neural operation is organised both in functional regions and in local and brain-wide neural circuits [1]. Much of this interplay remains to be understood, with progress typically achieved by piecing together wide-ranging and multidisciplinary data helped by technological development [2]. Of particular interest to this work is the superficial six-layered neocortex region of the mammalian brain (fig 1.1.a), responsible for higher cognitive functions, and whose circuit patterns are only now starting to emerge [3]. The devices developed in this work are designed to allow stimulation of multi-mm deep cortical and sub-cortical layers, typically inaccessible by otherwise powerful optical techniques such as multi-photon microscopy which are inherently limited by high scattering in the brain [4].

### 1.1.2 Neuron and action potentials

Much of the brain's complexity is thought to arise from few organising principles. Neuron structure and passive electrical properties determines their role in processing information within networks.

As an example, a stereotypical neuron may comprise a cell body (*soma*) and two types of connecting processes: short basal dendrites, mostly collecting signal input from afferent neurons, and a long tubular axon, capable of conveying specific electrical signals generated at the soma, without distortion, over distances from 0.1mm to 2m. The axon's end branches into tens to thousands of "terminals", connecting to the dendrites of downstream neurons through an electrochemical interface (synapse) across which the signal is transmitted and modulated by neurotransmitter release (fig 1.1.c).

The neuronal membrane is an insulating lipid bilayer riddled with various types of transmembrane protein complexes acting as ion-specific channels and pumps (fig 1.1.b). These respectively allow passive (diffusion/gradient based) and active (e.g chemically powered) ion transport to and from the extracellular medium. The sustained ion imbalance of  $K^+$ ,  $Na^+$  and  $Cl^-$  (and sometimes  $Ca^{2+}$ ) creates a local "resting" potential difference (e.g -70 to -75 mV) across the membrane at steady state, determined by the competing conductances of the various channels and calculable through the Goldman-Nernst equations [5].

Local depolarisation of the capacitor-like membrane over a certain threshold (+5 to +20 mV) causes an all-or-nothing, phased electrical spiking called an action potential (AP) observed and modelled in landmark studies by Hodgkin & Huxley in 1939 and 1952 [1], [6], [7]. AP comprise i) a fast (~1 ms) rising phase driven by the self-sustained opening of fast-kinetics  $Na^+$  channels, ii) a slower repolarisation phase driven by the delayed opening of  $K^+$  channels,



and iii) a “long” ( $\sim 3$  to  $10$ ms) return to the resting potential during which no more membrane depolarisation can be induced (absolute refractory period) or only with exceptionally strong stimuli (relative refractory period). The AP threshold (determining cell excitability), refractory periods (limiting cell firing rates), and pulse shape and amplitude vary across neurons and are crucial modulating factors for information processing in neural networks.

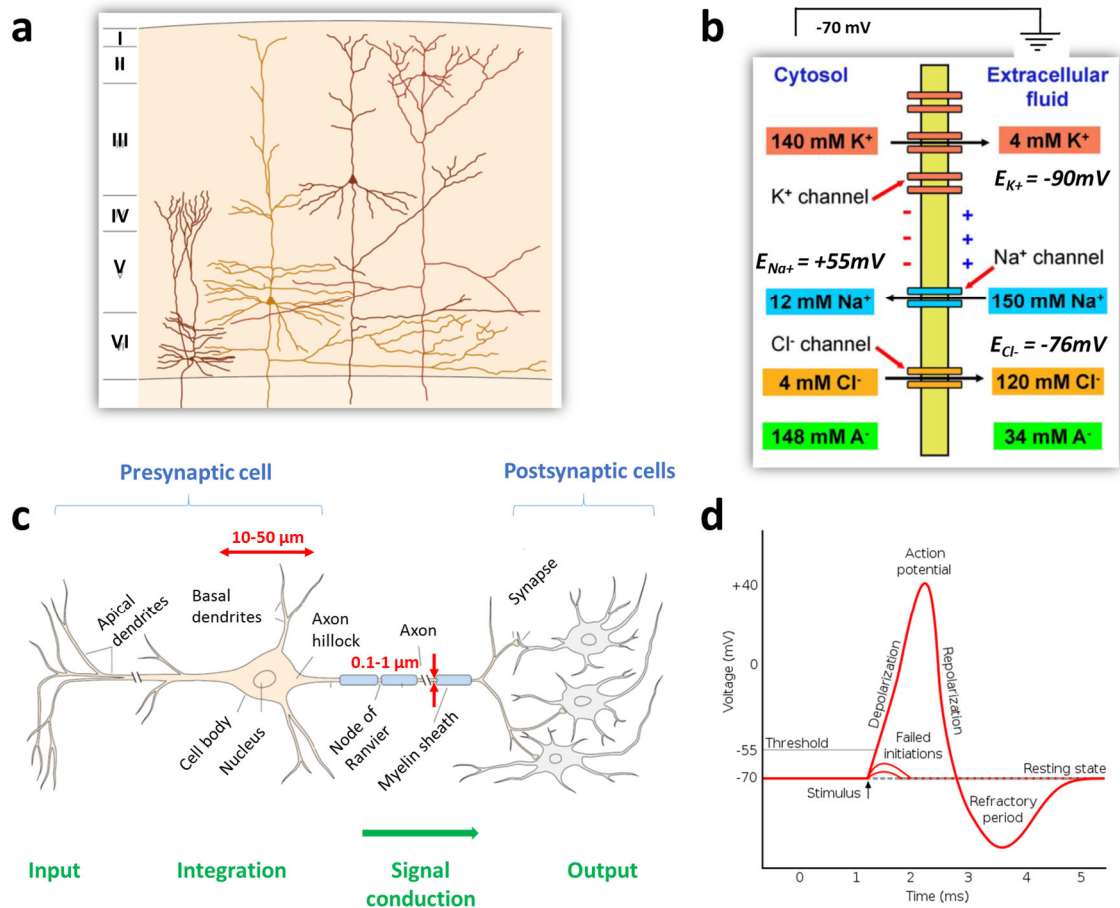


Figure 1.1 **a**) Schematic of the human neocortex (4-6mm deep) showing six distinctive layers characterised by their specific neuronal anatomies and connectivity, related to different functional roles (adapted from [1]). **b**) Schematic of a neuronal membrane, including extra/intra-cellular voltages and the main ion channels whose properties govern the electrical response of the cell (adapted from [8]). **c**) Schematic anatomy of a neuron, adapted from [1] (dimensions and number of dendrites/synapses may vary greatly across neuronal types) **d**) Schematic plot of an action potential (AP, intracellular voltage) showing both sub-threshold stimuli failing to trigger spiking, and a full AP cycle comprising membrane depolarisation, repolarisation and refractory period (from [9]).

Spikes are propagated along the axon at a speed of  $1$  to  $100 \text{ m}\cdot\text{s}^{-1}$ , regularly regenerated at the Nodes of Ranvier (fig 1.1.c), and passed on to downstream neurons either via a conducting bridge or via electrochemical conversion into excitatory/inhibitory postsynaptic potentials (EPSP/IPSP) through neurotransmitter release at the synaptic cleft. Each neuron

performs a temporal or spatial summation of all received upstream impulses at the dendrites, modulated at the axon hillock by the neuron's specific passive properties, thus providing a basic information computing block within a structured neural network.

### 1.1.3 Current devices for neural electrophysiology

The immense complexity of neural information processing may only be comprehended by a combination of the expanding array of techniques available to neuroscientists. Observational methods now include complex *in vitro* studies, brain-wide analysis through e.g magnetic resonance imaging / fMRI and positron emission tomography (PET) [10], cutting-edge histology via tissue clearing, cryoTEM, or super-resolution microscopy [11], [12], or advanced imaging using e.g fluorescence microscopy techniques [13]. For local circuit analysis *in vivo*, the recording of extracellular potential (<500  $\mu$ V range for AP) with penetrating electrodes, first developed in the 1930s, is an approach with exceptional versatility and spatiotemporal resolution. Key recording technologies have vastly improved in the last two decades and are introduced below.

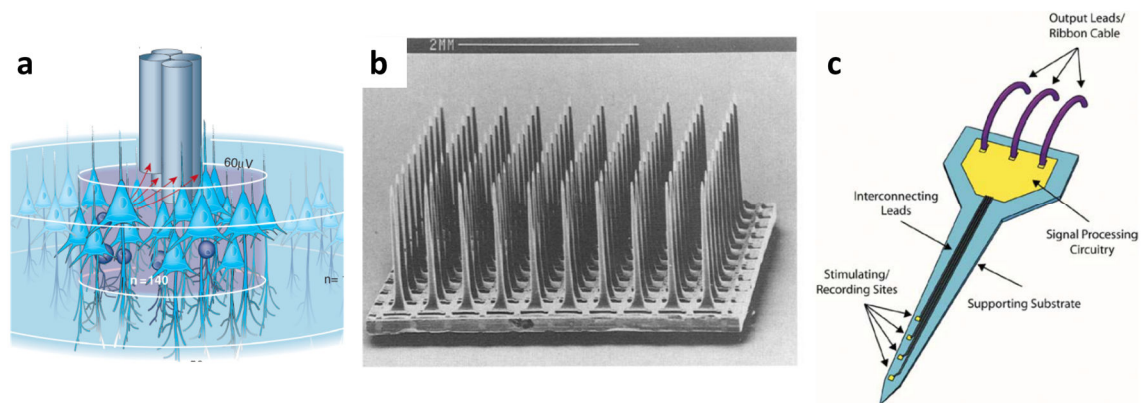


Figure 1.2 : Three influential technologies currently used for neural recordings in mammals. **a)** Schematic of a wire tetrode, registering signals from neurons in its vicinity [14]. **b)** SEM scan of an original 3-D “Utah array” of 100 recording shanks [15]. **c)** Schematic of a “Michigan” single-shank probe with multiple electrode site at the tip, microfabricated using semiconductor/MEMS-type manufacturing [16].

Electrode physics and requirements for electrophysiology have been reviewed elsewhere [17], [18]. Early wire-type microelectrode geometries, often arranged three-dimensionally, are still used [19], [20] including in a tetrode configuration where four very thin (<40 $\mu$ m) metal wires are bundled together (fig 1.2.a), and provide a reliable low-cost solution for deep recordings. A tetrode may record signals from hundreds of neurons within a  $\sim$ 140 $\mu$ m radius [14] and allow discrimination of a few close units thanks to characteristic signal amplitude

variation across its spatially distributed four-channels, but remains a single-depth device with electrode density limited by tetrode pitch.

In the last decades, advanced microfabrication techniques inspired by microelectromechanical systems and the semiconductor industry have been harnessed to produce recording probes with micron-scale features. The well-recognised, FDA-approved “Utah array” technology (fig 1.2.b, commercialised by Blackrock Microsystems [21]) is based on a 3-D array of electrode-tipped shank, with the original device comprising 100 individual recording shanks of 1.5mm length [15]. Later iterations yielded custom shank lengths, lower electrode impedance and higher densities [22]–[24]. These devices have been chronically implanted in primates and tested on humans, and used both in vision and motor prosthesis work [25]–[27].

Another defining design type is the “Michigan probe”, pioneered by Kensall Wise in the 1970s, based on a thin planar structure with photolithographically-defined electrode arrays and traces [28]–[30]. This versatile template has been adapted by many groups, with e.g high electrode density and very long shanks to target the deepest brain regions [16], [31], 3-D stacking for parallel recording [32]–[34], drug delivery [30], [35], mesh structuring for minimal local tissue damage [36], chronic implantation and pH sensing [37]–[39]. Silicon-based devices are commercialised e.g by NeuroNexus Technologies [40]. The Michigan geometry also inspired many impressive flexible polymer probe designs [41]–[43]. A recent notable development is the use of sub-micron technology to achieve ultra-high electrode counts with hundreds of electrode sites per shank [44], potentially with on-probe active electronics afforded by an underlying CMOS structures [45], two major milestones on the way to record from whole circuits at the single-unit level.

The probes developed in this work are of the Michigan type and incorporate both electrodes and light emitters for optical neuronal stimulation through optogenetics.

## 1.2 Optogenetics and guided light implants

While passive observational methods including electrode recording have brought tremendous insights on the structure and function of neural networks, it has long been acknowledged that spatiotemporally precise perturbational techniques could prove invaluable for circuit analysis [46]. Of particular interest is the stimulation of particular cells or circuits while monitoring cell response and its potential correlation to animal behaviour. In the 20<sup>th</sup> century, influence over neuronal activity has mainly been achieved by targeted drug delivery or electrical stimulation, which have brought impressive results both for

research and clinical purposes [47]–[49], but often lack either the cell-specificity or spatiotemporal resolution needed for targeted perturbation of specific neural circuits.

### 1.2.1 Optogenetics : concept, development and applications

In order to probe networks in a controlled manner, researchers aim to selectively activate/silence single cells within a neural environment characterised by its genetic diversity, high packing density ( $\sim 10^5 \text{.mm}^{-3}$  in the mouse cortex [50]) and ms-timescale dynamics. In the past 15 years, advances in optically-based methods and especially optogenetics are allowing this level of discrimination [51], [52].

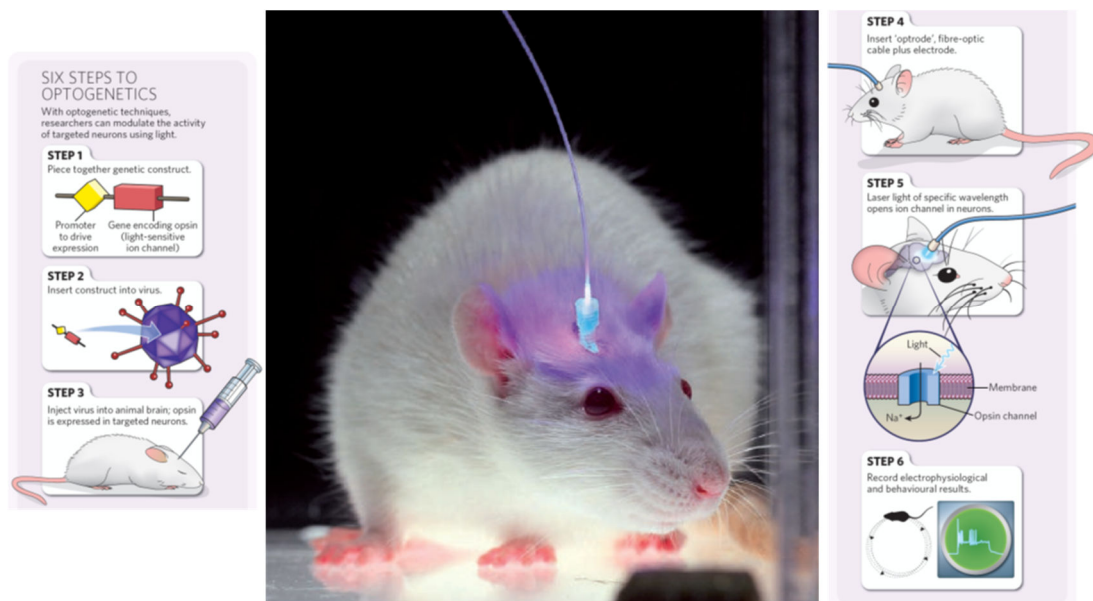


Figure 1.3 : Step-by-step description of an optogenetic experiment with “first-generation” optical fibre light delivery. Modified from [53].

Optogenetics introduces genetically tagged photosensitive proteins called opsins into neuronal membranes in a cell-specific manner, enabling optical control of transmembrane ion flow and the light-driven triggering or suppression of action potentials. Building upon previous work on biological constructs and delivery [54]–[59], single-construct optogenetics was first demonstrated in the live rodent cortex in 2005 [60], using an algal protein called channelrhodopsin (ChR2) acting as a light-gated cation channel, soon used on various animal models [61]–[66]. Selective opsin expression within specific neurons is ensured either by viral injection with a gene-specific promoter, or using *ad hoc* transgenic mice lines [67]. With a peak absorption at  $\sim 473 \text{ nm}$ , at irradiation levels above  $\sim 1 \text{ mW.mm}^{-2}$ , activated ChR2 induces large ( $>500 \text{ pA}$ ) depolarising photocurrents capable of triggering cell spiking with millisecond precision.

Furthermore, continuous work on microbial opsins has yielded a variety of tools to be used for multimodal optical control of neurons. The opsin HaloR/NpHR, a light-gated chloride pump responsive to yellow light (peak  $\sim 590$  nm), was first used in mammals in 2007 [68] and successfully shown to inhibit spiking *in vivo*, and could be co-expressed with ChR2 [69], [70]. Step function opsins can induce stable open/closed states upon initial exposure to blue light, reversible under green light exposure [71]. Multiple optimised tools have been developed since [72], [73], including “silencing” outward proton pumps such as archaerhodopsin (Arch) [74], [75], red-shifted rhodopsin variants such as VChR1 or Chrimson [76], [77], fast-kinetics “Chronos” enabling 60 Hz optical spiking at irradiances below  $0.1 \text{ mW}\cdot\text{mm}^{-2}$  [77], or slow-kinetics variants enabling sustained channel opening for minutes beyond initial light pulses [78].

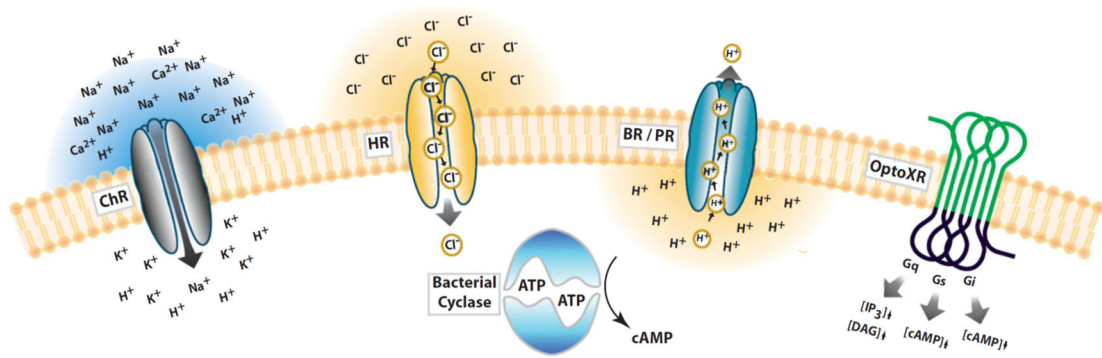


Figure 1.4 : Schematic of some main types of optogenetic tools (taken from [72]).

### 1.2.2 Technologies for intra-cranial light delivery by extraneous sources

In parallel to the continuous refinement of biological tools for neuronal photosensitisation, the development of efficient technologies for intracranial light delivery is essential for “deep” optogenetics to reach its full potential [52]. In the lipid-rich, highly scattering neural tissue, even advanced external-light methods such as multiphoton microscopy cannot achieve optical stimulation beyond a few hundred microns depth [79]. Optogenetics experiments probing  $> \text{mm}$ -deep cortical layers or brain regions therefore require penetrating implants. The large majority of optical probes for optogenetics are based on a guided-light approach, where an extracranial light source is coupled into a implantable, thin structure. This vibrant subfield of neural engineering has produced a great number of prototypes. These are extensively discussed in regularly published reviews of the field [80]–[82], but a few key examples of technologies are presented in figure 1.5.

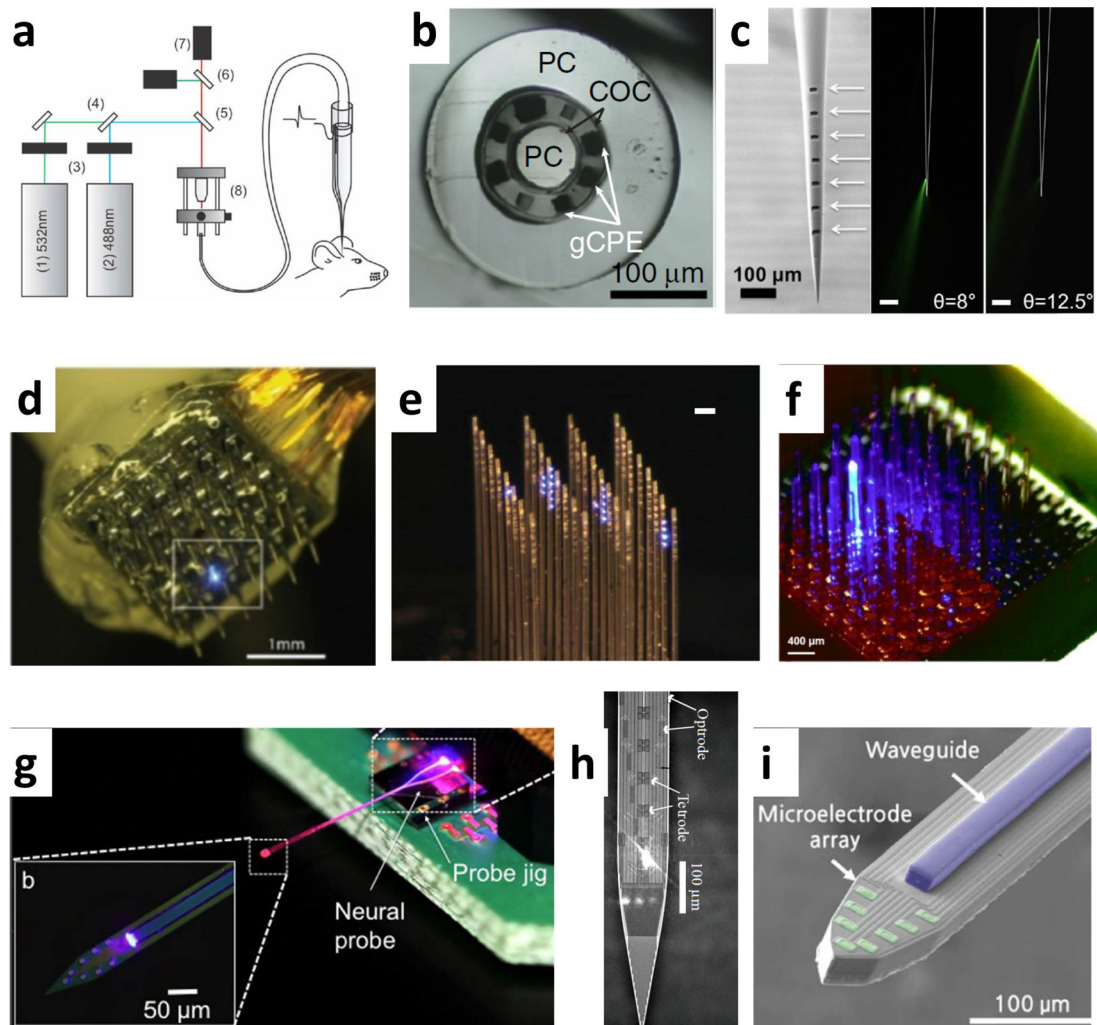


Figure 1.5 : Guided light delivery technologies for deep optogenetics. **a**) Setup for dual-core fiberoptic-based microprobe [83], **b**) Multifunctional fibre comprising a waveguide, six electrodes and two microfluidic channels for “one-step optogenetics” [84], **c**) Metal-coated tapered, windowed optical fibre allowing multipoint emission and mode-division multiplexing with various geometries [85], [86], **d**) Utah array with an electrode substituted with a fibre-coupled optical probe [87], **e**) Optical-fibre coupled 3-D waveguide array [88], **f**) LED-array coupled glass-based “Utah optrode array” [89], Michigan-type optoelectrodes with integrated waveguides coupled to **g**) laser diodes and an optical mixer [90], **h**) high-density  $\text{Si}_x\text{N}_y$  multi-site optrode fabricated with 193nm lithography [91] **i**) grooved probe with attached SU8 waveguide [92].

Design concepts of such guided-light probes can be separated into optical-fibre based devices (fig 1.5 a-c), waveguide devices inspired by the Utah electrode array design (fig 1.5 d and f) and Michigan-style probes embedded with waveguides (fig 1.5 e and g-i). The first optogenetic experiments were carried out with laser-coupled single-core optical fibres [93], [94], a reliable approach still widely used. Improvements on the initial optical fibre technologies include more reliable and size-adaptable devices [95], multi-core fibres for multi-color optogenetics [83], multifunctional fibres integrated with recording and fluidic

capabilities [84], [96], and low-footprint tapered fibres distinctly outcoupling light through multiple small apertures for site-selective light delivery [85], [86].

Other miniaturised optical probes are directly inspired from the Utah- and Michigan-style electrode arrays, and often present both optical stimulation and electrode recording capacity (“optrodes”) allowing simultaneous control and readout of neural circuits. Demonstrated concepts include Utah arrays integrated with optical fibers [87], or directly made of glass needles outcoupling light from backside illumination [89], [97]. 3D optical stimulation has also been proposed by e.g stacking 2D arrays of multi-waveguide Michigan probes [88]. Impressive Michigan recording probes integrated with microfabricated waveguides have also been demonstrated by leading groups in the last decade [90]–[92], [98]–[100], with notable examples shown in fig 1.5 g-i. More detailed comparative examination of such are given in reviews of the advances in the field [80], [82], [101], [102].

The strategy of coupling an external light source to a device yields distinct benefits. It enables modular designs with adaptable, multiple and tunable light inputs for complex optogenetic interrogation; spatially removes potentially damaging heat sources such as high-power laser diodes, etc. from brain tissue; and may facilitate integration with existing microscope setups. However, despite their reliability and proven experimental value, guided-light devices may present drawbacks for some optogenetic protocols. Many devices require tethering for light coupling, which may restrain animal movement with potential effects on behaviour. End-emitting optical fibres often exceed 100 $\mu$ m in lateral dimensions and are limited to a single downward, aperture-determined light emission profile. Microfabricated waveguides are subject to coupling and transmission losses (usually > 5-10dB total [82], [90], [100]), calling for high input optical powers, which can raise issues of stray light, heating of low-efficiency light sources and their surroundings [90], or even potentially detrimental tissue irradiation levels [103]. Finally, most waveguide-based devices are naturally limited to a single emission point as the number of optical emission sites proves a difficult tradeoff with coupling complexity and/or probe footprint, although these may be alleviated by using CMOS-type process platforms levelling high resolution lithographic tools [91].

A different design concept altogether harnesses the properties of e.g micro-sized light-emitting diodes ( $\mu$ LEDs) to directly embed light emitters onto the neural implants, typically as a complement to electrode recording capacities. This is the approach taken in this work and key devices are briefly described in the next section, along with the fundamentals of GaN-based  $\mu$ LEDs which allowed that technology to flourish.

## 1.3 In situ light emitters : LED-based neural implants

### 1.3.1 Light emitting diodes and $\mu$ LEDs

#### o History

Light-emitting diodes (LEDs), now ubiquitous in display, lighting and optoelectronic applications, are the product of decades of continuing technological development. LEDs are semiconductor devices based on electroluminescence, whereby light is spontaneously emitted upon application of an electric current. While the electroluminescence phenomenon was discovered in 1907 [104] and the LED itself in the 1920s [105], active development of LEDs materialised after the 1950s thanks to advances in semiconductor and thin film physics, and epitaxial growth techniques. Sustained research effort led to the first commercially available red GaAs- and GaAsP- based LEDs in the early 1960s, creating an exponentially growing market in numeric LED displays and indicators, followed by the invention of a yellow GaAsP LED by George Craford in 1972 and green LEDs using N-doped GaP, first reliably demonstrated by Ralph Logan in the early 1970s [106].

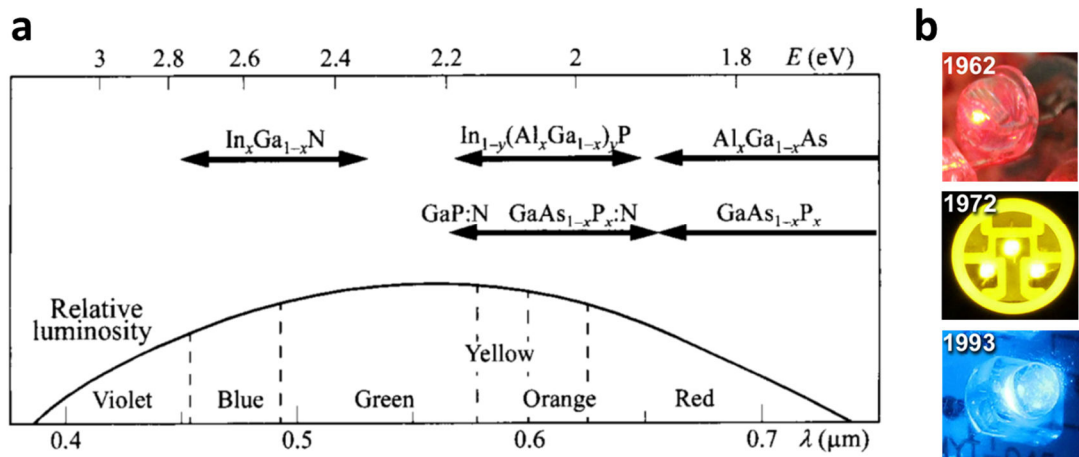


Figure 1.6 : **a)** Semiconductors of interest for LEDs (bottom : relative luminosity function of the human eye) – from [107], **b)** illustration of the development of commercially produced LEDs over 3 decades, including the first red LED based on GaAsP/GaAs (Holonyack 1962), the first yellow LED (GaAsP, Craford 1972) and the first bright blue LED (GaN/InGaN, Nakamura/Nichia 1993).

By contrast, the development of GaN-based devices, long halted after ground-laying work by Maruska and Pankove in the mid-1960s failed to achieve p-type conductivity in GaN, only really rose again in the early 1990s when researchers led notably by Akasaki, Amano and Nakamura in Japan successfully activated Mg acceptors by e-beam irradiation and post-growth annealing, thus demonstrating true p-type doping of GaN. This enabled the first



“bright” blue LEDs with efficiencies >10%, a feat rewarded by the 2014 physics Nobel prize. Commercial LED wavelengths now spans the whole visible spectrum and near infrared (fig 1.6.a), for a market exceeding \$15 billion a year [105].

o *Device physics*

LEDs are semiconductor devices. Semiconductors materials exhibit an electrical conductivity significantly higher than insulators, but lower than metals, and which can be usefully tailored by the controlled introduction of impurities (“doping”) in the crystal structure. According to band theory approximations, electrons within a crystalline semiconductor may only access certain ranges of energies arranged in near-continuous splits called “bands”. The main practically accessible ranges are the valence band (energies of the outermost non-conducting electrons) and the conduction band (energies allowing electronic mobility), separated in semiconductors by a relatively small “bandgap” of a few eV, allowing movement of excited electrons into the conduction band.

In LEDs, the fundamental optical process is that of spontaneous emission, whereby an electron in the conduction band spontaneously returns to an empty state (“hole”) in the valence band, with the emission of a photon. This radiative process is in competition with heat-generating non-radiative recombinations where the electron transition is mediated by phonons necessary to conserve crystal momentum, e.g within “indirect bandgap” materials where the optima of the conduction and valence band are not aligned in k space (fig. 1.7.a). However, even in “direct bandgap” materials normally used for LEDs, various undesired impurities and dislocations may create “trap” energy levels within the bandgap acting as non-radiative recombination centres. Along with Auger recombination, whereby the energy resulting from an electron-hole recombination is transferred to another electron or hole and later dissipated by lattice vibrations, these mechanisms are a major cause of heat losses and efficiency drop in LEDs. The radiative recombination rate  $R_{rad}$  is proportional to the the product of electron and hole densities  $n$  and  $p$ :

$$R_{rad} = Bnp \quad (1.1)$$

where B is the bimolecular radiative recombination coefficient with a unit of  $\text{cm}^3\text{s}^{-1}$ .

High rates of radiative electron-hole recombination are promoted by the fundamental building block of the LED which is the pn junction. A pn junction is formed by appending a region of semiconductor material which is heavily p-doped (implanted with atomic impurities acting as electron acceptors within the crystal structure) to another region which is heavily n-doped with electron donors. As an example, doping concentrations can exceed  $10^{21}.\text{cm}^{-3}$

for Si-doped n-GaN but usually no more than  $\sim 10^{19} \text{ cm}^{-3}$  in Mg-doped p-GaN, a well-known limitation caused by the deep acceptor levels, hydrogen passivation and self-compensation of Mg dopants [108]. Homojunctions employ a unique material, differentially implanted or grown, while heterojunctions such as those found in InGaN devices rely on two materials with different bandgap energies.

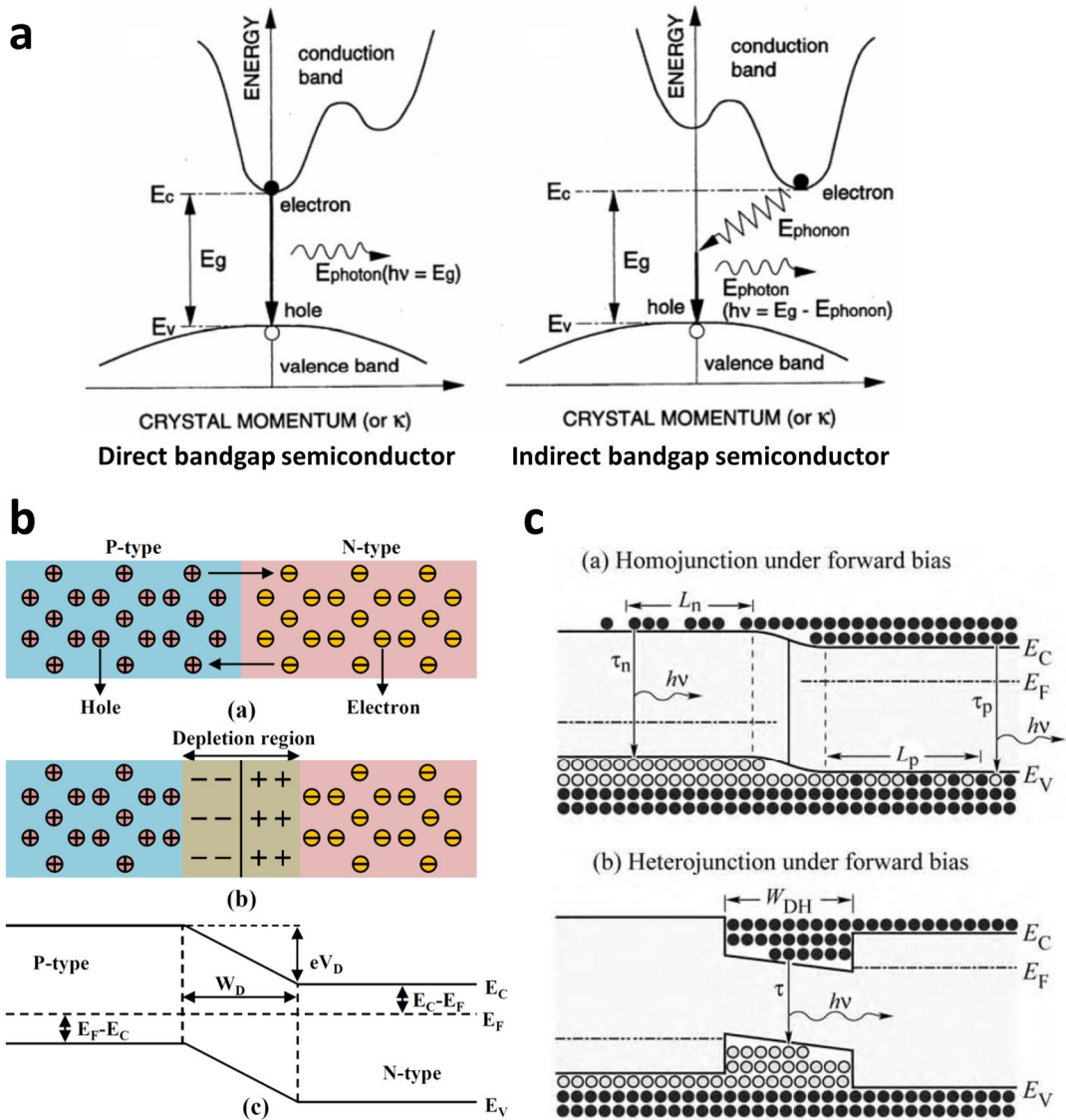


Figure 1.7 : **a**) Schematised band structures of direct (left) and indirect (right) bandgap semiconductors with their band-to-band electron transition processes (from [109]), **b**) Schematics of an unbiased pn junction and **c**) free carrier distribution in a homojunction (top) and a heterojunction (bottom) under forward bias. In heterojunctions, carriers are confined to the well region in contrast to homojunctions where they are distributed over the diffusion lengths, reducing the recombination efficiency.

In an unbiased pn junction, mobile majority carriers immediately diffuse along their gradient across the interface, creating a “depletion region” comprising static ionised dopants –

positively charged donors in the n-type region, negatively charged acceptors in the p-type region, see fig. 1.7.b – creating a barrier potential known as the diffusion voltage  $V_D$ . An external voltage applied to the junction is mainly dropped across the high-resistance depletion region, and will either increase the barrier (reverse bias) or decrease it to promote free carrier mobility (forward bias). Over a certain threshold voltage  $V_T$ , carriers can be injected into the opposite regions, leading to significant current flow, electron-hole recombination and photon generation. In highly doped direct-bandgap semiconductors, both  $V_D$  and  $V_T$  can be approximated by the bandgap energy  $E_g$  divided by the elementary charge  $e$  [106, p. 62]:

$$V_T \approx V_D \approx \frac{E_g}{e} \quad (1.2)$$

The current-voltage (I-V) characteristics of a pn junction are given by the Shockley equation, whose simplified form under forward-bias conditions ( $V \gg kT/e$ ) can be given as :

$$I = I_s \times \left( e^{\frac{V}{nV_t}} - 1 \right) \quad (1.3)$$

Where  $I$  is the diode current,  $I_s$  is the reverse bias leakage current,  $V_t = kT/q$  (with  $q$  the elementary charge) is the thermal voltage and  $n$  is the device-dependent ideality factor which quantifies real-world characteristic deviation from the theoretical diode.

In forward-biased homojunctions, excess carriers typically diffuse into the opposite-type region over an average distance of a few micrometres before recombination (diffusion length). This leads to relatively low carrier densities as shown (fig 1.7.c-, top), and therefore proportionally low radiative recombination rates according to equation (1.1). In order to achieve high  $R_{rad}$ , all high-performance LEDs are thus based on a more efficient heterojunction design, formed of two semiconductors with unequal bandgap energy. The smaller-bandgap material forms the undoped active region, sandwiched between heavily doped p-type and n-type barrier regions of the higher-bandgap material. Injected carriers are then confined to the active region, greatly shortening radiative recombination lifetimes (fig 1.7.c, bottom). When the active region thickness  $W_{DH}$  is comparable to the free carriers De Broglie wavelengths ( $W_{DH} < 10\text{nm}$ ), the active region behaves as a quantum well (QW) with carriers confined in one crystal direction and carrier density inversely proportional to the well width  $L_{QW}$  [106, p. 45]. As a first approximation, the quantized energies of the carriers may then be described, in appropriate situations, by the 1D-infinite well model:

$$E_n = \frac{h^2}{8m^*} \left[ \frac{(n+1)}{L_{QW}} \right]^2 \quad \text{with } n = 0,1,2,3 \dots \quad (1.4)$$

Where  $m^*$  is the effective mass of the carriers and  $h$  is the Planck constant. The emission energy of the QW differs from either bandgap energy of the two semiconductor materials used for the heterojunction, and may be intentionally tuned by changing the QW width or through the use of compounds with a specific bandgap (fig. 1.8). This simple model describes a double heterostructure forming one QW. In most high-performance LEDs such as the ones used in this work, the active region consists of several closely-packed quantum wells, referred to as a multi-quantum well (MQW) region.

o *GaN LEDs and material used in this work*

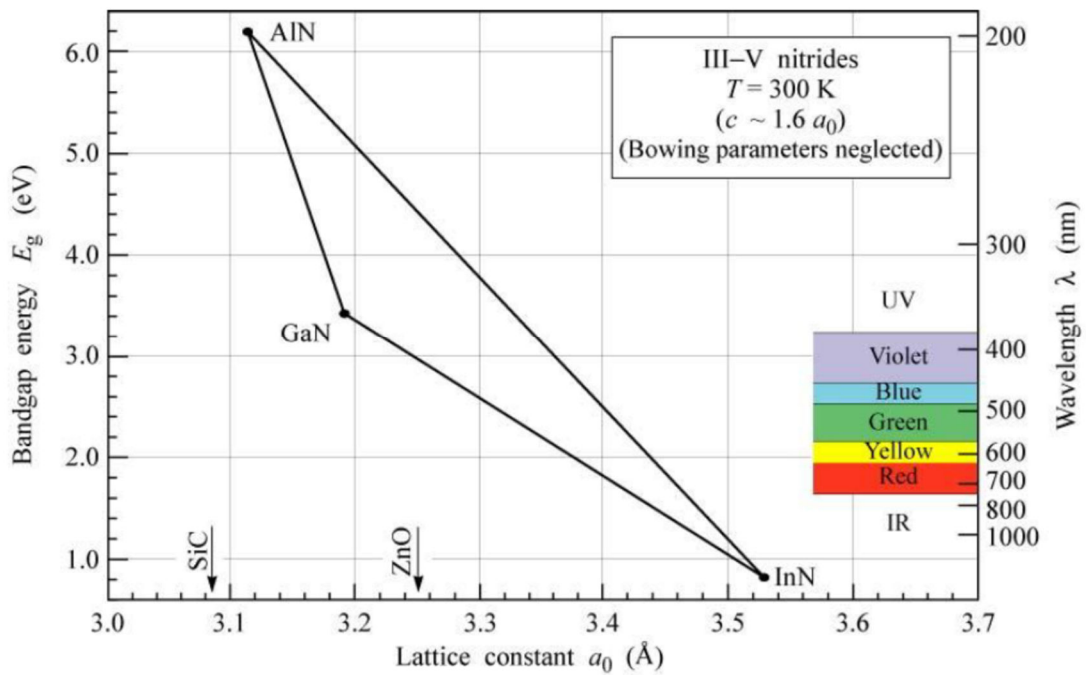


Figure 1.8 : Bandgap energy vs lattice constant  $a_0$  of III-nitride materials at room temperature. The  $\text{AlInGa}_x\text{N}$  system is typically employed in the fabrication of GaN-based LEDs, with  $\text{In}_x\text{Ga}_{1-x}\text{N}$  ternary alloys being direct bandgap materials. After [106], [110].

The micro-sized LEDs ( $\mu\text{LEDs}$ ) developed in this work are fabricated from III-nitride LED wafers, based on three basic binary alloys: AlN, GaN and InN, all exhibiting a hexagonal wurtzite structure in normal ambient conditions. These can form ternary and quaternary alloys with a large range of bandgap energies (see figure 1.8). Importantly,  $\text{In}_x\text{Ga}_{1-x}\text{N}$  ternary alloys are direct bandgaps material and therefore used for the LED active region. The development of efficient GaN-based LED structures is still an area of active research. Highly doped p-type III-nitride material with hole concentrations  $>10^{17} \text{ cm}^{-3}$ , usually based on Mg acceptors, is notoriously difficult to achieve due to the natural n-type of as-grown GaN and

the tendency of Mg to passivate, which can be mitigated by thermal activation post-growth through high-temperature annealing. While the most commonly used substrate for GaN-based LEDs is sapphire, the devices presented in this work were fabricated from material grown on silicon (111) substrates.

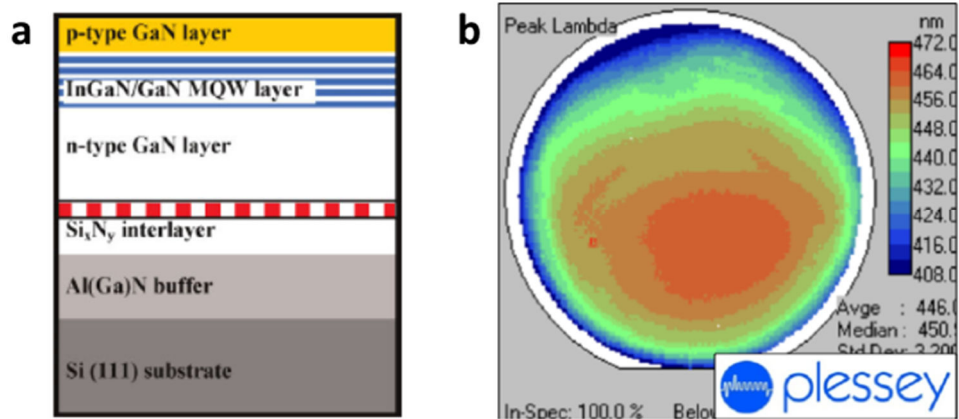


Figure 1.9 : Characteristics of 6-inch GaN-on-Si LED wafers grown by Plessey semiconductors, similar to the material used in this work for  $\mu$ LED fabrication. **a)** Schematic of the epitaxial structure (from [111] and **b)** surface photoluminescence mapping of a produced wafer, showing spatial variations in emission wavelength due to layer inhomogeneities (courtesy of Plessey / adapted from [112]).

The base LED material used in this work is a diced 6-inch GaN-on-Si LED wafer, grown by Plessey semiconductors Ltd using metalorganic vapour phase epitaxy (MOVPE). Full details and challenges of the growth process are found elsewhere [113]–[115]. The epistructure, shown on fig 1.9, is grown on Si(111) which shares a 3-fold symmetry with GaN. Growth starts with an AlN nucleation to prevent Ga reaction with the Si substrate at high temperature (meltback etching). A thick AlGaIn buffer layer, with a graded decrease in Al fraction is then grown on top for stress management: the compressive stress induced in the buffer layer by AlN/AlGaIn lattice mismatch is tailored to compensate the tensile stress resulting from a large (46%) mismatch in thermal coefficient of expansion between GaN and Si. An  $\text{Si}_x\text{N}_y$  interlayer is inserted to reduce threading dislocation densities by an order of magnitude [111], [114]. The LED structure as such is then grown from a Si-doped n-type GaN layer, followed by InGaIn/GaN multiple quantum wells, an high-bandgap AlGaIn current (electron) blocking layer, and an Mg-doped p-type GaN layer. The total III-nitride thickness is  $\sim 2\mu\text{m}$ , and the threading dislocation density is estimated at  $\sim 10^9\text{ cm}^{-3}$  [114], [116].

### 1.3.2 LED-based implantable probes for optogenetics

Compared to guided-light approaches, LED based devices present some very appealing characteristics for optogenetics. Dense, high irradiance micro-sized LED arrays can be fabricated with device lateral dimensions  $<10\mu\text{m}$ , enabling multisite light emission with low power consumption, stable illumination and fast light-switching ability [117]. LED-on shank devices provide depth-controllable, lateral emission profiles particularly suited to the stimulation of layered structures, as opposed to optical fibres or waveguides which are most often limited to downward emission within a light cone [118]. Untethered and with low current requirements,  $\mu\text{LEDs}$  are also more naturally compatible with wirelessly powered implants [118]–[120].

A variety of  $\mu\text{LED}$ -based devices were reported in the past five years, and some influential developments are briefly described below. More extensive discussions can be found in recent reviews of optrode technologies such as that by Alt et al. 2017 [82].

Early efforts by Cao et al. produced an optrode integrated with a commercial LED, capable of both optical stimulation and electrode readout, albeit with a very large ( $>600\times 200\ \mu\text{m}^2$ ) footprint making it unacceptably invasive for actual experiments [121]. An impressive landmark was set by Kim et al. in 2013 with the demonstration of an injectable, fully wireless, hybrid optrode integrating an electrode,  $\mu\text{LEDs}$ , a photodiode and a temperature sensor in multiple layers over a polymer substrate [118]. The device reached optical powers of  $\sim 20\text{mW}/\text{mm}^2$  while maintaining  $< 1^\circ\text{C}$  tissue heating during pulsed operation (10ms) up to 20Hz, and was successfully used to drive conditioned mouse behaviour. The same year, McAlinden et al. at the University of Strathclyde (the author's group) demonstrated a monolithic GaN-on-sapphire device integrated with five  $40\mu\text{m}$ -diameter LEDs capable of irradiances exceeding  $100\text{mW}\cdot\text{mm}^{-2}$  [122], later successfully tested in vivo [123]. Acknowledging the mechanical and thermal limitations of a sapphire substrate, our group then developed parylene-insulated, GaN-on-Si devices yielding multi-shank probe LED arrays with up to 96 efficient  $\mu\text{LEDs}$  (16 per shank), demonstrating layer-specific stimulation in the mouse neocortex with optical power output reaching up to  $400\ \text{mW}\cdot\text{mm}^{-2}$  (Scharf et al., 2016). Devices of a very similar concept, integrating 3 GaN-on-Si  $\mu\text{LEDs}$  onto a shank with 8 electrodes - corresponding to the Neuronexus "Buzsaki" configuration -, were reported by Wu et al. at the University of Michigan [124], with discriminatory stimulation/readout capable of eliciting oscillatory ripples in the CA1 cortical area. Other groups reported similarly-inspired "Michigan-type" probes, e.g as a modular implant with 10 integrated LEDs

but still exhibiting invasive dimensions with a cross-sectional area of  $250 \times 65 \mu\text{m}^2$  (Ayub et al. at IMTEK Freiburg [125]), or even utilising the reverse-biased LED as its own temperature sensor through on-probe circuitry [126].

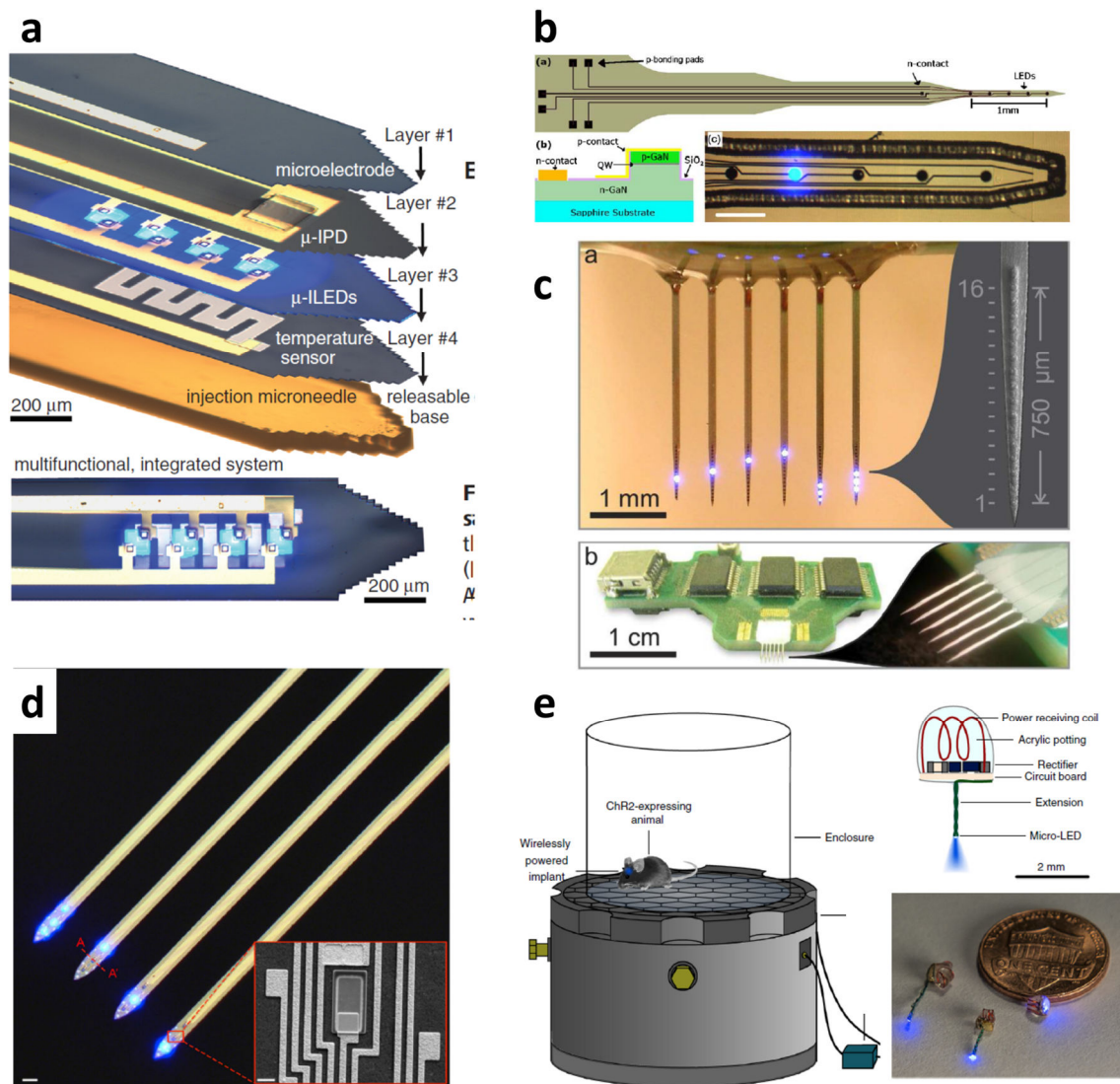


Figure 10 : LED-based optogenetic implants. **a)** Multifunctional, flexible polymer probe integrated with  $\mu$ LEDs by transfer-printing [118], **b)** monolithic GaN-on-sapphire probe design [122] and **c)** GaN-on-silicon multishank probe with 96 LEDs [127], both developed at the University of Strathclyde, **d)** monolithic GaN-on-Si "Neuronexus" probe design integrated with 3 LEDs and 8 electrodes per shank [124], **e)** wireless, low-cost LED implants for dissemination of untethered optogenetics [128].

By contrast, Montgomery et al. developed a low-cost, easily reproducible wireless device capable of single-LED stimulation [128]. Figure 10 presents some of those devices, all except the one in panel a) being capable of optogenetically relevant irradiance levels (i.e.  $>10\text{mW}\cdot\text{mm}^{-2}$  at probe surface) while maintaining a reasonably low cross section ( $< 150\mu\text{m}$  width and  $< 100\mu\text{m}$  thickness) compatible with limited tissue damage at insertion.

### 1.3.3 Thermal challenges of implanted $\mu$ LED emitters

The unique advantages afforded by embedded  $\mu$ LED probes come with potential concerns that must be addressed for this technology to fully mature. As an example,  $\mu$ LED operation typically produces varying, large electric field gradients (typically  $\sim 5V$  difference over a few  $\mu m$ ) within a few  $\mu m$  of wet, ionic brain tissue, likely increasing ion penetration into porous insulation layers and their corrosion/degradation rates. Successful long-term ( $> 1$ month) encapsulation of devices remains an area of active research [41].

Right from the concept stage, an overriding concern for any  $\mu$ LED-embedded design remains that of efficient heat dissipation away from fragile brain tissue. InGaN  $\mu$ LEDs grown on silicon substrates have typical wall-plug efficiencies (ratio of the number of photons emitted to the environment over the number of injected carriers) below 10%, due notably to numerous sidewall non-radiative recombination sites correlated with their high surface-to-volume ratio, and low extraction efficiencies caused by photon trapping in the high-index GaN. The net effect is a significant resistive heat loss squaring with the driving current as described by Joule's first law:

$$P_{heat} \propto RI^2 \quad (1.5)$$

where  $R$  is the dynamic  $\mu$ LED resistance. It is therefore essential to consider safe operation regimes for any LED-based implant to avoid thermally-induced damage in tissue, especially for probes with high densities of light emitters. While determination of definite safety thresholds are a matter of debate, a consensual recommendation states that both peak and average temperature perturbations induced in brain tissue by optical neural implants should not exceed  $1^\circ C$  [129], [130]. (Even more conservative thresholds of  $<0.5^\circ C$  average change have been suggested to avoid any significant perturbation of neural activity).

Despite the high heat capacity of brain tissue, relatively simple numerical models demonstrate that current devices may heat significant tissue volumes ( $>10^5 \mu m^3$ ) during LED operation at electrical powers of a few mW (see sections 5.2.2 and 5.4). Previous analytic and experimental studies of the thermal behaviour of  $\mu$ LEDs and  $\mu$ LED arrays [118], [131]–[134] quantify how heating effects can be mitigated, for a given LED/substrate configuration, by decreasing LED size, increasing LED separation within arrays, decreasing pulse duty cycle, and shaping pulses to limit operation time at peak power. The fundamental bottlenecks however remain i) the imperfect LED efficiency and ii) the thermal limitations of current substrates, which determine the amount and rate of heat dissipation in the brain for a given probe geometry. As an example, silicon-based probes cannot currently offer "heat-safe" high LED



irradiance (approx.  $>50 \text{ mW/mm}^2$ ) with pulse length  $> 100\text{ms}$ , delimiting experimental protocol restrictions. This work aims to push back the limitations of probe substrates by demonstrating neural optrodes based on synthetic diamond, the material with one of the very highest known thermal conductivities ( $\kappa \sim 2000 \text{ W}\cdot\text{m}^{-1}\cdot\text{K}^{-1}$ ).

## 1.4 Synthetic diamond and diamond-based devices

As a material with a unique combination of mechanical, thermal, and even electrical properties, diamond has long been of interest to physicists and engineers despite its rarity in natural form. Since the past two decades, breakthroughs in synthetic diamond growth are paving the way for vast potential applications, notably in photonics and optoelectronics [135], [136].

As a metastable allotrope of carbon, natural diamond occurs at  $\sim 200\text{km}$  underground depth, where temperature and pressure range up to  $1500^\circ\text{C}$  and  $70\text{-}80\text{kbar}$ . The first on high pressure, high temperature (HPHT) industrialised diamond synthesis was reported in 1955 [137]. Synthetic diamond is now grown by low-pressure, high-temperature chemical vapor deposition (CVD), developed at scale since the 1980s [138]. The CVD growth relies on a small carbon fraction ( $<5\%$ ) and high concentrations of dissociated hydrogen at growth temperatures  $> 700^\circ\text{C}$  to enhance surface kinetics. The CVD plasma is usually struck by hot filament methods or microwave [139], [140] in a  $\text{H}_2$  ambient.  $\text{H}_2$  reacts with  $\text{sp}/\text{sp}^2$  surface carbon to allow formation of the  $\text{sp}^3$  carbon needed for diamond growth.

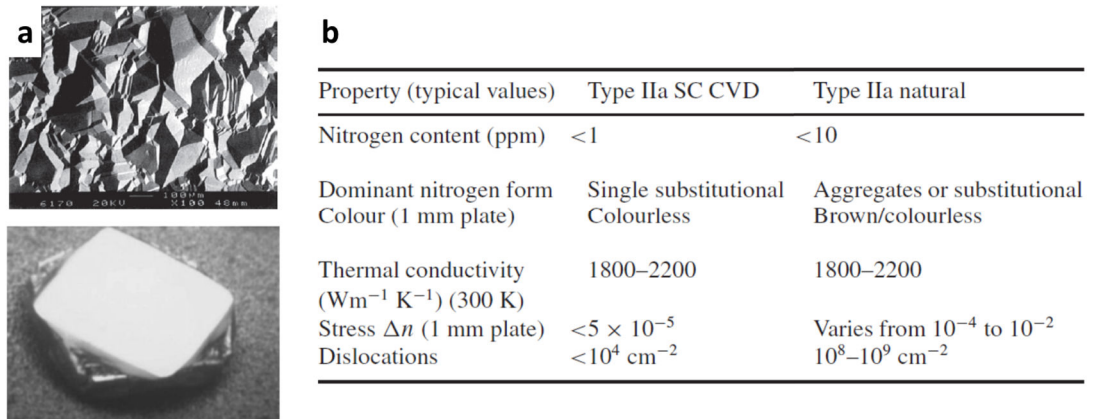


Figure 11 : Some characteristics of CVD diamond. **a)** (top) SEM scan of a polycrystalline sample showing granular structure and (bottom) image of a single-crystal sample grown atop a natural diamond seed (adapted from [140]). **b)** Comparison of properties for natural and synthetic diamond (from [138]).

CVD diamond can be grown as polycrystalline material (PC), of varying grain size controlled by deposition parameters [141] and grown from seed nucleation sites, or single-crystal

material (SC) typically grown atop a natural diamond crystal [142]. Both can then be lifted off or etched from their native substrate to provide freestanding films. As SC diamond is grown homoepitaxially, sample sizes are largely governed by the initial substrate sizes, and current SC membranes are typically smaller than 10x10mm<sup>2</sup>. However, SC diamond generally exhibits better mechanical or thermal properties than its PC counterparts, as grain interfaces provide both fracture points and phonon scattering sites lowering thermal conductivity.

Despite these practical challenges, CVD diamond is now being used in a variety of applications, notably as an established heat sink material for high-power lasers and LEDs [143], but also in the biomedical field. Thanks to its mechanical integrity and chemical inertness, CVD diamond does not degrade *in vivo* and shows high promise for biomedical coatings; furthermore, its electrical conductivity can be tuned through boron doping and diamond microelectrodes have been successfully demonstrated *in vivo* for both electrical recordings and electrochemical sensing [144]–[147].

In the specific context of LED-based optogenetics, diamond-based devices are becoming an even more appealing route thanks to the extraordinary thermal conductivity of diamond, the highest of any known bulk material at room temperature. CVD diamond is a natural candidate for a biocompatible, biostable, electrically insulating substrate acting as a very efficient heat sink for implanted LEDs operating at relatively high power (heat loss > mW). However, GaN LED epistuctures cannot directly be grown on diamond substrates and this design concept requires heterogeneous integration. Furthermore, etch-based micropatterning of diamond substrates with feature size similar to the more common Si devices presented above remains challenging due to the material's exceptional stability [148].

Because of these microfabrication challenges, only one diamond-based optrode has so far been reported. In 2015, Fan et al. demonstrated a polycrystalline diamond-based neural probe with 4 recording sites mounted with two commercial  $\mu$ LEDs [149]. The probe was able to excite and record ChR2-transfected neurons *in vivo* and exhibited vastly superior properties compared with a similar SU8-based design, with a measured maximum temperature increase at the tip of  $\Delta T < 2^\circ\text{C}$  for 1Hz, 100ms pulses at 3.4V stimulation voltage (versus  $\Delta T > 10^\circ\text{C}$  for the SU8 version; currents not given).

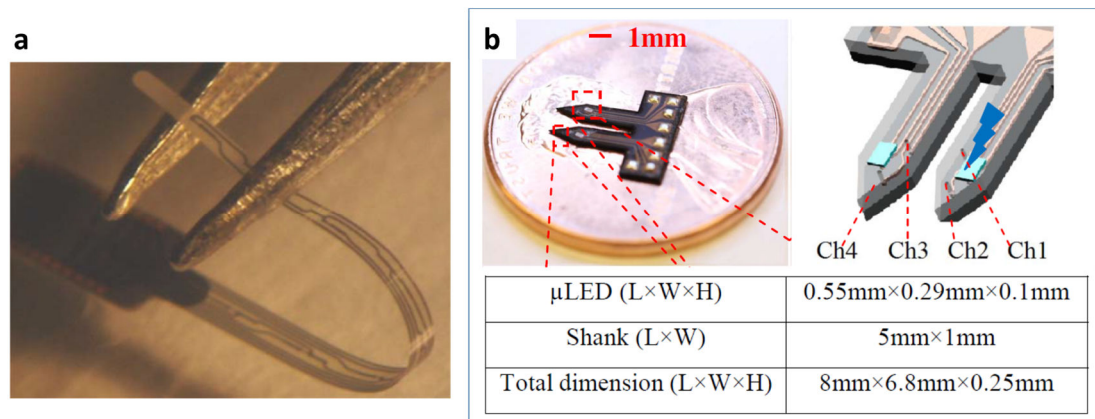


Figure 12 : Previous neural probes based on CVD diamond (polycrystalline). **a)** Flexible ultrathin probe with boron-doped electrodes for electrochemical sensing (from [146], [150]) and **b)** diamond-based optrode demonstrated by Fan et al. (adapted from [149]).

However, the relatively long ( $\sim 1$ s) cooloff times reported post-60s stimulation point to a limited thermal contact between probe and LED possibly due to the solder paste used, although this point was not fully characterised. A major limitation of these devices was their dimensions: with a  $300\mu\text{m}$ -wide LED atop a 1mm wide shank, the probe was still too invasive by an order of magnitude to be used in actual optogenetic experiments. While this work was not followed up, it still yielded a proof-of-concept prototype as a baseline for further improvement.

## 1.5 Targets for the present work – implant specifications

As described above, despite the substantial interest in the neuroscience community for LED-based implants for acute *in vivo* optogenetic experiments in mammals, suitable devices capable of high-irradiance protocols are lacking as current technologies fail in either optical output, insertion footprint, or heatsinking capacity. This creates a gap in opportunity for neuroscientists by hindering the development of protocols for e.g. circuit neuronal inhibition potentially requiring multisite long pulses, or lateral deep area stimulation difficult to attain through guided light schemes [72], [82].

The present work focuses on developing a novel diamond-based  $\mu$ LED implant seeking to bridge that capacity gap, working within the stringent requirements of electrophysiology. The desired performance metrics and design constraints were quantified from existing literature and direct exchanges with neuroscientist colleagues at the Strathclyde Institute of Pharmacy and Biomedical Sciences (SIPBS, University of Strathclyde). An example of specifications meeting the needs for current acute experiments in the deep cortical &

subcortical layers are given in table 1.1. These are given for a “Michigan-style” probe design, which is the one chosen for this work (see section 4.2).

Main parameters	Example of specifications : $\mu$ LED-based optrode for sub-cortical optogenetics & acute experiment in mammals
Device shank dimensions	Length > 4 mm to access deep sub-cortical structures [1, p. 345] Width : $\leq 100\mu\text{m}$ , Thickness : $\leq 40\mu\text{m}$ (minimal invasiveness [52])
Thermal budget	Chronic heating of brain tissue < 0.5°C to < 1°C threshold [72], [151]
Mechanical properties	(If rigid probe) No breaking point nor buckling. (Chronic experiments may favour flexible devices to limit tissue damage [41])
Light emission for optogenetics  And  Optical stimulation protocols	Multiple LEDs, at pitch < 300 $\mu\text{m}$ for cortical-layer confined excitation ChR2 excitation : $\lambda_{\text{peak}} \sim 470 \text{ nm}$ Irradiance range : 0.1 mW/mm <sup>2</sup> to >100 mW/mm <sup>2</sup> : excitation from single cell to $\sim 10^4$ neurons  <i>Typical protocols for blue wavelength activation :</i> ChR2 – 470 nm – 1mW/mm <sup>2</sup> (at soma) – pulses 1 to 50 ms, 0 to 100 Hz Chronos - 480 nm – 0.1mW/mm <sup>2</sup> – pulses 1 to 50 ms, 0 to 100 Hz
Electrodes recording	(Signal detection possible up to 150 $\mu\text{m}$ cell dist. from electrode [152]) Signal range (spikes) : $\sim 100\mu\text{V}$ to 500 $\mu\text{V}$ (noise $\sim 5\text{-}20\mu\text{V}$ ) Density/spacing: ideally cell-size ( $\sim 10 \mu\text{m}$ pitch). > 1 electrode per LED
Biocompatibility and lifetime in vivo	Biocompatible materials with limited insertion & inflammation damage
Other	Scalability to arrays (2D / 3D) Small-footprint, low-weight PCB connection

Table 1.1 : Selected examples of quantified requirements constraining the design of our diamond optrode, either drawn from the literature or from direct demand of neuroscientist collaborators.

The specifications listed above were carefully established to reflect the best possibilities offered by the microfabrication and hybrid integration technologies available within the project. They provided the driving constraints and targets for the design of all devices in this work (chapter 4).

## **1.6 Summary**

Optogenetics presents a very high potential for investigating causality in neural networks, and can greatly benefit from the development of efficient LED-based devices. This work is dedicated to the design, fabrication and testing of a novel diamond-based optrode able to meet the stringent specifications of optogenetic experiments, and to compete in dimensions and functional capabilities with similar silicon-based devices. To achieve this goal, an array of microfabrication techniques were used which are described in chapter 2 of this thesis. Efficient, low-footprint  $\mu$ LEDs were developed along with an advanced heterogeneous integration method based on the University of Strathclyde's transfer-printing platform, in order to accurately position light emitters with a good thermal contact on the diamond base (chapter 3). A full fabrication process was developed to yield a working diamond optrode with up to 8 LEDs and 16 electrodes per device (chapter 4), which was fully modelled and characterised (chapter 5).

## 1.7 References

- [1] E. R. Kandel, J. H. Schwartz, T. M. Jessell, S. A. Siegelbaum, and A. J. Hudspeth, *Principles of Neural Science, Fifth Edition*, vol. 3. 2014.
- [2] I. Soltesz, “The Brain Prize 2011. From Microcircuit Organization to Constellations of Brain Rhythms,” *Trends Neurosci.*, vol. 34, no. 10, pp. 501–503, 2011.
- [3] K. D. Harris and G. M. G. Shepherd, “The neocortical circuit: themes and variations,” *Nat. Neurosci.*, vol. 18, no. 2, pp. 170–181, 2015.
- [4] D. R. Miller, J. W. Jarrett, A. M. Hassan, and A. K. Dunn, “Deep tissue imaging with multiphoton fluorescence microscopy,” *Curr. Opin. Biomed. Eng.*, vol. 4, pp. 32–39, Dec. 2017.
- [5] B. Hille, “Ion Channels of Excitable Membranes,” *Sunderland, Mass Sinauer Assoc. Inc. p. 5. ISBN 0-87893-321-2.*, 2001.
- [6] A. L. HODGKIN and A. F. HUXLEY, “Action Potentials Recorded from Inside a Nerve Fibre,” *Nature*, vol. 144, no. 3651, pp. 710–711, Oct. 1939.
- [7] A. L. Hodgkin and A. F. Huxley, “A quantitative description of membrane current and its application to conduction and excitation in nerve,” *J. Physiol.*, vol. 117, no. 4, pp. 500–544, Aug. 1952.
- [8] A. Hiellermann, S. Hafizovic, and F. Heer, “Growing Cells Atop Microelectronic Chips: Interfacing Electrogenic Cells In Vitro With CMOS-Based Microelectrode Arrays,” *Adv. Funct. Mater.*, vol. 99, no. 2, 2011.
- [9] Wikimedia Foundation, “Wikimedia Commons,” *Online*. [Online]. Available: <http://commons.wikimedia.org>. [Accessed: 01-Aug-2018].
- [10] R. A. Poldrack and M. J. Farah, “Progress and challenges in probing the human brain,” *Nature*, vol. 526, no. 7573, pp. 371–379, 2015.
- [11] J. W. Lichtman and W. Denk, “The big and the small: Challenges of imaging the brain’s circuits,” *Science (80- )*, vol. 334, no. 6056, pp. 618–623, 2011.
- [12] K. Chung and K. Deisseroth, “CLARITY for mapping the nervous system,” *Nat. Methods*, vol. 10, no. 6, pp. 508–513, 2013.
- [13] D. S. Peterka, H. Takahashi, and R. Yuste, “Imaging Voltage in Neurons,” *Neuron*, vol. 69, no. 1, pp. 9–21, 2011.
- [14] G. Buzsáki, “Large-scale recording of neuronal ensembles,” *Nat. Neurosci.*, vol. 7, no. 5, pp. 446–451, 2004.
- [15] C. T. Nordhausen, E. M. Maynard, and R. A. Normann, “Single unit recording capabilities of a 100 microelectrode array,” *Brain Res.*, vol. 726, no. 1–2, pp. 129–140, 1996.
- [16] K. D. Wise, D. J. Anderson, J. F. Hetke, D. R. Kipke, and K. Najafi, “Wireless Implantable Microsystems: High-Density Electronic Interfaces to the Nervous System,” *Proc. IEEE*, vol. 92,

- no. 1, pp. 76–97, Jan. 2004.
- [17] D. R. Merrill, M. Bikson, and J. G. R. Jefferys, “Electrical stimulation of excitable tissue: Design of efficacious and safe protocols,” *J. Neurosci. Methods*, vol. 141, no. 2, pp. 171–198, 2005.
- [18] S. F. Cogan, “Neural stimulation and recording electrodes,” *Annu. Rev. Biomed. Eng.*, vol. 10, pp. 275–309, 2008.
- [19] J. C. Williams, R. L. Rennaker, and D. R. Kipke, “Long-term neural recording characteristics of wire microelectrode arrays implanted in cerebral cortex,” *Brain Res. Protoc.*, vol. 4, no. 3, pp. 303–313, 1999.
- [20] W. T. Tseng, C. T. Yen, and M. L. Tsai, “A bundled microwire array for long-term chronic single-unit recording in deep brain regions of behaving rats,” *J. Neurosci. Methods*, vol. 201, no. 2, pp. 368–376, 2011.
- [21] “Blackrock Microsystems.” [Online]. Available: <http://blackrockmicro.com/electrode-main/>.
- [22] H. A. C. Wark, K. S. Mathews, R. A. Normann, and E. Fernandez, “Behavioral and cellular consequences of high-electrode count Utah Arrays chronically implanted in rat sciatic nerve,” *J. Neural Eng.*, vol. 11, no. 4, 2014.
- [23] X. Xie, L. Rieth, S. Negi, R. Bhandari, R. Caldwell, R. Sharma, P. Tathireddy, and F. Solzbacher, “Self-aligned tip deinsulation of atomic layer deposited Al<sub>2</sub>O<sub>3</sub> and parylene C coated Utah electrode array based neural interfaces,” *J. Micromechanics Microengineering*, vol. 24, no. 3, 2014.
- [24] S. Negi, R. Bhandari, L. Rieth, and F. Solzbacher, “In vitro comparison of sputtered iridium oxide and platinum-coated neural implantable microelectrode arrays,” *Biomed. Mater.*, vol. 5, no. 1, p. 15007, 2010.
- [25] E. M. Maynard, C. T. Nordhausen, and R. A. Normann, “The Utah Intracortical Electrode Array: A recording structure for potential brain-computer interfaces,” *Electroencephalogr. Clin. Neurophysiol.*, vol. 102, no. 3, pp. 228–239, 1997.
- [26] L. R. Hochberg, D. Bacher, B. Jarosiewicz, N. Y. Masse, J. D. Simeral, J. Vogel, S. Haddadin, J. Liu, S. S. Cash, P. Van Der Smagt, and J. P. Donoghue, “Reach and grasp by people with tetraplegia using a neurally controlled robotic arm,” *Nature*, vol. 485, no. 7398, pp. 372–375, 2012.
- [27] R. A. Normann and E. Fernandez, “Clinical applications of penetrating neural interfaces and Utah Electrode Array technologies,” *J. Neural Eng.*, vol. 13, no. 6, p. 061003, 2016.
- [28] K. D. Wise, J. B. Angell, and A. Starr, “An Integrated-Circuit Approach to Extracellular Microelectrodes,” *IEEE Trans. Biomed. Eng.*, vol. BME-17, no. 3, pp. 238–247, 1970.
- [29] K. D. Wise and J. B. Angell, “A Low-Capacitance Multielectrode Probe for Use in Extracellular Neurophysiology,” *IEEE Trans. Biomed. Eng.*, vol. BME-22, no. 3, pp. 212–219, 1975.
- [30] K. D. Wise, A. M. Sodagar, Ying Yao, M. N. Gulari, G. E. Perlin, and K. Najafi, “Microelectrodes, Microelectronics, and Implantable Neural Microsystems,” *Proc. IEEE*, vol. 96, no. 7, pp. 1184–

- 1202, Jul. 2008.
- [31] K. Najafi, K. D. Wise, and T. Mochizuki, "A high-yield IC-compatible multichannel recording array," *IEEE Trans. Electron Devices*, vol. 32, no. 7, pp. 1206–1211, Jul. 1985.
- [32] J. Du, M. L. Roukes, and S. C. Masmanidis, "Dual-side and three-dimensional microelectrode arrays fabricated from ultra-thin silicon substrates," *J. Micromechanics Microengineering*, vol. 19, p. 075008, 2009.
- [33] F. Barz, O. Paul, and P. Ruther, "Modular assembly concept for 3D neural probe prototypes offering high freedom of design and alignment precision," *Conf. Proc. ... Annu. Int. Conf. IEEE Eng. Med. Biol. Soc. IEEE Eng. Med. Biol. Soc. Annu. Conf.*, vol. 2014, pp. 3977–3980, 2014.
- [34] G. Rios, E. V. Lubenov, D. Chi, M. L. Roukes, and A. G. Siapas, "Nanofabricated Neural Probes for Dense 3-D Recordings of Brain Activity," *Nano Lett.*, vol. 16, no. 11, pp. 6857–6862, 2016.
- [35] P. Rohatgi, N. B. Langhals, D. R. Kipke, and P. G. Patil, "In vivo performance of a microelectrode neural probe with integrated drug delivery," *Neurosurg. Focus*, vol. 27, no. 1, p. E8, 2009.
- [36] J. P. Seymour, "Advanced polymer-based microfabricated neural probes using biologically driven designs," *Univ. Michigan Diss.*, pp. 1–144, 2009.
- [37] J. P. Seymour, Y. M. Elkasabi, H. Y. Chen, J. Lahann, and D. R. Kipke, "The insulation performance of reactive parylene films in implantable electronic devices," *Biomaterials*, vol. 30, no. 31, pp. 6158–6167, 2009.
- [38] R. J. Vetter, J. C. Williams, J. F. Hetke, E. A. Nunamaker, and D. R. Kipke, "Chronic neural recording using silicon-substrate microelectrode arrays implanted in cerebral cortex," *IEEE Trans. Biomed. Eng.*, vol. 51, no. 6, pp. 896–904, 2004.
- [39] M. D. Johnson, O. E. Kao, and D. R. Kipke, "Spatiotemporal pH dynamics following insertion of neural microelectrode arrays," *J. Neurosci. Methods*, vol. 160, no. 2, pp. 276–287, 2007.
- [40] Neuronexus, "Neural Probes," 2018. [Online]. Available: <http://neuronexus.com/products/neural-probes/>. [Accessed: 01-Sep-2018].
- [41] M. Jorfi, J. L. Skousen, C. Weder, and J. R. Capadona, "Progress towards biocompatible intracortical microelectrodes for neural interfacing applications," *J. Neural Eng.*, vol. 12, no. October, p. 011001, 2015.
- [42] S. A. Hara, B. J. Kim, J. T. W. Kuo, C. D. Lee, E. Meng, and V. Píkov, "Long-term stability of intracortical recordings using perforated and arrayed Parylene sheath electrodes," *J. Neural Eng.*, vol. 13, no. 6, p. 066020, Dec. 2016.
- [43] L. Luan, X. Wei, Z. Zhao, J. J. Siegel, O. Potnis, C. A. Tuppen, S. Lin, S. Kazmi, R. A. Fowler, S. Holloway, A. K. Dunn, R. A. Chitwood, and C. Xie, "Ultraflexible nanoelectronic probes form reliable, glial scar-free neural integration," *Sci. Adv.*, vol. 3, no. 2, p. e1601966, 2017.
- [44] J. Scholvin, J. P. Kinney, J. G. Bernstein, C. Moore-Kochlacs, N. Kopell, C. G. Fonstad, and E. S. Boyden, "Close-packed silicon microelectrodes for scalable spatially oversampled neural recording," *IEEE Trans. Biomed. Eng.*, vol. 63, no. 1, pp. 120–130, 2016.



- [45] J. J. Jun, N. A. Steinmetz, J. H. Siegle, D. J. Denman, M. Bauza, B. Barbarits, A. K. Lee, C. A. Anastassiou, A. Andrei, Ç. Aydin, M. Barbic, T. J. Blanche, V. Bonin, J. Couto, B. Dutta, S. L. Gratiy, D. A. Gutnisky, M. Häusser, B. Karsh, P. Ledochowitsch, C. M. Lopez, C. Mitelut, S. Musa, M. Okun, M. Pachitariu, J. Putzeys, P. D. Rich, C. Rossant, W. L. Sun, K. Svoboda, M. Carandini, K. D. Harris, C. Koch, J. O’Keefe, and T. D. Harris, “Fully integrated silicon probes for high-density recording of neural activity,” *Nature*, vol. 551, no. 7679, pp. 232–236, 2017.
- [46] F. H. Crick, “Thinking about the brain.,” *Sci. Am.*, 1979.
- [47] M. R. Cohen and W. T. Newsome, “What electrical microstimulation has revealed about the neural basis of cognition,” *Curr. Opin. Neurobiol.*, vol. 14, no. 2, pp. 169–177, Apr. 2004.
- [48] N. K. Logothetis, M. Augath, Y. Murayama, A. Rauch, F. Sultan, J. Goense, A. Oeltermann, and H. Merkle, “The effects of electrical microstimulation on cortical signal propagation,” *Nat. Neurosci.*, vol. 13, no. 10, pp. 1283–1291, 2010.
- [49] H. S. Mayberg, A. M. Lozano, V. Voon, H. E. McNeely, D. Seminowicz, C. Hamani, J. M. Schwalb, and S. H. Kennedy, “Deep Brain Stimulation for Treatment-Resistant Depression,” *Neuron*, vol. 45, no. 5, pp. 651–660, Mar. 2005.
- [50] A. Schüz and G. Palm, “Density of neurons and synapses in the cerebral cortex of the mouse,” *J. Comp. Neurol.*, vol. 286, no. 4, pp. 442–455, Aug. 1989.
- [51] J. G. Bernstein and E. S. Boyden, “Optogenetic tools for analyzing the neural circuits of behavior,” *Trends Cogn. Sci.*, vol. 15, no. 12, pp. 592–600, Dec. 2011.
- [52] G. Buzsáki, E. Stark, A. Berényi, D. Khodagholy, D. R. Kipke, E. Yoon, and K. D. Wise, “Tools for probing local circuits: High-density silicon probes combined with optogenetics,” *Neuron*, vol. 86, no. 1, pp. 92–105, 2015.
- [53] L. Buchen, “Neuroscience: Illuminating the brain,” *Nature*, vol. 465, no. 7294, pp. 26–28, May 2010.
- [54] R. L. Fork, “Laser stimulation of nerve cells in *Aplysia*,” *Science (80- )*, 1971.
- [55] E. M. Callaway and L. C. Katz, “Photostimulation using caged glutamate reveals functional circuitry in living brain slices.,” *Proc. Natl. Acad. Sci.*, 1993.
- [56] B. V. Zemelman, G. A. Lee, M. Ng, and G. Miesenböck, “Selective photostimulation of genetically chARGed neurons,” *Neuron*, 2002.
- [57] B. V. Zemelman, N. Nesnas, G. A. Lee, and G. Miesenböck, “Photochemical gating of heterologous ion channels: Remote control over genetically designated populations of neurons,” *Proc. Natl. Acad. Sci.*, 2003.
- [58] S. Q. Lima and G. Miesenböck, “Remote control of behavior through genetically targeted photostimulation of neurons,” *Cell*, 2005.
- [59] M. Volgraf, P. Gorostiza, R. Numano, R. H. Kramer, E. Y. Isacoff, and D. Trauner, “Allosteric control of an ionotropic glutamate receptor with an optical switch,” *Nat. Chem. Biol.*, 2006.
- [60] E. S. Boyden, F. Zhang, E. Bamberg, G. Nagel, and K. Deisseroth, “Millisecond-timescale,

- genetically targeted optical control of neural activity.," *Nat. Neurosci.*, vol. 8, no. 9, pp. 1263–8, 2005.
- [61] G. Nagel, T. Szellas, W. Huhn, S. Kateriya, N. Adeishvili, P. Berthold, D. Ollig, P. Hegemann, and E. Bamberg, "Channelrhodopsin-2, a directly light-gated cation-selective membrane channel," *Proc. Natl. Acad. Sci.*, 2003.
- [62] G. Nagel, T. Szellas, S. Kateriya, N. Adeishvili, P. Hegemann, and E. Bamberg, "Channelrhodopsins: directly light-gated cation channels," *Biochem. Soc. Trans.*, 2005.
- [63] G. Nagel, M. Brauner, J. F. Liewald, N. Adeishvili, E. Bamberg, and A. Gottschalk, "Light activation of Channelrhodopsin-2 in excitable cells of *Caenorhabditis elegans* triggers rapid behavioral responses," *Curr. Biol.*, 2005.
- [64] C. Schroll, T. Riemensperger, D. Bucher, J. Ehmer, T. Völler, K. Erbguth, B. Gerber, T. Hendel, G. Nagel, E. Buchner, and A. Fiala, "Light-Induced Activation of Distinct Modulatory Neurons Triggers Appetitive or Aversive Learning in *Drosophila* Larvae," *Curr. Biol.*, 2006.
- [65] L. Petreanu, D. Huber, A. Sobczyk, and K. Svoboda, "Channelrhodopsin-2-assisted circuit mapping of long-range callosal projections.," *Nat. Neurosci.*, vol. 10, no. 5, pp. 663–8, 2007.
- [66] B. R. Arenkiel, J. Peca, I. G. Davison, C. Feliciano, K. Deisseroth, G. J. J. Augustine, M. D. Ehlers, and G. Feng, "In Vivo Light-Induced Activation of Neural Circuitry in Transgenic Mice Expressing Channelrhodopsin-2," *Neuron*, 2007.
- [67] F. Zhang, V. Gradinaru, A. R. Adamantidis, R. Durand, R. D. Airan, L. de Lecea, and K. Deisseroth, "Optogenetic interrogation of neural circuits: technology for probing mammalian brain structures.," *Nat. Protoc.*, vol. 5, no. 3, pp. 439–56, 2010.
- [68] F. Zhang, L.-P. Wang, M. Brauner, J. F. Liewald, K. Kay, N. Watzke, P. G. Wood, E. Bamberg, G. Nagel, A. Gottschalk, and K. Deisseroth, "Multimodal fast optical interrogation of neural circuitry," *Nature*, vol. 446, no. April, pp. 633–639, 2007.
- [69] V. Gradinaru, K. R. Thompson, and K. Deisseroth, "eNpHR: A *Natronomonas* halorhodopsin enhanced for optogenetic applications," *Brain Cell Biol.*, 2008.
- [70] V. Gradinaru, M. Mogri, K. R. Thompson, J. M. Henderson, and K. Deisseroth, "Optical deconstruction of parkinsonian neural circuitry," *Science (80-. )*, 2009.
- [71] I. Diester, M. T. Kaufman, M. Mogri, R. Pashaie, W. Goo, O. Yizhar, C. Ramakrishnan, K. Deisseroth, and K. V. Shenoy, "An optogenetic toolbox designed for primates," *Nat. Neurosci.*, 2011.
- [72] O. Yizhar, L. E. Fenno, T. J. Davidson, M. Mogri, and K. Deisseroth, "Optogenetics in Neural Systems," *Neuron*, vol. 71, no. 1, pp. 9–34, 2011.
- [73] E. G. Govorunova, O. A. Sineshchekov, H. Li, and J. L. Spudich, "Microbial Rhodopsins: Diversity, Mechanisms, and Optogenetic Applications," *Annu. Rev. Biochem.*, vol. 86, no. 1, pp. 845–872, Jun. 2017.
- [74] B. Y. Chow, X. Han, A. S. Dobry, X. Qian, A. S. Chuong, M. Li, M. A. Henninger, G. M. Belfort, Y.

- Lin, P. E. Monahan, and E. S. Boyden, “High-performance genetically targetable optical neural silencing by light-driven proton pumps,” *Nature*, 2010.
- [75] X. Han, B. Y. Chow, H. Zhou, N. C. Klapoetke, A. Chuong, R. Rajimehr, A. Yang, M. V. Baratta, J. Winkle, R. Desimone, and E. S. Boyden, “A High-Light Sensitivity Optical Neural Silencer: Development and Application to Optogenetic Control of Non-Human Primate Cortex,” *Front. Syst. Neurosci.*, 2011.
- [76] F. Zhang, M. Prigge, F. Beyrière, S. P. Tsunoda, J. Mattis, O. Yizhar, P. Hegemann, and K. Deisseroth, “Red-shifted optogenetic excitation: A tool for fast neural control derived from *Volvox carteri*,” *Nat. Neurosci.*, 2008.
- [77] N. C. Klapoetke, Y. Murata, S. S. Kim, S. R. Pulver, A. Birdsey-Benson, Y. K. Cho, T. K. Morimoto, A. S. Chuong, E. J. Carpenter, Z. Tian, J. Wang, Y. Xie, Z. Yan, Y. Zhang, B. Y. Chow, B. Surek, M. Melkonian, V. Jayaraman, M. Constantine-Paton, G. K.-S. Wong, and E. S. Boyden, “Independent optical excitation of distinct neural populations,” *Nat. Methods*, vol. 11, no. 3, pp. 338–46, 2014.
- [78] L. Alberio, A. Locarno, A. Saponaro, E. Romano, V. Bercier, S. Albadri, F. Simeoni, S. Moleri, S. Pelucchi, A. Porro, E. Marcello, N. Barsotti, K. Kukovetz, A. J. Boender, A. Contestabile, S. Luo, A. Moutal, Y. Ji, G. Romani, M. Beltrame, F. Del Bene, M. Di Luca, R. Khanna, H. M. Colecraft, M. Pasqualetti, G. Thiel, R. Tonini, and A. Moroni, “A light-gated potassium channel for sustained neuronal inhibition,” *Nat. Methods*, 2018.
- [79] A. M. Packer, L. E. Russell, H. W. P. Dalglish, and M. Häusser, “Simultaneous all-optical manipulation and recording of neural circuit activity with cellular resolution in vivo,” *Nat. Methods*, vol. 12, no. 2, pp. 140–146, 2014.
- [80] R. Pashaie, P. Anikeeva, J. H. Lee, R. Prakash, O. Yizhar, M. Prigge, D. Chander, T. J. Richner, and J. Williams, “Optogenetic brain interfaces,” *IEEE Rev. Biomed. Eng.*, vol. 7, pp. 3–30, 2014.
- [81] M. R. Warden, J. A. Cardin, and K. Deisseroth, “Optical Neural Interfaces,” *Annu. Rev. Biomed. Eng.*, vol. 16, pp. 103–29, 2014.
- [82] M. T. Alt, E. Fiedler, L. Rudmann, J. S. Ordonez, P. Ruther, and T. Stieglitz, “Let There Be Light-Optoprobes for Neural Implants,” *Proc. IEEE*, vol. 105, no. 1, pp. 101–138, 2017.
- [83] Y. Lechasseur, S. Dufour, G. Lavertu, C. Bories, M. Deschênes, R. Vallée, and Y. De Koninck, “A microprobe for parallel optical and electrical recordings from single neurons in vivo,” *Nat. Methods*, vol. 8, no. 4, pp. 319–325, 2011.
- [84] S. Park, Y. Guo, X. Jia, H. K. Choe, B. Grena, J. Kang, J. Park, C. Lu, A. Canales, R. Chen, Y. S. Yim, G. B. Choi, Y. Fink, and P. Anikeeva, “One-step optogenetics with multifunctional flexible polymer fibers,” *Nat. Neurosci.*, vol. 20, no. 4, pp. 612–619, Apr. 2017.
- [85] F. Pisanello, L. Sileo, I. A. Oldenburg, M. Pisanello, L. Martiradonna, J. A. Assad, B. L. Sabatini, and M. De Vittorio, “Multipoint-emitting optical fibers for spatially addressable in vivo optogenetics,” *Neuron*, vol. 82, no. 6, pp. 1245–1254, 2014.

- [86] F. Pisano, M. Pisanello, L. Sileo, A. Quattieri, B. L. Sabatini, M. De Vittorio, and F. Pisanello, "Focused ion beam nanomachining of tapered optical fibers for patterned light delivery," *Microelectron. Eng.*, vol. 195, no. March, pp. 41–49, Aug. 2018.
- [87] J. Wang, F. Wagner, D. A. Borton, J. Zhang, I. Ozden, R. D. Burwell, A. V. Nurmikko, R. van Wagenen, I. Diester, and K. Deisseroth, "Integrated device for combined optical neuromodulation and electrical recording for chronic in vivo applications," *J. Neural Eng.*, vol. 9, no. 1, p. 016001, Feb. 2012.
- [88] A. N. Zorzos, J. Scholvin, E. S. Boyden, and C. G. Fonstad, "Three-dimensional multiwaveguide probe array for light delivery to distributed brain circuits," *Opt. Lett.*, vol. 37, no. 23, pp. 4841–3, 2012.
- [89] R. Scharf, C. Reiche, N. McAlinden, Y. Cheng, E. Xie, R. Sharma, P. Tathireddy, L. Rieth, K. Mathieson, and S. Blair, "A compact integrated device for spatially-selective optogenetic neural stimulation based on the Utah Optrode Array," in *Optogenetics and Optical Manipulation 2018*, 2018, p. 15.
- [90] K. Kampasi, E. Stark, J. Seymour, K. Na, H. G. Winful, G. Buzsáki, K. D. Wise, and E. Yoon, "Fiberless multicolor neural optoelectrode for in vivo circuit analysis," *Sci. Rep.*, vol. 6, no. August, p. 30961, 2016.
- [91] L. Hoffman, M. Welkenhuysen, A. Andrei, S. Musa, Z. Luo, S. Libbrecht, S. Severi, P. Soussan, V. Baekelandt, S. Haesler, G. Gielen, R. Puers, and D. Braeken, "High-density optrode-electrode neural probe using SixNy photonics for in vivo optogenetics," in *2015 IEEE International Electron Devices Meeting (IEDM)*, 2015, vol. 2016–Febru, p. 29.5.1-29.5.4.
- [92] Y. Son, H. Jenny Lee, J. Kim, H. Shin, N. Choi, C. Justin Lee, E.-S. Yoon, E. Yoon, K. D. Wise, T. Geun Kim, and I.-J. Cho, "In vivo optical modulation of neural signals using monolithically integrated two-dimensional neural probe arrays," *Sci. Rep.*, vol. 5, no. 1, p. 15466, Dec. 2015.
- [93] A. M. Aravanis, L.-P. Wang, F. Zhang, L. a Meltzer, M. Z. Mogri, M. B. Schneider, and K. Deisseroth, "An optical neural interface: in vivo control of rodent motor cortex with integrated fiberoptic and optogenetic technology," *J. Neural Eng.*, vol. 4, no. 3, pp. S143–S156, 2007.
- [94] S. Shoham and K. Deisseroth, "Special issue on optical neural engineering: advances in optical stimulation technology," *J. Neural Eng.*, vol. 7, no. 4, p. 040201, 2010.
- [95] D. R. Sparta, A. M. Stamatakis, J. L. Phillips, N. Hovelsø, R. Van Zessen, and G. D. Stuber, "Construction of implantable optical fibers for long-term optogenetic manipulation of neural circuits," *Nat. Protoc.*, vol. 7, no. 1, pp. 12–23, 2012.
- [96] A. Canales, X. Jia, U. P. Friorip, R. A. Koppes, C. M. Tringides, J. Selvidge, C. Lu, C. Hou, L. Wei, Y. Fink, and P. Anikeeva, "Multifunctional fibers for simultaneous optical, electrical and chemical interrogation of neural circuits in vivo," *Nat. Biotechnol.*, vol. 33, no. 3, pp. 277–284, 2015.
- [97] T. V. F. Abaya, S. Blair, P. Tathireddy, L. Rieth, and F. Solzbacher, "A 3D glass optrode array for

- optical neural stimulation," *Biomed. Opt. Express*, vol. 3, no. 12, p. 3087, 2012.
- [98] M. Im, I. J. Cho, F. Wu, K. D. Wise, and E. Yoon, "A dual-shank neural probe integrated with double waveguides on each shank for optogenetic applications," *Proc. Annu. Int. Conf. IEEE Eng. Med. Biol. Soc. EMBS*, pp. 5480–5483, 2011.
- [99] M. Schwaerzle, K. Seidl, U. T. Schwarz, O. Paul, and P. Ruther, "Ultracompact optrode with integrated laser diode chips and SU-8 waveguides for optogenetic applications," *Proc. IEEE Int. Conf. Micro Electro Mech. Syst.*, pp. 1029–1032, 2013.
- [100] F. Wu, E. Stark, M. Im, I.-J. Cho, E.-S. Yoon, G. Buzsáki, K. D. Wise, and E. Yoon, "An implantable neural probe with monolithically integrated dielectric waveguide and recording electrodes for optogenetics applications," *J. Neural Eng.*, vol. 10, no. 5, p. 056012, 2013.
- [101] B. Fan and W. Li, "Miniaturized optogenetic neural implants: a review.," *Lab Chip*, vol. 15, no. 19, pp. 3838–55, 2015.
- [102] Z. Fekete, "Recent advances in silicon-based neural microelectrodes and microsystems: A review," *Sensors Actuators, B Chem.*, vol. 215, pp. 300–315, 2015.
- [103] J. M. Stujenske, T. Spellman, and J. A. Gordon, "Modeling the Spatiotemporal Dynamics of Light and Heat Propagation for In Vivo Optogenetics," *Cell Rep.*, vol. 12, no. 3, pp. 525–534, 2015.
- [104] H. J. Round, "A note on carborundum," *Electr. World*, 1907.
- [105] N. Zheludev, "The life and times of the LED - A 100-year history," *Nat. Photonics*, vol. 1, no. 4, pp. 189–192, 2007.
- [106] E. F. Schubert, *Light-emitting diodes*. Cambridge University Press, 2006.
- [107] S. M. Sze and K. K. Ng, *Physics of Semiconductor Devices*. 2007.
- [108] J. Cho, E. F. Schubert, and J. K. Kim, "Efficiency droop in light-emitting diodes: Challenges and countermeasures," *Laser Photon. Rev.*, vol. 7, no. 3, pp. 408–421, May 2013.
- [109] Donald A. Neamen, *Semiconductor physics and devices : basic principles 1 Donald A. Neamen. - 3rd ed. p.* 2006.
- [110] E. Xie, "High performance microstructured light emitting diodes - mechanisms and processes," University of Strathclyde, 2013.
- [111] D. Zhu, C. McAleese, M. Haebleren, M. J. Kappers, N. Hylton, P. Dawson, G. Radtke, M. Couillard, G. A. Botton, S.-L. Sahonta, and C. J. Humphreys, "High-efficiency InGaN/GaN quantum well structures on large area silicon substrates," *Phys. Status Solidi a-Applications Mater. Sci.*, vol. 209, no. 1, pp. 13–16, 2012.
- [112] A. J. Trindade, "Transfer printing of nitride based light emitting diodes," 2015.
- [113] D. Zhu, D. J. Wallis, and C. J. Humphreys, "Prospects of III-nitride optoelectronics grown on Si.," *Rep. Prog. Phys.*, vol. 76, no. 10, p. 106501, 2013.
- [114] D. Zhu, C. McAleese, K. K. McLaughlin, M. Häberlen, C. O. Salcianu, E. J. Thrush, M. J. Kappers, W. a Phillips, P. Lane, D. J. Wallis, T. Martin, M. Astles, S. Thomas, a Pakes, M. Heuken, and C.

- J. Humphreys, "GaN-based LEDs grown on 6-inch diameter Si (111) substrates by MOVPE," *Proc. SPIE*, vol. 7231, no. July 2015, pp. 723111–723118, 2009.
- [115] D. Zhu, C. McAleese, M. Häberlen, M. J. Kappers, N. Hylton, P. Dawson, G. Radtke, M. Couillard, G. A. Botton, S.-L. Sahonta, and C. J. Humphreys, "High-efficiency InGaN/GaN quantum well structures on large area silicon substrates," *Phys. status solidi*, vol. 209, no. 1, pp. 13–16, Jan. 2012.
- [116] P. Tian, J. J. D. McKendry, Z. Gong, S. Zhang, S. Watson, D. Zhu, I. M. Watson, E. Gu, A. E. Kelly, C. J. Humphreys, and M. D. Dawson, "Characteristics and applications of micro-pixelated GaN-based light emitting diodes on Si substrates," *J. Appl. Phys.*, vol. 115, no. 3, 2014.
- [117] I. P. Clements, A. G. Gnade, A. D. Rush, C. D. Patten, M. C. Twomey, and A. V. Kravitz, "Miniaturized LED sources for in vivo optogenetic experimentation," 2013, p. 85860X.
- [118] T. Il Kim, J. G. McCall, Y. H. Jung, X. Huang, E. R. Siuda, Y. Li, J. Song, Y. M. Song, H. A. Pao, R. H. Kim, C. Lu, S. D. Lee, I. S. Song, G. Shin, R. Al-Hasani, S. Kim, M. P. Tan, Y. Huang, F. G. Omenetto, J. A. Rogers, and M. R. Bruchas, "Injectable, cellular-scale optoelectronics with applications for wireless optogenetics," *Science (80-. )*, vol. 340, no. 6129, pp. 211–216, 2013.
- [119] M. A. Rossi, V. Go, T. Murphy, Q. Fu, J. Morizio, and H. H. Yin, "A wirelessly controlled implantable LED system for deep brain optogenetic stimulation," *Front. Integr. Neurosci.*, vol. 9, no. February, p. 8, 2015.
- [120] K. Y. Kwon, H. M. Lee, M. Ghovanloo, A. Weber, and W. Li, "A wireless slanted optrode array with integrated micro leds for optogenetics," *Proc. IEEE Int. Conf. Micro Electro Mech. Syst.*, pp. 813–816, 2014.
- [121] H. Cao, L. Gu, S. K. Mohanty, and J.-C. Chiao, "An Integrated  $\mu$ LED Optrode for Optogenetic Stimulation and Electrical Recording," *IEEE Trans. Biomed. Eng.*, vol. 60, no. 1, pp. 225–229, Jan. 2013.
- [122] N. McAlinden, D. Massoubre, E. Richardson, E. Gu, S. Sakata, M. D. Dawson, and K. Mathieson, "Thermal and optical characterization of micro-LED probes for in vivo optogenetic neural stimulation," *Opt. Lett.*, vol. 38, no. 6, pp. 992–4, 2013.
- [123] N. McAlinden, E. Gu, M. D. Dawson, S. Sakata, and K. Mathieson, "Optogenetic activation of neocortical neurons in vivo with a sapphire-based micro-scale LED probe," *Front. Neural Circuits*, vol. 9, no. May, p. 25, 2015.
- [124] F. Wu, E. Stark, P. C. Ku, K. D. Wise, G. Buzsáki, and E. Yoon, "Monolithically Integrated  $\mu$ LEDs on Silicon Neural Probes for High-Resolution Optogenetic Studies in Behaving Animals," *Neuron*, vol. 88, no. 6, pp. 1136–1148, 2015.
- [125] S. Ayub, L. J. Gentet, R. Fiáth, M. Schwaerzle, M. Borel, F. David, P. Barthó, I. Ulbert, O. Paul, and P. Ruther, "Hybrid intracerebral probe with integrated bare LED chips for optogenetic studies," *Biomed. Microdevices*, vol. 19, no. 3, pp. 1–12, 2017.
- [126] F. Dehkoda, A. Soltan, N. Ponon, A. Jackson, A. O'Neill, and P. Degenaar, "Self-sensing of

- temperature rises on light emitting diode based optrodes,” *J. Neural Eng.*, vol. 15, no. 2, 2018.
- [127] R. Scharf, T. Tsunematsu, N. McAlinden, M. D. Dawson, S. Sakata, and K. Mathieson, “Depth-specific optogenetic control in vivo with a scalable, high-density  $\mu$ LED neural probe,” *Sci. Rep.*, vol. 6, no. January, p. 28381, 2016.
- [128] K. L. Montgomery, A. J. Yeh, J. S. Ho, V. Tsao, S. Mohan Iyer, L. Grosenick, E. A. Ferenczi, Y. Tanabe, K. Deisseroth, S. L. Delp, and A. S. Y. Poon, “Wirelessly powered, fully internal optogenetics for brain, spinal and peripheral circuits in mice,” *Nat. Methods*, vol. 12, no. 10, pp. 969–974, 2015.
- [129] P. Andersen and E. I. Moser, “Brain temperature and hippocampal function,” *Hippocampus*, vol. 5, no. 6, pp. 491–498, 1995.
- [130] C. Childs, “Human brain temperature: Regulation, measurement and relationship with cerebral trauma: Part 1,” *British Journal of Neurosurgery*. 2008.
- [131] Y. Li, X. Shi, J. Song, C. Lü, T. Kim, J. G. McCall, M. R. Bruchas, J. a. Rogers, and Y. Huang, “Thermal analysis of injectable, cellular-scale optoelectronics with pulsed power,” *Proc. R. Soc. A Math. Phys. Eng. Sci.*, vol. 469, no. 2156, p. 20130142, 2013.
- [132] T. Il Kim, S. Hyun Lee, Y. Li, Y. Shi, G. Shin, S. D. Lee, Y. Huang, J. A. Rogers, and J. Su Yu, “Temperature- and size-dependent characteristics in ultrathin inorganic light-emitting diodes assembled by transfer printing,” *Appl. Phys. Lett.*, vol. 104, no. 5, pp. 1–4, 2014.
- [133] T. Kim, Y. H. Jung, J. Song, D. Kim, Y. Li, H. Kim, I.-S. Song, J. J. Wierer, H. A. Pao, Y. Huang, and J. A. Rogers, “High-Efficiency, Microscale GaN Light-Emitting Diodes and Their Thermal Properties on Unusual Substrates,” *Small*, vol. 8, no. 11, pp. 1643–1649, Jun. 2012.
- [134] Y. Li, Y. Shi, J. Song, C. Lu, T. Il Kim, J. A. Rogers, and Y. Huang, “Thermal properties of microscale inorganic light-emitting diodes in a pulsed operation,” *J. Appl. Phys.*, vol. 113, no. 14, 2013.
- [135] P. W. May, “Diamond thin films: a 21st-century material,” *Philos. Trans. R. Soc. A Math. Phys. Eng. Sci.*, vol. 358, no. 1766, pp. 473–495, Jan. 2000.
- [136] I. Aharonovich, A. D. Greentree, and S. Praver, “Diamond photonics,” *Nature Photonics*. 2011.
- [137] F. P. BUNDY, H. T. HALL, H. M. STRONG, and R. H. WENTORF, “Man-Made Diamonds,” *Nature*, 1955.
- [138] R. S. Balmer, J. R. Brandon, S. L. Clewes, H. K. Dhillon, J. M. Dodson, I. Friel, P. N. Inglis, T. D. Madgwick, M. L. Markham, T. P. Mollart, N. Perkins, G. a Scarsbrook, D. J. Twitchen, a J. Whitehead, J. J. Wilman, and S. M. Woollard, “Chemical vapour deposition synthetic diamond: materials, technology and applications,” *J. Phys. Condens. Matter*, vol. 21, no. 36, p. 364221, 2009.
- [139] M. Schwander and K. Partes, “A review of diamond synthesis by CVD processes,” *Diam. Relat. Mater.*, vol. 20, no. 9, pp. 1287–1301, Oct. 2011.
- [140] I. Friel, “Optical Quality Diamond Grown by Chemical Vapor Deposition,” *Opt. Eng. Diam.*, pp. 35–69, 2013.

- [141] P. W. May and Y. A. Mankelevich, "From ultrananocrystalline diamond to single crystal diamond growth in hot filament and microwave plasma-enhanced CVD reactors: A unified model for growth rates and grain sizes," *J. Phys. Chem. C*, 2008.
- [142] I. Friel, S. L. Clewes, H. K. Dhillon, N. Perkins, D. J. Twitchen, and G. A. Scarsbrook, "Control of surface and bulk crystalline quality in single crystal diamond grown by chemical vapour deposition," *Diam. Relat. Mater.*, vol. 18, no. 5–8, pp. 808–815, 2009.
- [143] A. J. Kemp, J. M. Hopkins, J. E. Hastie, S. Calvez, Y. Zhang, E. Gu, M. D. Dawson, and D. Burns, "Thermal Management of Lasers and LEDs Using Diamond," *Opt. Eng. Diam.*, pp. 353–384, 2013.
- [144] D. R. Kania and D. R. Kania, "Biocompatibility of chemical-vapour- deposited diamond," *Biomaterials*, vol. 16, no. 6, pp. 483–488, 1995.
- [145] J. Park, V. Quaiserová-Mocko, K. Pecková, J. J. Galligan, G. D. Fink, and G. M. Swain, "Fabrication, characterization, and application of a diamond microelectrode for electrochemical measurement of norepinephrine release from the sympathetic nervous system," *Diam. Relat. Mater.*, vol. 15, no. 4–8, pp. 761–772, 2006.
- [146] H.-Y. Chan, D. M. Aslam, S. H. Wang, G. M. Swain, and K. D. Wise, "Fabrication and testing of a novel all-diamond neural probe for chemical detection and electrical sensing applications," in *2008 IEEE 21st International Conference on Micro Electro Mechanical Systems*, 2008, pp. 244–247.
- [147] H.-Y. Chan, M. Varney, S. Hatch, and D. M. Aslam, "Implantable polycrystalline diamond neural probe for in vivo and in vitro physiological recording," in *TRANSDUCERS 2009 - 2009 International Solid-State Sensors, Actuators and Microsystems Conference*, 2009, no. 1, pp. 1202–1205.
- [148] H. W. Choi, E. Gu, C. Liu, C. Griffin, J. M. Girkin, I. M. Watson, and M. D. Dawson, "Fabrication of natural diamond microlenses by plasma etching," *J. Vac. Sci. Technol. B*, vol. 23, no. January, pp. 130–132, 2005.
- [149] B. Fan, K. Kwon, R. Rechenberg, A. Khomenko, M. Haq, M. F. Becker, A. J. Weber, and W. Li, "A polycrystalline diamond-based, hybrid neural interfacing probe for optogenetics," *2015 28th IEEE Int. Conf. Micro Electro Mech. Syst.*, pp. 616–619, 2015.
- [150] H. Chan, D. M. Aslam, S. Member, J. A. Wiler, and B. Casey, "A Novel Diamond Microprobe for Neuro-Chemical and -Electrical Recording in Neural Prosthesis," vol. 18, no. 3, pp. 511–521, 2009.
- [151] M. M. Elwassif, Q. Kong, M. Vazquez, and M. Bikson, "Bio-heat transfer model of deep brain stimulation-induced temperature changes.," *J. Neural Eng.*, vol. 3, no. 4, pp. 306–315, 2006.
- [152] J. Csicsvari, D. A. Henze, B. Jamieson, K. D. Harris, A. Sirota, P. Barthó, K. D. Wise, and G. Buzsáki, "Massively parallel recording of unit and local field potentials with silicon-based electrodes.," *J. Neurophysiol.*, vol. 90, no. 2, pp. 1314–23, 2003.



# Chapter 2

## Microfabrication and analysis

Microscale integrated circuits (IC) and devices are built up on a substrate by the successive addition or removal of planar metal, dielectric and semiconductor layers, patterned into geometric shapes at each step to create interconnects, physical features such as trenches or complex 3D shapes, contact windows and bonding-pad areas. This work utilised standard microfabrication techniques such as photolithography, various physical and chemical deposition techniques and wet/dry etch processes, all of which are briefly described below.

### 2.1 Pattern definition by photolithography

Photolithography is the process of transferring patterns of geometric shapes defined on a mask to a thin layer of photosensitive polymer (photoresist, PR) covering the surface of a substrate. Photoresists typically comprise a base resin, which determines its mechanical and thermal properties, a photoactive compound and a solvent controlling its viscosity [1]. Central to device conception and fabrication yield as it determines features resolution and relative alignment, photolithography is a multistep, manual process highly sensitive to environment (temperature, humidity) and sample surface conditions (energy, roughness, high-aspect ratio features and cleanliness).

The basic process of photolithography is shown in Figure 2.1.

#### 2.1.1 Film application

Samples are first cleaned either by a degreasing acetone/IPA solvent clean, or a thorough acid or base “piranha” clean (see annex A1) to remove organic, metallic and particle contaminants. Heat-dried samples are centred on a rotating vacuum chuck and a few mL of

liquid resist are dispensed at the centre of the wafer, if needed after application of an adhesion promoter such as hexa-methylene-disiloxane (HMDS) which renders the surface slightly hydrophobic [3].

The wafer is then spun up to a rotational speed of 2000 to 5000rpm for 30 to 120 seconds, giving a uniform coating film of 500nm to 10 $\mu$ m, with film thickness  $t$  depending mainly on resist viscosity  $\eta$  and spin speed  $\omega$  [1] :

$$t \propto \sqrt{\frac{\eta}{\omega}} \quad (2.1)$$

The wafer is then given a soft bake (typically 90°C-120°C on a hot plate for 60-120s) to remove the solvent from the PR film and improve its adhesion.

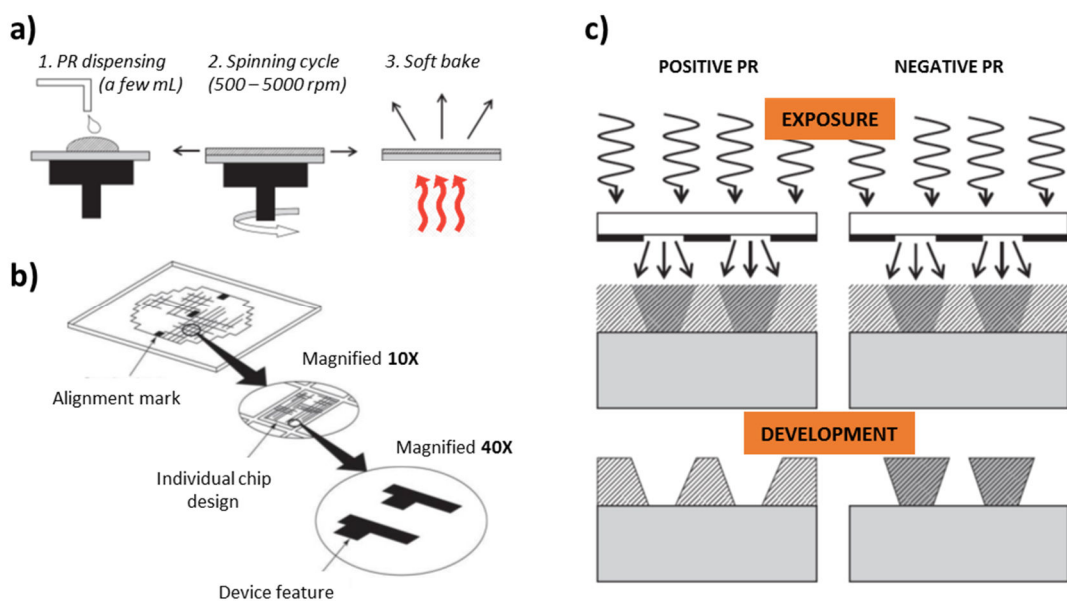


Figure 2.1 : Schematic of photolithography steps. a) Spincoating and baking of resist on sample, b) pattern on photomask along with fiducial markers, c) UV exposure through mask transfers the mask's features (positive resist) or its opposite (negative resist), in each case with a typical sloped profile. Schematics adapted from [1], [2].

### 2.1.2 PR exposure

A pattern is transferred onto the PR film by exposing it to UV light through a photomask. In unmasked areas, UV exposure induces either photodecomposition and generation of hydrophilic products (positive PR) or strengthening by photocrosslinking or photopolymerisation into an insoluble network (negative PR).

In this work, device layers were designed in CAD software (Tanner L-Edit [4]; see designs in annex A2) and an external vendor laser wrote these in  $\sim$ 100nm-thick chromium on a quartz

mask plate with  $\sim 0.5\mu\text{m}$  linewidth resolution to create the photomask (Deltamask B.V [5]). For pattern transfer, wafer and photomask are inserted and firmly secured by vacuum suction into a mask aligner (MA6 mask aligner, Suss MicroTech). This tool comprises three main parts: a high pressure mercury short-arc lamp ( $350\text{nm} < \lambda < 450\text{nm}$ ), a microscope with max. 40X magnification and a manually operated alignment stage allowing submicrometer lateral and rotational movement of the sample. After being brought in close proximity ( $< 60\mu\text{m}$ ) for visualisation, mask and wafer are precisely aligned using *ad hoc* fiducial markers previously etched on the sample when patterning the very first layer. When satisfactorily aligned, they are brought into vacuum or “soft” contact by the tool and the lamp shutter opens to expose unmasked areas of the sample to UV light, chemically modifying the PR film. During this step, alignment accuracy may vary widely, from submicron values for a skilled operator patterning a smooth sample with 500nm-thick PR, up to  $\sim 2\text{-}3\mu\text{m}$  misalignments sometimes unavoidable with highly textured samples coated with thick layers impeding visualisation. Furthermore, the minimum reliable linewidth attainable with the MA6 aligner system is  $\sim 1.5\mu\text{m}$ , as can be approximated from Fresnel diffraction [1] :

$$\text{linewidth} \approx \sqrt{\lambda x \left( g + \frac{d}{2} \right)} \quad (2.2)$$

Where  $g$  is the sample/mask gap,  $d$  the resist thickness and  $\lambda$  the UV wavelength.

These limitations and others linked to PR type and thickness, etc. must be anticipated and factored in during mask design, lest device yield drop dramatically.

### 2.1.3 PR development

Immediately after UV exposure, soluble areas of the PR film can be removed in *ad hoc* developer solution, either aqueous-based alkaline (positive PR) or organic-based (negative PR), rinsed and dried to produce the final patterned film. Precise control of development time and concentration is needed to ensure precise features with straight sidewalls. Under- or over-development typically lead to sloped PR sidewalls, a property used in this work to create a controlled undercut in thick negative PR for facilitating metal liftoff.

After development, postbaking at  $90^\circ\text{C}$ - $150^\circ\text{C}$  (hardbaking) may be used to increase PR adhesion to the substrate, allow controlled resist reflow or harden the PR film before an aggressive dry etch. The generic parameters used for coating, exposure and development of the resists used in this work are given in annex A1.

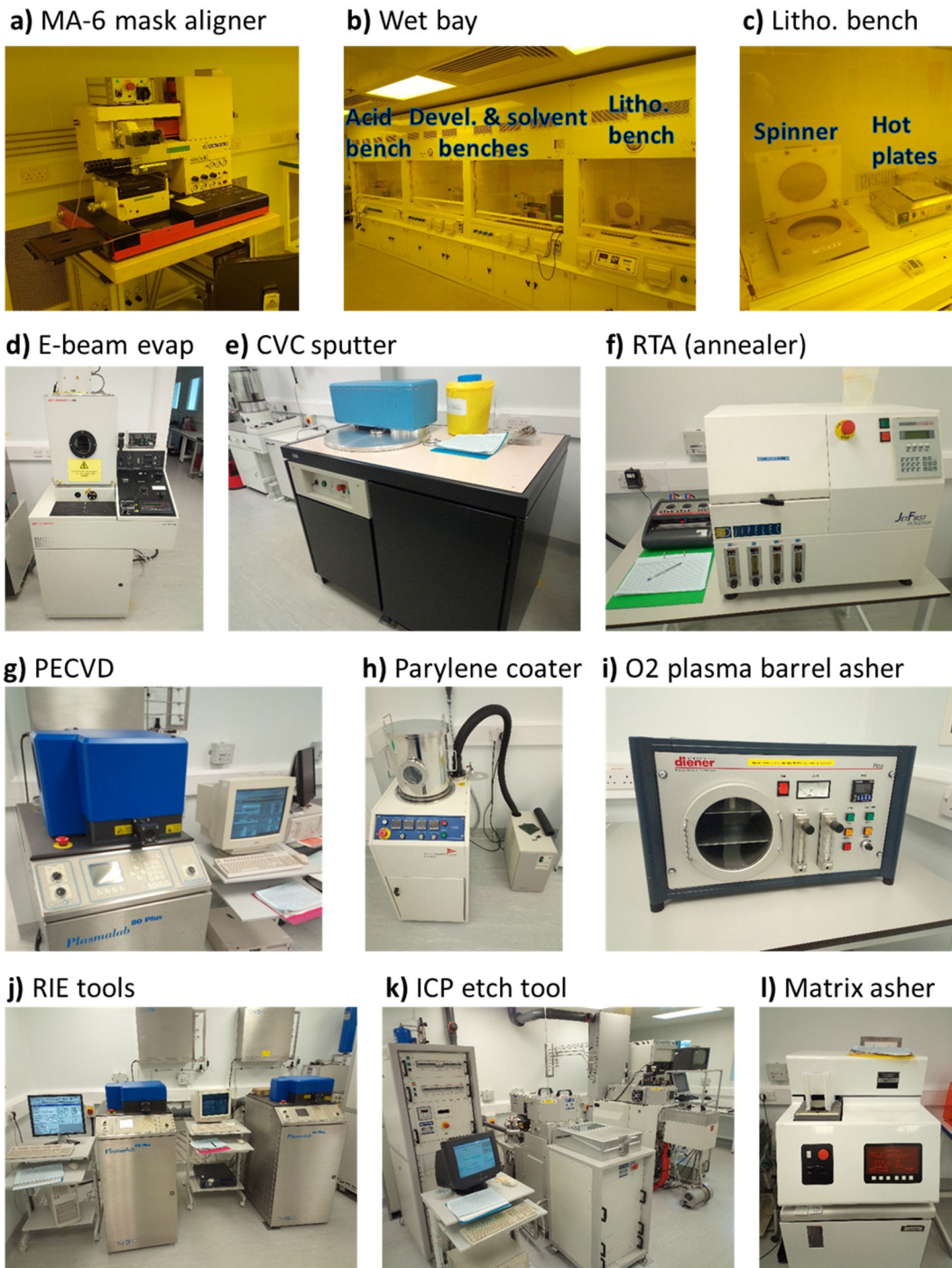


Figure 2.2 : Main microfabrication tools in Strathclyde University's Technology and Innovation Centre cleanroom used in this work. Wet "yellow" room tools include a) Suss MA6 mask aligner, b) separate wet benches for acid/base etches, developing photoresist, solvent cleaning and photoresist application with c) EMS spin-coaters. Deposition tools include d) Edwards Auto306 electron-beam evaporator and e) CVC 601 sputter coater with annealing by f) Jipelec JetFirst rapid thermal annealer, and g) Oxford 80+ Plasmalab PECVD tool for SiO<sub>2</sub> deposition and h) SCS Labcoater 2 for parylene-C coatings. Etch tools include i) Diener "Pico" O<sub>2</sub> barrel asher and l) Matrix SystemOne stripper for resist descum, and j) two Oxford 80+ Plasmalab tools for reactive ion etching of metals and dielectrics and k) two inductively coupled RIE STS Multiplex tools for ICP etch of GaN, diamond and aluminium.

## 2.2 Material deposition

In this work, a variety of metal and dielectric amorphous thin films have been deposited on the surface of samples and patterned into electrically conductive paths, insulation layers, protective coatings or “hard” masks for aggressive etch steps. In all cases, success in the deposition of a uniform, uncontaminated film with good adhesion hinges on thorough surface cleaning and preparation (annex A1) and deposition in adequate medium to high-vacuum (1mbar to 1e-6 mbar). Different methods of physical and chemical vapour deposition were used and are briefly described below.

### 2.2.1 Physical vapour deposition (PVD) of metallic films

In PVD, material is ejected from a solid target material and transported to the substrate surface in vacuum. Chamber pressure determines the chance of collisions during transport and thus affect both deposition energy and directionality. The ejected atoms mean free path (MFP)  $L$  in cm at a gas pressure of  $p$  mbar is approximately given by [6], [7]

$$L \approx \frac{7 \times 10^{-3}}{p} \quad (2.3)$$

In high vacuum ( $p < 1e-4$  mbar), the MFP  $L > 70$  cm is greater than the chamber dimensions and ejected atoms follow a line-of-sight route to the substrate.

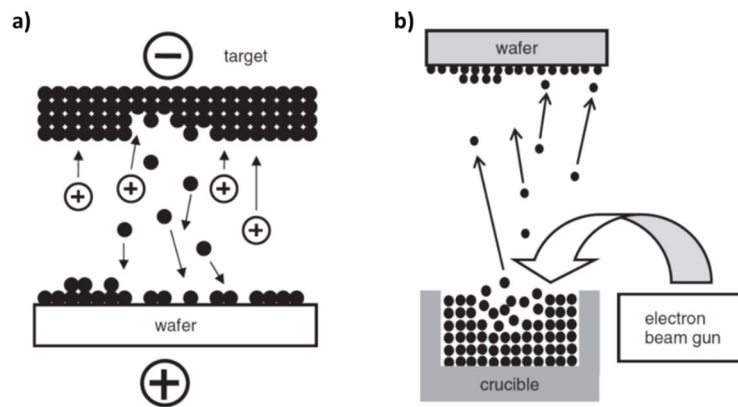


Figure 2.3 : Schematics of PVD techniques. In DC sputtering (a), bombarding ions knock off target atoms depositing at high energies on samples. Low-energy e-beam evaporation (b) heats up the target for a slower, more controllable deposition process suitable for very thin films. Samples are affixed to a rotating pallet in both methods to ensure uniform coverage. Schematics taken from [1].

**DC sputtering** was used to deposit Titanium, Gold or Aluminium films in the 50nm to micron range, with Titanium normally used as an adhesion layer. Argon ions ( $Ar^+$ ) from a glow discharge plasma hit the negatively biased target, ejecting highly energetic atoms for typical

deposition rates of 10-100nm/min. Since sputtering pressure is in the  $\sim 1\text{e-}3\text{mbar}$  range, atoms experience collisions en route to the substrate, leading to partial conformality of the deposited film to angled or trench features.

**Electron-beam evaporation (e-beam)** served to deposit thinner ( $<100\text{nm}$ ) films of Nickel, Gold or Palladium. A 3kV electron-beam gun vaporises the target metal held in a graphite crucible, and the evaporated atoms are transported to the substrate in high vacuum at room temperature, in a low-energy process with slow deposition rates (3-30nm/min). A typical deposition pressure of  $\sim 1\text{e-}6\text{mbar}$  ensures the deposition is directional. A film thickness monitor based on a quartz crystal resonator measures deposition thickness in real time.

### 2.2.2 Metal film annealing

Thermal annealing is widely used in semiconductor processing for contact formation [8] and defect recovery [9], [10]. In rapid thermal annealing (RTA), wafers can be brought to temperatures exceeding  $1000^\circ\text{C}$  in Air, Ar or  $\text{N}_2$  gas ambient by powerful tungsten-halogen lamps. The very short thermal cycling ( $<5\text{min}$ ) helps minimise diffusion or other temperature-dependent processes (grain growth, surface oxidation, etc.). In this work, specifically designed RTA recipes are used to form a low specific resistivity metal contact to p-GaN [11].

### 2.2.3 Chemical vapour deposition (CVD) of dielectric films

In CVD, the source materials are brought into the deposition chamber in the gas phase, may be broken down or activated in a plasma, and diffuse to the wafer surface where they adsorb or react to form a film. Byproducts are desorbed and pumped away. The process can be limited by reactant flow rate (“mass transport limited”) or adsorption rate (“surface reaction limited”), with deposition rates varying between 10-200nm/min. In this work, plasma-enhanced CVD of oxide and parylene CVD were regularly used and are described below.

- o *Plasma-enhanced CVD (PECVD) of silicon dioxide ( $\text{SiO}_2$ )*

By using a plasma to intensify source gas decomposition and reactions, PECVD enables oxide deposition at “low” temperatures ( $\sim 300^\circ\text{C}$ ) compatible with most metals films or semiconductors, although typically resulting in less dense films than thermally grown oxides. In this work, an Oxford 80+ PECVD tool (Figure 2.4) was used to deposit  $\text{SiO}_2$  for various uses as an insulation layer or hard mask. The chamber comprises two electrodes between which the plasma is struck. The top RF-driven electrode is operated at 100 kHz, which is slow enough for ions to follow the field and bombard the substrate. The bottom electrode is

heated to 300°C, promoting surface mobility and desorption of weakly bonded atoms. Both effects help increase film density and can help tailor film stress [1]. Precursor gases silane (SiH<sub>4</sub>) and oxygen (O<sub>2</sub>) are injected separately through the top showerhead and a layer of amorphous silicon dioxide is deposited on the sample via the reaction:

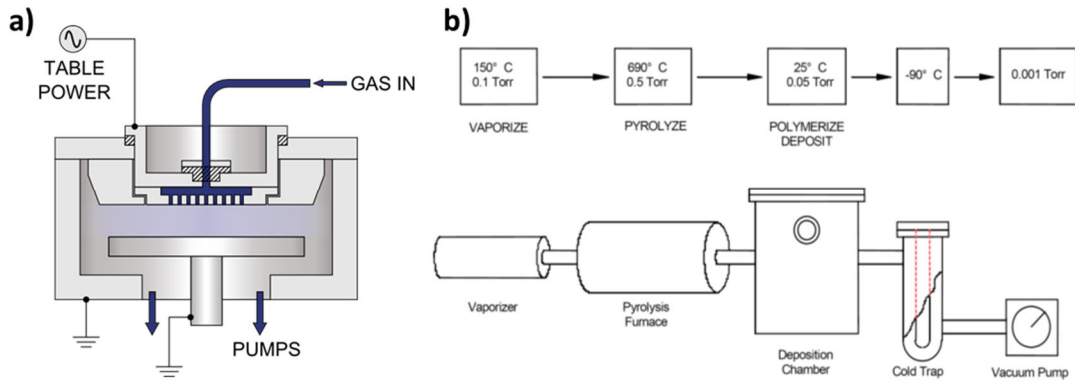
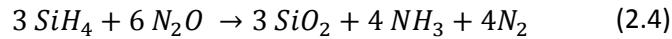


Figure 2.4 : Dielectrics deposition by CVD. a) In PECVD, a plasma of precursor gases is struck between the two chamber electrodes and SiO<sub>2</sub> molecules deposit on the samples heated by the bottom electrode. b) Parylene deposition results from a sequential process where the dimer is vaporised, cleaved and condensated at room temperature on the sample, leaving a fully conformal coating. Schematics from [12], [13].

#### o *Parylene-C vapour deposition*

A trademarked polymer, Parylene-C is widely used as a moisture, dielectric and thermal barrier for electric components and implantable medical devices [14], [15]. Deposited as a pinhole-free, highly conformal film, it was applied in our fabrication process both as a device bioinsulative coating, and a dielectric layer suitable for high step coverage (highly textured substrates), with properties in both cases far superior to those of more porous PECVD oxide [16].

In our cleanroom, parylene-C was deposited with a SCS Labcoter 2 tool, in a vapour polymerisation process shown on Figure 2.4. The granular initial dimer is sublimed in a vaporiser, flows downstream through a pyrolysis furnace at 690°C where it is cleaved into gaseous monomers, then enters the deposition chamber where the sample is placed on a rotating platform, at room temperature and medium vacuum ( $p < 4 \times 10^{-2}$  mbar) in a quasi-molecular, Knudsen-type flow [13]. Gas monomer condenses and polymerises on all ambient temperature surfaces, forming a highly homogenous, extremely conformal coating on the sample. Non-deposited molecules condense in the cold trap, so they do not enter the vacuum

pump. A feedback loop controls dimer sublimation rate to keep chamber pressure within set limits. Final film thickness is determined by the mass of initial dimer and the total samples area, with deposition rates around 80-120nm/min.

As a chemically inert polymeric compound, unmediated parylene adhesion to substrates is mostly governed by weak Van der Waals bonds and mechanical “tie-points” on textured surfaces [17]–[19]. This limited bonding strength can be greatly improved by using an adhesion promoter such as A-174 silane, applied in vapour phase immediately before deposition (see our characterisation of adhesion promoting methods in annex A4). Even then, ensuring a good and reliable adhesion of full parylene films on devices can still be challenging, a well-known problem in the field [20]–[22] also encountered in this work, and which is addressed in more detail in section 6.2.3.

## 2.3 Material etching

In the etching process, the substrate or deposited thin film is chemically and/or physically attacked and removed in sample areas unmasked by PR or a protective layer such as SiO<sub>2</sub>. Specific applications determine the etch technique used, with crucial parameters being etch rate of target material, etch selectivity (the ratio of material to mask erosion), and etch isotropy determining the fidelity of pattern transfer to the material (Figure 2.5). Both wet etching and plasma-assisted dry etching techniques used within our process flows are briefly presented below.

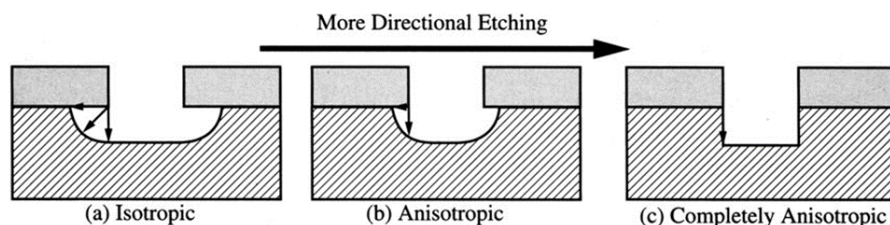


Figure 2.5 : Etching anisotropy influence on pattern transfer [1]. A fully isotropic etch (a), e.g by indiscriminate chemical attack typical in wet processes, creates a pronounced undercut affecting feature size and fidelity. By contrast, highly physical attacks by ion sputtering in some dry etch processes may yield very vertical sidewalls (c). In practice, etches are often partly anisotropic (b) and the influence on pattern transfer must be considered.

### 2.3.1 Dry etching

Plasma etching has replaced wet etching steps in many crucial steps in the semiconductor industry as a more reliable, adaptable process capable of producing very anisotropic etch



profiles and vertical sidewalls. Reactive gases are excited and ionised in a vacuum chamber by RF fields, combining into a chemical etch component (excited molecules may react with the substrate and greatly improve etch rate) and a physical process of pure ion bombardment (sputtering etch, creating very vertical sidewalls). Plasma chemistry, pressure and power can be adjusted to promote either component, and a combination of both is often needed: e.g aluminium is spontaneously etched by  $\text{Cl}_2$ , but ion bombardment is needed to first remove its native oxide layer. It is important that the etch byproducts be volatile to avoid re-deposition on the sample or chamber contamination (a recurrent issue with metal etches), and to choose an adequate hard mask for high-powered physical etches ( $P > 150\text{W}$ ) as energetic ion bombardment can quickly damage PR films [23], [24]

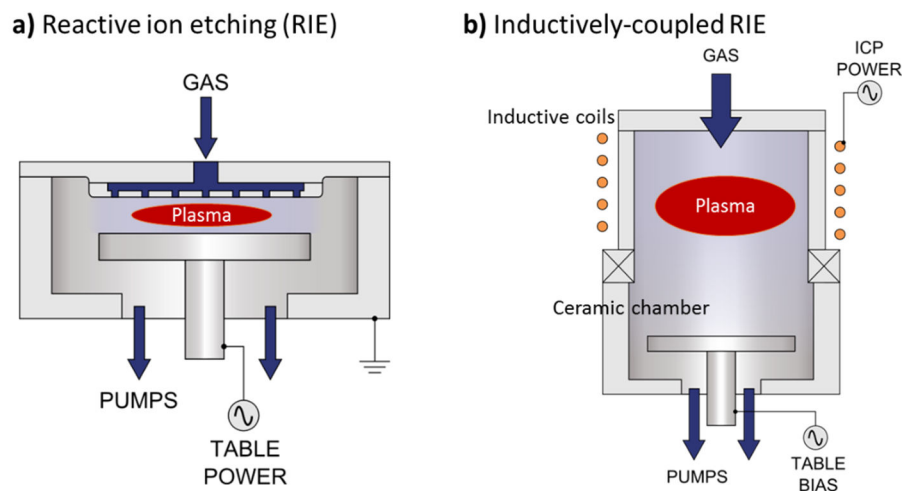


Figure 2.6 : Dry etching tools. In RIE (a), voltage biasing of the bottom electrode is linked to the plasma parameters, coupling physical and chemical components of the etch. More advanced ICP tools (b) rely on inductive coils to strike a denser plasma, fully independently from the shown table bias. Adapted from [25], [26].

- o *Reactive ion etching (RIE)*

RIE is carried out in our cleanroom in two Oxford 80+ RIE systems, dedicated to dielectric and metal/silicon etching respectively to avoid cross-contamination (Figure 2.6). Various application-specific plasma chemistries can be created from a combination of gases ( $\text{Ar}$ ,  $\text{CHF}_3$ ,  $\text{O}_2$ ,  $\text{SF}_6$ ). A medium density plasma ( $<5 \times 10^9 \text{ cm}^{-3}$ ) is initiated by an RF field oscillating at the standard frequency of 13.56 MHz, applied up to 300W power. Emitted electrons build up a charge (DC bias 300-700V) on the bottom electrode carrying the sample, causing vertical ion bombardment from the plasma.

o *Inductively-coupled plasma etching (ICP)*

ICP is an improved RIE-type process utilizing a set of inductive coils to apply the RF field, generating a lower pressure plasma at higher densities ( $\sim 5 \times 10^{11} \text{ cm}^{-3}$ ) without reactor walls sputtering, and fully decoupled from the wafer voltage biasing ensured by another RF generator to powers up to 800W. The system delivers higher etch rates, higher selectivities and more process adaptability than RIE while minimising sample damage. Two STS Multiplex ICP tools were used here to etch GaN compounds, diamond substrates and aluminium layers. Specialised ICP tools can also perform **deep reactive ion etching (DRIE / Bosch process)**, allowing high aspect ratio trenches in Silicon by continuous cycling between short  $\text{SF}_6$ -based etch and  $\text{C}_4\text{F}_8$  sidewall passivation steps. DRIE was used here on silicon prototype devices to etch 50um-deep separation trenches.

Finally, plasma-based tools were also used to **strip/descum residual organic films**. A “Matrix” asher uses both oxygen plasma (RF power 500W) and a heated chuck (up to 250°C) to strip damaged resist. A gentler, low power (50W-200W) Diener O2 plasma etcher was used to strip thin resist or parylene films on fragile samples.

### 2.3.2 Wet etching

Wet etching is a purely chemical process relying mostly on electron transfer (metal etching) or acid-base reaction (insulator etching) [1]. Considered cruder than dry etching, wet etching methods often have high but potentially variable etch rates and generally yield a very isotropic profile, a property detrimental to small feature definition but which can be harnessed to create an undercut if desired.

The full parameters of wet etching processes used in this project are given in annex A1. A solution of hydrofluoric acid (buffered oxide etch (BOE),  $\text{NH}_4\text{F}:\text{HF}(49\%)$ , 7:1) was used to either pattern-etch or fully strip PECVD-deposited  $\text{SiO}_2$  films, following the reaction:



Strong acid or base wet etchants were also used to remove native oxides before metal deposition (e.g 1:1 HCl:H<sub>2</sub>O for GaN cleaning), or as an initial thorough cleaning step to dissolve organic, particulate and metal contamination (hot acid or base “piranha” etches, see annex A1). Crystallographic-planes dependent wet etching of Silicon was regularly performed in the fabrication of elements needed for transfer-printing, as is explained below.

o *Silicon anisotropic etching for creation of suspended beams and pyramidal recesses*

Crystal-plane dependent etching of silicon to create 3D structures is a well-known technique in the semiconductor and MEMS industry [27]–[30]. Silicon has a cubic diamond lattice structure, with low-index planes (as defined by their Miller indices) being fourfold symmetric (100) and sixfold symmetric (110) and (111) respectively. The specific atomic packing and available bonds in each crystal plane determines their specific etch rate in alkaline solution [28]. As an example, the slowest-etching (111) plane exhibits the highest atomic packing density and only one dangling bond (versus three for the fast-etching (110) plane), thus limiting alkali-induced oxidation steps and subsequent etch (see Table 2.1).

Plane orientation	Etch rate ( $\mu\text{m}/\text{min}$ )
(100)	0.629
(110)	1.292
(111)	0.009

Table 2.1 : Plane-dependent etch rates of silicon in heated KOH (34% w/w, 70°C [31]).

Silicon wet etching was performed in heated KOH, a well-known and relatively safe technique [32], [33]. The process is schematised in Figure 2.7 and covered in annex A1. Briefly, samples were etched in a 40% w/w aqueous KOH solution inside a covered PTFE beaker, heated by a 80°C water bath. Two specially-oriented (top surface plane) silicon wafers were used depending on wanted end feature (Figure 2.7). Si (100) wafers, used in transfer-printing stamp fabrication (appendix A3) were hard masked with SiO<sub>2</sub> patterned in square openings beforehand, letting etching features progressively close on themselves along newly exposed (111) planes, yielding a final pyramidal feature with typical sidewall (111)/surface (100) plane angle of 54.7°. Si (111) substrate wafers, with epitaxial device layers, were used in LED fabrication (chapter 3.2.4): after exposing the substrate by trench etching, the etch progresses normal to the (110) planes, along the bottom (111) plane and leaving protected, suspended horizontal GaN epilayer features.

During this step, fragile features and epilayers must be adequately protected to withstand >30min in aggressive etchant. The optimised etch time and protection for our specific process flows are discussed in section 3.2 (device fabrication).

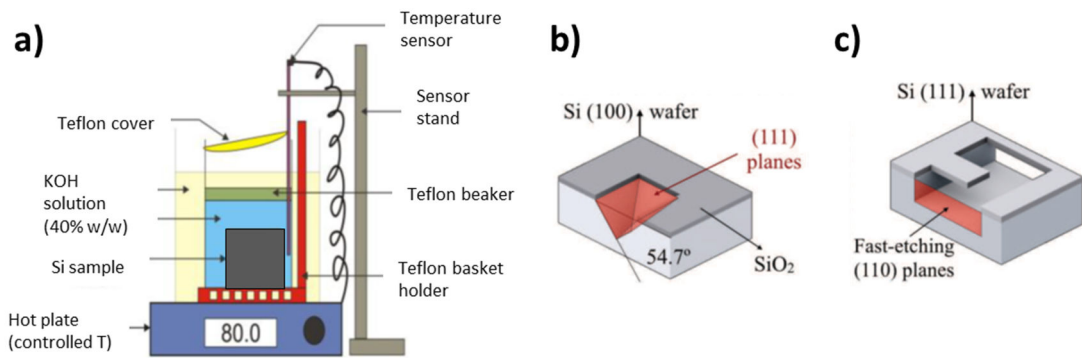


Figure 2.7 : Heated KOH etching can etch 3D structures in silicon. a) Setup schematic: the etch is performed in a PTFE beaker with magnetic agitation (80°C, ~400rpm). On patterned (100)- and (111)-oriented Si wafers, preferential attack of fast-etching planes can produce b) pyramidal recesses used in printing stamp fabrication or c) suspended beams or features needed for our LED fabrication. Schematics adapted from [34], [35].

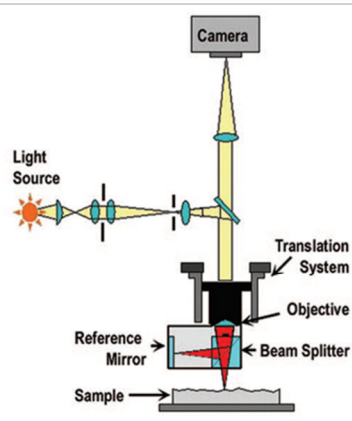
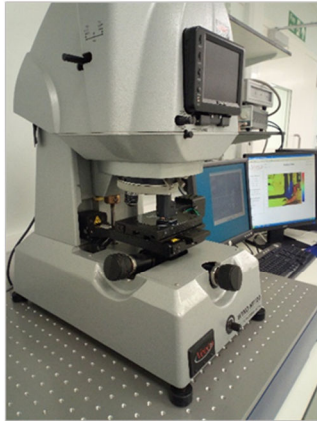
## 2.4 Analysis and characterisation techniques

In a university cleanroom equipped for experimental research rather than optimised volume production, the above manufacturing techniques may often deviate from ideality. Microfabrication processes may be affected by above-tolerance contamination, fluctuating environmental conditions influencing notoriously sensitive wet processes such as wet etches or photolithography, varying etch or deposition rates, or even possible tool dysfunctions. All of the above are not uncommon and, if left unchecked, degrade device yield or performance, an effect compounded for every process step needed.

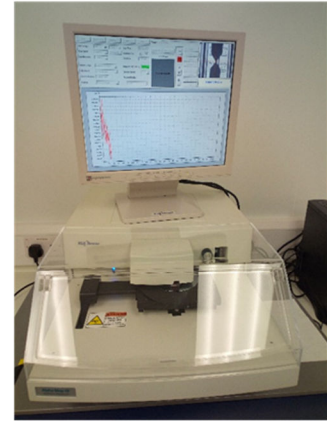
As such, the microfabrication process of complex integrated devices such as those realised in this work requires constant control and adjustment at every process step. Material and thin film quality and uniformity, pattern definition and etch profiles are monitored with tolerances defined by the process flow.

Beyond direct eye observation, the simplest and most immediate inspection technique is **microscope inspection**. A bright-field/dark-field Nikon ME600 was used, with magnification range 50X to 1000X, and with a differential interference contrast (DIC) mode allowing visualisation of  $<\lambda/4$  difference in surface height, useful for detection of defects, contamination or local variation of film thickness such as partially developed photoresist [36]. More specific analysis techniques were used in this work as follows.

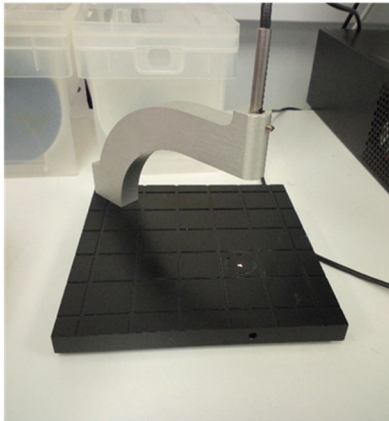
a) Optical profiler



b) Stylus profiler



c) TF ellipsometer



e) Scanning electron microscope



Figure 2.8 : Analysis and characterisation tools used in this work. a) Veeco WYKONT1100 optical profiler ([37]). b) Tencor AlphaStep IQ stylus profiler. c) Filmetrics F20 thin-film ellipsometer. e) JEOL JSM IT-100 scanning electron microscope, capable of energy-dispersive X-ray spectroscopy and with high and low-vacuum modes.

#### 2.4.1 Thin film thickness measurement by ellipsometry

A Filmetrics F-20 was used to precisely measure the thickness of optically smooth dielectric thin films. The F-20 measures the reflectance spectrum ( $400 < \lambda < 1100 \text{ nm}$ ) of an illuminated sample and compares it to a series of theoretical reflectance spectra calculated from thin-film interference models [38], based on the known refractive indices of the analysed materials. Under optimal conditions, film thickness can be determined with nm-level accuracy. This tool was used to precisely characterise photoresist,  $\text{SiO}_2$ , and parylene C film thicknesses after deposition and after etch steps.

## 2.4.2 Surface topography by stylus and optical profiling

Both contact and non-contact profilometry were used in this work to quantify critical sample surface parameters such as step sizes, curvature, waviness and roughness. **Stylus-based profilometers** (DEKTAK 3030 and KLA-Tencor Alpha-Step IQ) were used for quick, local surface texture measurement of robust samples such as trench depth measurement. Briefly, a diamond-tipped stylus is moved across the sample with a specified contact force and speed. Vertical deflections of the tip are electromechanically converted, digitised and stored into computer memory for display and measurement. Relevant tool features are given in Table 2.2 and contrasted with characteristics of optical profilometry.

	Detktak 3030	AlphaStepIQ	WYKO NT1100
Profiling type	Contact / stylus	Contact / stylus	Non-contact
Vertic. resolution	$Z_R < 10\text{nm}$	$Z_R < 1\text{nm}$	$Z_R < 1\text{nm}$
Vertic. range	$\Delta Z = 65.5\mu\text{m}$	$\Delta Z = 2\text{mm}$	$\Delta Z = 1\text{mm}$
Characteristics and limitations	Fixed force 15mg 10 $\mu\text{m}$ diamond tip XY range 50mm ~20s/scan	Force 1->100mg 5 $\mu\text{m}$ diamond tip XY range 10mm ~1->5min/scan	No damage risk Opaque mat. only XY range 100mm ~1->10min/scan

Table 2.2 : Comparative performance of profilers used in this work (data from [39]–[41]). Stylus profilers are quick and reliable, do not depend on post-processing reconstruction algorithms, but the pressure applied by the tip may damage very fragile samples. White-light interferometry is riskless, enables full 3D profiling of large areas with very good lateral and vertical resolution, but is typically challenged by thin layers of transparent material.

A **white-light interferometer** (Veeco WYKONT1100) in vertical scanning interferometry (VSI) mode was used for the non-contact profilometry of fragile samples or full areas (3D measurements). In this mode, the unfiltered light emitted from a broad-spectrum tungsten halogen lamp is split into two beams (see Figure 2.8, panel a). One beam is focussed on the surface to be imaged, the other reflected on a reference mirror. The reflected beams recombine through a magnifying objective to form an interferogram onto a CCD array. Because of the light's short coherence length ( $\sim 1\text{-}2\mu\text{m}$ ), sharp-contrast interference fringes are very localised [42], [43], appearing only when the two path lengths of the interferometer are closely matched. Focus is thus uniquely defined for each image pixel as the “coherence peak” reached while modulating the imaging beam path length by vertical scanning with a

high-precision piezoelectric translation stage. A single area scan is done in seconds, and a robust phase-mapping algorithm reconstructs the surface topography with theoretical sub-nm accuracy [42], [44], [45].

In practice, measurements may be affected by multiple reflections in transparent thin films or membrane, high sample surface roughness, highly sloped profiles, while layers of dissimilar materials may introduce phase shift leading to ~40nm height error [42], [46], [47]. With these caveats acknowledged, optical profiling was used as the method of choice in this work to quantify the curvature of ultrathin LEDs, assess the topography of fragile diamond membranes, and for area inspections such as etch uniformity.

### 2.4.3 Scanning electron microscopy (SEM)

SEM was used when micron-resolution device inspection was needed in this work, and **energy-dispersive X-ray spectroscopy (SEM-EDX)** when an elemental analysis was required. In SEM, a thermionically emitted electron beam of energy 1keV to 50keV is focused by magnetic lensing to a spot of diameter 0.5nm to 5nm. Scanning coils in the electron column can deflect the beam horizontally, allowing a raster scan over a rectangular area of the sample surface. The primary electrons are scattered and absorbed within a typical interaction volume of the sample, whose size depends on beam energy, specimen atomic number and density. Exploitable signals emitted from the interaction volume include shallow-depth secondary electrons (SE), deeper backscattered electrons (BE) and characteristic X-ray radiation, each of which can be detected by specialised detectors.

This work used a JEOL JSM-IT100 SEM microscope, most often in secondary electron detection mode. Within a few nanometres depth of the sample surface, low-energy electrons ( $E_g < 100\text{eV}$ ) ejected from the atom's outer shell by the primary beam can escape the sample and are emitted in all directions. A positively biased metal grid ( $V \sim 400\text{V}$ ) diverts them towards the detector, composed of a scintillator screen coupled to a photomultiplier tube (PMT). Because this detection mode is spot-localised, essentially blind to higher-energy BE electrons and particularly sensitive to steep surfaces and edges, it yields a high-resolution, high signal-to-noise-ratio (SNR) with a strong topographical contrast [48], [49].

**SEM-EDX** was typically used to determine or ascertain the elemental composition of processed samples. Within the interaction volume, inner-shell electrons from the specimen's atom may be ejected by the primary electron beam. Higher-energy electrons from outer

shells fill these vacant energy levels, emitting in the process quantised X-ray photons in a set of frequencies unique to each element [48].

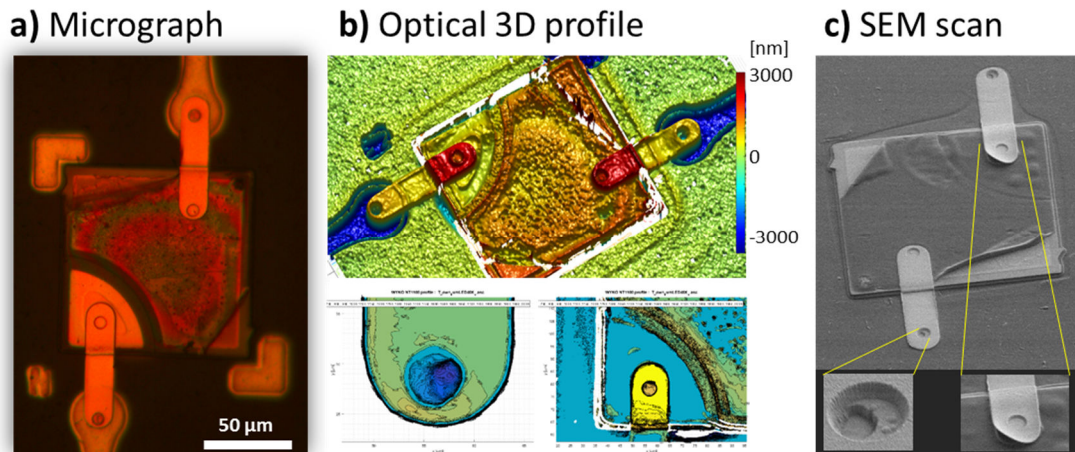


Figure 2.9 : Multi-tool inspection of an imperfect device uniquely allows complete characterisation and understanding of failure modes. a) Optical micrograph of an isolated LED transfer-printed on silicon. b) Optical profiling of the same devices shows crucial 3D features such as important step heights and unevenly etched vias, which can be further explored by c) SEM at high magnifications ( $\sim 1000\text{-}7000\times$ ), which reveals layer delamination.

**Electro-optical testing** was done using semiconductor probe analysers (HP4155A or Yokogawa GS610), where set voltage/current cycles are applied via micromanipulated probes, in conjunction with portable powermeters (Thorlabs PM100D/S120C) and/or spectrometers (Avantes AvaSpec). **Thermal characterisation** of final devices was carried out using a FLIR SC7000 infrared camera, as described in more detail in ch. 5.

## 2.5 Micro-transfer printing

### 2.5.1 Context and introduction

The fabrication techniques detailed above have been developed and scaled up over several decades by an industry focussed on the processing of monolithic, layered, planar materials. However monolithic devices are typically limited by the inherent mechanical, thermal or optical properties of their substrates. In particular, mismatches in atomic lattice constants or coefficient of thermal expansion (CTE) may stymie epitaxial growth of dissimilar layers, constraining semiconductor bandgap engineering or post-processing [2]. Thus the development of scalable, versatile methods for heterogeneous integration is a long-acknowledged need in the optoelectronics industry and research community [50]–[53].



While techniques such as wafer-scale layer transfer are successfully used to transfer thin epilayers in specific process flows, they are heavily material dependent and face yield and alignment issue [54]. By contrast, highly versatile pick-and-place methods may provide a route to a more “universal solution” for various heterogeneous integration needs in the next decades if full scalability and high throughput can be established [55]–[59].

Micro transfer-printing ( $\mu$ TP) was invented in 2005 by John Roger’s group at the University of Illinois as a scalable technique for the discrete integration of separately fabricated objects into functional systems, compatible with standard manufacturing techniques [60]. Inspired by MEMS approaches such as soft lithography, it relies on the controllable adhesion and release to and from a viscoelastic structure. A PDMS stamp can pick and place photonic components fabricated *ad hoc*.  $\mu$ TP has recently been implemented at the University of Strathclyde [61] and was optimised in the course of this work to CMOS and textured diamond substrates.

### 2.5.2 Mechanics of transfer-printing

The main steps of a full  $\mu$ TP cycle are shown in Figure 2.10. Transferrable optoelectronic devices or components (“inks”) must be manufactured upstream using an *ad hoc* process flow, ensuring a weak adhesion of the ink to its native substrate, thus allowing their controllable release. The manufacturing process must be tailored to each ink type, and typically relies on selective etching of an underlying sacrificial layer, generally leaving the active devices suspended to the substrate by thin breakable anchors. With the Rogers’ group laying the groundwork, many such device types have been fabricated in a scalable, high-yield fashion, including full transfer-printable ICs [64], AlGaS cells [65], and GaN & AlInGaP micro-LEDs [66]–[68] inspiring those demonstrated in this work (chapter 3).

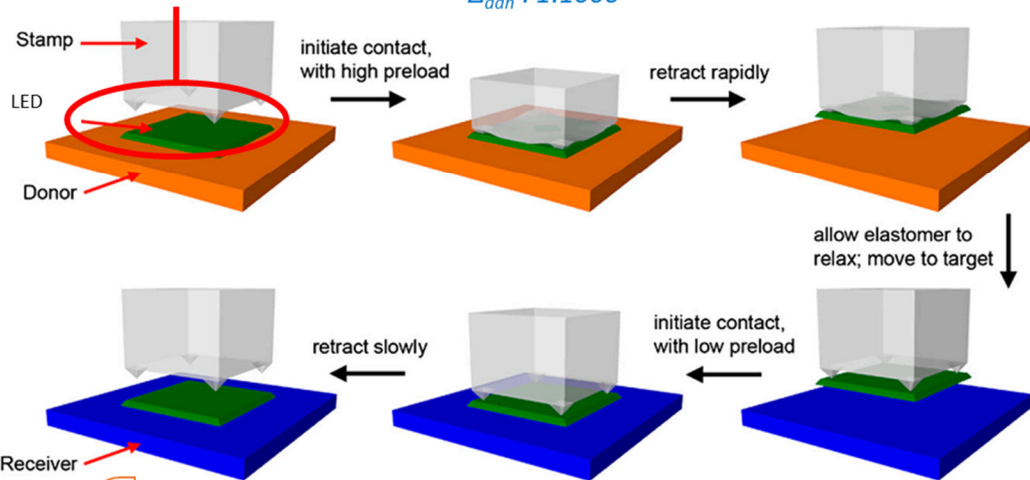
Pickup of the detachable ink from its donor substrate and release onto a new surface is performed by a PDMS stamp through harnessing of its viscoelastic properties. A viscoelastic polymer under load undergoes a time-dependent partial internal rearrangement of its polymer chain as it deforms (*creep*), building up a back stress in the material. When the initial load is taken away, the accumulated internal stress fully returns the material to its original shape (elastic behaviour), within a given *relaxation time* (viscous behaviour) dependent on material geometry and composition. This time-dependent strain of the stamp is used to kinetically modulate the contact area between stamp and ink, which is directly proportional to the adhesion force in a Van der Waals dominated regime ([69], see chapter 3).

## A/ Steps of a standard transfer-printing cycle

### 1. Releasable photonic devices Typical dim. : 10 $\mu$ m->500 $\mu$ m

Optimised stamps :  
reversible adhesion  
 $\Delta_{adh} : 1:1000$

### 2. Pick-up



Post-processing  
& interconnection

## B/ Influence of peel rate

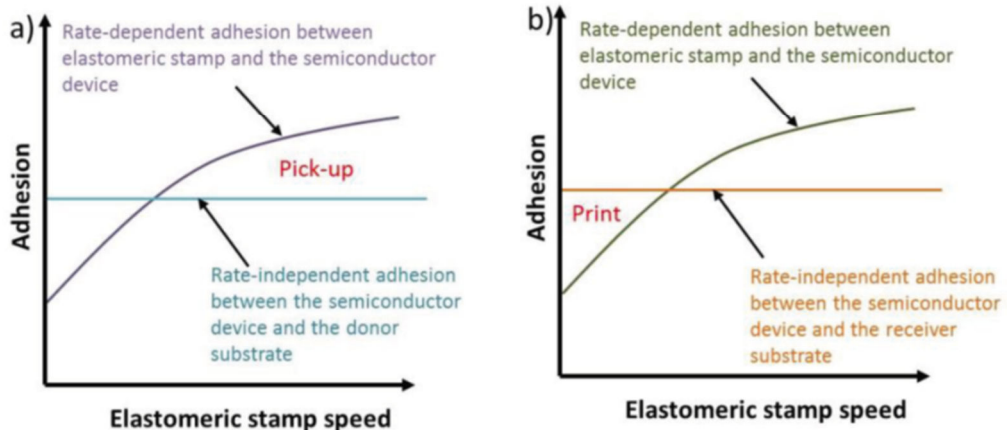


Figure 2.10 : Summary of the generic technique of micro-transfer printing now used both in academic research and for industrial production (schematics adapted from [59], [62], [63]). **A/** Typical main steps of the process include the fabrication of suitable devices, pickup by a polymeric stamp, positioning and printing on a receiver substrate. Each of these steps presents a set of practical challenges and may need to be adapted when developing a new process. **B/**  $\mu$ TP fundamentally relies on the time-dependence of the viscoelastic stamp strain rate. Adhesion between stamp and ink can be kinetically modulated, enabling deterministic switching between pickup and transfer regimes within the same printing cycle.

In a printing cycle, the soft PDMS stamp is initially pressed against the detachable ink, conforming to its textured surface and maximizing contact area, letting pressed-stamp/ink adhesion exceed ink/donor adhesion. The ink can thus be detached from its initial substrate by fast vertical retraction of the stamp (high peel rate,  $\sim$ constant adhesion). The ink is then precisely positioned over the receiver substrate and contacted to its printing site. A low stamp retraction speed (low peel rate) allows the stamp to slowly relax and promote stamp/ink delamination. Printing is possible if receiver/ink adhesion exceeds the minimal relaxed-stamp/ink adhesion.

In practice, microstructuring of the stamp can efficiently maximise the stamp-ink adhesion range. John Rogers' group demonstrated that square stamps with pyramid-shaped edge microtips [69] were capable of a  $\sim$ 1:1000 adhesion switch between pressed (collapsed) state, and relaxed state where the ink hangs to the stamp only by the very tip of the pyramids. A similar stamp geometry has been used in this work. Furthermore, adhesion enhancement layers are routinely used on the receiver substrate to facilitate printing. The issues and limitations associated with this generic transfer-printing strategy will be discussed in more detail in section 3.3.

### 2.5.3 Transfer-printing at Strathclyde

The  $\mu$ TP realised in this work was performed using a repurposed nanolithography system (NLP2000), developed at the Institute of Photonics as part of a previous work [61], [35]. Initially designed to deposit nanodroplets with atomic force microscopy (AFM) tips, this computer-controlled tool uses piezoelectric-driven linear stages to position samples with  $\pm$ 75nm precision or less in the xyz directions, over an area of  $\sim$ 10x10cm<sup>2</sup>. The samples can be imaged in real time through an integrated microscope system of magnification 20X and  $<$ 1 $\mu$ m optical resolution.

The initial AFM tip holder has been modified to carry the PDMS stamps, whose fabrication is detailed in chapter 3. Since stamp and stamp holder are transparent, the full printing cycle can be directly viewed and recorded from above by the tool operator. Varying stamp peel rates can be applied by varying the z-axis step motion size. With a full relaxation time of  $\sim$ 20s for the stamps developed in this work, the above-described complete basic printing cycle for a micro-LED requires  $\sim$ 40s.

This system of unprecedented accuracy and high versatility has been used in the Institute of Photonics to push the limits of transfer-printing, allowing pick and place of multiple GaN-based  $\mu$ LEDs [61], semiconductor nanowires [70] or ultrathin silicon membranes [71]. This work explored a new possibility of the machine, picodroplet adhesive (PA) transfer-printing, to release high-efficiency GaN  $\mu$ LEDs onto textured substrates with good thermal contact.

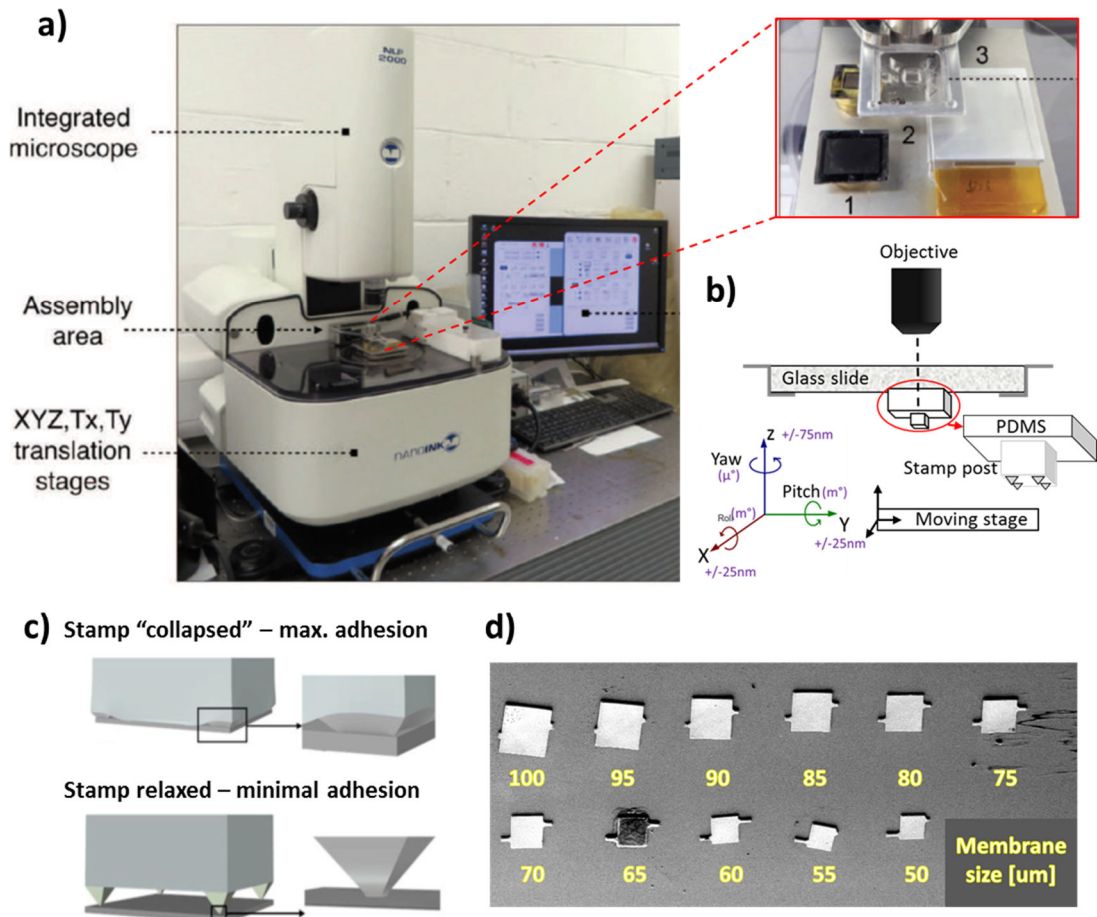


Figure 2.11 : Transfer-printing setup used in this work. a) A modified NLP2000 [35] tool allows vertical and lateral positioning down to submicron accuracy. Inset: 1) donor sample, 2) stamp platform, 3) receiver mount. b) The microstructured PDMS stamp is mounted face down on a transparent glass slide, allowing microscope imaging from above. c) Mechanics of the pyramid stamp allows up to 1:1000 switching in adhesion force between relaxed and collapsed state [72]. d) SEM scan of GaN membranes of various sizes printed in line on glass using this tool.

## 2.6 Conclusion

This chapter covered the main microfabrication techniques and tools used in this work. Standard photolithography, material deposition and etching methods were outlined as well as the various analysis and testing techniques crucial to characterise our devices during fabrication. The generic concept and physics of micro-transfer printing were summarised. All these tools were used extensively to develop high-efficiency, suspended GaN-based LEDs (**chapter 3**) and manufacture the first ultrathin, single-crystal diamond optogenetic probe (**chapter 4**). Furthermore, the physics of micro-scale adhesion were exploited to establish an advanced version of  $\mu$ TP, allowing reliable release of devices on highly textured substrates including commercial CMOS chips (**chapter 3**).

## 2.7 References

- [1] S. Franssila, *Introduction to microfabrication*. John Wiley & Sons, 2010.
- [2] S. M. (1936-. . . ). Sze and M. Lee, *Semiconductor devices physics and technology : international student version*. J. Wiley & Sons, 2013.
- [3] M. J. Madou, *Fundamentals of microfabrication : the science of miniaturization*. CRC Press, 2002.
- [4] “L-Edit IC layout software page.” [Online]. Available: <https://www.mentor.com/tanneredit/l-edit>. [Accessed: 01-Aug-2018].
- [5] “Deltamask B.V,” 2018. [Online]. Available: <http://www.deltamask.nl/frames.html>. [Accessed: 01-Aug-2018].
- [6] A. Chambers, R. K. Fitch, and B. S. Halliday, *Basic vacuum technology*. Institute of Physics Pub, 1998.
- [7] N. S. Harris, *Modern vacuum practice*. Nigel S. Harris, 2007.
- [8] J. K. Sheu, Y. K. Su, G. C. Chi, W. C. Chen, C. Y. Chen, C. N. Huang, J. M. Hong, Y. C. Yu, C. W. Wang, and E. K. Lin, “The effect of thermal annealing on the Ni/Au contact of p-type GaN,” *J. Appl. Phys.*, vol. 83, no. 6, p. 3172, Jun. 1998.
- [9] S. J. Pearton, J. C. Zolper, R. J. Shul, and F. Ren, “GaN: Processing, defects, and devices,” *J. Appl. Phys.*, vol. 86, no. 1, pp. 1–78, 1999.
- [10] X. A. Cao, H. Cho, S. J. Pearton, G. T. Dang, A. P. Zhang, F. Ren, R. J. Shul, L. Zhang, R. Hickman, and J. M. Van Hove, “Depth and thermal stability of dry etch damage in GaN Schottky diodes,” *Appl. Phys. Lett.*, vol. 75, no. 2, pp. 232–234, Jul. 1999.
- [11] E. Xie, “High performance microstructured light emitting diodes - mechanisms and processes,” University of Strathclyde, 2013.
- [12] Oxford instruments plasma technology, “PECVD.” [Online]. Available: <https://plasma.oxinst.com/campaigns/technology/pecvd>. [Accessed: 01-Aug-2018].
- [13] Specialty Coating Systems, “PDS 2010 LABCOTER™ 2 Parylene Deposition System Operator’s Manual,” pp. 1–153, 2010.
- [14] G. E. Loeb, M. J. Bak, E. M. Schmidt, and M. Salcman, “Parylene as a Chronically Stable, Reproducible Microelectrode Insulator,” *IEEE Trans. Biomed. Eng.*, vol. BME-24, no. 2, pp. 121–128, 1977.
- [15] J. P. Seymour, Y. M. Elkasabi, H. Y. Chen, J. Lahann, and D. R. Kipke, “The insulation performance of reactive parylene films in implantable electronic devices,” *Biomaterials*, vol. 30, no. 31, pp. 6158–6167, 2009.

- [16] Speciality Coating Systems, "Parylene Conformal Coating Specifications & Properties," pp. 1–12, 2013.
- [17] J. Charmet, J. Bitterli, O. Sereda, M. Liley, P. Renaud, and H. Keppner, "Optimizing parylene C adhesion for MEMS processes: Potassium hydroxide wet etching," *J. Microelectromechanical Syst.*, vol. 22, no. 4, pp. 855–864, 2013.
- [18] J. M. Hsu, L. Rieth, R. A. Normann, P. Tathireddy, and F. Solzbacher, "Encapsulation of an integrated neural interface device with parylene C," *IEEE Trans. Biomed. Eng.*, vol. 56, no. 1, pp. 23–29, 2009.
- [19] R. K. Sathir, W. J. James, H. K. Yasuda, A. K. Sharma, M. F. Nichols, and A. W. Haln, "The adhesion of glow-discharge polymers, Silastic and Parylene to implantable platinum electrodes: results of tensile pull tests after exposure to isotonic sodium chloride," *Biomaterials*, vol. 2, no. 4, pp. 239–243, 1981.
- [20] S. A. Hara, B. J. Kim, J. T. W. Kuo, C. D. Lee, E. Meng, and V. Píkov, "Long-term stability of intracortical recordings using perforated and arrayed Parylene sheath electrodes," *J. Neural Eng.*, vol. 13, no. 6, p. 66020, Dec. 2016.
- [21] C. Pang, "Parylene Technology for Neural Probes Applications," vol. 2008, p. 191, 2008.
- [22] R. Huang and Y. C. Tai, "Parylene to silicon adhesion enhancement," in *TRANSDUCERS 2009 - 2009 International Solid-State Sensors, Actuators and Microsystems Conference*, 2009, pp. 1027–1030.
- [23] S. J. Fonash, "An Overview of Dry Etching Damage and Contamination Effects," *J. Electrochem. Soc.*, vol. 137, no. 12, p. 3885, Dec. 1990.
- [24] L. Walter, "Photoresist Damage in Reactive Ion Etching Processes," *J. Electrochem. Soc.*, vol. 144, no. 6, p. 2150, Jun. 1997.
- [25] Oxford instruments plasma technology, "Reactive Ion Etching." [Online]. Available: <https://plasma.oxinst.com/campaigns/technology/rie>. [Accessed: 01-Aug-2018].
- [26] Oxford instruments plasma technology, "ICP etching." [Online]. Available: <https://plasma.oxinst.com/campaigns/technology/icp>. [Accessed: 01-Aug-2018].
- [27] D. B. Lee, "Anisotropic etching of silicon," *J. Appl. Phys.*, vol. 40, no. 11, pp. 4569–4574, 1969.
- [28] K. E. Bean and K. E. Bean, "Anisotropic etching of silicon," *IEEE Trans. Electron Devices*, vol. 25, no. 10, pp. 1185–1193, 1978.
- [29] H. Seidel, "Anisotropic Etching of Crystalline Silicon in Alkaline Solutions," *J. Electrochem. Soc.*, vol. 137, no. 11, p. 3626, 1990.
- [30] O. Powell and H. B. Harrison, "Anisotropic etching of {100} and {110} planes in (100) silicon," *J. Micromechanics Microengineering*, vol. 11, no. 3, pp. 217–220, 2001.
- [31] M. Shikida, K. Sato, K. Tokoro, and D. Uchikawa, "Comparison of anisotropic etching properties between KOH and TMAH solutions," in *Technical Digest. IEEE International MEMS 99 Conference. Twelfth IEEE International Conference on Micro Electro Mechanical Systems (Cat. No.99CH36291)*, 1999, pp. 315–320.

- [32] M. Shikida, K. Sato, K. Tokoro, and D. Uchikawa, "Differences in anisotropic etching properties of KOH and TMAH solutions," *Sensors Actuators, A Phys.*, vol. 80, no. 2, pp. 179–188, 2000.
- [33] S. Dutta, M. Imran, P. Kumar, R. Pal, P. Datta, and R. Chatterjee, "Comparison of etch characteristics of KOH, TMAH and EDP for bulk micromachining of silicon (110)," *Microsyst. Technol.*, vol. 17, no. 10–11, pp. 1621–1628, 2011.
- [34] U. Abidin, B. Y. Majlis, and J. Yunas, "FABRICATION OF PYRAMIDAL CAVITY STRUCTURE WITH MICRON-SIZED TIP USING ANISOTROPIC KOH ETCHING OF SILICON (100)," *J. Teknol.*, vol. 74, no. 10, Jun. 2015.
- [35] A. J. Trindade, "Transfer printing of nitride based light emitting diodes," 2015.
- [36] Nikon, "Differential Interference Contrast." [Online]. Available: <https://www.microscopyu.com/techniques/dic>.
- [37] EPFL - Centre of Micro & Nanotechnology, "WYKO NT1100 optical profiler - schematic." [Online]. Available: [https://cmi.epfl.ch/metrology/Wyko\\_NT1100.php](https://cmi.epfl.ch/metrology/Wyko_NT1100.php). [Accessed: 01-Aug-2018].
- [38] I. Filmetrics, "Filmetrics F20 Operations Manual." 2007.
- [39] Sloan Technology Corporation, "Dektak 3030 surface profiling system operations manual." p. 94, 1983.
- [40] KLA-Tencor, "AlphaStep-IQ surface profilometer manual." .
- [41] Veeco Instruments, "WYKO NT1100 Operator's guide," *East*, no. June. 2002.
- [42] J. Schmit, K. Creath, and J. C. Wyant, "Surface Profilers, Multiple Wavelength, and White Light Interferometry," in *Optical Shop Testing*, Hoboken, NJ, USA: John Wiley & Sons, Inc., 2006, pp. 667–755.
- [43] J. C. Wyant, "White light interferometry," in *Proceedings of the SPIE - The International Society for Optical Engineering*, 2002, vol. 4737, no. 2002, pp. 98–107.
- [44] J. C. Wyant and K. Creath, "Advances in interferometric optical profiling," *Int. J. Mach. Tools Manuf.*, vol. 32, no. 1–2, pp. 5–10, Feb. 1992.
- [45] A. Harasaki, J. Schmit, and J. C. Wyant, "Improved vertical-scanning interferometry," *Appl. Opt.*, vol. 39, no. 13, p. 2107, May 2000.
- [46] Veeco Instrument, "WYKONT100 Optical profiling system - specifications sheet." 2002.
- [47] Veeco Instruments, "WYKO NT1100 Setup Guide." 2007.
- [48] J. Goldstein, D. E. Newbury, J. R. Michael, N. W. M. Ritchie, J. H. J. Scott, and D. C. Joy, *Scanning electron microscopy and x-ray microanalysis*. .
- [49] I. JEOL, "JSM-IT100 Scanning Electron Microscope Operations Manual." 2015.
- [50] AIM Photonics Academy, MIT Microphotonics Centre, and iNEMI, "2017 Integrated Photonic Systems Roadmap (IPSR)," no. March. 2018.
- [51] J. Yoon, S. M. Lee, D. Kang, M. A. Meitl, C. A. Bower, and J. A. Rogers, "Heterogeneously Integrated Optoelectronic Devices Enabled by Micro-Transfer Printing," *Adv. Opt. Mater.*, vol. 3, no. 10, pp. 1313–1335, 2015.



- [52] M. Lapisa, G. Stemme, and F. Niklaus, "Wafer-level heterogeneous integration for MOEMS, MEMS, and NEMS," *IEEE J. Sel. Top. Quantum Electron.*, vol. 17, no. 3, pp. 629–644, 2011.
- [53] C. A. Bower, M. A. A. Meitl, B. Raymond, E. Radauscher, R. Cok, S. Bonafede, D. Gomez, T. Moore, C. Prevatte, B. Fisher, R. Rotzoll, G. A. Melnik, A. Fecioru, and A. J. Trindade, "Emissive displays with transfer-printed assemblies of  $8\ \mu\text{m} \times 15\ \mu\text{m}$  inorganic light-emitting diodes," *Photonics Res.*, vol. 5, no. 2, pp. 23–29, 2017.
- [54] B. Corbett, R. Loi, W. Zhou, D. Liu, and Z. Ma, "Transfer print techniques for heterogeneous integration of photonic components," *Prog. Quantum Electron.*, vol. 52, pp. 1–17, Mar. 2017.
- [55] M. Lapisa, G. Stemme, and F. Niklaus, "Wafer-Level Heterogeneous Integration for MOEMS, MEMS, and NEMS," *IEEE J. Sel. Top. Quantum Electron.*, vol. 17, no. 3, pp. 629–644, May 2011.
- [56] †,‡ Zhiyong Fan, †,‡ Johnny C. Ho, †,‡ Zachery A. Jacobson, †,‡ Roie Yerushalmi, † Robert L. Alley, † and Haleh Razavi, and †,‡ Ali Javey\*, "Wafer-Scale Assembly of Highly Ordered Semiconductor Nanowire Arrays by Contact Printing," 2007.
- [57] S. Khan, L. Lorenzelli, and R. S. Dahiya, "Technologies for Printing Sensors and Electronics Over Large Flexible Substrates: A Review," *IEEE Sens. J.*, vol. 15, no. 6, pp. 3164–3185, Jun. 2015.
- [58] J. Nah, H. Fang, C. Wang, K. Takeji, M. H. Lee, E. Plis, S. Krishna, and A. Javey, "III–V Complementary Metal–Oxide–Semiconductor Electronics on Silicon Substrates," *Nano Lett.*, vol. 12, no. 7, pp. 3592–3595, Jul. 2012.
- [59] A. Carlson, A. M. Bowen, Y. Huang, R. G. Nuzzo, and J. A. Rogers, "Transfer printing techniques for materials assembly and micro/nanodevice fabrication," *Adv. Mater.*, vol. 24, no. 39, pp. 5284–5318, 2012.
- [60] M. a. Meitl, Z.-T. Zhu, V. Kumar, K. J. Lee, X. Feng, Y. Y. Huang, I. Adesida, R. G. Nuzzo, and J. a. Rogers, "Transfer printing by kinetic control of adhesion to an elastomeric stamp," *Nat. Mater.*, vol. 5, no. 1, pp. 33–38, 2006.
- [61] A. J. Trindade, B. Guilhabert, D. Massoubre, D. Zhu, N. Laurand, E. Gu, I. M. Watson, C. J. Humphreys, and M. D. Dawson, "Nanoscale-accuracy transfer printing of ultra-thin AlInGaN light-emitting diodes onto mechanically flexible substrates," *Appl. Phys. Lett.*, vol. 103, no. 25, 2013.
- [62] T. H. Kim, A. Carlson, J. H. Ahn, S. M. Won, S. Wang, Y. Huang, and J. A. Rogers, "Kinetically controlled, adhesiveless transfer printing using microstructured stamps," *Appl. Phys. Lett.*, vol. 94, no. 11, pp. 2007–2010, 2009.
- [63] M. B. Tucker, D. R. Hines, and T. Li, "A quality map of transfer printing," *J. Appl. Phys.*, vol. 106, no. 10, pp. 1–8, 2009.
- [64] C. A. Bower, E. Menard, S. Bonafede, J. W. Hamer, and R. S. Cok, "Active-matrix OLED display backplanes using transfer-printed microscale integrated circuits," in *2010 Proceedings 60th Electronic Components and Technology Conference (ECTC)*, 2010, pp. 1339–1343.

- [65] W. Choi, C. Z. Kim, C. S. Kim, W. Heo, T. Joo, S. Y. Ryu, H. Kim, H. Kim, H. K. Kang, and S. Jo, "A Repeatable Epitaxial Lift-Off Process from a Single GaAs Substrate for Low-Cost and High-Efficiency III-V Solar Cells," *Adv. Energy Mater.*, vol. 4, no. 16, p. 1400589, Nov. 2014.
- [66] S. I. Park, Y. Xiong, R. H. Kim, P. Elvikis, M. Meitl, D. H. Kim, J. Wu, J. Yoon, C. J. Yu, Z. Liu, Y. Huang, K. C. Hwang, P. Ferreira, X. Li, K. Choquette, and J. A. Rogers, "Printed assemblies of inorganic light-emitting diodes for deformable and semitransparent displays," *Science (80-. )*, vol. 325, no. 5943, pp. 977–981, 2009.
- [67] H. Kim, E. Brueckner, J. Song, Y. Li, S. Kim, C. Lu, J. Sulkin, K. Choquette, Y. Huang, R. G. Nuzzo, and others, "Unusual strategies for using indium gallium nitride grown on silicon (111) for solid-state lighting," *Proc. Natl. Acad. Sci.*, vol. 108, no. 25, p. 10072, 2011.
- [68] T. Il Kim, Y. H. Jung, J. Song, D. Kim, Y. Li, H. S. Kim, I. S. Song, J. J. Wierer, H. A. Pao, Y. Huang, and J. A. Rogers, "High-efficiency, microscale GaN light-emitting diodes and their thermal properties on unusual substrates," *Small*, vol. 8, no. 11, pp. 1643–1649, 2012.
- [69] S. Kim, J. Wu, A. Carlson, S. H. Jin, A. Kovalsky, P. Glass, Z. Liu, N. Ahmed, S. L. Elgan, W. Chen, P. M. Ferreira, M. Sitti, Y. Huang, and J. A. Rogers, "Microstructured elastomeric surfaces with reversible adhesion and examples of their use in deterministic assembly by transfer printing," *Proc. Natl. Acad. Sci.*, vol. 107, no. 40, pp. 17095–17100, 2010.
- [70] B. Guilhabert, A. Hurtado, D. Jevtics, Q. Gao, H. H. Tan, C. Jagadish, and M. D. Dawson, "Transfer Printing of Semiconductor Nanowires with Lasing Emission for Controllable Nanophotonic Device Fabrication," *ACS Nano*, vol. 10, no. 4, pp. 3951–3958, Apr. 2016.
- [71] J. McPhillimy, B. Guilhabert, C. Klitis, M. D. Dawson, M. Sorel, and M. J. Strain, "High accuracy transfer printing of single-mode membrane silicon photonic devices," *Opt. Express*, vol. 26, no. 13, p. 16679, Jun. 2018.
- [72] S. Kim, J. Wu, A. Carlson, S. H. Jin, A. Kovalsky, P. Glass, Z. Liu, N. Ahmed, S. L. Elgan, W. Chen, P. M. Ferreira, M. Sitti, Y. Huang, and J. A. Rogers, "Microstructured elastomeric surfaces with reversible adhesion and examples of their use in deterministic assembly by transfer printing.," *Proc. Natl. Acad. Sci. U. S. A.*, vol. 107, no. 40, pp. 17095–100, 2010.

# Chapter 3

## Micro-LED fabrication, advanced transfer-printing and demonstrator on CMOS

### 3.1 Introduction

While investigating novel hybrid devices for optogenetics, this work relied heavily on the development of micro-transfer printing ( $\mu$ TP) and transfer-printable GaN/InGaN micro-sized light-emitting diodes (TP- $\mu$ LEDs). Necessary improvements to these were imposed by two factors : a) the stringent requirements of *in vivo* optogenetics on LED performance and size (see chapter 4), and b) the need for a reliable release method providing a strong bond and a thermally conductive path between  $\mu$ LEDs and their receiver substrate to limit Joule heating. This chapter explains how these challenges were addressed.

**Section 1** details how limitations of previous Strathclyde TP- $\mu$ LEDs were overcome by optimising the fabrication process, greatly improving performance and yielding the first small-footprint ( $50 \times 50 \mu\text{m}^2$ ), high-efficiency TP- $\mu$ LEDs suitable for high-power optogenetics.

**Section 2** details printing challenges and the new technique of picodroplet adhesive printing developed to allow direct  $\mu$ LED printing on “real-world” textured surfaces. By abolishing intermediate adhesive layers, this technique enhances substrate heatsinking and allows versatile, reliable  $\mu$ LED integration on a range of substrates.

**Section 3** demonstrates this capacity in the first working integration of  $\mu$ LEDs on a commercial CMOS chip, opening the way to more complex embedded devices.

## 3.2 Optimised fabrication for high-efficiency, top emitting $50 \times 50 \mu\text{m}^2$ LEDs for micro transfer-printing

### 3.2.1 Previous work and limitations

First conceived by John Rogers' group in 2011 [1], GaN-on-Silicon-based TP- $\mu$ LEDs have recently been developed at the Institute of Photonics by Antonio Trindade et al. [2], and used primarily as demonstrators for heterogeneous integration [3], [4] or visible-light communication (VLC) [5]. While sufficient for these applications, the printed devices performance was invariably poor compared to their monolithic counterparts, an indication that the manufacturing process was not optimal and may be damaging the LED epistructure [5]. Specifically, top-emitting devices exhibited parasitic resistances (fig 3.1.a) and their optical power output plateaued below  $100 \mu\text{W}$  ( $< 10 \text{mW}/\text{mm}^2$  surface irradiance). Pickup yield of the suspended devices was variable, and could be null (no retrieval possible) on some batches contaminated by underlying PR residues.

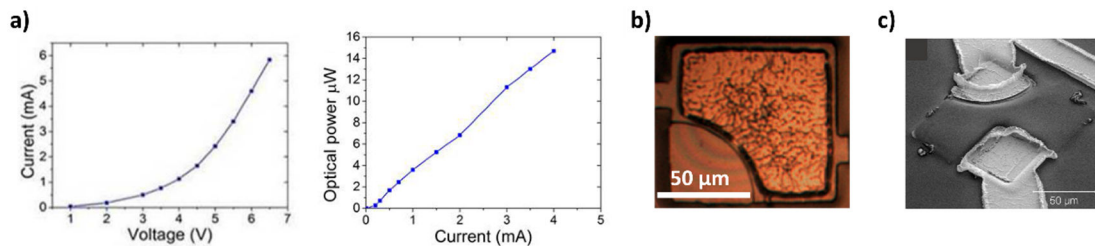


Figure 3.1 : Previous TP- $\mu$ LEDs demonstrated at Strathclyde ( $100 \times 100 \mu\text{m}^2$ , Pd spreading layers). **a)** IV and LI characteristics of a Pd-layer LED printed on glass (taken from [6]). The noticeable parallel resistance (shunt) may be caused by epistructure damage or deficient sidewall insulation creating leakage paths [7]. **b)** Micrograph of a finished device (from [4]) and **c)** SEM scan of a device insulated with a thick, spin coated SU-8 photoresist layer and contacted by gold tracks [2].

### 3.2.2 Electro-optical performance requirements for $\mu$ LEDs in this work

These performance levels fell quite short of this work's requirements for high-illumination optogenetics, relying on low-footprint devices capable of hundreds of  $\text{mW}/\text{mm}^2$  irradiance at reasonable drive currents ( $< \sim 3 \text{mA}$ ) (see chapter 4), and maintaining relatively high efficiency in electrical-to-optical power conversion to limit Joule heating. Furthermore, the post-printing SU8-based encapsulation and contacting strategy (fig 3.1.c) then used was not adaptable to our diamond probes (subsection 3.3.4) and needed to be replaced. For all these reasons, process failure modes were analysed as described in subsection 3.2.2 and a new, optimised process flow was established (subsection 3.2.3), compatible with halved-size LEDs ( $50 \times 50 \mu\text{m}^2$ ) to help limit the invasiveness of the neural probe.

### 3.2.3 Optimisation of manufacturing process

#### o Reduction of LED size to $50 \times 50 \mu\text{m}^2$

To avoid excessive tissue damage, a width of  $\sim 100 \mu\text{m}$  is often considered the acceptable maximum for brain implants designed for electrophysiology experiments in mice and rats [8]. Resizing of the TP- $\mu$ LEDs was therefore necessary, along with efficiency improvements. In this work, we opted for a square  $50 \times 50 \mu\text{m}^2$  LED design, allowing probe dimensions (section 4.2.3) comparable with state-of-the-art monolithic optrode designs [9], [10] and integrated prototypes [11].

Adequately-sized LED designs and new  $50 \times 50 \mu\text{m}^2$  stamps (see annex A3) were implemented on masks AB2 and “uTP” respectively (see annex A2). A study was performed with the help of Dr. Benoit Guilhabert to determine KOH etch times needed to fully underetch various membrane sizes (fig 3.2). The etch was found to progress at a rate of  $\sim 2\text{--}3 \mu\text{m}/\text{min}$ , faster and more linearly for smaller membranes ( $< 75 \times 75 \mu\text{m}^2$ ), whose lesser “crowding” (see inset) may help better fluid flow. The final etch of the anchors was slower, warranting up to 50% overetch to ensure complete removal of silicon below the whole structure.

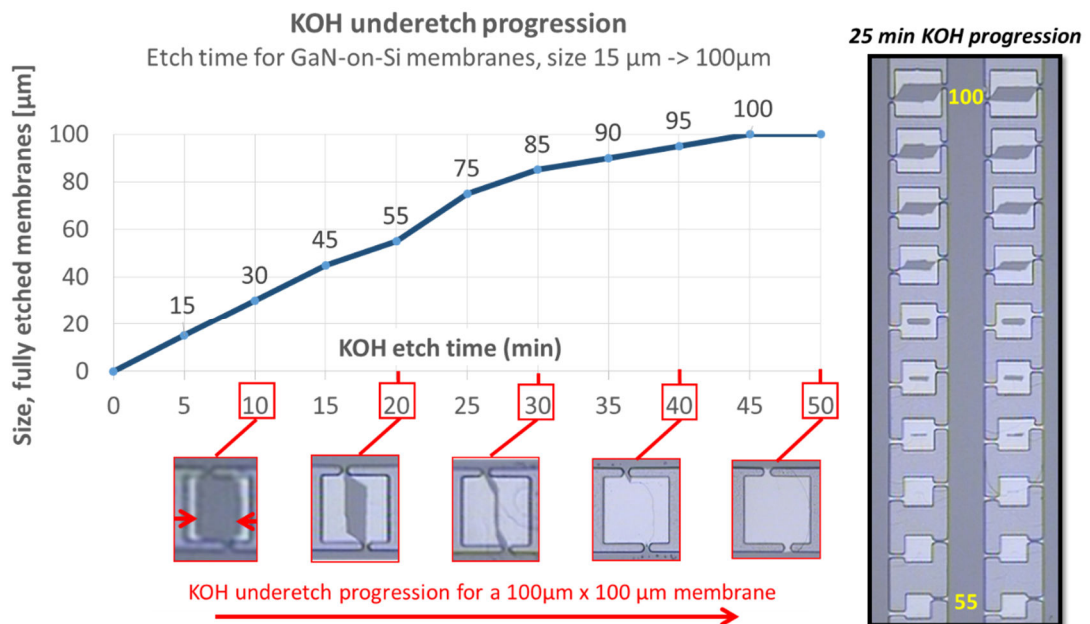


Figure 3.2 : Silicon underetch duration for various sizes of GaN membranes. GaN-on-Si membranes ( $15 \times 15 \mu\text{m}^2$  to  $100 \times 100 \mu\text{m}^2$ ) were etched in hot KOH solution and the time of full underetch recorded for each size (graph). Right inset: micrograph of etch progression at  $t=25 \text{ min}$  for a row, size  $55 \mu\text{m}$  to  $100 \mu\text{m}$ . Black areas indicate silicon remaining, while white platelets are fully underetched.

o *Process failures analysis and improvements*

A number of failure modes were identified in the pre-existing fabrication process described in [2], with the main ones listed in table 3.1 below, along with the solutions which were sequentially implemented.

<b>Fabrication process optimisation - <math>\mu</math>LEDs for transfer-printing (top emission)</b>				
<b>Batch name</b>	<b>Dimensions [<math>\mu\text{m}^2</math>] / SL*</b>	<b>Yield &amp; Quality (IV/LI)**</b>	<b>Issue identified</b>	<b>Working solution</b>
A1 (initial process)	100x100 / Ni/Au	50%, low	PR from SL pattern under LEDs prevents pickup	Dep and pattern SL before KOH
LEDAB	100x100 / Ni/Au	<25%, low	SL metal peeloff in KOH	SiO <sub>2</sub> re-coating before KOH
LEDTHIN	50x50 / Ni/Au	<20%, improved	Straight anchors do not break; LED cracking	New mask design; handling
LNIA50	50x50 / Ni/Au	>90%, ~OK	PR hard to strip after SL etch (residues)	Optimised PR & etch time
LPD50-D	50x50 / Pd(30nm)	>95%, good	SL reflective (Pd too thick)	Thinner Pd dep
LTHIN2 N3	100x100 / Pd(8nm)	> 95%, ~OK	Turn-on V > 5V (prob. more resistive SL)	
<b>LNIAU X2,X3</b>	<b>50x50 / Ni/Au</b>	<b>&gt;95%, good</b>	<b>IV-LI characteristics similar to monolithic devices, high pickup yield, very little cracking</b>	
<b>LNIAU X1</b>	<b>100x100 / Ni/Au</b>	<b>&gt;95%, good</b>		
* <i>Current spreading layer</i>				
** <b>Yield:</b> usable devices (pickup, lighting up). <b>"Quality"</b> as a measure of electrical characteristics based on turn-on voltage [ $<4\text{V}$ (good) – $7\text{V}$ (low)] & optical power at $5\text{V}$ [ $<10\mu\text{W}$ (low) to $>100\mu\text{W}$ (good)]				

Table 3.1 : Optimisation of the manufacturing process for TP- $\mu$ LEDs. The failure modes were addressed sequentially, over several prototype batches, leading to highly-efficient devices with reliable opto-electrical performance and high pickup yield.

To prevent metal peel off during the KOH underetch, metal deposition and patterning had been used as the final step, leading to major complications including residual PR trapped below the membranes blocking pickup, and potential metal deposition on LED sidewalls liable to create shorts. The metal deposition was instead reinstated as a first step, with a second protective layer of SiO<sub>2</sub> being deposited just before wet etching. An extensive study of anchor design was conducted (see below), improving pickup yield 5-fold to more than 95%. Particular attention was given to spreading layer patterning, minimising etch time to prevent damage to the very thin metal, underlying p-GaN and to the PR mask – unnecessarily long etch times used previously were found to leave hard to remove thin PR residue on top of the metal, affecting spreading layer quality and subsequent electrical contacts to the anode. Finally, thin layers of Palladium were examined as a spreading-layer replacement for standard Ni(11nm)/Au(22nm) bilayer used for top-emitting devices. Pd is known for its capacity to form a superior ohmic contact with p-GaN [12]–[14]. However, 30nm-thick Pd

proved too reflective for our use (towards emission <10%, vs >40% for Ni/Au [14]–[17]), while thinner layers (8nm to 10nm) translated to an increased LED turn-on voltage, probably caused by excessive resistivity of such palladium films below 20nm thickness [18], [19].

o *Optimisation of anchor design*


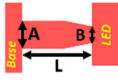
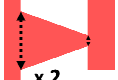
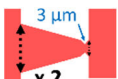
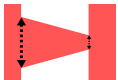
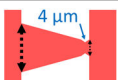
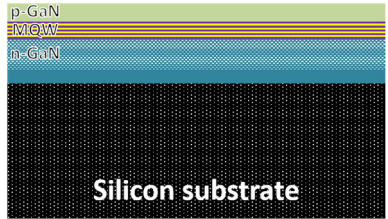
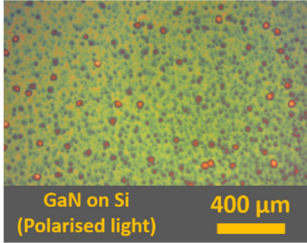
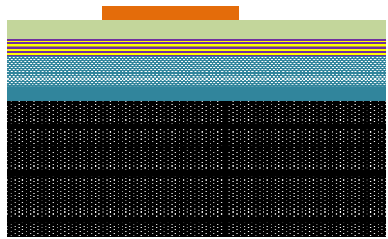
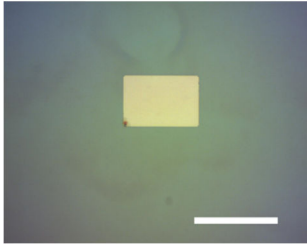
Anchor type vs pickup yield - $\mu$ LEDs, $50 \times 50 \mu\text{m}^2$					
Anchor dimensions [ $\mu\text{m}$ ] and shape (A,B,L) : (base width, joint width, length)		Detached in process	% pickup, first try	% pickup, multi-try	Number of samples
Previous work ([3], [20]) : 2 beams (A,L)=(6,5) $\mu\text{m}$		0%	< 25%*	< 50%*	n = 20 2 samples
This work - various anchor geometries tested					
2 anchors, beam + end bevel (A,B,L)=(10,6,25) [ $\mu\text{m}$ ]		<1%	0%	20%**	n = 30 3 samples
2 anchors, wide bevel (A,B,L) = (22,4,25) [ $\mu\text{m}$ ]		<1%	75%	>90%	n>30 3 samples
2 anchors, bevel + notch (A,B,L) = (18,6,25) [ $\mu\text{m}$ ]		<1%	80%	>90%	n>30 3 samples
Single anchors, wide bevel (A,B,L) = (22,6,25) [ $\mu\text{m}$ ]		<2.5%	90%	>95%	n>50 3 samples
Single anchors, bevel + notch (A,B,L) = (18,6,25) [ $\mu\text{m}$ ]		<2.5%	>95%	100%	n>50 3 samples
* Pickup impossible on one sample due to residual, unstripped PR below LEDs. ** At least 80% of "incorrect" pickups : anchors picked up with device due to breaking at beam base					

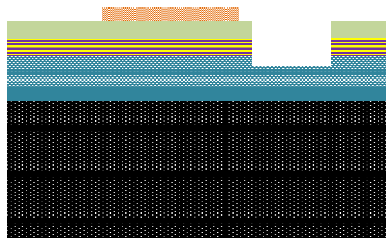
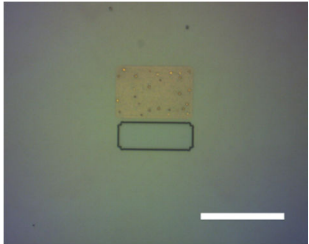
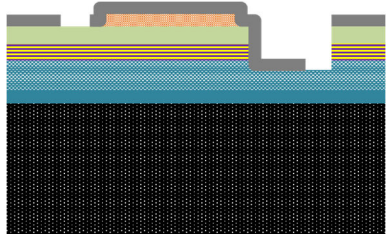
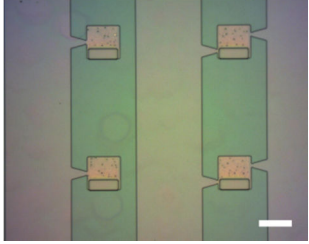
Table 3.2 : Anchor shape optimisation for  $50 \times 50 \mu\text{m}^2$  pixels. Pickup yields of more than 95% were reliably obtained with single, notched anchors (designs on Mask AB2).

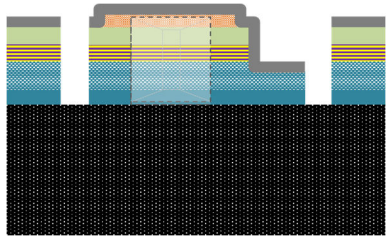
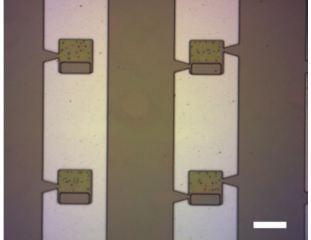
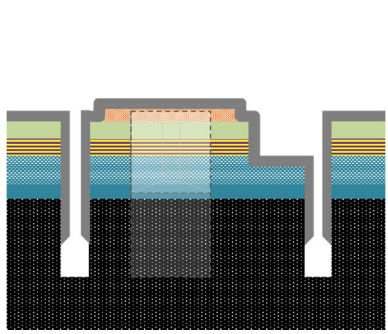
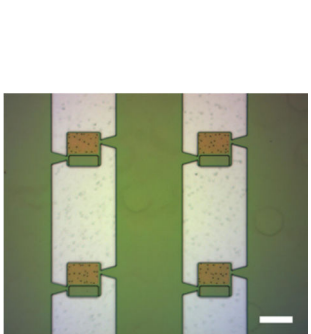
Simple homothetic downscaling of anchors used for larger,  $100 \times 100 \mu\text{m}^2$  devices proved ineffective, with anchors very difficult to break unless impractically high loads are applied using the PDMS stamp. This may be explained in part by a decrease in width-to-thickness ratio, but also by the reduced anchor strain due to inbuilt epilayer stress leading to membrane bowing (subsection 3.2.5), an effect roughly squaring with membrane size (fig 3.4). Table 3.2 shows the pickup results afforded by various anchor geometries. Right angles created fracture points and were discarded. The best results (pickup yield > 95%) were obtained for single narrow anchors comprising a notch acting as an effective fracture point separated from the LED sidewall, thus preventing crack propagation on the devices.

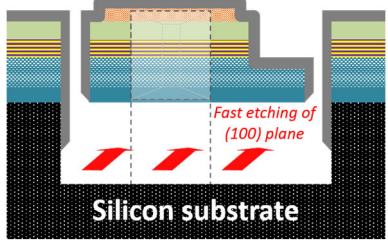
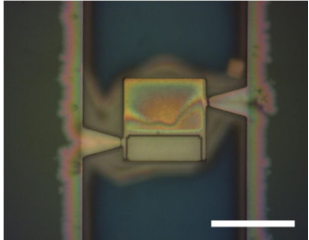
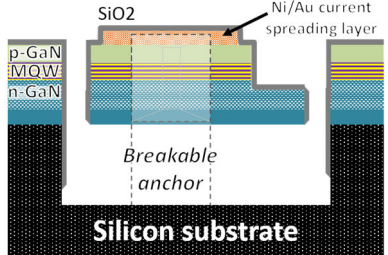
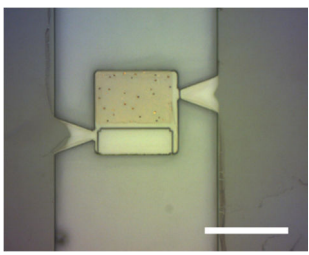
**3.2.4 Fabrication process: GaN-based  $\mu$ LEDs for transfer printing - (all white scale bars 50 $\mu$ m) – Mask AB2 (annex A2)**

Process step & description	Schematic & Micrograph	(All white scale bars 50 $\mu$ m)
<p><b>1. Initial sample cleaning and surface preparation for e-beam evaporation</b></p> <p>This thorough clean step ensures a good electrical contact will form with the metal current spreading layer evaporated in the next step. The samples are left in ultrasonic cleaning in acetone for 10min to remove photoresist, grease and particulate contamination, then cleaned in IPA for 10min and blow-dried with N2 jet. Any remaining protective photoresist or organic residues are further dry-stripped (Diener asher, 5min O<sub>2</sub> plasma, 200W). The samples are then dipped for 2min in pure HCl to remove native oxides forming on top of the GaN layer, rinsed in generously running DI for 3min and blow-dried. After cleaning, the samples are Kapton-taped onto a clean Silicon carrier wafer and immediately loaded into the e-beam chamber.</p>	 <p><b>Silicon substrate</b></p> <p><i>Schematised LED epistructure</i>  Top : p-doped GaN layer  Middle : multiple InGaN/GaN quantum wells  Bottom : n-doped GaN layer</p>	 <p>GaN on Si (Polarised light) 400 <math>\mu</math>m</p>
<p><b>2. Metal evaporation (Ni/Au or Pd) &amp; 3. Patterning and etch into current spreading layer</b></p> <p>High-transparency Ni/Au was preferred over thin Pd layers capable of ohmic contact to GaN.</p> <p><b>2. Evaporation (Ni/Au) :</b> a first layer of 10nm Ni is evaporated at a rate of 0.05nm/s (current: 120-140mA), followed by a second layer of 20nm Au evaporated at 0.05nm/s (current: 75-90mA). For Pd-based devices, a layer of 20-25nm Pd is evaporated at a rate of 0.03nm/s (current: 30-40mA).</p> <p><b>3.a) Patterning:</b> samples are coated with 500nm-thick S1805 resist spun at 3600rpm for 60s, and soft baked on a hot plate at 115°C for 60s. Vertical mask features of cell “SL” are aligned with the Si&lt;110&gt; direction before a 7.8s UV exposure, then developed for 40s in a 1:1 mix of MicroDVP:DI water. The PR mask is then hard-baked (2min at 115°C) to help withstand the upcoming aggressive dry etch.</p> <p><b>3.b) Metal etch &amp; resist strip :</b> the metal layers are sputter-etched in RIE#2 (minimised etch times) :  - Ni/Au 10/20nm layer : recipe “niautest.rec” for 2min (Pd 25nm layer : recipe “pdetch.rec” for 2min15s)  The damaged PR is stripped immediately by Matrix plasma ashing (6min at 150°C).</p>		



Process step & description	Schematic & Micrograph	(All white scale bars 50µm)
<p><b>4. n-GaN contact patterning and etching &amp; 5. Spreading layer annealing</b></p> <p><b>4.a) Cathode patterning:</b> the samples are spin coated with 1µm-thick maN-1410 negative resist, spun at 2500rpm for 60s, and soft baked for 1min40s on a hot plate at 100°C. They are then exposed for 18s using cell “n-contact”, and developed for 40s in pure maD533S.</p> <p><b>4.b) ICP etching to n-GaN:</b> the LED cathode is defined by ICP etching ~680nm through GaN down to the underlying n-doped GaN, using the recipe “KHSGaN4” for 1min40s. The PR mask is fully stripped by Matrix ashing (6min at 150°C) followed by solvent clean (acetone 10min, IPA 5min).</p> <p><b>5. Spreading layer annealing :</b> to improve the GaN/metal electrical contact and allay etch damage, samples are annealed as follows :</p> <p>Ni/Au devices : RTA recipe n°3 (annealing step at 510°C in air) (Pd devices : RTA recipe n°5)</p>		
<p><b>6. Thick SiO<sub>2</sub> hard mask deposition &amp; 7. Patterning into devices with anchors for µTP</b></p> <p><b>6. SiO<sub>2</sub> deposition:</b> A thick SiO<sub>2</sub> protective layer is needed to withstand the upcoming steps, especially the aggressive Silicon sputter-etch by heavy SF<sub>6</sub> ions. A 1100nm-thick layer of PECVD SiO<sub>2</sub> is deposited at a temperature of 300°C, running recipe “oxide200” for 35min.</p> <p><b>7.a) Patterning of individual devices :</b> after application of HMDS primer (spun at 4000rpm for 10s) to help PR adhesion to the SiO<sub>2</sub> surface, the samples are spin coated with 500nm-thick S1805 positive resist spun at 3600rpm for 60s, and soft baked for 60s at 115°C on a hot plate. Using mask cell “suspended pixels”, they are exposed for 2.8s and developed for 32s in 1:1 MicroDVP:DI.</p> <p><b>7.b) SiO<sub>2</sub> etch:</b> the hard mask is defined by etching the unprotected SiO<sub>2</sub> in RIE#1 using recipe “mlesio2.rec” for 65min. The 40% overetch (w.r.t. blanket rate) ensures faithful definition of slower-etching, narrow anchor notches, adequately tailoring their ultimate mechanical strength for µTP use.</p>		

Process step & description	Schematic & Micrograph	(All white scale bars 50μm)
<p><b>7.c) ICP etching through the GaN layer down to the Si substrate</b></p> <p>Using ICP etching, the 2μm-thick GaN layer is then fully etched through down to the underlying Si layer using recipe “KHSGaN4” for 8min, and defining the individual devices. The remaining PR mask is stripped by Matrix ashing (6min at 150°C) and samples are solvent cleaned (acetone 5min, IPA 5min) before proceeding to the substrate etch.</p>		
<p><b>7.d) Silicon substrate etching &amp; 8. Protective remasking of devices by SiO<sub>2</sub></b></p> <p><b>7.d) Si etching:</b> the Si substrate is etched to a depth of ~1600nm using RIE#2 recipe “sietch2.rec” for 3min, creating pillared structures to be underetched to yield suspended individual μLEDs. The remaining hard mask, damaged and thinned (down to 500nm-700nm) by this low-selectivity etch, provides insufficient protection of the GaN and top metal layers for the upcoming KOH process.</p> <p><b>8. SiO<sub>2</sub> deposition :</b> an additional layer of SiO<sub>2</sub> (1000nm) is deposited by PECVD at a temperature of 300°C, running recipe “oxide200” for 30min. The partially conformal PECVD process can coat device top surfaces and sidewalls, adequately protecting them from KOH chemical attack, but leaves the bottom of the trenches exposed, allowing the wet etch of the silicon substrate to proceed. The SiO<sub>2</sub> layer also structurally reinforces the 2-μm thin GaN membranes, limiting cracking during the hot KOH etch.</p>		

Process step & description	Schematic & Micrograph	(All white scale bars 50µm)
<p><b>9. Directional etching of silicon in heated KOH</b></p> <p>The (111) silicon substrate is anisotropically etched along the (110) fast-etching planes in hot KOH, leaving individual µLEDs suspended by anchors : (see full KOH etch protocol in annex A1.4.c)</p> <p>Using a covered PTFE beaker, the samples are etched in a 40% w/w KOH solution, heated to 80°C in a water bath and magnetically stirred to ~400rpm. Complete under etch of the devices is obtained after 30min for 50x50µm<sup>2</sup> devices, and 60min for 100x100µm<sup>2</sup> devices.</p> <p>Suspended devices are fragile and prone to cracking upon thermal or mechanical shock. At etch completion, samples are gently taken out of the KOH beaker and immersed in heated DI water. After rinsing in running DI water for 3 min, samples are briefly transferred in IPA to lower surface-tension induced stress before drying under gentle N<sub>2</sub> jet.</p>		
<p><b>10. Removal of damaged oxide &amp; 11. Final thin insulation layer</b></p> <p><b>10. Two-step stripping of oxide mask:</b> the useless, roughened oxide mask is fully removed along with etch contamination in two steps. First, the SiO<sub>2</sub> layer is thinned down by an optimally timed dry etch to ~150-200nm thickness. Typically for 50µm pixels, this involves a 16-20min etch in RIE#1 using “mlesio2” recipe. The remaining layer is then etched by 3 successive 15s dips in buffered 7:1 HF (BOE), followed by gentle rinsing under DI for 3min. Cumulative etch time in BOE must be kept below 1 minute to prevent delamination of the spreading layer.</p> <p><b>11. Thin SiO<sub>2</sub> deposition:</b> samples are coated with a thin protective SiO<sub>2</sub> layer (100nm PECVD, recipe oxide200.rec run for 3min at 300°C), compatible with our post-printing contacting scheme (section 3.3.4).</p>		
<p><b>PROCESS END:</b> µLEDs suspended by breakable anchors to their native GaN-on-Si substrate are ready for pickup and transfer to new substrates.</p>		

### 3.2.5 LED performance

Electro-optical characteristics of the first batches of  $100 \times 100 \mu\text{m}^2$  and  $50 \times 50 \mu\text{m}^2$  LEDs fabricated through this optimised process (batches “LNIAU X1, X2, X3”) are given in figure 3.3 (red curves), and contrasted (bottom row) with previously reported Strathclyde  $\mu$ LEDs manufactured from the same initial wafer material. All devices show peak emission at  $\lambda = 455$  nm (fig 3.3.a). While a remaining  $\sim 10\%$  of larger devices showed cracking, no  $50 \times 50 \mu\text{m}^2$  exhibited any structural damage (3.3.b and c), and none showed metal delamination, with  $>99\%$  devices suitable for operation.

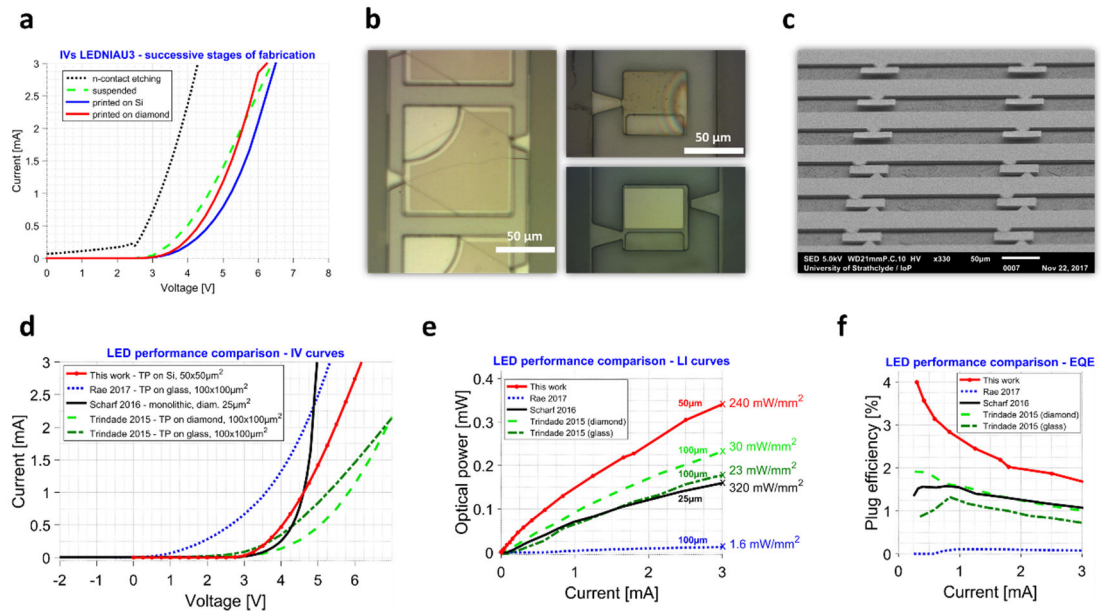


Figure 3.3 : Optimised TP- $\mu$ LEDs electro-optical performance and comparison to previous IoP work. **a)** IV curve at different stages of fabrication. **b), c)** micrographs and SEM scan of final arrays of suspended LEDs. (Larger  $\mu$ LEDs may still exhibit cracking as visible on **b)**, left). **Bottom row** : direct performance comparison of our  $50 \times 50 \mu\text{m}^2$  LED (red curve) printed on silicon with previously reported IoP devices ([4], [10], [21]) manufactured using the same initial device material, in terms of **d)** IV characteristics, **e)** LI output and **f)** external quantum efficiency (electrical-to-optical power conversion). Black curve shows performance of a monolithic LED for reference [10].

When compared to previous performance obtained by TP- $\mu$ LEDs at Strathclyde (fig 3.3, bottom row and table 3), devices in this work consistently showed lower turn-on voltage, lower linear resistance and much lower sub-turn-on leakage current (3.3.d) with two-fold to more than twenty-fold increase in external quantum efficiency at various driving currents (3.3.f). Crucially,  $50 \times 50 \mu\text{m}^2$  strongly outperformed previous, larger devices in optical power with irradiances of hundreds of  $\text{mW/mm}^2$  now suitable for high-power optogenetics. These results put those TP- $\mu$ LEDs almost on par with the output achieved by monolithic GaN-on-Si

devices (fig 3.3 bottom, black curves; see also table 3), indicating that the fabrication process caused minimal or no damage to the device epilayers. Indeed, the last fabricated  $\mu$ LED batches, used for integration onto diamond probes, yielded even superior characteristics (see chapter 5), with only minute performance degradation from monolithic devices.

Table 3 extends the performance comparison to similar non-monolithic devices recently reported in the literature, which were transferred on various substrates using transfer-printing, wafer-bonding, and/or laser-liftoff from a GaN-on-sapphire substrate. Our devices, while amongst the lowest footprints, also rank within the highest absolute optical power outputs and mark the best performance of released GaN-on-Si  $\mu$ LEDs to date.

### Comparison of $\mu$ LED performance to previous work (GaN LEDs for transfer-printing only)

	Area [ $\mu\text{m}^2$ ]	Turn-on Voltage $V_T$	Leak. Current @ $V_T/2$	EQE [%] @ 2mA	Optical power [mW] @ 2mA
<b>Kim et al. 2013</b> [11] GaN/Sapph, LLO + uTP	40x40	~3.5 V	NA	8 % (array of 4)	0.2
<b>Goßler et al. 2014</b> [22] GaN/Sapph, LLO + WB	50x50	~3.1 V	NA	@1 mA: ~ 1.7 %	@1 mA: 0.015
<b>Ayub et al. 2016</b> [23] GaN/Sapph, LLO + WB <sup>#</sup>	112x112	~6 V	NA	~0.1 %	0.015
<b>Ayub et al. 2017</b> [24] Commercial LED chips (50 $\mu\text{m}$ thick)	270x220	~2.8 V	NA	2 %	0.12
<b>Soltan et al. 2017</b> [25] GaN/Sapph, ball bond.	100x100	3.6-4.5 V	NA (>0.1 mA)	< 0.7%	< 0.04
<b>Prev. IoP work :</b> GaN/Si, <b>monolithic</b> [10]	25 $\mu\text{m}$ diameter	~4.5 V	<10 nA	1.3 %	0.12
<b>Prev. IoP (uTP, GaN /Si**)</b> - [2]-[4], [21]	150x150 [3] 100x100 [4], [21]	~3.5 V 4.5-6 V	NA $\leq$ ~0.5 mA	< 0.4 % 0.1-1 %	~ 0.05 0.007 to 0.15
<b>This work</b> GaN/Si, uTP, Ni/Au	<b>50x50</b>	<b>~ 3.9 V</b>	<b>&lt; 10 nA</b>	<b><math>\leq</math> 2.6 %</b>	<b>0.28</b>

\*GaN/Sapph : GaN-on-sapphire; \*\*GaN/Si : GaN-on-Si; \*\*\*LLO : laser liftoff; <sup>#</sup>WB : wafer bonding

Table 3 : Comparison table of electro-optical performance of  $\mu$ LEDs from both GaN-on-sapphire and GaN-on-Si native substrates, integrated on other substrates by various methods including transfer-printing. Previous IoP work shaded in green, devices fabricated in this work in red. Our devices represent to date both the most compact and efficient GaN-on-Si  $\mu$ LEDs demonstrated, with optical power and EQE besting all similar reported devices but those from the landmark study by Kim et al. (array of four  $\mu$ LEDs [11]), fabricated from highly efficient GaN-on-Sapphire substrates.

### 3.2.6 LED curvature

As previously reported [3], released TP- $\mu$ LEDs exhibit convex, quasi-circular curvature. This is caused by compressive stress voluntarily introduced in the AlGaIn buffer layer during growth, in order to compensate the significant tensile stress observed in post-growth cooling between GaN layers and the Si substrate, and due to a  $\sim 46\%$  mismatch in coefficients of thermal expansion between the substrate and epi-layers [26]. After KOH underetch of the silicon removes that balance, suspended  $\mu$ LEDs present a bow which strongly reduces their backside contact area to printing substrates, and therefore the strength of the associated van der Waals attraction (3.3.2).

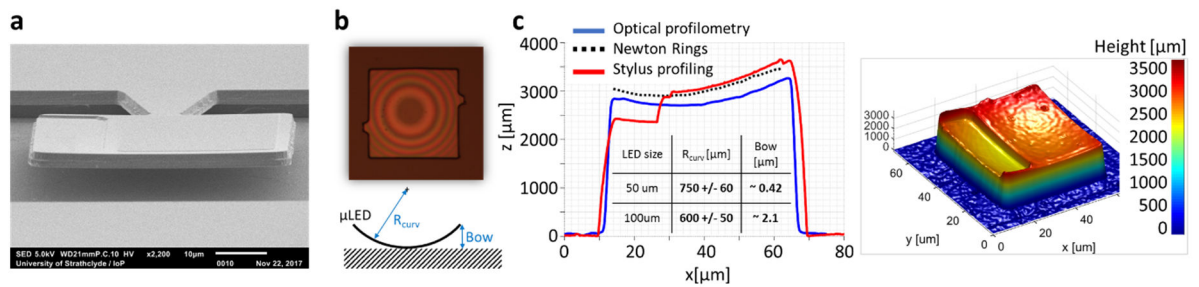


Figure 3.4 : Inbuilt stress in the epilayers induces significant bowing in the released  $\mu$ LEDs. **a)** SEM scan of a  $50 \times 50 \mu\text{m}^2$  device. **b)** Micrograph of a  $100 \times 100 \mu\text{m}^2$  LED printed on glass shows “Newton rings”, which can be used to deduce LED curvature (see annex A6). **c)** Left graph: optical profile, stylus profile and Newton rings reconstruction of a printed  $50 \times 50 \mu\text{m}^2$  LED. Inset: values for radius of curvature and bow for the two LED sizes considered. Right: optical profiling 3D reconstruction of  $50 \times 50 \mu\text{m}^2$  LED.

Accurate analysis of the bowing was important for process optimisation. The LED bow (centre-to-edge deflection, in both lateral directions) was initially quantified by analysis of “Newton rings” fringes (fig 3.4.b), using a MATLAB program written for this purpose given in annex A6. Optical profiling was later used as a more efficient and practical method as it was found to reliably correlate with both “Newton rings” and direct stylus profiling measurements (fig 3.4.c). Typical radii of curvatures of  $\sim 0.75$  mm and  $\sim 0.6$  mm were found for  $100 \times 100 \mu\text{m}^2$  and  $50 \times 50 \mu\text{m}^2$  respectively, translating to bows exceeding  $2 \mu\text{m}$  and  $400$  nm which must be considered during e.g post-printing insulation and contacting (section 3.3.4).

### 3.3 Development of a strategy for advanced integration

This work faced a specific set of challenges for the integration of TP- $\mu$ LEDs on processed ultrathin diamond membranes (see probe fabrication process in chapter 4). “Standard” transfer-printing methods were found unsuitable for thermally efficient integration, while new LED contacting strategies were needed to accommodate very fragile substrates. This section details the innovative solutions developed to accommodate fundamental physical limitations in micro-scale adhesion, allowing us to integrate devices on a wide range of substrates including CMOS commercial chips.

#### 3.3.1 Specific challenges for transfer-printing in this project

- o *Standard adhesive layers cannot be used for most efficient thermal transfer*

In the past decade, maturing transfer-printing technologies have succeeded in integrating a wide range of releasable devices on many different substrates at wafer scale, from arrays of printable solar cells [27], [28] or integrated circuits [29], [30], to III-V laser integration on silicon chips [31], versatile wearable electronics [32], [33] and glass or plastic displays using LEDs comparable to those fabricated in this work [34], [35].

Underpinning this impressive track record is the high-yield transfer capacity afforded by adhesive layers coating the receiving substrates. Most commonly, a layer of polymer such as SU-8 photoresist, polyimide (PI) or benzocyclobutene (BCB) is spin-coated on the substrates immediately before printing ( $\sim$ 500nm to 2 $\mu$ m thickness [36]), routinely allowing >99.9% transfer yields with micron-level accuracy in laboratory environments [35].

While greatly simplifying the transfer process, intermediary adhesive layers create a thermally resistive path between TP- $\mu$ LEDs and their receiving substrates preventing their use for heat sinking [36], [37]. A simple FEA numerical simulation run in COMSOL can predict the detrimental effects of even submicron-thickness intermediary layers on heat extraction by a silicon substrate of a printed LED (figure 3.5).

Printing surfaces of the diamond probes developed in this work are highly textured, with step heights exceeding 800nm. Any SU-8 adhesive layer thick enough for good step coverage would almost fully negate the advantage afforded by diamond’s extraordinary thermal properties, besides complicating diamond handling. For all these reasons, the standard route of adhesive bonding could not be used in this work and a novel integration solution was needed. The specific requirements for this are quickly outlined below.

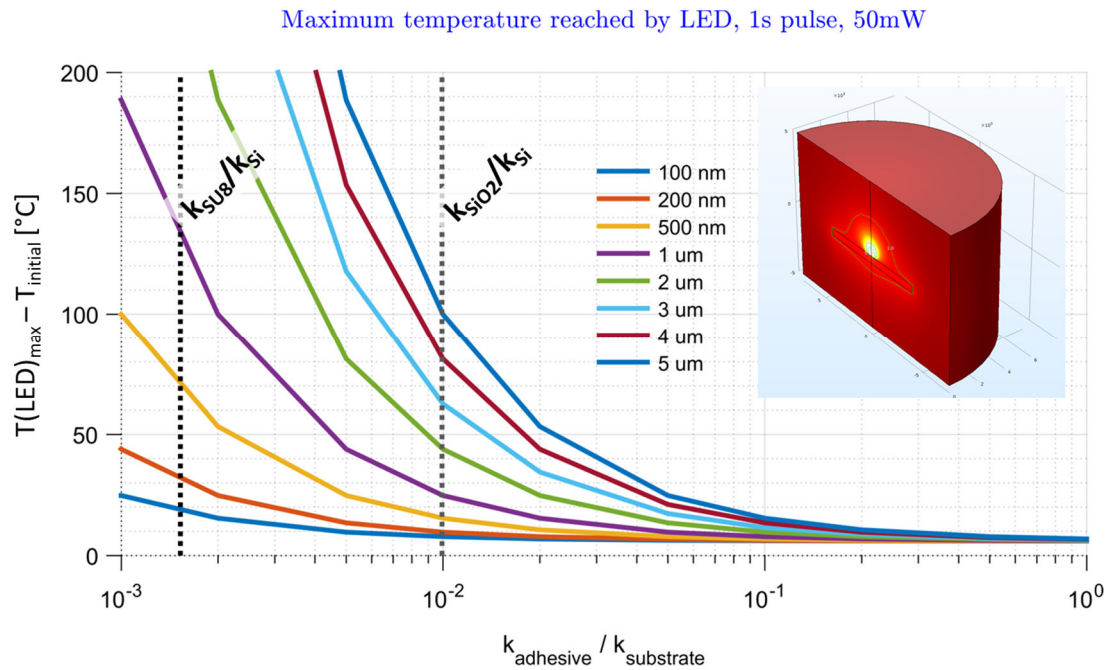


Figure 3.5 : Elementary heat transfer model of a LED heat source (50mW pulse for 1s in air ambient, geometry in inset), printed on a substrate with thermal conductivity  $k_{\text{substrate}}$  with help of an intermediary adhesive layer of varying thickness (coloured curves) and thermal conductivity  $k_{\text{adhesive}}$ . When no adhesive is present ( $k_{\text{adhesive}} = k_{\text{substrate}}$ ), the maximum temperature increase at the LED is  $\Delta T_{\text{max}} < 7^\circ\text{C}$ . For a SU8 adhesive layer ( $k_{\text{SU8}} = 0.2 \text{ W}\cdot\text{m}^{-1}\cdot\text{K}^{-1}$ ) on a silicon substrate ( $k_{\text{Si}} = 131 \text{ W}\cdot\text{m}^{-1}\cdot\text{K}^{-1}$ ),  $k_{\text{adhesive}}/k_{\text{substrate}} \sim 1.53 \times 10^{-3}$  (left vertical dotted line) and even very thin adhesive layers strongly impede heat transfer ( $\Delta T_{\text{max}} \sim 70^\circ\text{C}$  for a 500nm layer). (All  $\Delta T_{\text{max}}$  reached within  $\sim 150\text{ms}$  of pulse start).

o *Requirements for TP- $\mu$ LED integration on diamond probes*

Parameter	Requirement	Comment
“Membrane” (LED) size	$100 \times 100 \mu\text{m}^2$ and $50 \times 50 \mu\text{m}^2$	Bowed membranes (see 3.2.6)
Printing surface	PECVD $\text{SiO}_2$ (over traces) Highly textured, steps $> 800\text{nm}$	No chemical bond VDW limitation (see 3.3.2)
Thermal contact	Direct (no interlayer) or non-detrimental ( $K_{\text{contact}} \geq K_{\text{SiO}_2}$ )*	
Positioning accuracy	$\leq 1 \mu\text{m}$	i.e similar to lithography tolerance
Transfer yield	$> 80\%$ , no uncontrolled release	32 devices to print per chip

\*  $K$ : thermal conductivity. On probes, LEDs are printed on a  $< 400\text{nm}$   $\text{SiO}_2$  tracks insulation layer.

Table 4 : Main requirements for the transfer-printing of  $\mu$ LEDs used in the manufacturing of diamond-based optrodes described in chapter 4.

Both the fabrication process of our diamond probes (chapter 4) and the optical/thermal specifications of the devices (section 3.2.2) strictly determined the requirements for transfer-printing of the  $\mu$ LEDs. The main parameters are given in Table 4.



The ideal solution to fulfil the need for direct thermal contact between LED backside and receiving substrate would be an adhesiveless method. Unfortunately, fundamental physical limitations of micro-scale adhesion generally precludes direct release on textured surfaces as explained in the next sections.

o *Existing “adhesiveless” printing methods could not be used in the scope of this work*

With the drawbacks of using bonding layers being well acknowledged [36], [38], [39], “adhesiveless” printing methods have been demonstrated in specific contexts. The detachment of a picked-up membrane from the stamp can be facilitated by microstructured PDMS minimising stamp/membrane adhesion [40], or promoted by applying shear loads to initiate separation [41]. Conversely, membrane/substrate attraction forces can be enhanced by harnessing specific surface chemistries inducing bonding [42], exploiting favourably high surface energies [43] or even under different heat or pressure regimes [44]. These methods are however heavily context-dependent. Experimentally, they only enable release of rigid micro-sized inks such as our  $\mu$ LEDs onto very smooth and clean surfaces but cannot be applied for transfer to patterned/textured substrates such as microchips, rough or stepped sample areas or processed devices such as those used in this work. Recognising this fact, Saiedpourazar et al. have developed a fully versatile technique where membrane release can be triggered at will by laser-induced stress at the stamp/membrane interface [37], but the associated setup is relatively unpractical and the technique does not necessarily ensure good bonding of the membrane with the receiver substrate, a crucial step for post-processing.

o *Surface-tension-driven release methods could not be replicated*

Alternatively, recent work from colleagues at the Institute of Photonics had reported that membrane release could be achieved through the surface-tension pull of an intermediary solvent [4], mirroring a process demonstrated by Z.L. Liao for strong bonding of smooth wafers of cm-scale [45]. In this “capillary bonding” process, a solvent drop of diameter similar to that of the  $\mu$ LED would first be deposited on the  $\mu$ LED’s backside, before positioning the latter above the receiver and bringing the two in close contact; the liquid surface-tension pull would then delaminate the  $\mu$ LED from the stamp; finally, the growing hydrostatic pressure (fig 3.6.a) exerted by the evaporated liquid would bring  $\mu$ LED and substrate to close contact. This process could unfortunately not be replicated experimentally, especially since solvent or even water drops of the volumes involved (10-100 pL, for drop radius  $R \sim 20$ -50  $\mu$ m) fully evaporated within seconds (<5s for acetone or IPA), making solvent-only wetting of the LED

backside impossible. This is in accordance with the predicted evaporation rate of a sessile droplet on a solid substrate, which for high contact angles can be approximated as [46] :

$$E(t) = 2\pi D(1 - H)c_v R \quad (3.1)$$

where  $R$  is the (drop) contact-line radius,  $D$  is the vapour diffusivity in air,  $H$  the relative humidity and  $c_v$  the saturated vapour concentration. Using standard values for water [46],  $2\pi D(1 - H)c_v \sim 2 \times 10^{-6} \text{ g} \cdot \text{mm}^{-1} \cdot \text{s}^{-1} = 2 \text{ pL} \cdot \mu\text{m}^{-1} \cdot \text{s}^{-1}$ , initial evaporation rates on the order of 40-100 pL/s (decreasing with  $R$ ) are predicted for 20-50  $\mu\text{m}$ -radius droplets (evaporation rates for solvents would be even higher). It is therefore unlikely that a solvent-driven “capillary bonding” process can be harnessed in a standard humidity cleanroom environment for release and bonding of such small devices, and more probable that the adhesion results from other factors.

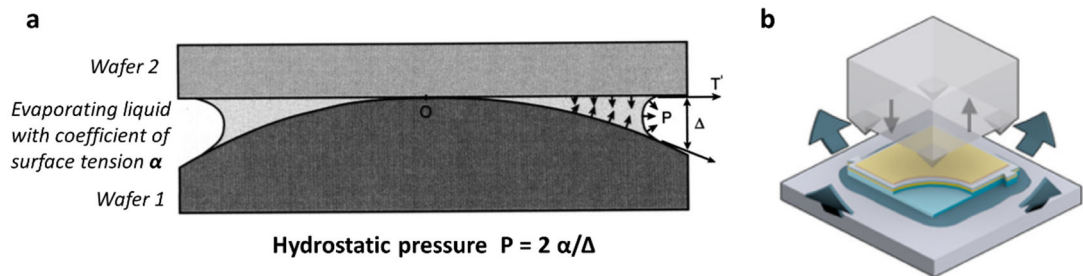


Figure 3.6 : The process of capillary bonding. **a)** Macro-scale samples can be pulled together by the hydrostatic pressure exerted by an evaporating interfacial liquid ([45]). **b)** The concept, erroneously applied to  $\mu$ LED bonding ([4]). Fast droplet evaporation means this method is impractical and very challenging to successfully apply at the microscale.

More generally, all adhesiveless release strategies presented above eventually come up against fundamental limitations imposed by the physics of adhesion at the microscale, dominated here by van der Waals forces. Understanding these limitations is important to devise successful and reliable transfer strategies.

### 3.3.2 Fundamental limitations to fully adhesiveless printing: VDW forces

Adhesion between bodies at the microscale can be generated by (in decreasing order of magnitude) strong chemical bonds, electrostatic forces, capillary forces and van der Waals (VDW) forces [47]. In our case, the first three of these do not apply to interactions between stamp (PDMS), LED ( $\text{SiN}_x$  backside) and receiver substrate ( $\text{SiO}_2$ , diamond, Si) within a static- and humidity-controlled cleanroom environment. Both the adhesion between stamp and LED, and between LED and substrate are therefore fully dominated by VDW forces [36], [40], specifically London dispersion forces (LDF) prevailing between non-polar surfaces [48]–[51].

It should be noted that in our case these are at least 5 orders of magnitude stronger than the LED's weight (fig 3.7), as the mass of AlInGaN TP- $\mu$ LEDs (average density  $\rho_{LED} \sim 4700 \text{ kg.m}^{-3}$ , thickness  $\sim 2.5 \mu\text{m}$ ) ranges from  $\sim 30 \text{ ng}$  ( $50 \times 50 \mu\text{m}^2$ ) to  $\sim 120 \text{ ng}$  ( $100 \times 100 \mu\text{m}^2$ ).

VDW/LDF are ubiquitous, short-range forces arising from dynamic interactions between molecule multipoles. Rigorous calculation of VDW forces between macroscopic bodies is an active area of research [49] but good approximations of non-retarded, additive interactions can be obtained for common geometries by integrating a Lennard-Jones type potential for all atoms over the bodies considered [47], [49], [52], [53]. Resulting attraction forces between two bodies can conveniently be given in terms of the system Hamaker constant  $A$ , which is directly related to the bodies' surface energy  $\gamma_1$  and  $\gamma_2$ :

$$A = \pi^2 C_{disp} \times \rho_1 \rho_2 \cong 24\pi \times \gamma_{12} r_0^2 \quad (3.1)$$

$$\text{with} \quad C_{disp} \cong \frac{24\gamma_{1 \rightarrow 2} r_0^2}{\pi \rho_1 \rho_2} \quad \text{and} \quad \gamma_{12} = \sqrt{\gamma_1 \gamma_2} \quad (3.2)$$

where  $C_{disp}$  is the London dispersion constant [48],  $\rho_1$  and  $\rho_2$  the atomic number density of bodies 1 and 2,  $\gamma_{12}$  the surface interaction energy and  $r_0 \sim 0.5 \text{ nm}$  the "contact distance" between the bodies.

The Hamaker formulation for two relevant geometries are given in fig 3.7.a as a function of the separation distance  $D$  between the two bodies considered. The parallel-plate system can satisfactorily model the VDW attraction between stamp and LED, a flat LED backside and a smooth substrate, and even stamp tips and the LED topside [40]. The sphere-surface approximation, recently found to agree very closely with experimental values despite its simplicity [54], [55], can be used to estimate the interaction force between a near-spherically curved LED and a flat substrate since only atoms in very close proximity to the contact point provide a significant contribution to the attraction term ("ring" models or more complex curved membrane geometries do not meaningfully modify results, see fig 3.7.b). Both systems result in negligible VDW attraction at "long" range ( $> 1 \mu\text{m}$ ), but parallel surfaces (fig 3.7.b, dotted lines) yield a much higher attraction force as separation decreases ( $\frac{1}{D^3}$  dependence). This is directly proportional to facing areas, explaining the  $\sim 1000$  times less adhesion to the stamp of an LED held only by four  $1 \mu\text{m}^2$  pyramidal tips compared to a fully collapsed stamp (fig 3.7.c).

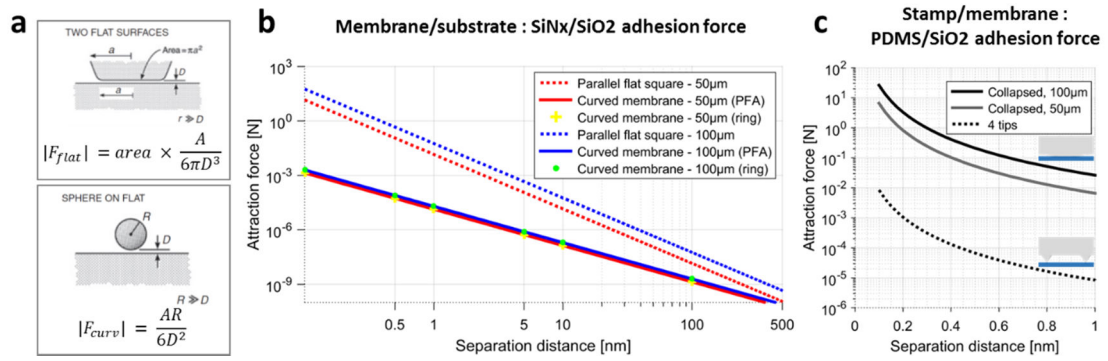


Figure 3.7 : van der Waals (VDW) forces can vary by orders of magnitudes depending on body separation and geometries. **a**) Approximated VDW attraction force  $F$  between rigid bodies of different geometries in terms of their Hamaker constant  $A$  (adapted from [48]). **b**) Calculated VDW attraction force between a SiO<sub>2</sub>-coated substrate and our TP- $\mu$ LEDs (SiN<sub>x</sub> backside), modelled as flat squares, spheres, or curved “part ring” membranes. **c**) Calculated VDW attraction force between a TP- $\mu$ LED and a microstructured stamp when latter is fully collapsed (full line) or fully relaxed (dotted line). Non-retarded Hamaker constants:  $A_{\text{SiN}_x} = 17 \times 10^{-20}$  J;  $A_{\text{SiO}_2} = 6 \times 10^{-20}$  J;  $A_{\text{PDMS}} = 6.4 \times 10^{-20}$  J, corresponding to typical surface energies in air of 20-50 mJ.m<sup>-2</sup>.

Importantly, the Hamaker constants of most solids are found to lie within a narrow range  $(0.4\text{-}4) \times 10^{-19}$  J ([48, p. 255], [56]), indicating that preferential LED adhesion to stamp or substrate is dictated by contact area geometries and topologies rather than characteristics of the materials involved. This model predicts an adhesion force of a membrane to a microtipped stamp ranging from  $\sim 0.5$  to  $50 \mu\text{N}$  depending on tip area (fig 3.8 : red area), which corresponds to experimental values of  $\sim 1.5 \mu\text{N}$  estimated by John Roger’s group ([40], fig 3.8 : black dotted line) with PDMS stamps very similar to those used in this work. In the ideal case of atomically smooth surfaces, VDW-driven release (“jump” [50]) of a curved LED onto a flat substrate may thus happen within a 1 nm to 5 nm separation distance (fig 3.8).

In practice, this means that VDW-driven release of curved membranes may only happen at extremely close range and therefore even a low surface roughness will affect substrate attraction. While the LED backside might be assumed to be almost atomically flat after the heated KOH etch [3], “real-world” unpolished substrates may present a typical roughness of at least a few nm RMS, and often much more when samples have been previously etched or patterned. The effect of surface roughness on VDW body-to-body attraction is an area of current investigation and well beyond the scope of this section [49], [54], but both experimental studies and early corrective models concur that the presence of “high peaks” and a local roughness of the same order of magnitude than the system-specific “jumping” distance may dramatically decrease VDW attraction forces [57].

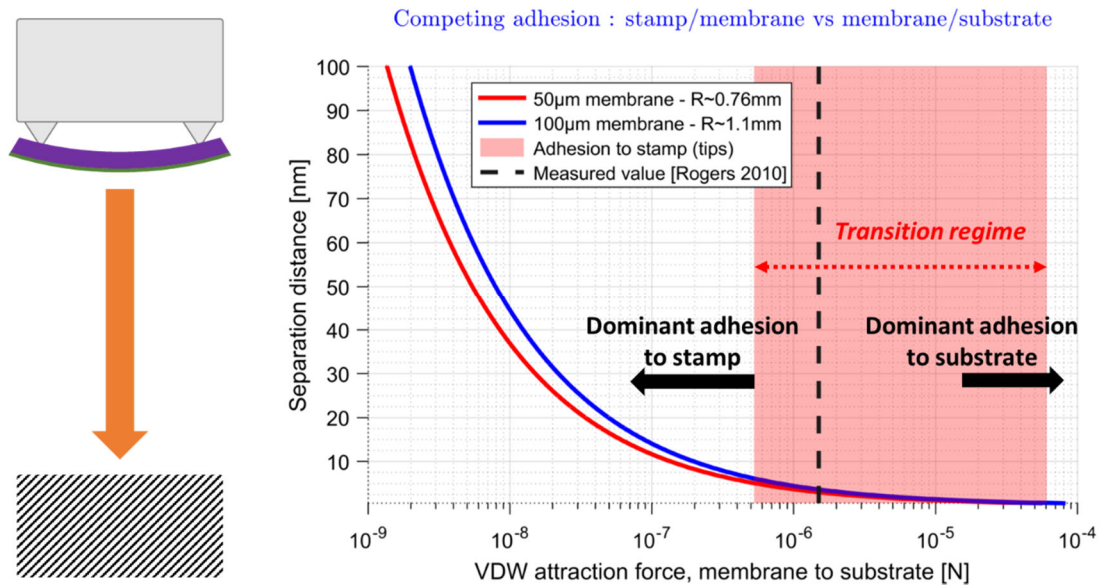


Figure 3.8 : Relative importance of stamp/LED to LED/substrate attraction during approach of a flat, smooth receiver substrate in VDW-dominated regime, for a fully relaxed stamp holding the LED by 4 low-area microtips. LED-stamp adhesion force is mostly dependent on tip contact area and ranges from  $\sim 5 \times 10^{-6}$  N to  $\sim 5 \times 10^{-5}$  N. For our curved LEDs, release should be possible when LED/substrate separation is  $< 5$  nm (“jumping distance”). LED weight (0.3-1.2 nN) is negligible.

As a practical conclusion, approximate models indicate that VDW-driven LED release may not be possible on most substrates of RMS roughness  $> 5$  nm and/or presenting “peaks”  $> 10$  nm. This corresponds directly to experimental observations made in this work and by others workers including John Rogers’ group [36], [37], where unmediated LED printing typically cannot be reliably achieved on generic rigid and non-polished substrates with RMS roughness  $> \sim 10$  nm, e.g pre-processed samples. By contrast, direct VDW attraction is often sufficient to drive the release of flexible membranes partly conforming to the substrate [58] or of nano-sized structures with very high surface-to-volume ratio [59].

### 3.3.3 $\mu$ LED transfer on highly textured substrates by picodroplet adhesive printing

In this work, our probe manufacturing process (chapter 4) yields a printing surface typically consisting of up to 13  $\text{SiO}_2$ -insulated tracks (2  $\mu\text{m}$  width) separated by  $\sim 2$   $\mu\text{m}$ -wide,  $\sim 800$  nm-deep trenches (see fig. 3.11.a). To achieve printing on these surfaces and *a fortiori* many other common, highly textured substrates without the use of thick intermediary layers, we developed a novel technique called **picodroplet adhesive (PA) printing**. The technique relies on the local application of a volume-controlled, picolitre-range ( $\sim 1$ -50 pL) droplet of pressure-sensitive adhesive (PSA) creating an ultrathin ( $< 50$  nm) adhesive interface at the surface of contact between LED backside and receiver substrate. This allows high yield printing with

high accuracy and strong bonding on unconventional surfaces while preserving good thermal contact, a crucial feature for our probes. The technique was initially developed by first depositing the picodroplet from a reservoir at a given printing site using the PDMS stamp, and then printing LEDs directly on top. This points to direct scalability using inkjet printing techniques. Within this work however, a more practical single-step method was implemented as described below.

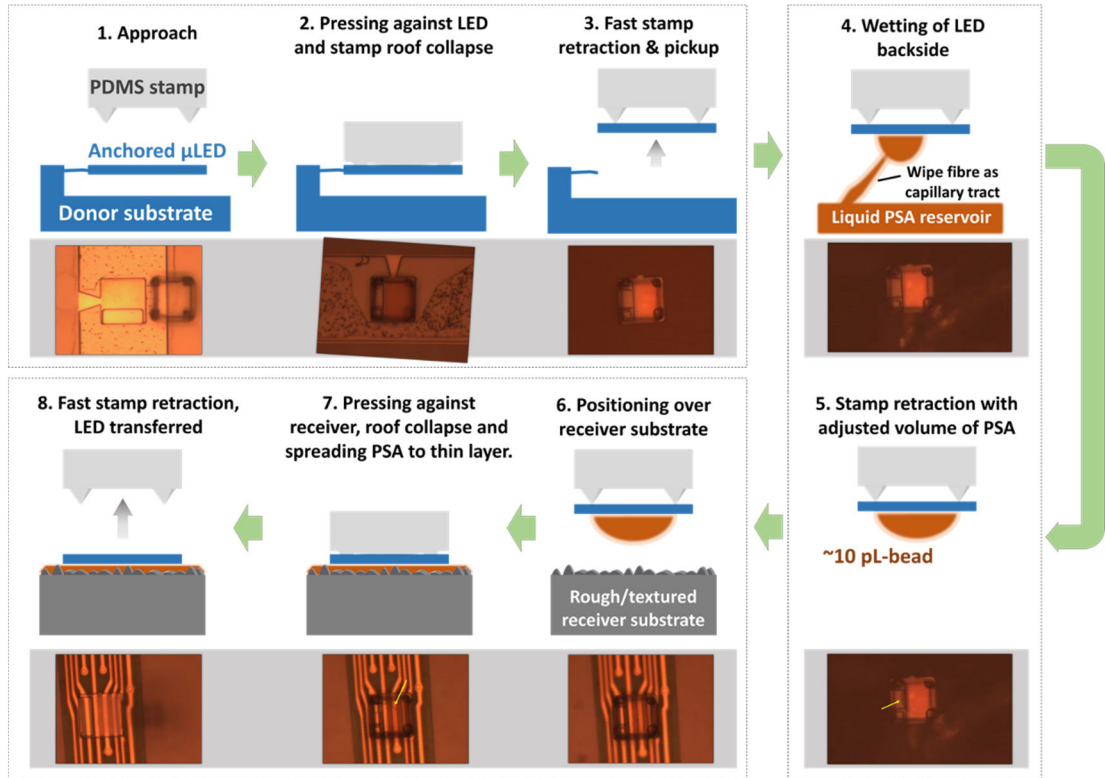


Figure 3.9 : Schematics and micrographs of a full PA printing cycle ( $50 \times 50 \mu\text{m}^2$  LED printed on a very textured area of a patterned diamond membrane). Yellow arrows on micrographs 5 and 7 point to the visible PSA picodroplet under LED backside. The full cycle (not automated) takes  $\sim 30\text{s}$ - $60\text{s}$  to complete.

The full picodroplet adhesive (PA) printing process is shown in fig 3.9. In the preparation stage, a low-viscosity PSA reservoir is created by mixing adhesive with a few drops of solvent in a mL-sized container, or by soaking a lint-free wipe with dissolved adhesive. After pickup, the  $\mu$ LED bottom is carefully brought in contact with the top of a capillary tract leading to the reservoir (a single protruding wipe fibre nicely fits the required dimensions) and the liquid PSA slowly wets the  $\mu$ LED backside (estimated rate of  $\sim 2.5\text{pL/s}$ ), building up the picodroplet over a few seconds. Droplet volume is adjusted by increasing or decreasing wetting time, and droplet radius can be microscope-monitored in real time through the transparent stamp and LED. Wetted LEDs are positioned over the substrate, and slowly pressed against it, spreading

the droplet into an ultrathin interstitial layer whose border is also visible under the microscope. Fast vertical retraction fully delaminates the stamp from the LED as the PSA layer creates a strong bond [47], leaving the LED printed on site with typical sub-micron accuracy. Since the LEDs are curved, the ultrathin PSA layer can provide an “underfill” at the LEDs edge, whose profile can be controlled by the picodroplet volume. A  $> 20$  pL droplet for a  $50 \times 50 \mu\text{m}^2$  LED will produce an overspill on a relatively flat surface (fig 3.10.a), while a  $\sim 5$  pL droplet may result in a smooth edge underfill (fig 3.10.b), and even smaller PSA volumes may yield such a thin interface layer that it is not visible under SEM scanning (fig 3.10.c). The layer itself does not strongly evaporate, leaving most of these profiles intact under heat up to  $\sim 300^\circ\text{C}$  and making the process compatible with e.g. PECVD  $\text{SiO}_2$  deposition. The bonding is strong and easily accommodates further processing involving spincoating, DI rinsing, etc.

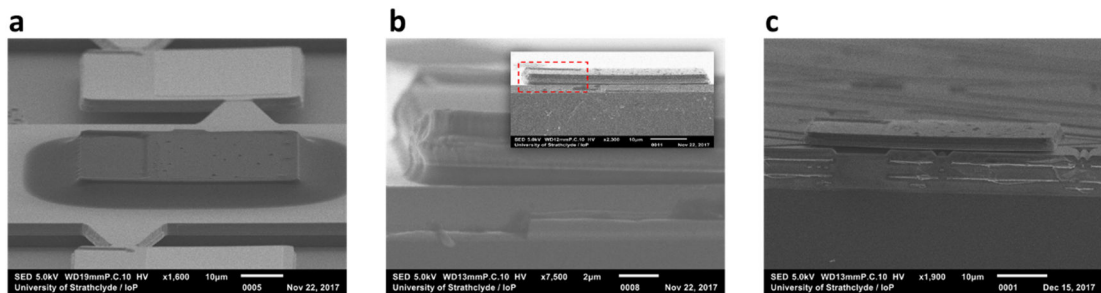


Figure 3.10 : SEM scans of  $\mu$ LEDs printed with various PSA droplet volumes (post 2hrs heating at  $150^\circ\text{C}$ ). a) Large ( $\sim 25 \mu\text{m}$  radius) droplets create a “polymer skirt” overspill with gently sloping profile. b) Tailored droplet size leaves a thin underfill visible at the LED edge, but not at the central contact surface. c) Minimal wetting still allows LED transfer, without detectable underfill, on the ridged surface of a cleaved photodetector chip showing underlying CMOS structure.

To determine the capabilities of the technique,  $\mu$ LEDs of varying sizes were printed on different textured substrates where LED release was previously not possible without thick adhesive layers (fig 3.11). A 100% success rate at first try was obtained for two different CMOS chips ( $n_{\text{LED}} = 16$ ). On our diamond probe designs, adjustment of droplet volume was sometimes necessary to achieve printing on the most patterned areas, where yield at first try could drop down to a minimum of 60% (roughest printing sites,  $n_{\text{LED}} = 20$ ; all LEDs printed within 3 trials). Finally, a highly textured patterned sapphire substrate (PSS), with irregular peak heights up to  $5 \mu\text{m}$  and very low potential contact area to the LED proved the limitation of PA printing, with multiple trials needed to transfer the LEDs.

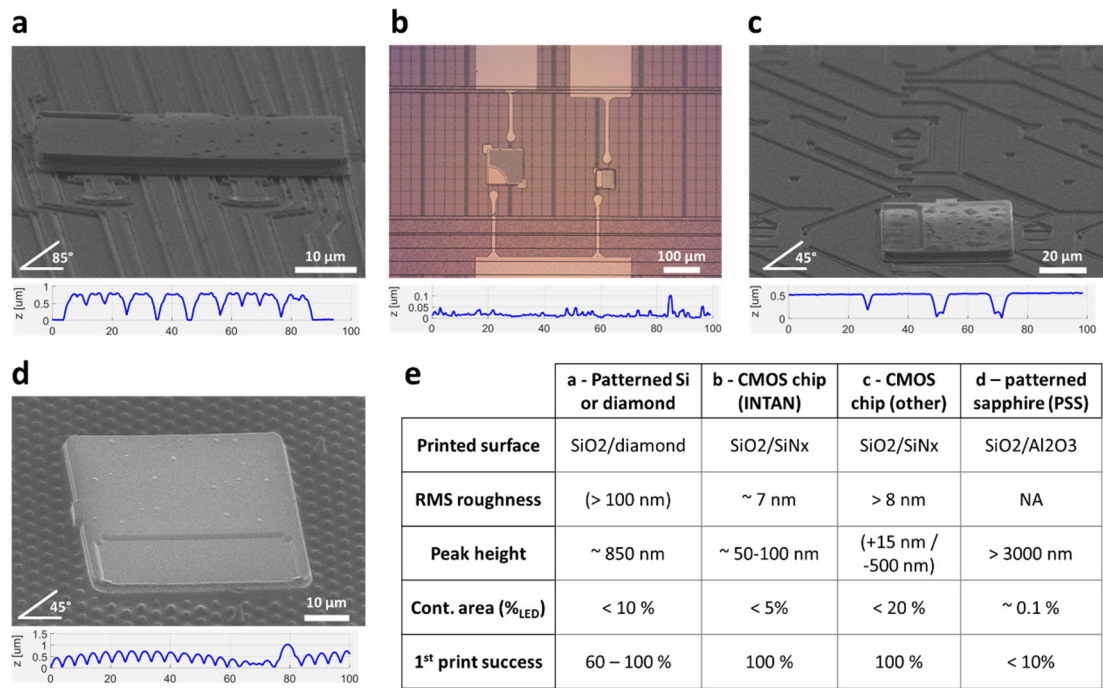


Figure 3.11 : PA printing allows LED release with high bonding strength on a variety of surfaces including a) striated insulated tracks of a diamond or silicon optrode fabricated in this work, b) & c) CMOS chips presenting significant surface roughness and/or local peaks and trenches, or in the limiting case d) highly textured patterned sapphire substrate (PSS) with minimal potential contact area to the LED backside. Capabilities of the technique are summarised in e). (Printing success on low-roughness surfaces ( $R_a < 7\text{nm}$ ) is 100% as with CMOS structures.)

These simple demonstrators prove that PA printing is particularly suitable for controlled and precise TP- $\mu$ LED release onto most “real-world” substrates, including pre-processed samples and commercial chips. It provides a reliable alternative to thick adhesive layers with a potential for much improved LED-substrate thermal contact, which is crucial to best harness the heatsinking properties of diamond substrates used in this work. As such, PA printing was the method of choice for LED integration during the whole manufacturing process of diamond probes detailed in chapter 4.

### 3.3.4 Parylene-based contacting strategy

Once printed,  $\mu$ LEDs must be contacted by electrical traces. Both anode and cathode connections must be made on the top surface since the LED’s backside, comprising SiN<sub>x</sub>/AlGaN layers, usually proves too resistive for a good direct cathodic contact from the bottom. In this work, where both track density and upward light emission must be maximised (see chapter 4), we favoured low-footprint “bridging” contacts to reflective metal tracks underlying the devices (fig 3.12).



To avoid contact shorts or breaks, both complete insulation of the LED surface and sidewalls and good metallisation step coverage must be achieved. The step height from the LED thickness ( $\sim 2.5\mu\text{m}$ ) is compounded by the bow, more pronounced on  $100\times 100\mu\text{m}^2$  devices. PECVD  $\text{SiO}_2$  deposition is not conformal enough to insulate the LED sidewalls, and both IoP workers and others typically use a  $5\mu\text{m}$  to  $10\mu\text{m}$ -thick spin coated SU8 layer for encapsulation [3], [21], [36], [60].

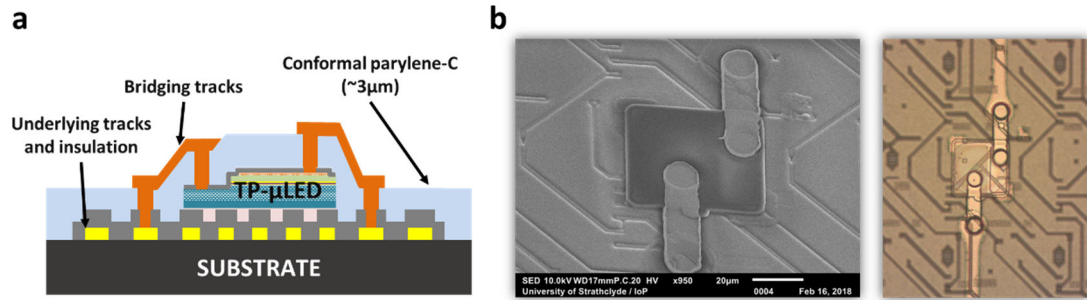


Figure 3.12 : Contacting strategy used in this work to address printed  $\mu$ LEDs. a) Schematic of the device encapsulated with parylene-C ( $\sim 3\mu\text{m}$  thickness for  $50\times 50\mu\text{m}^2$  LEDs) and contacted by metal “bridges” to underlying tracks. b), c) SEM scan and micrograph of the same device addressed on a CMOS chip.

The context of our work however strongly discourages the use of this technique. Thick, viscous SU8 layers are especially unwieldy to spincoat on ultrathin samples, may induce detrimental thermal stress in these from curing, may complicate the fine patterning of small vias and significantly add to the final probe footprint. As a replacement strategy,  $\sim 3\mu\text{m}$ -thick parylene-C layers were used instead for encapsulation. Parylene-C provides an extremely conformal insulating coating deposited at room temperature [61], without any stress or force applied to the sample during coating. Extensive etch tests were conducted to ensure satisfactory patterning of vias ( $< 6\mu\text{m}$  diameter), as well as series of pull-tests to fully characterise the adhesion of parylene to glass surfaces (see annex A4). A thin  $\text{SiO}_2$  layer was used to protect the LED’s p-GaN from adverse effects of the oxygen-based etch and removed down the open vias through a quick BOE dip, leaving a very clean, deoxidised surface ideal for contacts (see chapter 4). The bridging contacts were patterned by metal lift-off. The implementation of this insulation strategy allowed contacting of LEDs on a variety of surfaces more precisely and efficiently than would be possible using SU8 (fig 3.12.b).

## 3.4 Demonstrator: $\mu$ LED printing on CMOS chip

### 3.4.1 Context and motivation

The techniques presented above were developed in this work as a solution to the need for seamlessly integrating and insulating efficient  $\mu$ LEDs onto patterned diamond membrane, as part of a complete fabrication process, detailed in the following chapter. They can however be applied in other contexts of interest for the semiconductor, electronics or MEMS industries. Picodroplet adhesive printing enables device transfer onto a wide range of textured substrates inaccessible to other printing methods, while parylene coatings ensure conformal insulations and facilitate contacting on fragile samples.

A particular area of interest with far-reaching possibilities is optoelectronic integration with complementary metal-oxide semiconductor technology (CMOS). A mature technology critical for high transistor density with characteristic high noise immunity and low static power consumption, silicon-based CMOS circuits are the cornerstone of modern very-large scale integration (VLSI) chips and are ubiquitous in today's digital and analog devices, from microprocessors to RAM to image sensors [62]. The development of complex transceivers through direct interfacing of monolithic CMOS circuits with a range of optoelectronics devices is an area of active research, with potential high-volume applications in the telecom market, sensing technologies and electrophotonics [63], and bright outlooks for biomedical devices [64]. Direct integration of  $\mu$ LEDs onto generic CMOS chips has not yet been achieved.

### 3.4.2 Concept of a $\mu$ LED-on-CMOS demonstrator

As a proof of concept showing the potential of picodroplet adhesive printing, we engineered the first such integration of our  $\mu$ LEDs onto a commercial INTAN RHS2116 CMOS microchip [65]. Such INTAN electrophysiology interface chip series are popular among the neuroscience research community and used for electrode signals amplification and digitisation. The RHS2116 specifically allows both signal amplification and electrical stimulation up to 2.5mA current on each of its 16 channels (see annex A7 for detailed characteristics), an output range directly allowing driving of our  $\mu$ LEDs up to high optical power densities (section 3.2.5).

### 3.4.3 Integration process flow

The integration process was performed on a RHS2116 INTAN bare die and briefly described below. Test cell layers designed on mask AB2 were opportunistically used as pattern sizes and alignment mark separation were compatible with the microchip's dimensions. For all

photolithographic steps, the chip was bonded with unpatterned photoresist on a 20mm x 20 mm silicon carrier for handling, and released in solvent when needed.

Negative photoresist was first spun on the sample (ma-N1420, spun at 3000 rpm for 60s, soft baked at 100°C for 120 s) and UV-exposed in two successive steps. The first exposure (cell AB2-N1A) negatively defined alignment marks and bondpads/traces at the centre of the chip. The second exposure, using cell AB2-“recess”, ensured full photocrosslinking of the PR covering the chip bondpads and edges. The PR was ~40% overdeveloped (100 s in ma-D533S) to create a substantial ~ 1  $\mu$ m undercut. The chip was then sputter coated with a Ti/Au bilayer (50nm/200nm), which was lifted off in heated acetone (40°C, 2 hours) to leave only an array of 4 metal structures over different functional areas of the chip (fig 3.13.c). 8 TP- $\mu$ LEDs (4 pairs of (Pd layer)-100x100 $\mu$ m<sup>2</sup> and (Ni/Au layer)-50x50 $\mu$ m<sup>2</sup>) were printed on the chip using picodroplet adhesive printing. A 3  $\mu$ m layer of parylene C was deposited on the chip for LED insulation, and then patterned and etched with an additional BOE dip to open vias to chip bondpads, structure bondpads and LEDs. After another patterning using ma-N1420, for contact bridges, samples were sputtered with a second bilayer of Ti/Au (50nm/300nm) and lifted off in acetone. Contacted LEDs were once more insulated in 2  $\mu$ m parylene for protection, and a last patterning and etch step opened vias to the INTAN chip and LED bondpads for addressing.

After LED integration and insulation, the die was bonded with silicon thermal grease (RS components Ltd) onto a custom-made PCB designed for the RHS2116. Ruaridh Winstanley designed the PCB and the interfacing setup. Yunzhou Cheng wirebonded the chip to the PCB (16 I/O channels, see annex A7). The chip was driven by SPI commands through a microcontroller, which was connected through another custom-made PCB to an USB-to-SPI bridge providing both a direct computer interface (LabVIEW program) and power to the system (fig 3.14, panels a to c). The whole setup was fully shielded by panels and foil forming a Faraday cage and all external light sources were screened during operation to minimise electromagnetic interference picked up by the very sensitive chip amplifiers.

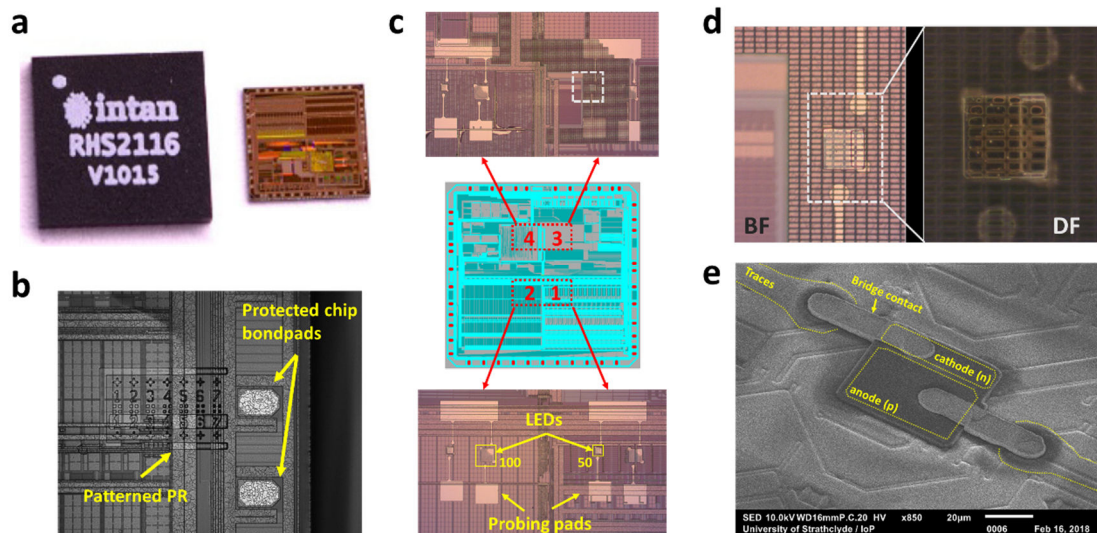


Figure 3.13 : Direct integration of LED on a commercial CMOS chip by picodroplet adhesive printing. **a)** INTAN RHS2116 packaged chip (left) and bare die as used in this work (right,  $W \times L = 4.94 \text{ mm} \times 4.74 \text{ mm}$ ) (from [65]), **b)** micrograph of patterned chip during fabrication, **c)** a total of 8 LEDs were printed over 4 different functional areas corresponding to 1/ chip registers, 2/ metal-insulator-metal capacitors, 3/ power supply wires, 4/ SPI-related CMOS circuitry, **d)**  $50 \times 50 \mu\text{m}^2$  LED printed on area 3 (inset : dark field micrograph of same showing underlying CMOS structure) and **e)** SEM image of a fully contacted LED on CMOS (LED from same batch printed on another CMOS chip).

### 3.4.4 Results

Measurements on the integrated chip were taken along with Ruaridh Winstanley, who also analysed the chip recording data. LEDs were driven by an external power source (Yokogawa GS610) via manipulated microprobes, while the chip was operated in recording mode.

#### o *Successful LED integration and operation on chip*

Despite this process being implemented as a single-trial proof-of-concept and without a dedicated photomask, no major issue was encountered during fabrication. Transfer-printing resulted in a 100% success rate at first try, with submicron placement accuracy on all areas (max peak height/max RMS roughness: 200 nm/10 nm, AlphaStep IQ measurement). Out of 8 printed LEDs, 1 failed to turn on and 5 performed at the expected LIV characteristics (yield of 63%), i.e within 10% of typical LIV curves reported in section 3.2.5.

Furthermore, the INTAN RHS2116 could be powered up normally and initialisation procedures via SPI commands [65] could be performed satisfactorily with correct register reading from the chip. Each of the 16 channels could be sampled at 30kS/s, with a noise level  $< 30 \mu\text{V}$ . This indicates that the die was not damaged by the manufacturing process.

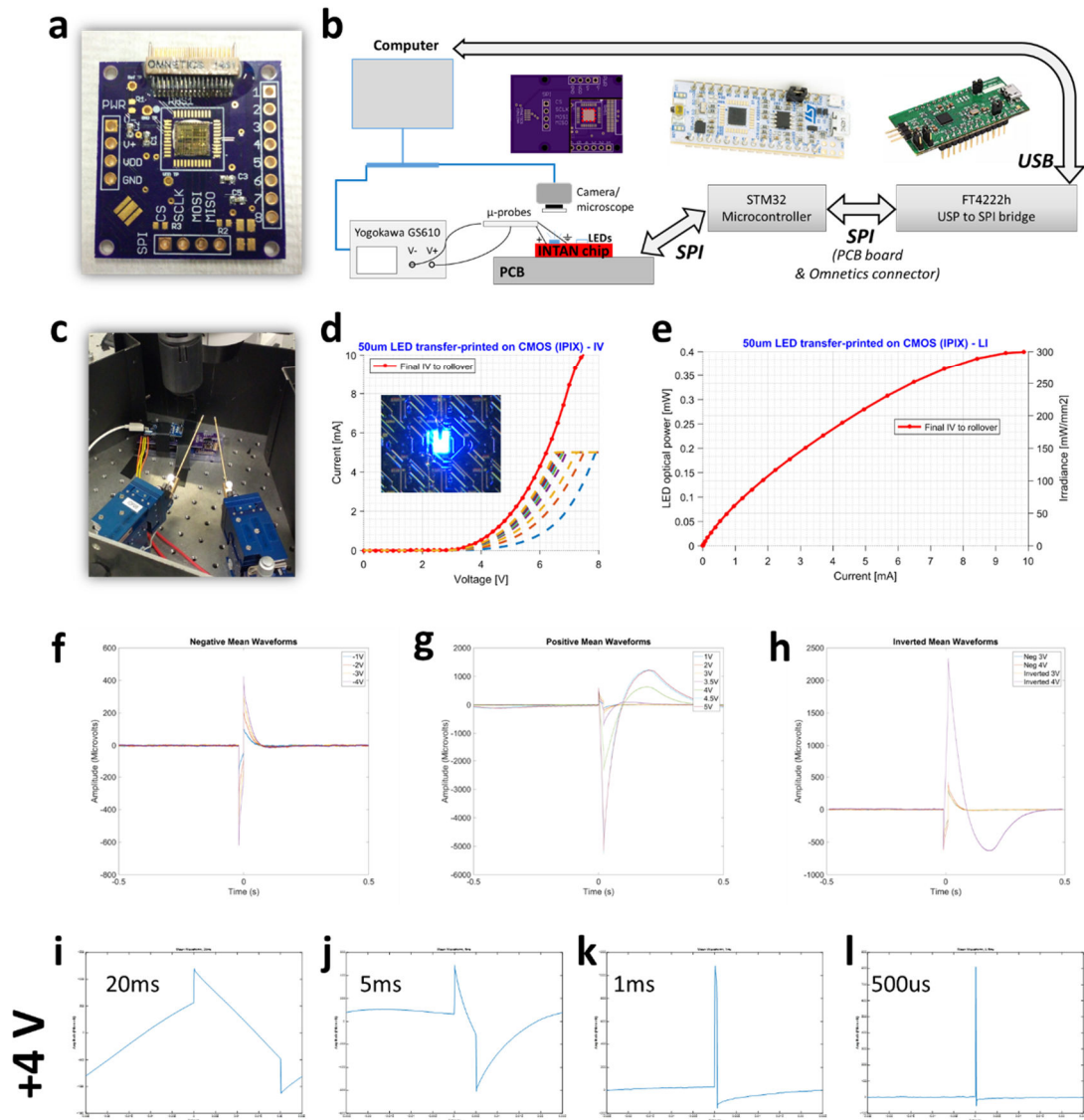


Figure 3.14 : LED-on-CMOS operation induces distinct electrical transients in recording channels. **a)** INTAN RHS2116 chip bonded on PCB, **b)** schematic of setup for simultaneous LED driving and chip channel recording (setup shielded in Faraday cage), **c)** photograph showing chip control system and manipulated microprobes, **d-e)** on-chip LED opto-electrical performance (inset micrograph taken on another CMOS chip), **f-h)** average electrical signals recorded on channel 1 during LED2 ( $50 \times 50 \mu\text{m}^2$ ) pulsed operation (20ms, 1 Hz) at **f)** negative voltages (no light emitted) and **g)** positive voltages (significant light output for  $V > 3.5\text{V}$ , modifying transient shape), **h)** superposition of signal absolute values for  $\pm 3\text{V}$  &  $\pm 4\text{V}$  clearly differentiating optically- vs electrically-induced transients, **i-l)** average signals during LED pulsed operation at +4V (20 Hz) for various pulse widths. All noise levels  $< 30 \mu\text{V}$ .

These positive results demonstrates that the integration process initially devised for the diamond devices described in chapter 4 is directly applicable to a standard CMOS chip, with potential high success yield once fully optimised. Process optimisation may focus first-hand on better protection of the chip sidewalls during lift-off metallisation, as it is believed that

local metal flakes on sidewalls led to shorts impairing chip operation (see below). A dedicated photomask would solve this issue by allowing selective parylene conservation on sidewalls.

o *Effect of LED pulsed operation on chip readings: optical and electrical transients*

Direct pulse-driving of the LEDs at both negative and positive voltages (-4 V to +5 V) elicited transient electrical signals on all recording channels left floating, for all chip areas tested (fig 3.14, panels f-h). Negative 20ms pulses (panel f) resulted in a two-step response of sub-mV amplitude roughly proportional to the bias voltage used : i) a negative spike at pulse start and ii) a “rebound” positive spike at pulse end, both decaying exponentially with a similar time constant of ~20-30ms. A return to the normal noise levels was observed ~100 ms after the pulse. Pulses of identical length and frequency at positive voltages (panel g) elicited identical (mirrored) responses up until  $V = 3V$ , corresponding to the LED turn-on voltage. At  $V \geq 3.5V$ , with significant light output by the LED, the post-pulse rebound was up to ~10x more prominent (up to 5mV for  $V = 5 V$ ) and showed an underdamped oscillatory decay over a much longer timescale (up to ~700ms for  $V = 5 V$ ).

These characteristics clearly delineate two response regimes of the underlying CMOS circuitry to the stimulation (panel h). Electrically-induced transients are produced by every driving pulse, while LED irradiance specifically causes photo-generated transients of higher amplitude and longer timescales, an issue anticipated by other groups seeking to combine CMOS and optoelectronic stimulation in vivo [66], [67]. While such transients may affect the use of such an integrated INTAN chip for electrophysiological measurements, they may be mitigated. With appropriate filtering, meaningful recordings should be possible during transient decay as noise levels plummet down to normal a few ms post-pulse. The chip electrodes’ charge recovery switch (annex figure A7.1) could be used to bleed off the charge buildup. Optimised layout design of CMOS chips may help mitigate the charge generation in the underlying diode structures.

Finally, the transients’ duration exponentially decreases with pulse width (fig 3.14, panel i-l). Average signals recorded for 20Hz pulsed operation at 4V, i.e above optical output threshold, shows optically-induced transients continually bias the electrode voltage (no return to baseline between pulses). Shorter pulse widths however reduce that effect, with 0.5 ms pulses registering the pulse spike with a return to baseline within less than 3 ms. When possible, protocols with sub-ms pulses at high duty cycles could then be envisaged to allow LED operation with minimal disturbance to the recordings.

### 3.4.5 Conclusion regarding demonstrator

The next step in this demonstrator was to directly drive the LED through the INTAN chip and study different regimes of operation. Unfortunately, after the fabrication process, metal spots were found on some parts of the chip sidewalls (see annex A7.2), causing shorts between wires leading to channels VSTIM and chip ground, and preventing operation of the chip in stimulation mode. This could be easily averted in later processes by better sidewall protection (i.e by first depositing and patterning a thin, conformal layer of Parylene on the chip), and *ad hoc* wirebonding.

Despite that drawback, this proof-of-concept experiment demonstrated that TP- $\mu$ LEDs (or potentially, other optoelectronic devices) can easily be directly integrated on standard, highly versatile CMOS technology by means of picodroplet adhesive printing. The integration process is robust and can likely be easily perfected to attain very high success yields. On-chip LED driving by CMOS circuits, also capable of signal processing, opens the door to large scale optoelectronic integration with complex circuits for a vast range of applications. As an example, in the case of our INTAN device, CMOS-driven LEDs could be used either for single-chip closed-loop optogenetics; alternatively, on-chip LEDs could be used for high-bandwidth, wireless, low-power data transmission via visible-light communication [20], [68], [69], a potential solution to the growing problem of ever-larger datasets generated by massively parallel electrophysiology recordings [64].

## 3.5 Conclusion

This chapter detailed the development of essential building blocks for hybrid diamond optrodes, and applied those to other promising uses. The manufacturing process for TP- $\mu$ LEDs was fully revised and optimised to yield low-footprint, high-efficiency devices capable of irradiances  $> 200 \text{ mW/mm}^2$  needed for high-power optogenetics. Recognising the specific challenges and fundamental limitations of transfer-printing for rough substrates, the method of picodroplet adhesive printing was conceived to enable reliable transfer of  $\mu$ LEDs with high bonding strength and good thermal contact. A versatile encapsulation and contacting method was devised. The resulting new capabilities, of wide potential applications, were harnessed to demonstrate the first direct integration of  $\mu$ LEDs on a commercial CMOS chip.

### 3.6 References

- [1] H. Kim, E. Brueckner, J. Song, Y. Li, S. Kim, C. Lu, J. Sulkin, K. Choquette, Y. Huang, R. G. Nuzzo, and others, “Unusual strategies for using indium gallium nitride grown on silicon (111) for solid-state lighting,” *Proc. Natl. Acad. Sci.*, vol. 108, no. 25, p. 10072, 2011.
- [2] A. J. Trindade, “Transfer printing of nitride based light emitting diodes,” 2015.
- [3] A. J. Trindade, B. Guilhabert, D. Massoubre, D. Zhu, N. Laurand, E. Gu, I. M. Watson, C. J. Humphreys, and M. D. Dawson, “Nanoscale-accuracy transfer printing of ultra-thin AlInGaN light-emitting diodes onto mechanically flexible substrates,” *Appl. Phys. Lett.*, vol. 103, no. 25, 2013.
- [4] a. J. Trindade, B. Guilhabert, E. Y. Xie, R. Ferreira, J. J. D. McKendry, D. Zhu, N. Laurand, E. Gu, D. J. Wallis, I. M. Watson, C. J. Humphreys, and M. D. Dawson, “Heterogeneous integration of gallium nitride light-emitting diodes on diamond and silica by transfer printing,” *Opt. Express*, vol. 23, no. 7, p. 9329, 2015.
- [5] K. Rae, C. Foucher, B. Guilhabert, N. Laurand, D. Zhu, C. J. Humphreys, D. J. Wallis, and M. D. Dawson, “InGaN micro-LEDs integrated onto an ultra-thin , colloidal quantum dot functionalized glass platform,” *Opt. Express*, vol. 25, no. 16, pp. 19179–19184, 2017.
- [6] K. J. Rae, E. Xie, C. Foucher, B. Guilhabert, R. Ferreira, D. Zhu, D. Wallis, C. Humphreys, R. Oliver, E. Gu, N. Laurand, and M. D. Dawson, “Transfer Printed Multi-color Integrated Devices for Visible Light Communication Applications,” in *Light, Energy and the Environment*, 2016, p. SSM2C.4.
- [7] E. F. Schubert, *Light-emitting diodes*. Cambridge University Press, 2006.
- [8] G. Buzsáki, E. Stark, A. Berényi, D. Khodagholy, D. R. Kipke, E. Yoon, and K. D. Wise, “Tools for probing local circuits: High-density silicon probes combined with optogenetics,” *Neuron*, vol. 86, no. 1, pp. 92–105, 2015.
- [9] F. Wu, E. Stark, P. C. Ku, K. D. Wise, G. Buzsáki, and E. Yoon, “Monolithically Integrated  $\mu$ LEDs on Silicon Neural Probes for High-Resolution Optogenetic Studies in Behaving Animals,” *Neuron*, vol. 88, no. 6, pp. 1136–1148, 2015.
- [10] R. Scharf, T. Tsunematsu, N. McAlinden, M. D. Dawson, S. Sakata, and K. Mathieson, “Depth-specific optogenetic control in vivo with a scalable, high-density  $\mu$ LED neural probe,” *Sci. Rep.*, vol. 6, no. January, p. 28381, 2016.
- [11] T. Il Kim, J. G. McCall, Y. H. Jung, X. Huang, E. R. Siuda, Y. Li, J. Song, Y. M. Song, H. A. Pao, R. H. Kim, C. Lu, S. D. Lee, I. S. Song, G. Shin, R. Al-Hasani, S. Kim, M. P. Tan, Y. Huang, F. G. Omenetto, J. A. Rogers, and M. R. Bruchas, “Injectable, cellular-scale optoelectronics with applications for wireless optogenetics,” *Science (80- )*, vol. 340, no. 6129, pp. 211–216, 2013.
- [12] G. Greco, F. Iucolano, and F. Roccaforte, “Ohmic contacts to Gallium Nitride materials,” *Appl. Surf. Sci.*, vol. 383, pp. 324–345, 2016.



- [13] J.-L. Lee, M. Weber, J. K. Kim, J. W. Lee, Y. J. Park, T. Kim, and K. Lynn, "Ohmic contact formation mechanism of nonalloyed Pd contacts to p-type GaN observed by positron annihilation spectroscopy," *Appl. Phys. Lett.*, vol. 74, no. 16, p. 2289, Apr. 1999.
- [14] E. Xie, "High performance microstructured light emitting diodes - mechanisms and processes," University of Strathclyde, 2013.
- [15] E. D. Palik, *Handbook of optical constants of solids*. Academic Press, 1998.
- [16] J. Weaver, "Optical properties of Rh, Pd, Ir, and Pt," *Phys. Rev. B*, vol. 11, no. 4, pp. 1416–1425, 1975.
- [17] B. T. Sullivan, "Optical properties of palladium in the visible and near UV spectral regions," *Appl. Opt.*, vol. 29, no. 13, p. 1964, 1990.
- [18] S. M. Shivaprasad, L. A. Udachan, and M. A. Angadi, "Electrical resistivity of thin palladium films," *Phys. Lett. A*, vol. 78, no. 2, pp. 187–188, Jul. 1980.
- [19] W. E. Vargas, I. Rojas, D. E. Azofeifa, and N. Clark, "Optical and electrical properties of hydrided palladium thin films studied by an inversion approach from transmittance measurements," *Thin Solid Films*, vol. 496, no. 2, pp. 189–196, 2006.
- [20] K. Rae, "Micro-transfer printing for visible light communications applications," University of Strathclyde, 2017.
- [21] K. Rae, C. Foucher, B. Guilhabert, M. S. Islim, L. Yin, D. Zhu, R. A. Oliver, D. J. Wallis, H. Haas, N. Laurand, and M. D. Dawson, "InGaN  $\mu$ LEDs integrated onto colloidal quantum dot functionalized ultra-thin glass," *Opt. Express*, vol. 25, no. 16, p. 19179, Aug. 2017.
- [22] C. Goßler, C. Bierbrauer, R. Moser, M. Kunzer, K. Holc, W. Pletschen, K. Köhler, J. Wagner, M. Schwaerzle, P. Ruther, O. Paul, J. Neef, D. Keppeler, G. Hoch, T. Moser, and U. T. Schwarz, "GaN-based micro-LED arrays on flexible substrates for optical cochlear implants," *J. Phys. D: Appl. Phys.*, vol. 47, p. 205401, 2014.
- [23] S. Ayub, C. Gossler, M. Schwaerzle, E. Klein, O. Paul, U. T. Schwarz, and P. Ruther, "High-density probe with integrated thin-film micro light emitting diodes ( $\mu$ LEDs) for optogenetic applications," *Proc. IEEE Int. Conf. Micro Electro Mech. Syst.*, vol. 2016–Febru, no. January, pp. 379–382, 2016.
- [24] S. Ayub, L. J. Gentet, R. Fiáth, M. Schwaerzle, M. Borel, F. David, P. Barthó, I. Ulbert, O. Paul, and P. Ruther, "Hybrid intracerebral probe with integrated bare LED chips for optogenetic studies," *Biomed. Microdevices*, vol. 19, no. 3, pp. 1–12, 2017.
- [25] A. Soltan, B. McGovern, E. Drakakis, M. Neil, P. Maaskant, M. Akhter, J. S. Lee, and P. Degenaar, "High Density, High Radiance  $\mu$ LED Matrix for Optogenetic Retinal Prostheses and Planar Neural Stimulation," *IEEE Trans. Biomed. Circuits Syst.*, vol. 11, no. 2, pp. 347–359, Apr. 2017.
- [26] D. Zhu, C. McAleese, K. K. McLaughlin, M. Häberlen, C. O. Salcianu, E. J. Thrush, M. J. Kappers, W. a Phillips, P. Lane, D. J. Wallis, T. Martin, M. Astles, S. Thomas, a Pakes, M. Heuken, and C. J. Humphreys, "GaN-based LEDs grown on 6-inch diameter Si (111) substrates by MOVPE," *Proc. SPIE*, vol. 7231, no. July 2015, pp. 723111–723118, 2009.

- [27] X. Sheng, C. A. Bower, S. Bonafede, J. W. Wilson, B. Fisher, M. Meitl, H. Yuen, S. Wang, L. Shen, A. R. Banks, C. J. Corcoran, R. G. Nuzzo, S. Burroughs, and J. A. Rogers, "Printing-based assembly of quadruple-junction four-terminal microscale solar cells and their use in high-efficiency modules," *Nat. Mater.*, vol. 13, no. 6, pp. 593–598, Jun. 2014.
- [28] W. Choi, C. Z. Kim, C. S. Kim, W. Heo, T. Joo, S. Y. Ryu, H. Kim, H. Kim, H. K. Kang, and S. Jo, "A Repeatable Epitaxial Lift-Off Process from a Single GaAs Substrate for Low-Cost and High-Efficiency III-V Solar Cells," *Adv. Energy Mater.*, vol. 4, no. 16, p. 1400589, Nov. 2014.
- [29] C. A. Bower, E. Menard, S. Bonafede, J. W. Hamer, and R. S. Cok, "Active-matrix OLED display backplanes using transfer-printed microscale integrated circuits," in *2010 Proceedings 60th Electronic Components and Technology Conference (ECTC)*, 2010, pp. 1339–1343.
- [30] J. W. Hamer, R. S. Cok, G. J. Parrett, D. Winters, B. Primerano, C. A. Bower, E. Menard, and S. Bonafede, "AMOLED Displays using Transfer-Printed Integrated Circuits," *J. Soc. Inf. Disp.*, vol. 19, no. 335, pp. 947–950, 2011.
- [31] J. Justice, C. Bower, M. Meitl, M. B. Mooney, M. A. Gubbins, and B. Corbett, "Wafer-scale integration of group III–V lasers on silicon using transfer printing of epitaxial layers," *Nat. Photonics*, vol. 6, no. 9, pp. 610–614, Sep. 2012.
- [32] D. Kim, R. Ghaffari, N. Lu, and J. A. Rogers, "Flexible and Stretchable Electronics for Biointegrated Devices," 2012.
- [33] Tae-il Kim, Rak-Hwan Kim, and J. A. Rogers, "Microscale Inorganic Light-Emitting Diodes on Flexible and Stretchable Substrates," *IEEE Photonics J.*, vol. 4, no. 2, pp. 607–612, Apr. 2012.
- [34] S.-I. Park, Y. Xiong, R.-H. Kim, P. Elvikis, M. Meitl, D.-H. Kim, J. Wu, J. Yoon, C.-J. Yu, Z. Liu, Y. Huang, K. Hwang, P. Ferreira, X. Li, K. Choquette, and J. A. Rogers, "Printed assemblies of inorganic light-emitting diodes for deformable and semitransparent displays," *Science*, vol. 325, no. 5943, pp. 977–81, Aug. 2009.
- [35] C. A. Bower, M. A. A. Meitl, B. Raymond, E. Radauscher, R. Cok, S. Bonafede, D. Gomez, T. Moore, C. Prevatte, B. Fisher, R. Rotzoll, G. A. Melnik, A. Fecioru, and A. J. Trindade, "Emissive displays with transfer-printed assemblies of  $8\ \mu\text{m} \times 15\ \mu\text{m}$  inorganic light-emitting diodes," *Photonics Res.*, vol. 5, no. 2, pp. 23–29, 2017.
- [36] A. Carlson, A. M. Bowen, Y. Huang, R. G. Nuzzo, and J. A. Rogers, "Transfer printing techniques for materials assembly and micro/nanodevice fabrication," *Adv. Mater.*, vol. 24, no. 39, pp. 5284–5318, 2012.
- [37] R. Saeidpourazar, M. D. Sangid, J. A. Rogers, and P. M. Ferreira, "A prototype printer for laser driven micro-transfer printing," *J. Manuf. Process.*, vol. 14, no. 4, pp. 416–424, 2012.
- [38] M. B. Tucker, D. R. Hines, and T. Li, "A quality map of transfer printing," *J. Appl. Phys.*, vol. 106, no. 10, pp. 1–8, 2009.
- [39] H. J. Kim-Lee, A. Carlson, D. S. Grierson, J. A. Rogers, and K. T. Turner, "Interface mechanics of adhesiveless microtransfer printing processes," *J. Appl. Phys.*, vol. 115, no. 14, 2014.
- [40] S. Kim, J. Wu, A. Carlson, S. H. Jin, A. Kovalsky, P. Glass, Z. Liu, N. Ahmed, S. L. Elgan, W. Chen,

- P. M. Ferreira, M. Sitti, Y. Huang, and J. A. Rogers, "Microstructured elastomeric surfaces with reversible adhesion and examples of their use in deterministic assembly by transfer printing," *Proc. Natl. Acad. Sci. U. S. A.*, vol. 107, no. 40, pp. 17095–100, 2010.
- [41] A. Carlson, H. J. Kim-Lee, J. Wu, P. Elvikis, H. Cheng, A. Kovalsky, S. Elgan, Q. Yu, P. M. Ferreira, Y. Huang, K. T. Turner, and J. A. Rogers, "Shear-enhanced adhesiveless transfer printing for use in deterministic materials assembly," *Appl. Phys. Lett.*, vol. 98, no. 26, pp. 5–7, 2011.
- [42] H. Kim, B. Yoon, J. Sung, D.-G. Choi, and C. Park, "Micropatterning of thin P3HT films via plasma enhanced polymer transfer printing," *J. Mater. Chem.*, vol. 18, no. 29, p. 3489, Jul. 2008.
- [43] C. Kim, Y. Cao, W. O. Soboyejo, and S. R. Forrest, "Patterning of active organic materials by direct transfer for organic electronic devices," *J. Appl. Phys.*, vol. 97, no. 11, p. 113512, Jun. 2005.
- [44] D. Li and L. J. Guo, "Micron-scale organic thin film transistors with conducting polymer electrodes patterned by polymer inking and stamping," *Appl. Phys. Lett.*, vol. 88, no. 6, p. 063513, Feb. 2006.
- [45] Z. L. Liao, "Semiconductor wafer bonding via liquid capillarity," *Appl. Phys. Lett.*, vol. 77, no. 5, pp. 651–653, 2000.
- [46] H. Hu and R. G. Larson, "Evaporation of a Sessile Droplet on a Substrate," *J. Phys. Chem. B*, vol. 106, no. 6, pp. 1334–1344, Feb. 2002.
- [47] Popov, "Contact mechanics and friction," in *Metal Machining*, 2000, pp. 363–374.
- [48] J. N. Israelachvili, *Van der Waals Forces between Particles and Surfaces*. 2011.
- [49] V. Adrian Parsegian, *Van der Waals forces: A handbook for biologists, chemists, engineers, and physicists*. 2005.
- [50] K. Kendall, "Adhesion: Molecules and Mechanics," *Science (80-. )*, vol. 263, no. 5154, pp. 1720–1725, Mar. 1994.
- [51] M. Gauthier, S. Alvo, J. Dejeu, B. Tamadazte, P. Rougeot, and S. Régnier, "Analysis and specificities of adhesive forces between microscale and nanoscale," *IEEE Trans. Autom. Sci. Eng.*, vol. 10, no. 3, pp. 562–570, 2013.
- [52] J. N. Israelachvili, "Van der Waals Forces," *Intermol. Surf. Forces*, pp. 107–132, 2011.
- [53] H. Search, C. Journals, A. Contact, M. Iopscience, and I. P. Address, "The London – van der Waals interaction energy," *J. phys Condens. Mater*, vol. 195, pp. 195–202, 2001.
- [54] A. W. Rodriguez, F. Capasso, and S. G. Johnson, "The Casimir effect in microstructured geometries," *Nat. Photonics*, vol. 5, no. 4, pp. 211–221, 2011.
- [55] H. B. Chan, "Quantum Mechanical Actuation of Microelectromechanical Systems by the Casimir Force," *Science (80-. )*, vol. 291, no. 5510, pp. 1941–1944, Mar. 2001.
- [56] L. Bergström, "Hamaker constants of inorganic materials," *Adv. Colloid Interface Sci.*, vol. 70, pp. 125–169, 1997.
- [57] V. B. Svetovoy and G. Palasantzas, "Influence of surface roughness on dispersion forces," *Adv. Colloid Interface Sci.*, vol. 216, pp. 1–19, 2015.

- [58] J. McPhillimy, B. Guilhabert, C. Klitis, M. D. Dawson, M. Sorel, and M. J. Strain, "High accuracy transfer printing of single-mode membrane silicon photonic devices," *Opt. Express*, vol. 26, no. 13, p. 16679, Jun. 2018.
- [59] B. Guilhabert, A. Hurtado, D. Jevtics, Q. Gao, H. H. Tan, C. Jagadish, and M. D. Dawson, "Transfer Printing of Semiconductor Nanowires with Lasing Emission for Controllable Nanophotonic Device Fabrication," *ACS Nano*, vol. 10, no. 4, pp. 3951–3958, Apr. 2016.
- [60] L. Li, C. Liu, Y. Su, J. Bai, J. Wu, Y. Han, Y. Hou, S. Qi, Y. Zhao, H. Ding, Y. Yan, L. Yin, P. Wang, Y. Luo, and X. Sheng, "Heterogeneous Integration of Microscale GaN Light-Emitting Diodes and Their Electrical, Optical, and Thermal Characteristics on Flexible Substrates," *Adv. Mater. Technol.*, vol. 1700239, p. 1700239, 2017.
- [61] Speciality Coating Systems, "Parylene Conformal Coating Specifications & Properties," pp. 1–12, 2013.
- [62] S. M. Sze and M.-K. Lee, *Semiconductor Devices: Physics and Technology*. 2013.
- [63] AIM Photonics Academy, MIT Microphotonics Centre, and iNEMI, "2017 Integrated Photonic Systems Roadmap (IPSR)," no. March. 2018.
- [64] N. A. Steinmetz, C. Koch, K. D. Harris, and M. Carandini, "Challenges and opportunities for large-scale electrophysiology with Neuropixels probes," *Curr. Opin. Neurobiol.*, vol. 50, pp. 92–100, 2018.
- [65] Intan Technologies, "INTAN RHS2116 Datasheet," pp. 1–47, 2016.
- [66] J. J. Jun, N. A. Steinmetz, J. H. Siegle, D. J. Denman, M. Bauza, B. Barbarits, A. K. Lee, C. A. Anastassiou, A. Andrei, Ç. Aydin, M. Barbic, T. J. Blanche, V. Bonin, J. Couto, B. Dutta, S. L. Gratiy, D. A. Gutnisky, M. Häusser, B. Karsh, P. Ledochowitsch, C. M. Lopez, C. Mitelut, S. Musa, M. Okun, M. Pachitariu, J. Putzeys, P. D. Rich, C. Rossant, W. L. Sun, K. Svoboda, M. Carandini, K. D. Harris, C. Koch, J. O'Keefe, and T. D. Harris, "Fully integrated silicon probes for high-density recording of neural activity," *Nature*, vol. 551, no. 7679, pp. 232–236, 2017.
- [67] B. C. Raducanu, R. F. Yazicioglu, C. M. Lopez, M. Ballini, J. Putzeys, S. Wang, A. Andrei, V. Rochus, M. Welkenhuysen, N. van Helleputte, S. Musa, R. Puers, F. Kloosterman, C. van Hoof, R. Fiáth, I. Ulbert, and S. Mitra, "Time Multiplexed Active Neural Probe with 1356 Parallel Recording Sites," *Sensors*, vol. 17, no. 10, p. 2388, Oct. 2017.
- [68] J. J. D. McKendry, D. Massoubre, S. Zhang, B. R. Rae, R. P. Green, E. Gu, R. K. Henderson, A. E. Kelly, and M. D. Dawson, "Visible-Light Communications Using a CMOS-Controlled Micro-Light-Emitting-Diode Array," *J. Light. Technol.*, vol. 30, no. 1, pp. 61–67, Jan. 2012.
- [69] D. Tsonev, H. Chun, S. Rajbhandari, J. J. D. McKendry, S. Videv, E. Gu, M. Haji, S. Watson, A. E. Kelly, G. Faulkner, M. D. Dawson, H. Haas, and D. O'Brien, "A 3-Gb/s Single-LED OFDM-Based Wireless VLC Link Using a Gallium Nitride  $\mu$ LED," *IEEE Photonics Technol. Lett.*, vol. 26, no. 7, pp. 637–640, Apr. 2014.

# Chapter 4

## Development of hybrid diamond optrodes for new regimes of optogenetic in vivo

### 4.1 Introduction

As decades of neuroscience research pointed out [1]–[4], controlled excitation or suppression of neural circuits is a key milestone towards exposing causal links between neural activity and behaviour, although the determination of causality itself proves heavily case-dependent and is often still out of reach at least for complex neural networks [5]. Optogenetics plays a part in this revolution of the study of biological neural networks by allowing genetically targeted, millisecond-timescale, localised optical stimulations of neurons [6]–[8]. This presents a strong challenge for neural implant technology. Investigation of deep, layered brain structures *in vivo* may require structured light delivery covering a large volume of tissue, achievable using independent implant-embedded  $\mu$ LEDs, with simultaneous electrode recordings. However, monolithic optrodes show inherent limitations, notably for heat extraction but also through electrical artifacts propagated in semiconductor substrates, and current hybrid devices suffer from prohibitively invasive footprints.

This chapter details the development of the first hybrid devices overcoming these hurdles: minimally invasive, thermally efficient diamond-based optrodes were created with dimensions and performance approaching those of their best monolithic counterparts. The devices integrate up to 8  $\mu$ LEDs and 16 electrodes for two-way optogenetics *in vivo*.

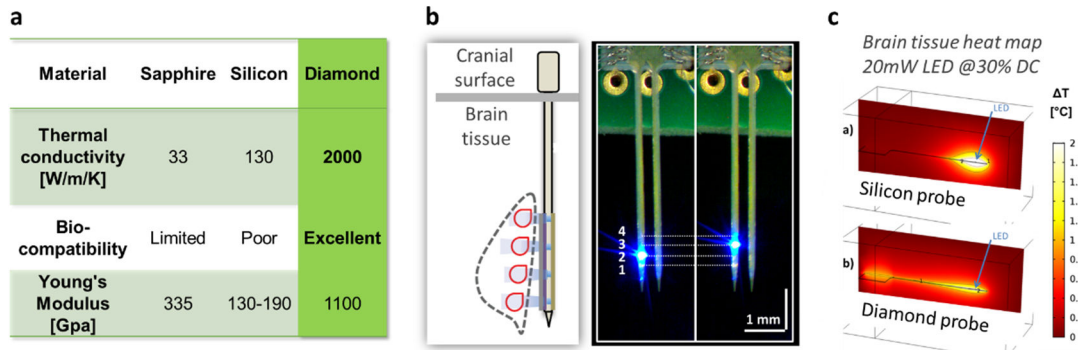


Figure 4.1 : Principle of a diamond optrode. **a)** Diamond present attractive properties for LED-based probes, **b)** a multi-site design may address multiple cortical depths (left : schematic adapted from [9], right : probes realised in this work, with LEDs 2 and 3 turned on sequentially), **c)** early modelling work predicts a marked thermal advantage of diamond probes over similar silicon designs (from [10]).

**Section 1** introduces design requirements, material limitations and prototype design.

**Section 2** covers the very specific challenges of ultrathin diamond processing and the techniques developed to manufacture optrodes with state-of-the-art performance.

**Section 3** lays out the finalised manufacturing process of the devices.

**Section 4** specifically details the last step of probe singulation, and compares the final fabricated device with the current state-of-the-art diamond and silicon devices.

Device electrical, optical and thermal performance are explored in **chapter 5**.

## 4.2 Design of hybrid diamond optrodes

### 4.2.1 Recall of neuroscience-driven targets

Detailed example specifications and design constraints are given in table 1.1, section 1.5. These must be set against the fabrication capabilities which were available to us during this project. For the “Michigan-style” design used in this work, a shank width around  $100\mu\text{m}$  limits the maximum number of single-level traces to  $\sim 15$  (with a minimum attainable trace width of  $\sim 2\mu\text{m}$  & electrodes on shank). This of course limits in turn the number of  $\mu$ LED/electrodes which can be integrated per shank.

The technique of picodroplet adhesive transfer-printing (see 3.3) developed in this work opens up powerful fabrication routes for integrated probes within these requirements. Novel

probe substrates materials with exceptional properties can be explored fully independently from transferrable light emitters such as  $\mu$ LEDs of various wavelengths and sizes, or even optoelectronic components such as photodiodes.

#### 4.2.2 Inherent advantages and limitations of synthetic diamond substrates

These capabilities were leveraged to create optrodes with unique thermal properties, enhanced biocompatibility and demonstrable scalability, thus widening the protocol options available to neuroscientists. Small-footprint GaN-on-Si TP- $\mu$ LEDs, fitting for sub-100 $\mu$ m shanks, were fabricated with efficiency similar to their monolithic counterparts (section 3.2). As was motivated in chapter 1, “synthetic” CVD diamond was chosen as the probe substrate for its outstanding properties (see also fig 4.1). CVD diamond’s thermal conductivities can reach those of bulk material [11]–[13]. While medium-term tissue damage may be best limited by reducing stiffness mismatch between an implant and the surrounding brain tissue, i.e. opting for flexible materials [14], bulk diamond shows promise as a material for widely used “rigid” probes. As an electrochemically inert material with virtually null corrosion rates *in vivo*, CVD diamond has exhibited very good biocompatibility displayed through minimal local inflammatory reaction of tissue, e.g. similar to the best Ti-based implants [15], [16]. Its dielectric properties facilitate the insulation of patterned metal traces and limit capacitively-induced transients, and it can provide a natural waveguide structure if needed thanks to its high refractive index ( $n \sim 2.42$ ).

While high-quality CVD diamond is becoming more available at reasonable cost due to recent leaps in growth technology [11], the material is not yet ready to compete with more standard dielectric or semiconductor substrates and single-crystal diamond especially faces important limitations in wafer size and growth reliability. Polycrystalline diamond, while less costly and now available in ultrathin wafers up to 4” size (e.g. [17]), may exhibit reduced thermal and mechanical properties and higher internal stress.

These limitations constrain manufacturing possibilities and dictate probe design. Single-crystal (SC) diamond membranes were chosen as the substrate material of choice. Challenging sub-50 $\mu$ m thickness, large-area (>40mm<sup>2</sup>) SC diamond membranes were required. The four SC samples (8x8mm<sup>2</sup>,  $\sim$ 30 $\mu$ m thickness) used in this work were sourced from EDP corporation in Japan [18]. EDP proved uniquely able to fabricate freestanding single-plate SC samples up to 9x9mm<sup>2</sup> via ion implantation and post-growth liftoff, although samples could only be top-polished, leaving a rough backsurface (4.3.1). In addition, a 20mm

diameter circular polycrystalline diamond (PC) was sourced from Diamond Materials GmbH [17] in Germany and used to demonstrate manufacturing process scalability.

### 4.2.3 Prototype design

The generic prototype design is shown in fig. 4.2. Variations of this layout were adapted into designs “D100”, “D50” and “N50” whose details are given in table 4.2. Minimum trace width and interspacing was set at  $2\mu\text{m}$ , yielding a maximum of 4  $\mu\text{LEDs}$  and 8 electrodes per shank. The use of TP- $\mu\text{LEDs}$  allowed a connection scheme based either on common cathode or common anode and discrete, fully encapsulated traces, while monolithic devices such as GaN-on-Si/Sapphire probes usually depend on a large shared cathode n-GaN plane [19]–[21] restricting the range of drivers usable and providing more cross-sectional area for detrimental capacitive coupling effects.

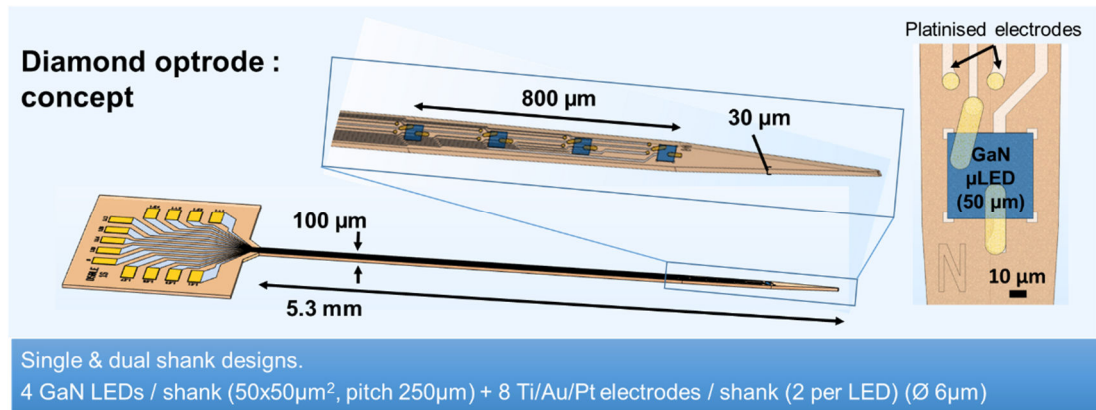


Figure 4.2 : Generic concept for the diamond optrode in this work. Multiple independently addressable GaN-based TP- $\mu\text{LEDs}$ , overlaying patterned traces, are spaced over a  $\sim 0.8\text{mm}$  length on a diamond shank tip, with a  $550\mu\text{m}$ -long taper to both facilitate insertion and increase heat spreading. Dual electrodes per LED allow electrophysiological feedback.

The chosen optrode layout seeks to meet the needs of common optogenetic experiments. The shank width ( $100\mu\text{m}$ ) and thickness ( $30\mu\text{m}$ ) broadly match those of many widely-used recording probes such as Neuronexus devices [22]. Furthermore, for rigid probes, these lateral dimensions are often taken as an upper limit for minimal invasiveness corresponding to low insertion damage [23], [24]. The sub-cm shank length allows deep insertion into e.g rodent brain, potentially allowing optogenetic stimulation of all but the deepest brain structures in rat and mice. In our design, the spatial spreading of the  $\mu\text{LEDs}$  is intended to broadly match the thickness of cortical structures, allowing layer-specific stimulation while



avoiding overlaps in the emitter emission profiles as predicted by optical modelling (section 5.2). Each  $\mu$ LED is flanked with two electrodes intended for electrical recording of neurons in the direct vicinity of the emitter, thus enabling simultaneous “write” and “readout” operations with neuronal localisation helped by the duotrode configuration. The long tapered probe end was introduced as an additional heat spreading element, while also providing an improved form factor for insertion in the mammal brain.

These designs were implemented by CAD Tanner L-EDIT software in masks AB1 and AB2 (annex A2). Taking into account the challenges of lithography and reduced sample space afforded by edge bead, a limited number of probes could be fit on the samples. The initial design “D100” was refined to accommodate experimental difficulties encountered in lithography and handling (4.3.c).

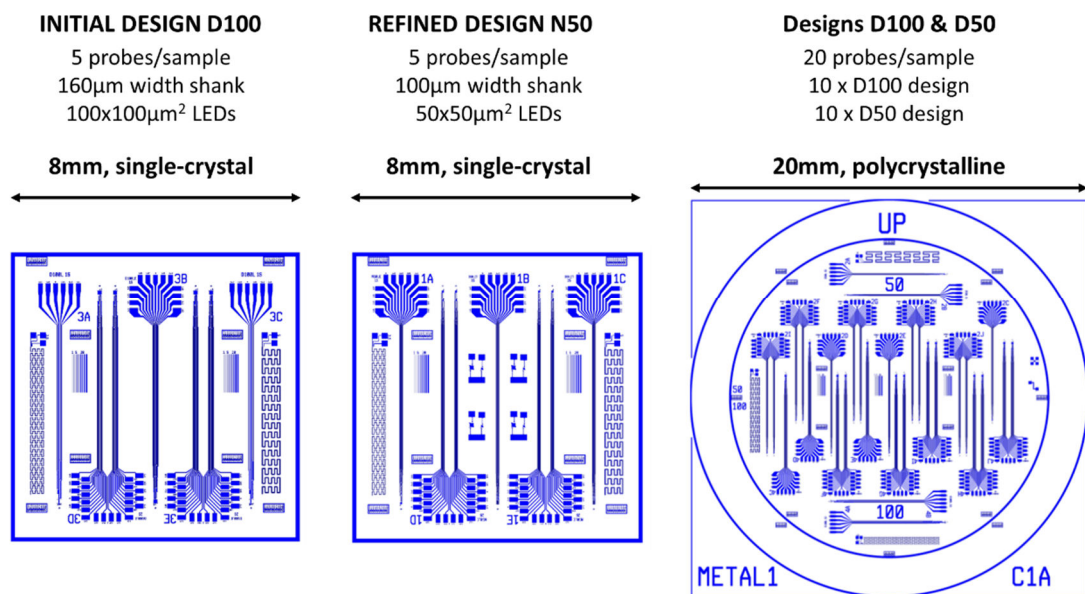


Figure 4.3 : Schematic layout of the probes over the actual diamond samples. Only 5 probes can be fitted per SC diamond sample (8x8mm<sup>2</sup>), while the larger PC membrane can accommodate 20 devices.

In design N50, probes 1B and 1C also included a serpentine thermistor (see chapter 6) to be used as a four-point temperature sensor, with a reduced number of  $\mu$ LEDs and electrodes. Test structures were included for monitoring of every stage of fabrication.

Name		Shank			μLEDs			Electrodes			
Design	Probe names	#[]	Width [μm]	Length [mm]	Wiring : shared track	Size [μm <sup>2</sup> ]	# per shank []	Pitch [μm]	Total number	# per LED []	Thermistor
D100*	3A,3C	1	160	5.3	cathode	100x100	5	300	0	0	N
D100	3B	1	160	5.3	cathode	100x100	4	300	8	2	N
D100	3D-E	2	160	5.3	cathode	100x100	4	300	8	2	N
D50**	1A,1C	1	100	5.3	cathode	50x50	5	250	0	0	N
D50	1B	1	100	5.3	cathode	50x50	4	250	8	2	N
D50	1D-E	2	100	5.3	cathode	50x50	4	250	8	2	N
N50	1A	1	100	5.3	anode	50x50	4	250	8	2	N
N50	1D-E	2	100	5.3	anode	50x50	4	250	8	2	N
N50	1B-C	1	100	5.3	anode	50x50	2	250	4	2	Y

\* D100 initial design used both for single-crystal and polycrystalline diamond samples.  
\*\* D50 initial design – used only for polycrystalline sample, superseded by N50 for single-crystal.

Table 4.1 : Overview of fabricated diamond optrodes showing, per design and probe name, the main characteristics including number of shanks, dimensions and connection of LEDs and electrodes.

### 4.3 Optrode development and specific challenges

Microfabrication of multilayered devices with tight resolution and alignment tolerances can be challenging already on monolithic substrates. These complexities are compounded for hybrid devices by the challenges of the integration process, and furthermore in this work by the unconventional demands of handling and lithography on ultrathin, fragile membranes. Solutions were developed sequentially for each of these issues. The development of picodroplet adhesive printing (3.3.3) cleared the main obstacle to the transfer of TP-μLEDs onto pre-patterned diamond membranes without a thermally resistive polymer interlayer. The main other challenges and identified failure modes of process development are described below.

#### 4.3.1 Starting material: ultrathin diamond membranes

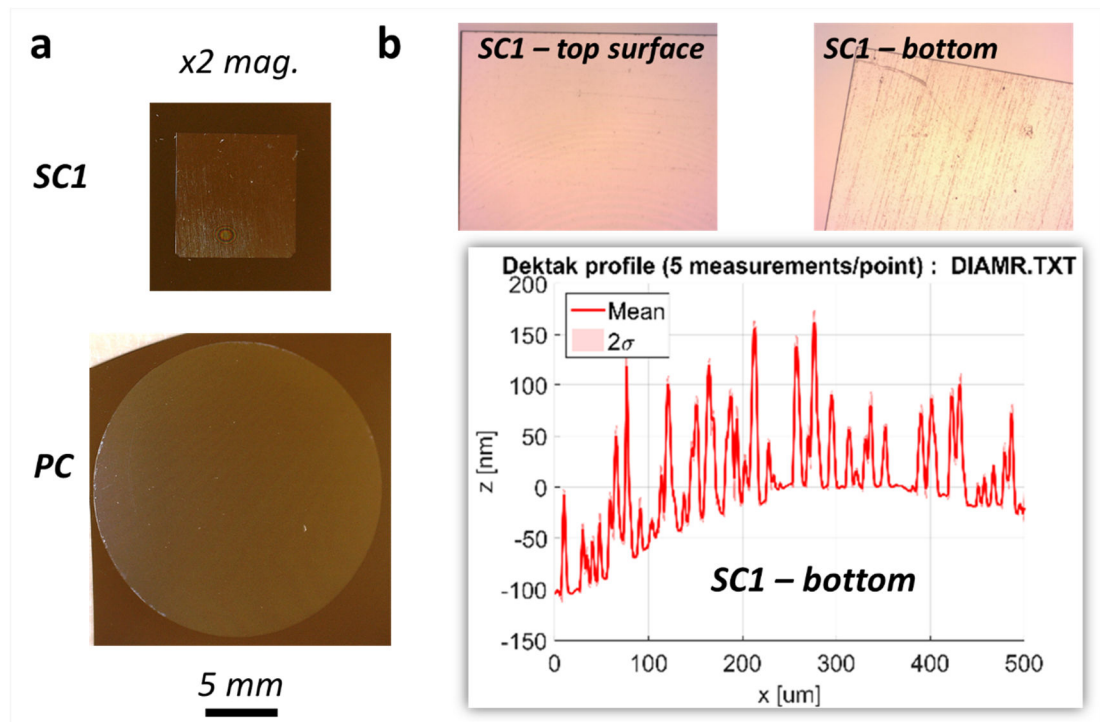


Figure 4.4 : Diamond samples used in this work. **a)** SC and PC samples at 2X real size. **b)** Details of SC sample with (top) micrographs of smooth top surface and bottom surface with pits/inclusion apparent, and (bottom) Dektak scan of bottom surface showing >100nm roughness.

Four SC diamond samples were obtained from EDP corp. (Japan). These (100)-oriented membranes were grown by chemical vapour deposition (CVD) on a diamond seed implanted with 3MeV  $C^+$  ions, and released after growth to the desired thickness by electrochemical etching. This process allows polishing of the top (growth) surface to an average surface roughness of  $R_a < 5\text{nm}$  (fig 4.4.a), but the bottom (liftoff) face may exhibit  $\mu\text{m}$ -level waviness and >100nm roughness peaks (fig 4.4.b), complicating both handling and lithography. By contrast, PC diamond growth does not rely on homoepitaxy, enabling larger wafer sizes with both sides smoothed.

### 4.3.2 Ultrathin membrane handling

Due to their fragility, ultrathin diamond membranes cannot be directly handled by metal or carbon tweezers. Vacuum pens or gelpaks cannot be used either during any cleaning, etch, deposition, or lithography steps, for which a simple and reliable reversible bonding method to a carrier sample is needed. Bonding the membranes onto fresh PR patterned on a clean silicon carrier sample (fig 4.5.d) was experimentally found to be the most reliable solution for lithography and most dry etches. (Depositing the membrane on freshly spun, unpatterned PR was experimentally found to yield an unacceptable curvature of the membrane during

subsequent hot plate steps, a fact attributed to membrane stress induced by PR expansion during baking. As a consequence, a line pattern covering the whole membrane area was specifically designed on mask AB2 for the purpose of forming an adhesive underlayer, with enough space between lines for the baking PR to expand without inducing membrane stress. When such bonding was needed, the carrier sample was first patterned with thick ( $>2\mu\text{m}$ ) resist, and clean membranes were deposited on the fresh PR immediately after its development. A progressive heat rampup helped bond the membranes).

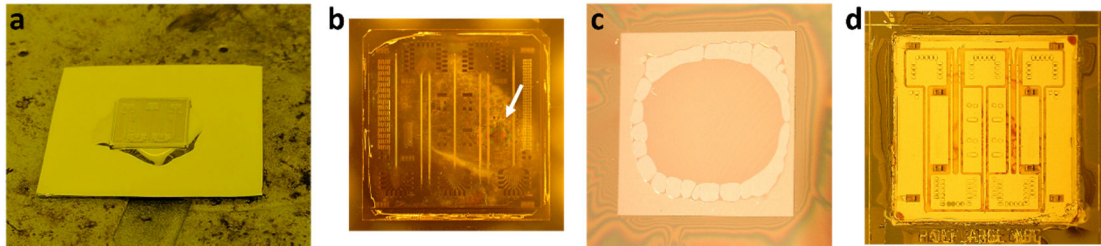


Figure 4.5 : Handling of ultrathin, freestanding diamond membranes via carrier wafers. **a)** capillary bonding of a sample to a silicon wafer on a hot plate and **b)** diamond (weakly) bonded after full droplet evaporation. White arrow shows interference fringes indicating contact bonding on a small area of the sample, **c)** plain membrane directly bonded on unpatterned photoresist exhibits severe bowing (uncontacted edges), **d)** membrane bonded onto a line-patterned PR layer during normal processing.

By contrast, water-based capillary-bonding (fig 4.5.a&b) was found to provide a weak (due to backside roughness) bond to smooth silicon carriers. While insufficient for lithographic processes, this bonding technique was used for high-temperature processes where PR bonding was impossible (e.g PECVD at  $300^{\circ}\text{C}$ , high-power dry etches).

Custom PTFE dippers and baskets were realised for solvent cleaning and acid clean/etch steps. For the RCA-1, a custom-made holder cap was affixed to the basket holder to prevent the hydrophobic diamond membranes from floating up to the surface during DI water rinses or from flipping in bubbling RCA-1 solution.

### 4.3.3 Challenges to photolithography and processing

In order to ensure a reasonable number of  $\mu\text{LEDs}$  and electrodes per shank, lithographic requirements were kept similar to those of more standard monolithic samples (minimum feature size  $\sim 1.5\mu\text{m}$ ; alignment tolerance  $\sim 1\mu\text{m}$  or  $<2\mu\text{m}$  for later steps).

Photolithographic processing on these ultrathin diamond membranes raised important challenges and adapted techniques were devised to reach these goals. The main challenges included a) difficult handling both in dry and wet environment, b) the need to avoid

mechanical shock or press during exposure due to membrane fragility, c) the management of photoresist edge-bead typical of small-sample photoresist spinning.

Handling of the membranes during photolithography was accomplished using the PR-bonding technique described in 4.3.2, requiring a first photoresist spin/expose/develop/bake cycle for the carrier before photolithography could be conducted on the sample. In order to limit mechanical stress on the membranes without compromising lithographic resolution, PR exposure was exclusively done in soft contact mode. Care was taken to reduce the number of contact alignment checks to the bare needed minimum (<4), to limit damage risks to the sample. With our MA6 mask aligner tool, well defined traces of width and spacing 2 $\mu\text{m}$  were reliably obtained with this method, along with alignment accuracies of <1.5 $\mu\text{m}$ , corresponding to less than 1 $\mu\text{m}$  loss in feature size and accuracy compared with the best performance attainable on larger, standard thick polished silicon samples.

Edge-bead on these 8x8mm<sup>2</sup> membranes (see fig 4.6.a; <250 $\mu\text{m}$  width, prevalent on corners) was mitigated by *ad hoc* spinning cycles (3-step speed rampup from 200rpm to 4000rpm). The photoresist was dispensed at the centre of the membrane and in the minimal amount needed to limit PR buildup at corners or below the membrane, liable to cause corner chipping during the alignment state (fig 4.6.a, inset).

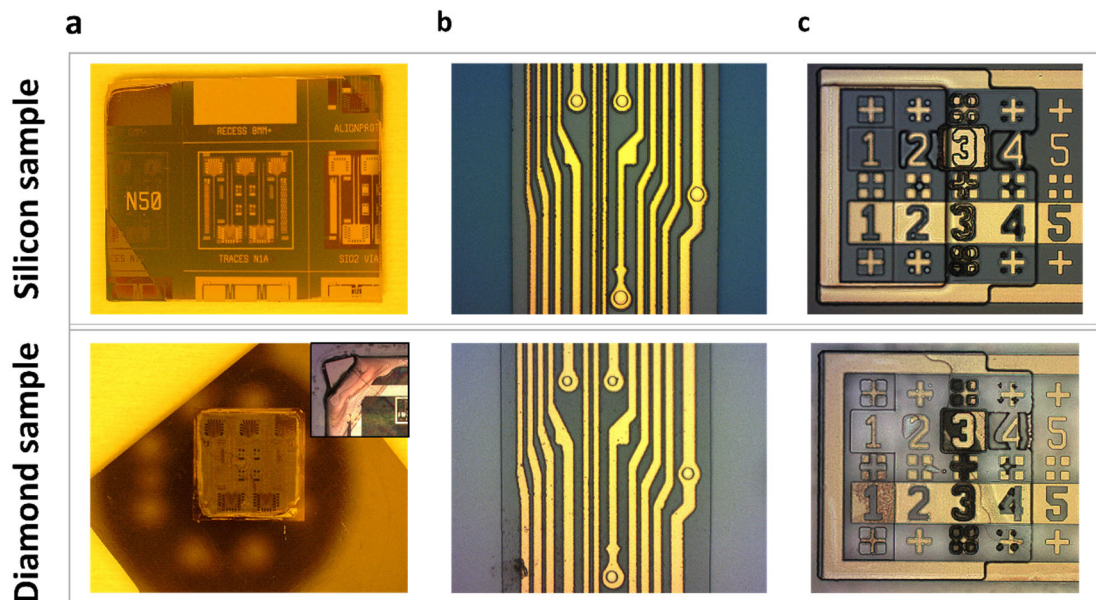


Figure 4.6 : Comparison of photolithography on prototype, standard GaN-on-Si sample (top row) and ultrathin diamond membrane (bottom row). **a)** full samples (bottom inset: chipped corner of a diamond sample), **b)** micrograph of a representative 100µm-wide shank, **c)** micrograph of an alignment mark (vertical dimension = 240µm) after 4 patterning steps.

With these precautions in place, satisfactory photolithography could be carried out on diamond membranes, albeit with slightly less resolution than on silicon pieces, mostly due to increased diffraction in soft contact mode (fig 4.6.b&c). Alignment proved challenging beyond the 3d patterning step (process step 9 onwards), with an actual tolerance of up to 2µm, which was accounted for in the second round of mask design.

#### 4.3.4 Process development and identification of failure modes

This subsection summarizes the main hurdles and successive stages cleared during development of the finalised process presented in section 4.4.

##### o *Sequential improvements towards a finalised process*

Process groundwork was laid on thin glass and silicon samples (fig 4.7). These allowed adjustments in printing technique and mask design while awaiting for the actual diamond material, although they could not mimic the challenges in handling and photolithography which warranted design refinements through mask AB2. Still, these proof-of-concept devices were essential to clear early hurdles and reduce unknowns, helping limit risk as only 4 diamond samples could be ordered and used in this project.

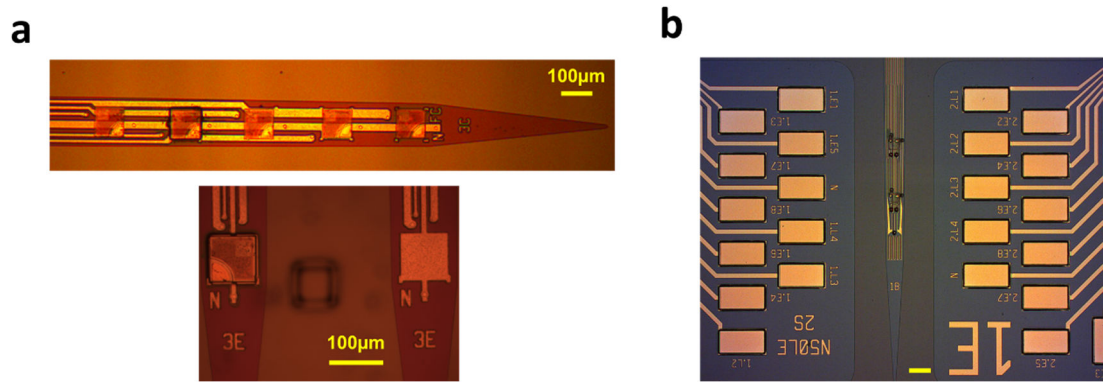


Figure 4.7 : Testbed samples for process development. The process principle was first demonstrated on a glass sample (**a**, adapted from [10]). The finalised process was also replicated on silicon samples (**b**) for comparison purposes, although those unfortunately failed at the separation stages (see XX).

When manufacturing moved to the diamond samples, many of the challenges listed above became apparent. During processing, the first three of the samples experienced critical failure at (advancing) stages of the process, although a wealth of experience was collected at each iteration and by analysing the failure modes.

A summary of this iterative improvement process is given in table 4.3. Main modifications include switching from Titanium/Aluminium to less reactive Titanium/Gold traces, which withstand immersion in TMAH-laden photoresist developer (while the additional hard masking step complicates handling, this also affords the possibility of BOE etching vias in SiO<sub>2</sub> in further steps), optimising parylene step coverage, defining the best photolithography procedure preventing PR over/re-flow in the membrane corners (this caused sample SC2 to stick to the mask and crack along its full length during alignment) and determining a suitable masking & dry etch process for probe separation (section 4.5.X). All major obstacles were finally overcome during processing of the last sample (SC4), yielding operational, singulated probes whose electrical, optical and thermal properties could be characterised (chapter 5).

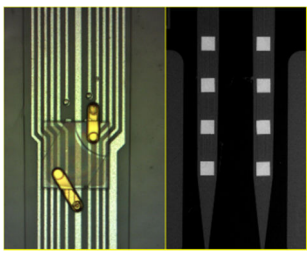
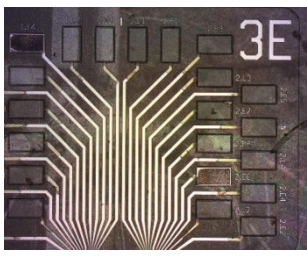
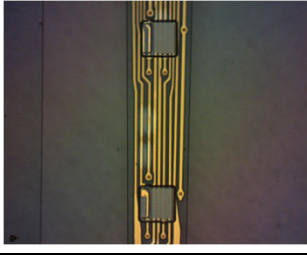
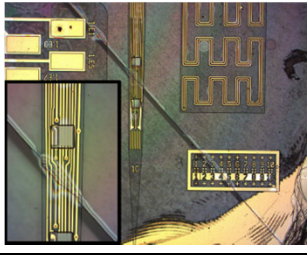

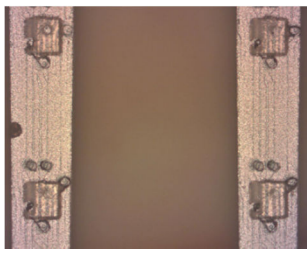
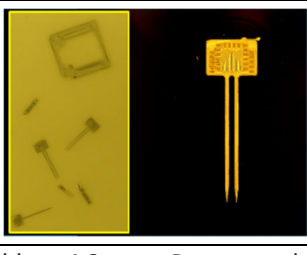

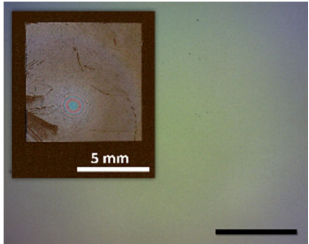
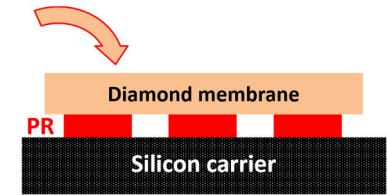
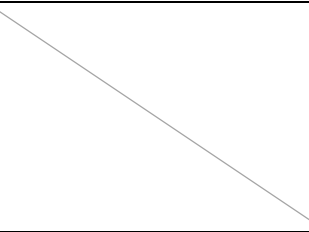
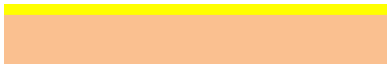
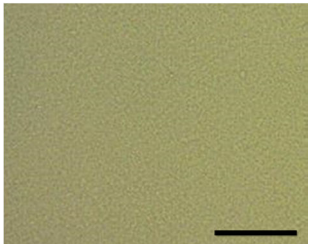
SC diamond sample	Micrograph : During process	Micrograph : Failure mode	Details
SC1			D100, Al traces, direct dry etch to LEDs. Initial sample, tests for lithographic alignment & handling <b>Failure:</b> bad PR/parylene step coverage at LED, contacting fail, LED damage from via etch, Al tracks damage from acid etch and negative PR development.
SC2			N50, Ti/Au traces by dry etching, Pd $\mu$ LEDs. NB Ti/Au traces added hard masking steps. <b>Improvements :</b> move to Ti/Au traces, protective SiO <sub>2</sub> layer deposited on LEDs <b>Failure:</b> diamond sample fractured during one of the last litho steps, due to PR overcoating & too many align checks.
SC3			N50 design – Ti/Au traces, Ni/Au $\mu$ LEDs. All steps validated but diamond through-etch. <b>Improvements:</b> stringent litho handling, switch to optimised Ni/Au LEDs only with on-LED SiO <sub>2</sub> layer, via etch and contacting. <b>Failure:</b> critical Al mask erosion during diamond etch, LEDs damaged / non-operational.
SC4			N50 design – Ti/Au traces, Ni/Au $\mu$ LEDs. All steps validated. <b>Improvements:</b> probe separation etch. Fabrication process successful: singulated diamond probes with functioning $\mu$ LEDs. Electrodes not tested. <b>Possible failure mode includes parylene delamination (see ch 5).</b>

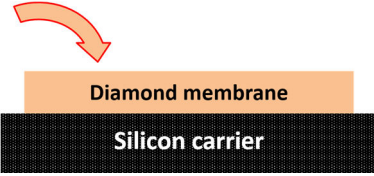
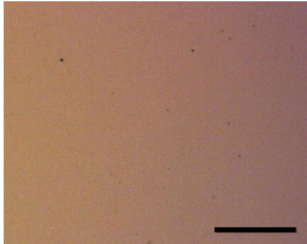

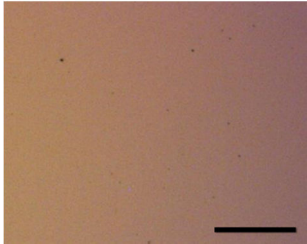
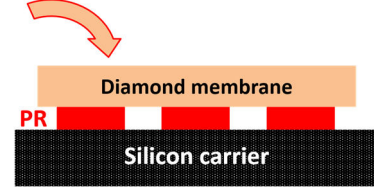
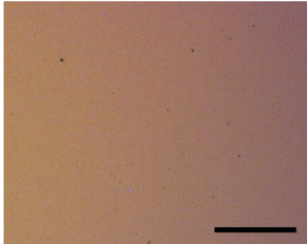
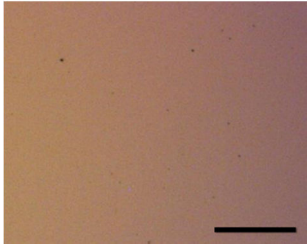
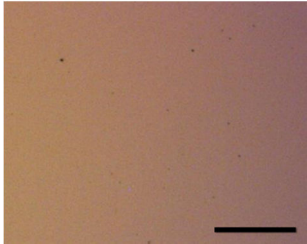
Table 4.2 : Process development stages, through sequential tests, failures and solutions/improvements on the 4 diamond membrane samples used in this work.


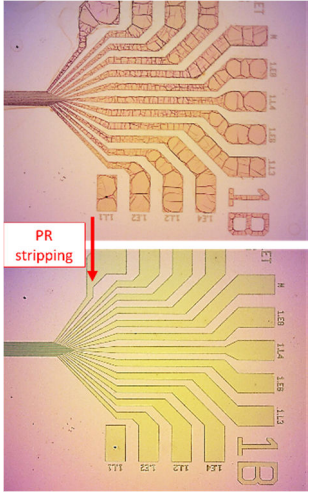
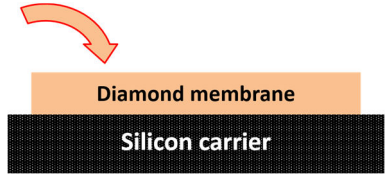

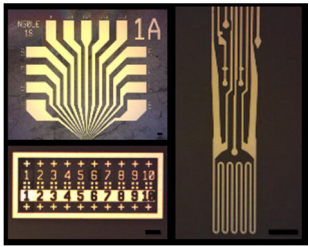
The next section details the finalised manufacturing process carried out on sample SC4 and incorporating all specific improvements detailed in table 4.3. The same process was used for the polycrystalline diamond membrane.


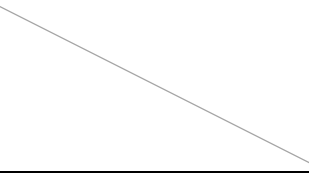

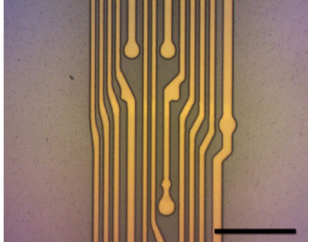
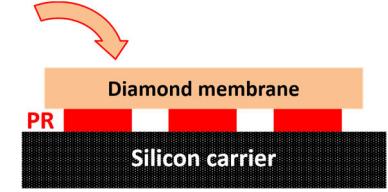
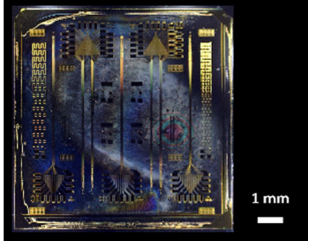
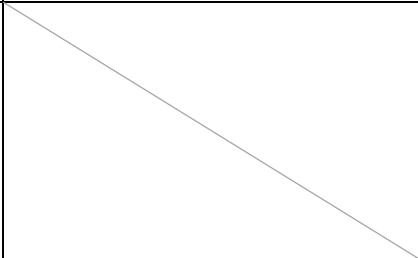
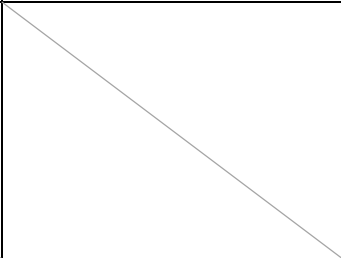



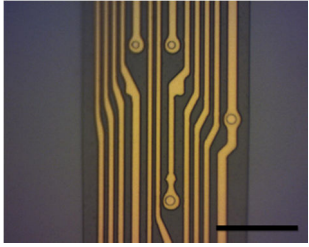
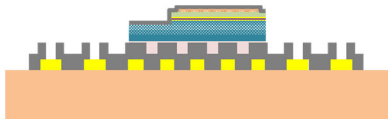
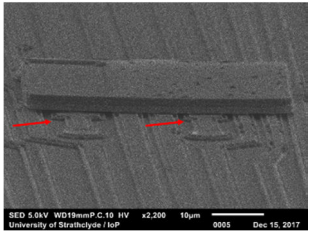
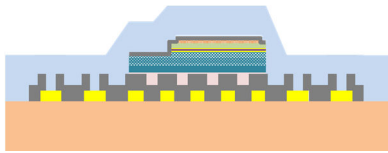
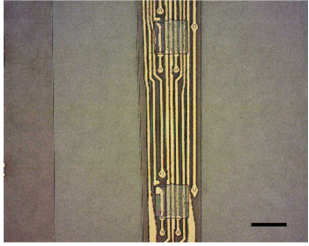
#### 4.4 Fabrication process: Diamond-based optrodes – (all black scale bars 50µm) – Mask AB1, AB2 (annex A2)

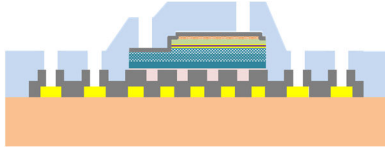
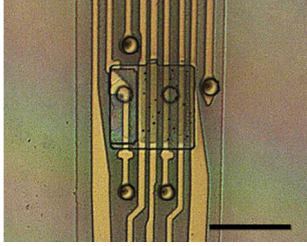

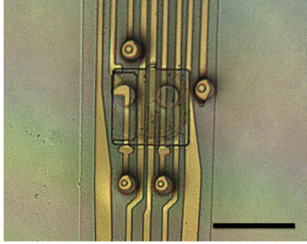
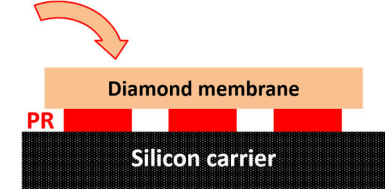
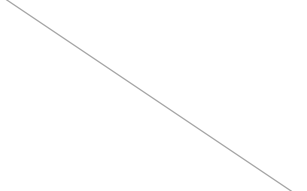
Process step & description <i>(recipes in appendix A.1)</i>	Schematic	(All black scale bars 50µm)
<p><b>0. Initial sample cleaning :</b></p> <p>A thorough clean of the diamond surface is crucial to ensure a high quality metal film in step 1, without delamination or contamination-induced shorts. The diamond samples are first degreased in solvent (acetone 15min, methanol 10min, IPA 10min), then cleaned from particulate and organic contamination via <b>RCA-SC1 clean</b> (heated “base piranha”, 20min, see annex A1.4.b), DI-rinsed and blow-dried with N<sub>2</sub>.</p> <p><i>NB1 : Dangerous etch – acid bench only, appropriate PPE must be worn and temperature checked – cf. SOP</i></p> <p><i>NB2 : Handling during RCA-SC1 : use PTFE holder with custom-made cap to prevent diamond floating away</i></p>		
<p><b>Carrier change -&gt; PR-bonding to C1 :</b> Immediately after the clean, the samples are bonded to silicon carrier C1 freshly patterned with thick PR, heat-dried on a hot plate (120°C, 10min) to let the photoresist fully reflow and remove traces of water vapour. Samples and carrier are then stuck to a 4-inch silicon carrier wafer using Kapton tape and loaded into the sputter.</p>		
<p><b>1. First metal deposition by sputtering (traces, Ti/Au) :</b></p> <p>Samples are sputtered with a Ti (80nm) /Au (300nm) bilayer as follows :</p> <p>Ti : pre-deposition 3'00 / deposition 5'00 (260 V, 6 A)</p> <p>Au : pre-deposition 30'' / deposition 4'00 (470 V, ~3.4 A)</p> <p><i>In order to tailor the thickness of oxide hard mask needed, the precise total thickness of the metal stack is assessed by stylus profiling on a test Silicon sample added to the run and patterned using PR liftoff.</i></p>		

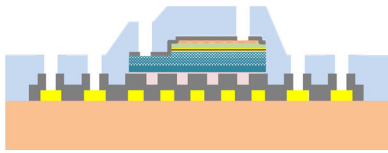
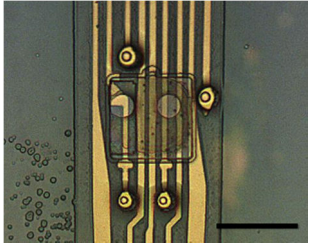
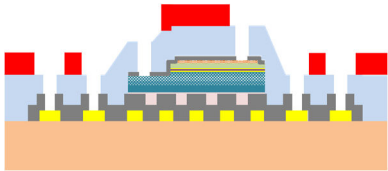
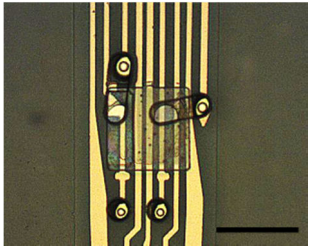
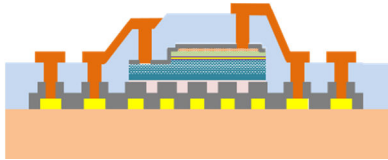
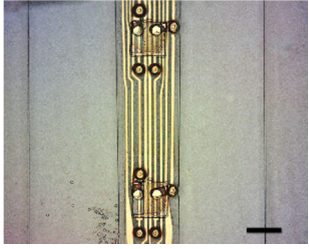

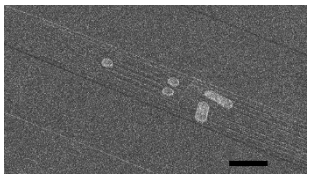
Process step & description ( <i>recipes in appendix A.1</i> )	Schematic	(All black scale bars 50µm)
<p><b>Carrier change C1 -&gt; capillary bonding to C2:</b> Before the following PECVD step (300°C), all traces of photoresist are removed. Samples are detached from carrier C1 by soaking in acetone for 10min, then transferred and capillary-bonded to silicon carrier C2 using a drop of DI water, and heat-dried on a hot plate (150°C, 15min) to remove traces of water vapour.</p>		
<p><b>2. SiO<sub>2</sub> Hard mask deposition</b>  An SiO<sub>2</sub> layer of equal thickness to that of the metal stack is deposited (520nm, PECVD recipe "oxide200.rec" for 16min) to allow up to 50% overetch during metal etching (metal/mask selectivity &gt; 1.5). <i>The precise layer thickness is checked using a F-20 ellipsometer on a plain silicon sample added to the run.</i></p>		
<p><b>Carrier change C2 -&gt; PR-bonding to C3 :</b> Samples are detached from carrier C2 in acetone, cleaned in IPA, dried then PR-bonded to silicon carrier C3 and heat-dried on a hot plate at 120°C for 10min just before patterning.</p>		
<p><b>3.1 Patterning of traces and alignment marks (mask AB2 – cell N1A)</b>  A photoresist mask is created using S1805 (HMDS primed, spincoated at 3500rpm for 60s and followed by a hot plate soft-bake at 115°C for 70s). The samples are then exposed for 2.8s, using soft contact lithography. Photoresist is developed in MICROPOSIT developer concentrate (1:1 with deionised water) for 35s (corresponding to a ~5s overdevelopment ensuring good definition of thin inter-traces trenches).</p>		

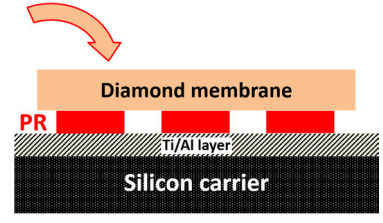
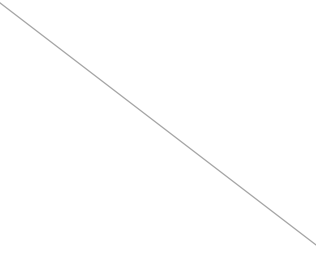
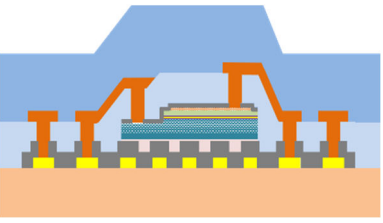
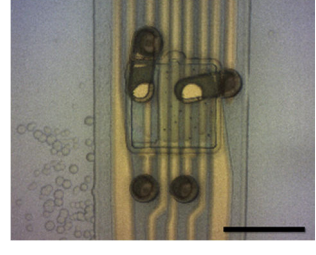
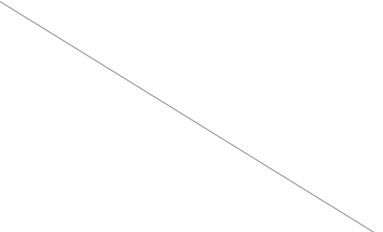
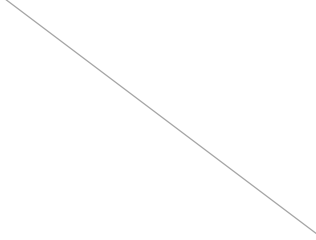
Process step & description ( <i>recipes in appendix A.1</i> )	Schematic	(All black scale bars 50µm)
<p><b>3.2-3.3 Descum and SiO<sub>2</sub> hard mask etch</b></p> <p>An oxygen plasma descum (Diener “Pico” asher, 50 sccm O<sub>2</sub>, 80W for 20s) is performed after the lithography to remove residual photoresist within trenches and improve profile verticality.</p> <p>The pattern is transferred onto SiO<sub>2</sub> by etching in RIE#1 using recipe <b>mlesio2</b> for 30min, factoring in a 50% overetch to remove all potential oxide residues in thin trenches and limit the risk of shorting traces.</p> <p><i>A conductivity check is performed using micromanipulated probes on the exposed metal.</i></p>		
<p><b>3.4 PR stripping before high-power metal etch</b></p> <p>To prevent PR carbonisation during high-power sputtering etches (see annex A1.5.c), diamond samples are soaked in 1165 photoresist stripper (80°C, 3hrs) then plasma cleaned (Diener asher, 50 sccm O<sub>2</sub>, 200W for 20min). Less fragile glass- or silicon-based testbeds can simply be Matrix-ashed (8 min at 150°C).</p>		
<p><b>Carrier change C3 -&gt; capillary bonding to C4:</b> following PR stripping, samples were transferred and capillary-bonded to silicon carrier C4 using a drop of DI water, and heat-dried on a hot plate at 150°C to remove traces of water vapour.</p>		
<p><b>3.5 Metal etch : traces and alignment marks</b></p> <p>Probe traces are etched in RIE#2 in two steps, with etch times adjusted to the measured metal stack thickness for a minimum overetch of 30%. The etch starts with recipe “<b>Auetch</b>” (typical time 15min) followed by recipe “<b>Tietch</b>” (5min). A conductivity check is performed to confirm all metal had been cleared in trenches and metal traces were not yet exposed (hard mask layer remaining).</p>		

Process step & description <i>(recipes in appendix A.1)</i>	Schematic	(All black scale bars 50µm)
<p><b>3.6 Dry stripping of remaining SiO<sub>2</sub> mask</b></p> <p>The remaining uneven thin layer of SiO<sub>2</sub> on top of traces and bondpads was etched in RIE#1 (<b>mlesio2</b>, 14min) to facilitate further processing steps by improving surface smoothness.</p>		
<p><b>4. SiO<sub>2</sub> deposition : 1 µm-thick traces passivation bilayer</b></p> <p>1000 nm of PECVD SiO<sub>2</sub> is deposited as a bilayer (recipe <b>oxide200</b>, 500nm/500nm, 15min/15min) to help avoid pinhole formation linked to lower material density compared to native oxides. The precise layer thickness is checked using a Filmetrics F-20 ellipsometer on a plain silicon sample added to the run.</p>		
<p><b>Carrier change C4 -&gt; PR-bonding to C5</b> : Samples are detached from carrier C4 in acetone, cleaned in IPA, dried then PR-bonded to silicon carrier C5 and heat-dried on a hot plate at 120°C for 10min just before patterning.</p>		
<p><b>5.1 Patterning of SiO<sub>2</sub> vias to bondpads and electrodes (mask AB2 – cell N2A)</b></p> <p>A photoresist mask is created using S1805 (HMDS primed, spincoated at 3500rpm for 60s and followed by a hot plate soft-bake at 115°C for 60s). The samples are then exposed for 2.8s, using soft contact lithography. Development is done using MICROPOSIT developer concentrate (1:1 with deionised water) for 40s (10s overdevelopment to compensate for shrinking of vias size due to soft contact lithography).</p>		

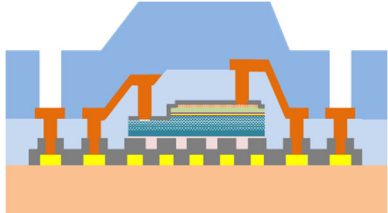
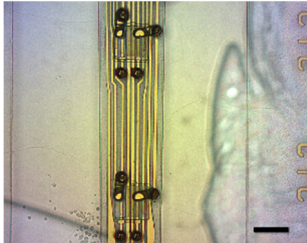
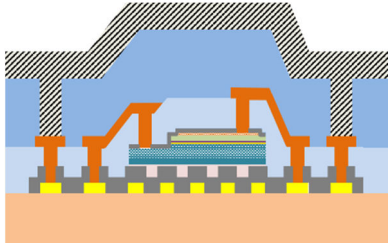
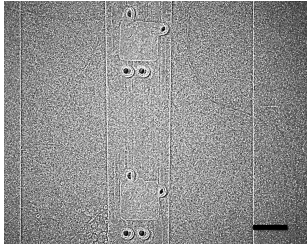
Process step & description <i>(recipes in appendix A.1)</i>	Schematic	(All black scale bars 50µm)
<p><b>5.1-5.2 Descum and SiO<sub>2</sub> etching to open vias</b></p> <p>A oxygen plasma descum is used to remove residual PR in vias (Diener asher, 50 sccm O<sub>2</sub>, 80W for 20s). Vias are etched using RIE#1 recipe “mlesio2” for a total of 60min, with etch depth being checked using a Filmetrics F-20 ellipsometer on a plain silicon sample added to the SiO<sub>2</sub> deposition run. The remaining PR mask is stripped by oxygen plasma ashing (Diener asher, 50 sccm O<sub>2</sub>, 200W for 5min).</p>		
<p><b>6. Transfer-printing of 50x50µm<sup>2</sup> GaN-based µLEDs</b></p> <p>Separately fabricated TP-µLEDs (50x50µm<sup>2</sup>, with Ni/Au current spreading layer; see 3.2.4) are printed on top of the passivated traces, using bead-mediated transfer printing (see 3.3.3). Placement cues patterned in the metal traces allowed for submicron positioning accuracy.</p>		
<p><b>7. Parylene C deposition : insulation layer 1</b></p> <p>A 3.2 µm-thick conformal layer of Parylene C (dimer weight: 4.2g, vapour A-174 silane priming) is deposited on the samples, placed on a 4” Si wafer during deposition to avoid carrier backside coating. The deposition is only started after a minimum of 1h30 cold trap operation and a base vacuum pressure of &lt;7mTorr to ensure the best possible film quality. The film precise thickness is ascertained using a Filmetrics F-20 ellipsometer on a plain silicon sample added to the run.</p>		

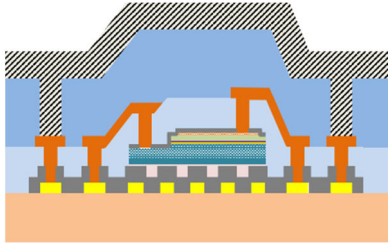
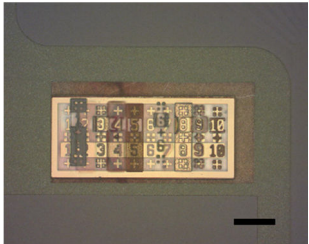
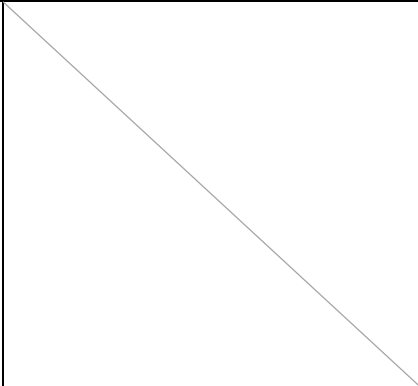
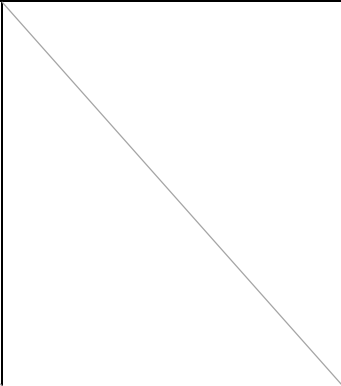
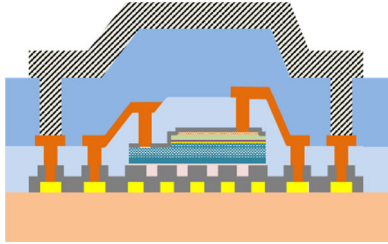
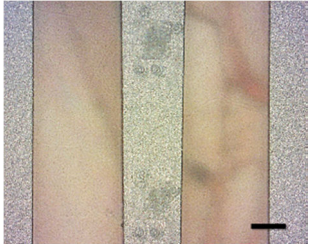
Process step & description <i>(recipes in appendix A.1)</i>	Schematic	(All black scale bars 50μm)
<p><b>8.1 Patterning of parylene vias to LEDs, electrodes &amp; bondpads (mask AB2 – cell N3A)</b></p> <p>Samples are cleaned in IPA (5min) and blow dried before patterning. A ~5μm-thick photoresist mask is created using SPR220-4.5 (2800rpm/60s spin, hot plate soft-bake at 105°C for 130s). The samples are then exposed for 18s, using soft contact lithography and developed in MICROPOSIT developer concentrate (1:1 with DI) for 52s. The precise PR mask thickness is determined using stylus profiling.</p>		
<p><b>8.2 Parylene staggered etching to open vias</b></p> <p>Samples are etched in RIE#1 using recipe “paryl_rs”. The total etch time is adjusted for a 50% overetch (~11min for 2500nm), or as close to this value as is possible without fully eroding the mask. The etch is fractioned into runs of &lt; 4 minutes as longer etch runs were experimentally found to fail to fully open vias of width &lt; 10μm, possibly by leaving a thin residual burnt layer. The precise etch depth attained through each run is monitored both in parylene and PR using stylus profiling and/or ellipsometry on test samples.</p>		
<p><b>8.3 PR stripping and carrier change C5 -&gt; PR-bonding to C6</b> : samples are soaked in acetone for 1hr, then cleaned in methanol and IPA (5min each), dried then PR-bonded to silicon carrier C6 and heat-dried on a hot plate at 120°C for 10min. A gentle plasma descum (Diener asher, 50 sccm O<sub>2</sub>, 80W for 20s) is performed to remove any thin residual layer of PR before proceeding.</p>		

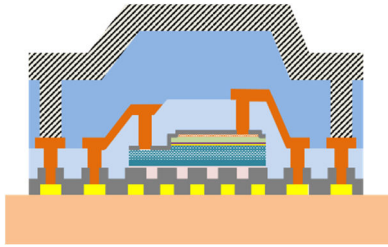
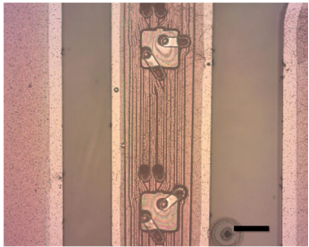
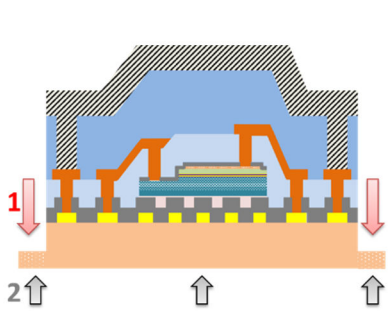
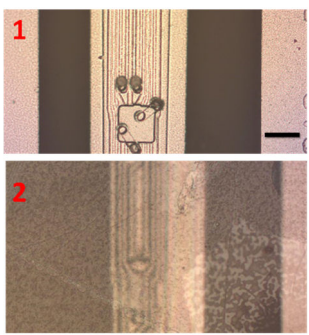
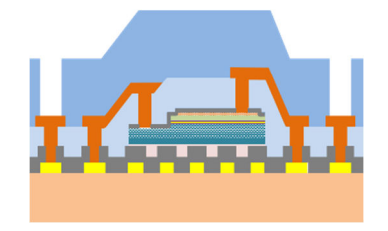
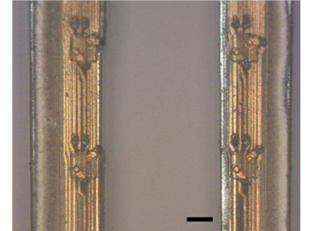
Process step & description ( <i>recipes in appendix A.1</i> )	Schematic	(All black scale bars 50 $\mu$ m)
<p><b>8.4 SiO<sub>2</sub> wet etching to open contacts to the LEDs</b></p> <p>The 100nm layer of protective SiO<sub>2</sub> covering the LED is etched in <b>buffered oxide etch</b> (BOE, diluted 7:1) for 25s. After the etch, samples are rinsed in deionized water and blow-dried.</p> <p><i>NB: BOE is a dangerous chemical. The etch must be performed with caution in a closed extract bench, using a PTFE beaker with adapted handling tools (ad hoc basket holder) and appropriate PPE must be worn.</i></p>		
<p><b>9.1 Patterning for metal liftoff : bridge-contacting structures (mask AB2 – cell N4Z)</b></p> <p>A negative photoresist mask is created using ma-N 1420 (spincoated at 3000rpm for 60s, followed by a hot plate soft-bake at 100°C for 130s). The samples are exposed for 25s using soft contact lithography, and developed in pure maD-533S developer for 105s (35s overdevelopment to create ~1 <math>\mu</math>m undercut).</p>		
<p><b>9.2. Second metal deposition by sputtering (bridging contacts, Ti/Au) :</b></p> <p>A thick, partly conformal deposition is needed to ensure good step coverage between LEDs and underlying traces. A thick titanium layer is used to ensure good adhesion of the metal to parylene.</p> <p>Samples are sputtered with a Ti (100nm) /Au (400nm) bilayer as follows :</p> <p>Ti : pre-deposition 3'00 / deposition 6'00 (260 V, 6 A)</p> <p>Au : pre-deposition 30'' / deposition 6'00 (470 V, ~3.4 A)</p>		
<p><b>9.3 Metal liftoff in acetone</b></p> <p>Samples are soaked in heated acetone (55°C, in water bath) overnight. Metal liftoff is encouraged by gently squirting acetone on top of the samples with a plastic pipette.</p>		

Process step & description <i>(recipes in appendix A.1)</i>	Schematic	(All black scale bars 50µm)
<p><b>Bonding to final carrier C6 -&gt; PR-bonding to C7</b> : Samples are transferred and soaked in IPA for 15min, dried then PR-bonded to a Ti/Al-coated silicon carrier C7, and heat-dried on a hot plate at 120°C for 10min.</p> <p><b>10.1 O<sub>2</sub> plasma activation to promote parylene-to-parylene adhesion</b>            Sample are exposed to a gentle oxygen plasma (Diener asher, 50 sccm O<sub>2</sub>, 80W for 20s), to clean off organic contaminants and possibly help promote adhesion of the upcoming parylene layer ([25], [26]).</p>		
<p><b>10.2 Parylene C deposition : insulation layer 2</b>            A 3.5 µm-thick conformal layer of Parylene C (dimer weight: 4.8g, vapour A-174 silane priming) is deposited on the samples, placed on a 4'' silicon wafer to avoid carrier backside coating. The deposition is only started after a minimum of 1h30 cold trap operation and a base vacuum pressure of &lt;7mTorr to ensure the best possible film quality. The film precise thickness was ascertained using a Filmetrics F-20 ellipsometer on a plain silicon sample added to the run.</p>		
<p><b>11.1 Patterning of parylene vias to electrodes and bondpads (mask AB2 – cell N5A)</b>            Samples are cleaned in IPA (5min) and blow dried before patterning. A ~5µm-thick photoresist mask is created using SPR220-4.5 (2500rpm/60s spin, hot plate soft-bake at 105°C for 140s). The samples are then exposed for 18s, using soft contact lithography and developed in MICROPOSIT developer concentrate (1:1 with DI) for 52s. The precise PR thickness post-patterning is determined using stylus profiling.</p>		



Process step & description ( <i>recipes in appendix A.1</i> )	Schematic	(All black scale bars 50µm)
<p><b>11.2 Parylene staggered etching to open vias</b></p> <p>Vias are etched open in RIE#1 using recipe <b>paryl_rs</b>, exposing the surface of electrodes and bondpads. The total etch time is adjusted for a 50% overetch (~13.5min for 3000nm), or as close to this value as possible without fully eroding the mask, fractioning the total etch-time in 4-min long runs as explained above. The precise etch depth attained through each run is monitored both in parylene and PR using stylus profiling and/or ellipsometry on test samples, and parameters for the next runs are adapted in consequence.</p>	 <p>A cross-sectional schematic diagram showing a blue parylene mask layer on top of a substrate. The mask has a central opening. Below the mask, there are several orange structures representing electrodes or bondpads. The diagram illustrates the etching process where the mask is being removed to expose the underlying structures.</p>	 <p>A scanning electron micrograph (SEM) showing a series of vertical lines (vias) on a substrate. The vias are spaced out and have a consistent width. A black scale bar is visible in the bottom right corner.</p>
<p><b>11.3 PR stripping:</b> samples are solvent cleaned in acetone (30min), methanol (10min) and IPA (10min), blow-dried with N2 then descummed in oxygen plasma (Diener "Pico" asher, 50 sccm O2, 100W for 30s).</p>		
<p><b>12. Thick Aluminium layer deposition (hard mask)</b></p> <p>Samples were heat-dried on a hot plate set at 120°C for 10min prior to deposition.</p> <p>A 2000nm thick layer of Aluminium was then sputtered with a 20nm Ti adhesion seed layer :</p> <p>Ti : pre-deposition 1'20 / deposition 6'00</p> <p>Al : pre-deposition 3'00 / three-step deposition : 30'00 + 30'00 +30'00</p> <p>Multiple test silicon samples patterned with thick negative PR were added to the run, and underwent subsequent metal liftoff in acetone. These were used to determine the precise thickness of the deposited Aluminium layer by stylus profiling and to monitor mask thickness and erosion on the same features as these patterned on the diamond samples during the following etch steps.</p>	 <p>A cross-sectional schematic diagram showing a blue parylene mask layer on top of a substrate. The mask has a central opening. Below the mask, there are several orange structures representing electrodes or bondpads. The diagram illustrates the deposition of a thick aluminium layer (hatched pattern) over the mask and the underlying structures.</p>	 <p>A scanning electron micrograph (SEM) showing a textured surface, likely the deposited aluminium layer. The surface has a granular appearance. A black scale bar is visible in the bottom right corner.</p>

Process step & description <i>(recipes in appendix A.1)</i>	Schematic	(All black scale bars 50µm)
<p><b>13. (optional) Opening vias to alignment marks (mask AB1 – cell 8Z) by dry etching</b></p> <p>The thick Aluminium layer lowers contrast visibility across the sample and blurs feature edges. To obtain the best alignment of the probe contour cell it is best to remove the metal covering the alignment marks. The samples are patterned with thick positive photoresist (SPR220-7.0, spun at 2500rpm for 60s, soft baked at 105°C for 130s, exposure 35s in soft contact lithography, developed for 125s in 1:1 MICROPOSIT developer concentrate:DI). The exposed aluminium was etched for a &lt;10min in ICP#1 using recipe “AlRobert”, minimising etch duration to avoid detrimental thinning of the mask at edges/steps.</p>		
<p><b>14.1 Probe contour patterning (mask AB2 – cell N6C)</b></p> <p>After PR solvent cleanoff (acetone 10min / methanol 5min / IPA 5min), a 8.5µm-thick positive photoresist mask is created using SPR220-7.0, spincoated at 2200rpm for 60s and soft baked on a hot plate at 105°C for 130s. The samples are exposed for 35s using soft contact lithography and developed for for 125s in 1:1 MICROPOSIT developer concentrate:DI water. The PR is hard baked for 5min at 110°C and a careful visual inspection is carried out to ensure mask integrity and good coverage of critical features and high steps (esp. LEDs and bondpads with steps ~6µm).</p> <p><i>NB: Challenging alignment through ~8µm layers + ~8µm PR. Expected best possible alignment is +/-1.5µm.</i></p>		
<p><b>14.2 Aluminium etch</b></p> <p>Separated probe contours are etched in ICP#1 using recipe <b>AlRobert</b> for 15min (colour change visible after ~11-12min indicating complete etch). This duration is carefully adjusted for an overetch limited to 20-30%, ensuring complete etch of the aluminium in the trenches while limiting as much as possible the lateral etching of the mask along the thin probe shanks, which further decreases alignment tolerance.</p> <p><i>(NB: lateral etching estimated at ~1.5µm+ on each feature).</i></p>		

Process step & description ( <i>recipes in appendix A.1</i> )	Schematic	(All black scale bars 50µm)
<p><b>15. PR stripping (optional) and parylene etch</b></p> <p>Samples are solvent cleaned, blow-dried with N<sub>2</sub> then further dry-stripped in oxygen plasma (Diener “Pico” asher, 50 sccm O<sub>2</sub>, 200W for 5min).</p> <p>The parylene layer around probe is etched in RIE#1 using recipe paryl_rs, for a total etch time adjusted for a 50% overetch (~24min for 5500nm). The etch is fractioned into runs of 4 minutes or less as explained above.</p>		
<p><b>14. Etching through diamond – repeated etch cycles, top then bottom side (see 4.5.1)</b></p> <p><b>Topside etch :</b> samples are etched in ICP#1 using staggered runs (30min to 60min long) of recipe <b>DIA_ARO2</b> up to a total maximum of 180min (depth ~25µm+), corresponding to the maximum acceptable erosion of the Al mask. Mask condition is thoroughly monitored under the microscope after each run.</p> <p>After 180min topside etch or if mask condition is less than optimal, samples are debonded from their carrier wafer, flipped and bonded upside down with patterned PR on a new carrier.</p> <p><b>Backside etch :</b> sample backsides are blanket etched in ICP#1 using staggered runs of recipe <b>DIA_ARO2</b> (15-30min long until full separation, max 90min for ~13µm), leaving singulated probes bonded on wafer.</p>		
<p><b>15. Removal of hard mask, probe release and bonding to PCB</b></p> <p>Samples are soaked in acetone, helping to clear PR residues and triggering release from the carrier wafer, collected on a cleanroom wipe, cleaned with IPA and left to dry. The remaining hard mask is removed by dry etch (ICP#1, AlRobert, 10min). Individual probes are then mounted on an <i>ad hoc</i> PCB using a vacuum pen for handling and a small drop of nail polish for bonding the base to the PCB edge.</p>		
<p><b>PROCESS END: 5 free-standing, 30µm thick diamond optrodes are released per initial diamond membrane.</b></p>		

## 4.5 Probe singulation and final device

### 4.5.1 Deep diamond etch with Aluminium hard masking

After on-chip probe manufacturing and testing, individual probes must be separated by a full through-membrane etch (depth  $>30\mu\text{m}$ ). Diamond is a notoriously difficult material to etch, requiring high-power ICP sputter etches with either chlorine (“slow” etch) or oxygen (“fast” etch) assisting chemistries [27]–[29]. Tran et al. recently reported Aluminium to be used as a suitable hard mask for diamond etches with high selectivity ( $>50$ ) for oxygen-based diamond etching [30]. This was chosen as the preferred route over a more conventional  $\text{SiO}_2$  hard mask, incompatible with parylene coatings and presenting much lower selectivities ( $<10$ ). Based on previous studies at the IoP [31], a 800W-power Ar/ $\text{O}_2$  ICP etch was used (ICP#1 recipe DIA\_ARO2). Aluminium mask erosion for the feature size used in this work was studied using  $2\mu\text{m}$  Al layers on silicon test samples (fig 4.8 a-c).  $5\mu\text{m}$ -wide features were found able to withstand  $>4$  hours of etch, with an Al etch rate eventually dropping below  $4\text{nm}/\text{min}$ . On actual diamond samples, very dense grassing was observed within trenches (fig 4.8 d-e), with SEM-EDX analysis indicating that redeposition of sputtered  $\text{Al}_2\text{O}_3$  compounds may be responsible for heavy micromasking. The pillars themselves were found to be highly vertical and up to  $28\mu\text{m}$  high, although their presence complicated etch rate analysis for diamond. Insufficient PR thickness coverage in sample SC3 led to mask critical erosion at the edge of high-step features ( $>3\mu\text{m}$ ) such as bondpads or  $\mu\text{LEDs}$  (fig 4.8 g-h). Further, the mask was found to erode faster at edges and sloping points leading to potentially catastrophic degradation after  $>3\text{hrs}$  etching. As a result, the two-step technique of top face etching down to  $\sim 25\mu\text{m}$  depth followed by sample flipping and etching was implemented.

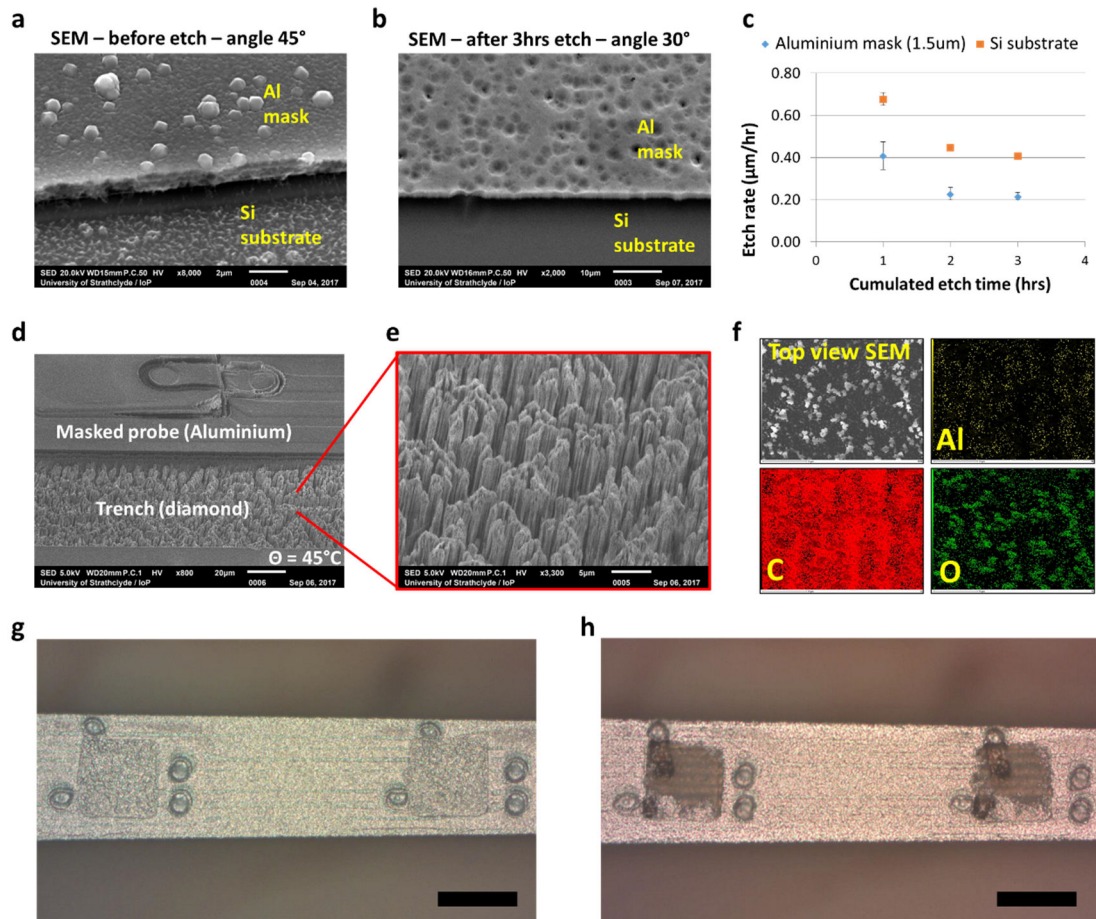


Figure 4.8 : Diamond oxygen etch (ICP#1 DIA\_ARO2) with an Aluminium hard mask. **a-c)** Al etch rate and erosion were studied on silicon test samples. **d,e)** On diamond samples, the etch produced heavy grassing within trenches, with vertical pillars up to  $>25\mu\text{m}$  length. **f)** SEM-EDX analysis of pillars with color-coded display of detected elements shows aluminium/oxide compounds location (green-coloured O, bottom right inset and yellow-coloured Al, top right inset) matches that of the top of the diamond pillars (seen in white in top view). Red-coloured carbon is detected everywhere. **g,h)** diamond sample SC3 after 2 hrs etch (**g**, mask stable) and 3hrs etch (**h**, mask failure and LED critical damage).

#### 4.5.2 Final fabricated device

The top panel of fig. 4.9 shows the polycrystalline and single-crystal (SC4) membranes at their final stage after through-diamond etch, and one released probe immediately after the final etch (a). After cleaning, the singulated probes are bonded onto a custom-designed PCB using a low viscosity adhesive (b). Devices were wirebonded by Yunzhou Cheng for later electrical, thermal, and optical characterisation (chapter 5).

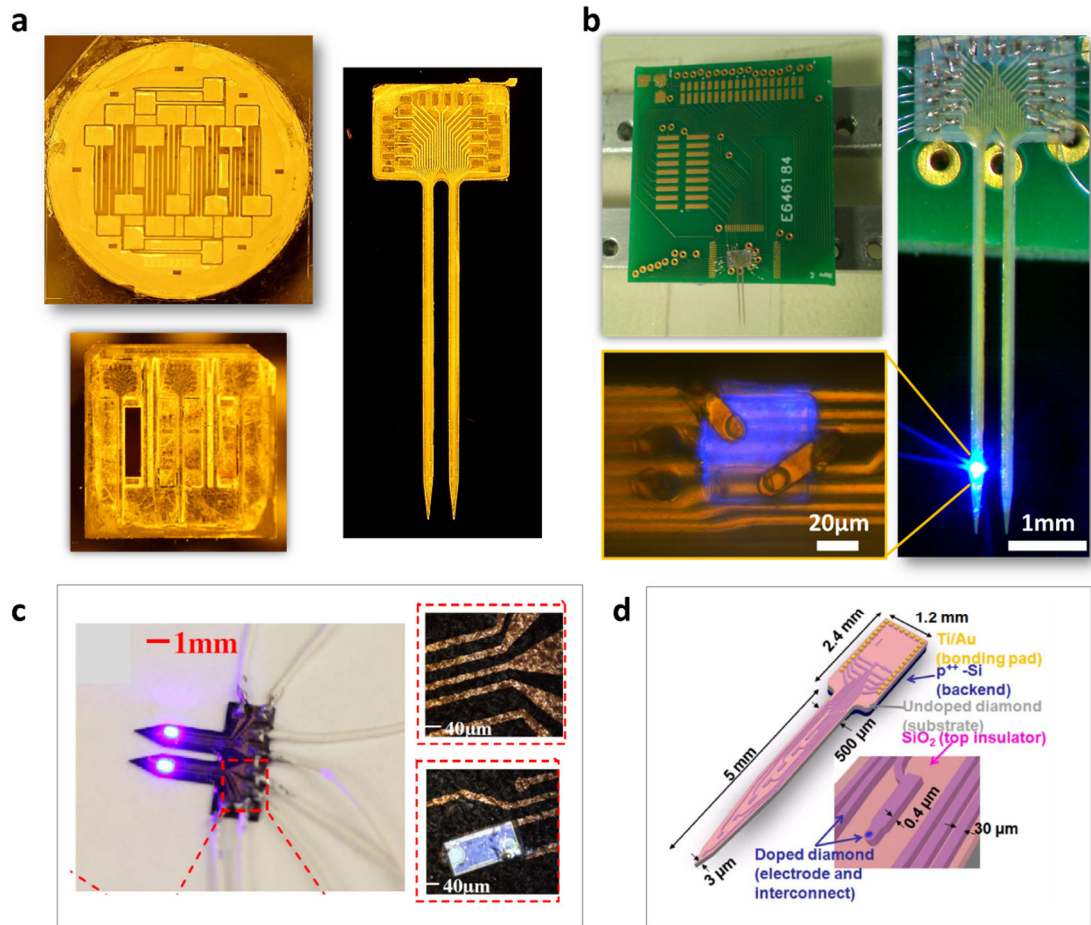


Figure 4.9 : Final fabricated devices (from sample SC4) and comparison to previous diamond probes. **a)** PC (top) and SC4 (bottom) samples during probe separation etches, and singulated probe as retrieved on wipe (right). **b)** Dual-shank diamond optrode wirebonded on PCB and close-up micrograph on lighted LED. **c,d)** Previous state of the art showed prohibitive footprints and limited versatility : **c)** polycrystalline diamond probe incorporating a soldered commercial  $\mu$ LED [32] and **d)** a recording-only flexible polycrystalline diamond probe for neuro-chemical analysis [33].

The optrode shown on fig 4.9.b incorporates 8  $\mu$ LEDs and 16 electrodes on 150 $\mu$ m-wide, 25 $\mu$ m-thick single-crystal diamond shanks. Both in implant dimensions and capability, this device represents a genuine step change from the few previously demonstrated diamond-based probes shown in the bottom panel of fig 4.9. Chan et al. were the first to manufacture a diamond-based probe for chemical and electrical recording [33], although with no light emission capability. The device was successfully demonstrated in vivo but still suffered from invasive dimensions (>500 $\mu$ m width). More recently, Fan et al. demonstrated the first ever PC diamond-based optrode [32], integrated with one commercial  $\mu$ LED and two microelectrodes on each shank. While a successful proof of concept, this optrode exhibited

very prohibitive footprints (>1mm width) and low irradiance threshold (<2mW/mm<sup>2</sup>) preventing its use in realistic optogenetic protocols. By contrast, the device presented in this work approaches dimensions of state-of-the art silicon-based monolithic optrodes [20], [21] while maintaining on-shank  $\mu$ LED and electrode densities which are relevant for e.g cortical layer-specific optogenetics, thus potentially enabling novel research protocols.

## 4.6 Conclusion

This chapter covered the specific requirements and design parameters of the diamond optrodes fabricated in this project, along with the serious challenges faced during process development in terms of handling ultrathin membranes, and performing photolithography and other processing steps. Sequential failures and improvements over four SC samples yielded a finalised manufacturing process given in full detail in section 4.4. The final step of probe singulation was covered and the optrodes obtained were shown to approach the dimensions and LED/electrode density of silicon-based devices, with an order of magnitude improvement over previous diamond-based efforts. Optrode electrical, thermal and optical performance will be assessed in the next chapter and compared to modelling insights.

## 4.7 References

- [1] M. R. Cohen and W. T. Newsome, “What electrical microstimulation has revealed about the neural basis of cognition,” *Curr. Opin. Neurobiol.*, vol. 14, no. 2, pp. 169–177, Apr. 2004.
- [2] W. PENFIELD and P. PEROT, “THE BRAIN’S RECORD OF AUDITORY AND VISUAL EXPERIENCE. A FINAL SUMMARY AND DISCUSSION.,” *Brain*, vol. 86, pp. 595–696, Dec. 1963.
- [3] C. D. Salzman, K. H. Britten, and W. T. Newsome, “Cortical microstimulation influences perceptual judgements of motion direction,” *Nature*, vol. 346, no. 6280, pp. 174–177, Jul. 1990.
- [4] E. R. Kandel, J. H. Schwartz, T. M. Jessell, S. A. Siegelbaum, and A. J. Hudspeth, *Principles of Neural Science, Fifth Edition*, vol. 3. 2014.
- [5] S. B. Wolff and B. P. Ölveczky, “The promise and perils of causal circuit manipulations,” *Curr. Opin. Neurobiol.*, vol. 49, pp. 84–94, Apr. 2018.
- [6] E. E. Steinberg, R. Keiflin, J. R. Boivin, I. B. Witten, K. Deisseroth, and P. H. Janak, “A causal link between prediction errors, dopamine neurons and learning,” *Nat. Neurosci.*, vol. 16, no. 7, pp. 966–973, Jul. 2013.
- [7] J. G. Bernstein and E. S. Boyden, “Optogenetic tools for analyzing the neural circuits of behavior,” *Trends Cogn. Sci.*, vol. 15, no. 12, pp. 592–600, Dec. 2011.
- [8] O. Yizhar, L. E. Fenno, T. J. Davidson, M. Mogri, and K. Deisseroth, “Optogenetics in Neural Systems,” *Neuron*, vol. 71, no. 1, pp. 9–34, 2011.
- [9] T. Il Kim, J. G. McCall, Y. H. Jung, X. Huang, E. R. Siuda, Y. Li, J. Song, Y. M. Song, H. A. Pao, R. H. Kim, C. Lu, S. D. Lee, I. S. Song, G. Shin, R. Al-Hasani, S. Kim, M. P. Tan, Y. Huang, F. G. Omenetto, J. A. Rogers, and M. R. Bruchas, “Injectable, cellular-scale optoelectronics with applications for wireless optogenetics,” *Science (80-. )*, vol. 340, no. 6129, pp. 211–216, 2013.
- [10] A. Boudet, R. Scharf, M. Dawson, and K. Mathieson, “A diamond-based, hybrid optrode for multisite optogenetics,” in *Frontiers in Optics 2016*, 2016, p. FTh4D.5.
- [11] R. S. Balmer, J. R. Brandon, S. L. Clewes, H. K. Dhillon, J. M. Dodson, I. Friel, P. N. Inglis, T. D. Madgwick, M. L. Markham, T. P. Mollart, N. Perkins, G. a Scarsbrook, D. J. Twitchen, a J. Whitehead, J. J. Wilman, and S. M. Woollard, “Chemical vapour deposition synthetic diamond: materials, technology and applications,” *J. Phys. Condens. Matter*, vol. 21, no. 36, p. 364221, 2009.
- [12] I. Friel, “Optical Quality Diamond Grown by Chemical Vapor Deposition,” *Opt. Eng. Diam.*, pp. 35–69, 2013.
- [13] M. Trejo, K. D. Chabak, B. Poling, R. Gilbert, A. Crespo, J. K. Gillespie, D. E. Walker, G. D. Via, G. H. Jessen, D. Francis, F. Faili, D. Babic, and F. Ejeckam, “Free-Standing Diamond and Silicon



- Substrates for Thermal Effects,” *IEEE Compd. Semicond. Integr. Circuit Symp.*, pp. 1–4, 2010.
- [14] M. Jorfi, J. L. Skousen, C. Weder, and J. R. Capadona, “Progress towards biocompatible intracortical microelectrodes for neural interfacing applications,” *J. Neural Eng.*, vol. 12, no. October, p. 011001, 2015.
- [15] D. R. Kania and D. R. Kania, “Biocompatibility of chemical-vapour- deposited diamond,” *Biomaterials*, vol. 16, no. 6, pp. 483–488, 1995.
- [16] J. Park, V. Quaiserová-Mocko, K. Pecková, J. J. Galligan, G. D. Fink, and G. M. Swain, “Fabrication, characterization, and application of a diamond microelectrode for electrochemical measurement of norepinephrine release from the sympathetic nervous system,” *Diam. Relat. Mater.*, vol. 15, no. 4–8, pp. 761–772, 2006.
- [17] “Diamond materials GmbH - products.” [Online]. Available: [http://www.diamond-materials.com/EN/products/disks\\_films\\_membranes/disks.htm](http://www.diamond-materials.com/EN/products/disks_films_membranes/disks.htm). [Accessed: 01-Sep-2018].
- [18] F. P. Bevilacqua, D. Pigué, P. Marquet, J. D. Gross, B. J. Tromberg, and C. D. Depeursinge, “<title>In-vivo local determination of tissue optical properties</title>,” 1998, pp. 262–268.
- [19] N. McAlinden, D. Massoubre, E. Richardson, E. Gu, S. Sakata, M. D. Dawson, and K. Mathieson, “Thermal and optical characterization of micro-LED probes for in vivo optogenetic neural stimulation,” *Opt. Lett.*, vol. 38, no. 6, pp. 992–4, 2013.
- [20] F. Wu, E. Stark, P. C. Ku, K. D. Wise, G. Buzsáki, and E. Yoon, “Monolithically Integrated  $\mu$ LEDs on Silicon Neural Probes for High-Resolution Optogenetic Studies in Behaving Animals,” *Neuron*, vol. 88, no. 6, pp. 1136–1148, 2015.
- [21] R. Scharf, T. Tsunematsu, N. McAlinden, M. D. Dawson, S. Sakata, and K. Mathieson, “Depth-specific optogenetic control in vivo with a scalable, high-density  $\mu$ LED neural probe - SUPPLEMENTARY,” *Sci. Rep.*, vol. 6, 2016.
- [22] Neuronexus, “Neural Probes,” 2018. [Online]. Available: <http://neuronexus.com/products/neural-probes/>. [Accessed: 01-Sep-2018].
- [23] G. Buzsáki, “Large-scale recording of neuronal ensembles,” *Nat. Neurosci.*, vol. 7, no. 5, pp. 446–451, 2004.
- [24] G. Buzsáki, E. Stark, A. Berényi, D. Khodagholy, D. R. Kipke, E. Yoon, and K. D. Wise, “Tools for probing local circuits: High-density silicon probes combined with optogenetics,” *Neuron*, vol. 86, no. 1, pp. 92–105, 2015.
- [25] C. Pang, “Parylene Technology for Neural Probes Applications,” vol. 2008, p. 191, 2008.
- [26] J. Ortigoza-Díaz, K. Scholten, C. Larson, A. Cobo, T. Hudson, J. Yoo, A. Baldwin, A. Weltman Hirschberg, and E. Meng, “Techniques and Considerations in the Microfabrication of Parylene C Microelectromechanical Systems,” *Micromachines*, vol. 9, no. 9, p. 422, 2018.
- [27] H. W. Choi, E. Gu, C. Liu, C. Griffin, J. M. Girkin, I. M. Watson, and M. D. Dawson, “Fabrication of natural diamond microlenses by plasma etching,” *J. Vac. Sci. Technol. B*, vol. 23, no. January, pp. 130–132, 2005.

- [28] C. L. Lee, H. W. Choi, E. Gu, M. D. Dawson, and H. Murphy, "Fabrication and characterization of diamond micro-optics," *Diam. Relat. Mater.*, vol. 15, no. 4–8, pp. 725–728, 2006.
- [29] C. L. Lee, E. Gu, M. D. Dawson, I. Friel, and G. A. Scarsbrook, "Etching and micro-optics fabrication in diamond using chlorine-based inductively-coupled plasma," *Diam. Relat. Mater.*, vol. 17, no. 7–10, pp. 1292–1296, 2008.
- [30] D. T. Tran, C. Fansler, T. A. Grotjohn, D. K. Reinhard, and J. Asmussen, "Investigation of mask selectivities and diamond etching using microwave plasma-assisted etching," *Diam. Relat. Mater.*, vol. 19, no. 7–9, pp. 778–782, 2010.
- [31] Y. Zhang, "Diamond and GaN Waveguides and Microstructures for Integrated Quantum Photonics," p. 138, 2012.
- [32] B. Fan, K. Kwon, R. Rechenberg, A. Khomenko, M. Haq, M. F. Becker, A. J. Weber, and W. Li, "A polycrystalline diamond-based, hybrid neural interfacing probe for optogenetics," *2015 28th IEEE Int. Conf. Micro Electro Mech. Syst.*, pp. 616–619, 2015.
- [33] H. Chan, D. M. Aslam, S. Member, J. A. Wiler, and B. Casey, "A Novel Diamond Microprobe for Neuro-Chemical and -Electrical Recording in Neural Prosthesis," vol. 18, no. 3, pp. 511–521, 2009.

# Chapter 5

## Diamond optrode modelling and characterisation

### 5.1 Introduction

The probes developed and fabricated as detailed in chapter 4 are hybrid devices, assembled by heterogeneous integration of custom-made GaN-based  $\mu$ LEDs onto unusual and novel substrates such as large area single-crystal diamond membranes. The performance of such devices may be harder to predict than that of their more common monolithic counterparts, and requires both full experimental characterisation and extensive modelling to understand and predict device behaviour under a range of operation protocols.

The electro-optical and thermal properties of the devices were extensively modelled, both during the design phase, to inform prototype development and after fabrication of the devices. The model was checked against experimental measurements and, once validated, run to derive predictions of the behaviour of such probes *in vivo*.

**Section 5.2** introduces the modelling of light propagation and radiative heating in tissue by Monte-Carlo methods, as well as the FEM modelling of device heating using COMSOL.

**Section 5.3** covers the electro-optical and thermal characterisation of the probe, and the validation of the FEM thermal model against experimental data. The diamond optrode is able to output high optical power densities ( $>250$  mW/mm<sup>2</sup> per  $\mu$ LED), with each lambertian emitter potentially stimulating a large (up to  $\sim$ mm<sup>3</sup>) volume of brain tissue, and shows ms-timescale heat dissipation along its shank, thermally outperforming comparable silicon-based devices by an order of magnitude.

**Section 5.4** details model predictions of optrode-induced tissue heating *in vivo*, extracts the bounds for “safe” operation even at various stimulation powers, and contrasts expected *in vivo* diamond optrode performance with that of comparable silicon-based devices. The diamond optrode is expected to uniquely allow new ranges of protocol with high-power / extended pulse widths while keeping heat tissue buildup below the 0.5°C threshold.

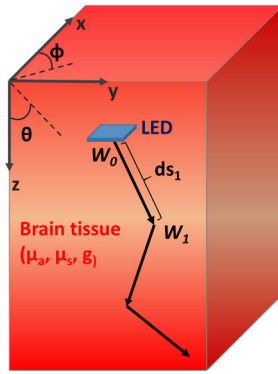
## 5.2 Modelling tools for optical and thermal analysis

### 5.2.1 Simulation of light propagation *in vivo*

In optogenetics, the range, spread and resolution of tissue excitation is determined by the spatial distribution of irradiance. This can be predicted by simulation and depends on both source and propagation medium properties.  $\mu$ LED sources are known to behave as Lambertian emitters, with roughly 50% topward and 50% downward emission [1], [2] and with the initial radiation profile modified by the transparent, high-index diamond substrate and device patterned layers. Mammalian brain tissue is a highly scattering medium, and light propagation is typically studied by diffusion theory [3], [4] or more versatile Monte Carlo simulations [5]–[7].

To help initial design and to contrast final device measurements, Monte Carlo simulations have been conducted to analyse the expected light propagation in brain tissue. The model was based on a simple algorithm invented by Jacques et al. [8], expanded to account for Fresnel refraction and reflection at interfaces with the transparent substrate. Figure 5.1 shows the working principle of the model, which was coded in C++ and Matlab. Briefly, photon “packets” are propagated in a 3-dimensional isotropic media and lose energy in voxels according to Beer’s law (absorption coefficient  $\mu_a$ ), exhibit a mean-free path distribution governed by the medium’s scattering coefficient  $\mu_s$ , and experience anisotropic scattering ( $g$ ) as defined by the Henyey-Greenstein distribution [9], [10]. At the boundary between two layers, the probability that photons incident with an angle  $\theta_i$  will be reflected is determined by the Fresnel reflection coefficient  $R$  calculated for unpolarised light, with outgoing angle  $\theta_t$  determined by the refractive indices of the incident and transmission layer:

$$R(\theta_i) = \frac{1}{2} \left\{ \frac{\sin^2(\theta_i - \theta_t)}{\sin^2(\theta_i + \theta_t)} + \frac{\tan^2(\theta_i - \theta_t)}{\tan^2(\theta_i + \theta_t)} \right\} \quad \text{Reflection if } R > \text{rand}([0;1]) \quad (5.1)$$

**a) Simulation of photon random walk in a layer**

 $\mu_a$  : Energy deposited in tissue through absorption (Beer-Lambert)

$$\frac{dW_i}{W_i} = \frac{W_{i+1} - W_i}{W_i} = 1 - e^{-\mu_a * ds_i}$$

 $\mu_s$  : Scattering determines step length in a given medium

$$ds_i = \frac{-\ln(\text{rand}_i([0;1]))}{\mu_s}$$

 $g$  : Scattering polar angle  $\theta$  sampled from Henyey-Greenstein function (anisotropic)

$$\cos \theta_i |_{g \neq 0} = \frac{1}{2g} * \left\{ 1 + g^2 - \left[ \frac{1 - g^2}{1 - g + 2g * \text{rand}_i([0;1])} \right]^2 \right\}$$

$$\varphi_j = 2\pi * \text{rand}_j([0;1])$$

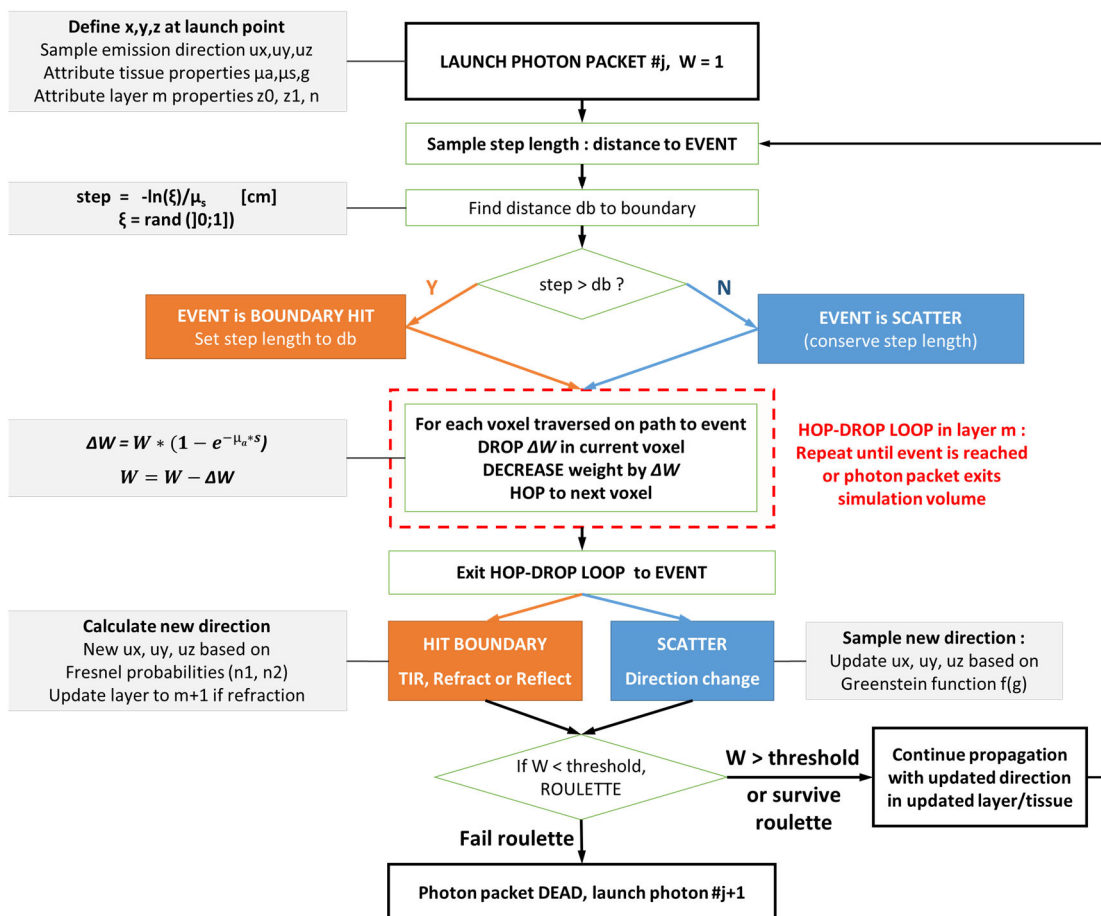
**b) Monte Carlo algorithm**


Figure 5.1 : Monte-Carlo modelling of light propagation in tissue. **a)** Photons “packets” undergo a probabilistic random walk in media defined by their absorption and scattering coefficient  $\mu_a$  and  $\mu_s$ , and their scattering anisotropy  $g$ . **b)** Algorithm used in this work, based on work by Jacques et al [8].

Tissue optical properties are notoriously difficult to measure *in vivo*. Reported values for absorption coefficients can vary by a factor of 5 for mammalian cortical grey matter, and  $\mu_a/\mu_s$  vary widely across tissue types depending notably on lipid concentration [6], [7], [11]–[15]. Optical absorption typically occurs over mm ranges, with half-value thicknesses reported between 0.65mm and 12mm. Scattering is the dominant process with a much lower scattering mean-free path on the order of 10 $\mu$ m–50 $\mu$ m for grey matter. Even though it is characterised by a well-defined “forward” anisotropy (literature values report  $g \sim 0.88 \pm 0.03$ ), scattering strongly affects the irradiance profile of cone-shaped emitting devices, such as optical fibres or waveguides, due to the high event probability. As such, the very high scattering coefficients recently reported by Yona et al. [13] in mouse cortical tissue may lead to a re-evaluation of the optical range and resolution of these devices *in vivo*.

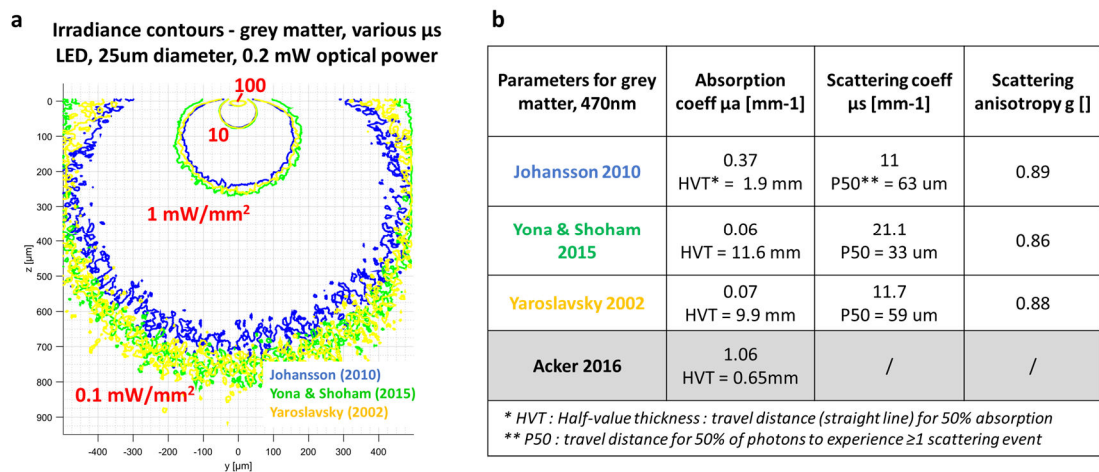


Figure 5.2 : MC model is robust against medium uncertainty. a) Irradiance contours simulated in mouse brain tissue (LED at  $[y,z] = [0,0]$ ) for different scattering parameters reported in the literature and listed in panel b). The large variations in  $\mu_s$  and  $\mu_a$  have limited effects on Lambertian emitters. Tissue parameters taken from [12]–[15].

In the case of  $\mu$ LED Lambertian emitters, however, the Monte Carlo model predicts that both range and resolution remain broadly constant (within a sub-mm<sup>3</sup> volume) over the spread of reported  $\mu_a$ ,  $\mu_s$  and  $g$  (fig 5.2). This is because the forward scattering does not significantly modify the already diffuse emission profile. Furthermore, lateral optical spreadout can be limited at constant depth penetration for high-resolution stimulation by decreasing  $\mu$ LED size, with interference-free LED array stimulation possible when LED diameter is below half the array pitch [16].

As an example, the model was run with parameters corresponding to the devices produced in this work, i.e 50 $\mu\text{m}$ -diameter  $\mu\text{LED}$  emitting 0.2mW of optical power in mouse cortical grey matter (fig. 5.2). The models predicts irradiance levels exceeding 1mW/mm<sup>2</sup> (ChR2 photoactivation threshold) up to  $\sim 260\mu\text{m}$  downward from the LED, with a maximum lateral spread of +/-  $\sim 115\mu\text{m}$  (fig 5.2.a). Very similar profiles and spread values were obtained irrespective of the various scattering or absorption coefficients used (fig 5.2.b), allowing us to confidently use this simple Monte-Carlo model to simulate actual protocol conditions.

### 5.2.2 FEM simulation of device and tissue heating

A potential major limitation of implantable  $\mu\text{LED}$ -based probes is the relatively low external quantum efficiency of some GaN-based LEDs (typically 0.5%-5%), meaning that a considerable proportion of electrical input power is converted to Joule heating, at a risk of damaging or affecting the tissue surrounding the probe. It is a real possibility that probe-induced heat directly influence cell activity, introducing a confounding factor within an optogenetic protocol. The associated temperature change threshold is a matter of debate, but is often estimated at 0.5°C or 1°C, although this may vary between tissue and brain regions, chronic vs acute implantation, and whether the temperature change considered is peak or average. Therefore, it is paramount that thermal properties of such devices be well analysed and (conservatively) predicted through appropriate modelling.

Variable	Parameter	Value	Units
$\rho$	Density (brain)	1040	kg.m <sup>-3</sup>
$C$	Heat capacity (brain)	3650	J.kg <sup>-1</sup> .K <sup>-1</sup>
$k$	Thermal diffusivity (brain)	0.527	W.m <sup>-1</sup> .K <sup>-1</sup>
$\rho_b$	Density (blood)	1060	kg.m <sup>-3</sup>
$c_b$	Heat capacity (blood)	3600	J.kg <sup>-1</sup> .K <sup>-1</sup>
$w_b$	Blood perfusion rate	$8.5 \times 10^{-3}$	s <sup>-1</sup>
$q_m$	Metabolic heat production (brain)	$9.7 \times 10^{-3}$	mW.mm <sup>-3</sup>
$T_A$	Core body temperature (arterial)	34.5	°C
$T_0$	Initial brain temperature	34	°C

Table 5.1 : Parameters used in FEM simulation of the Pennes bio-heat transfer equation.

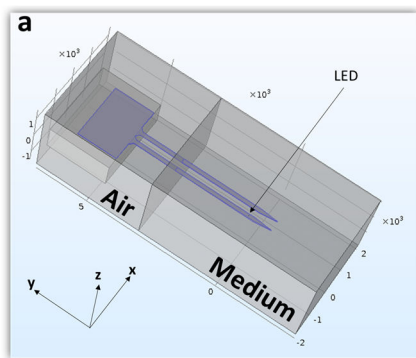
Following the practice of previous work [16]–[20], a finite element simulation implementing the Pennes bio-heat model was developed using COMSOL Multiphysics to analyse heat transfer due to conduction and convection between the probe, the LED and the surrounding media. COMSOL uses the finite element method (FEM) to numerically solve partial

differential equations at a discrete number of points subdividing the simulation volume into a user-defined mesh. The model solved the Pennes bio-heat transfer equation [21] for the temperature  $T$  in °C over the whole simulation volume :

$$\rho C \frac{\partial T}{\partial t} = \nabla k \nabla T + \rho_b c_b w_b (T_A - T) + q_m + Q_{LED} \quad (5.3)$$

where  $\mu\text{LED}$  Joule heating contribution is modeled as the heat source  $Q_{LED}$  [ $\text{W}\cdot\text{m}^{-3}$ ] applied to the LED volume, and all other parameters are given in table 5.1.

The model geometry is shown in fig. 5.3.a. Materials are attributed to the different geometric elements and defined by their density, thermal conductivity and heat capacity as listed in fig. 5.3.b. Briefly, the optrode is modelled whole and to scale, made of pure diamond material (poly- or monocrystalline), with its base attached to a volume of epoxy material representing the PCB. The patterned layer geometry (esp. metal traces) are not modelled as these greatly increase computational requirements and similar models have previously shown such thin traces have negligible effect on heat transfer [16]. The optrode base and the top sections of the shanks are surrounded by a cuboid of air, while the bottom 4mm of the shanks is surrounded by a cuboid of either air or brain tissue.  $\mu\text{LED}$ s are represented to scale at their various positions on the shank tip and the probe are covered by a  $5\mu\text{m}$  layer of parylene-C.



**b**

Parameters for COMSOL model	Density $\rho$ [ $\text{kg}/\text{m}^3$ ]	Thermal conductivity $k$ [ $\text{W}/\text{m}\cdot\text{K}$ ]	Heat capacity $C$ [ $\text{J}/\text{kg}\cdot\text{K}$ ]
Silicon*	2329	130	700
Diamond**	3530	1500 (PC) 2200 (SC)	520
Parylene C	1289	0.084	712
Medium : Brain tissue (Elwassif et al.)	1040	0.527	3650
Medium : Air*	Temperature-dependent		

\* From COMSOL material library  
\*\* Taken from NIST database and sample suppliers.

Figure 5.3 : Finite element model (FEM) of heat transfer between probe and tissue using COMSOL. **a**) Generic model geometry: a single- or two-shank parylene-coated probe, with base stuck on a plastic holder in a volume of air (left volume), is inserted 4mm deep into brain tissue (right volume).  $\mu\text{LED}$ s are modelled as square heat sources at their real positions on shank tips. The model is solved in 3 dimensions with results extracted either as specific volume averages or cutplanes ( $yz$ ) or ( $xz$ ) containing the LED heat source. **b**) Material parameters used in the heat transfer equation. Values for parylene C and brain tissue taken from [22] and [17] respectively.

The  $\mu\text{LED}$ s were defined as volume Joule heat sources. To accurately represent the devices, a  $800\text{nm}$  layer of  $\text{SiO}_2$  material was interposed between the  $\mu\text{LED}$ s and the underlying substrate. LEDs were assumed to be perfectly inefficient (worst-case scenario : all input



electrical power converted to heat), with the simulated electrical power directly taken from a typical IV curve ( $P = V \times I$ ). Simulation volume boundaries were modelled as open to heat flow. Both steady-state and time-dependent model studies were carried out with  $\mu$ LEDs in pulsed operation, for varying electrical powers, pulse frequencies and pulse widths.

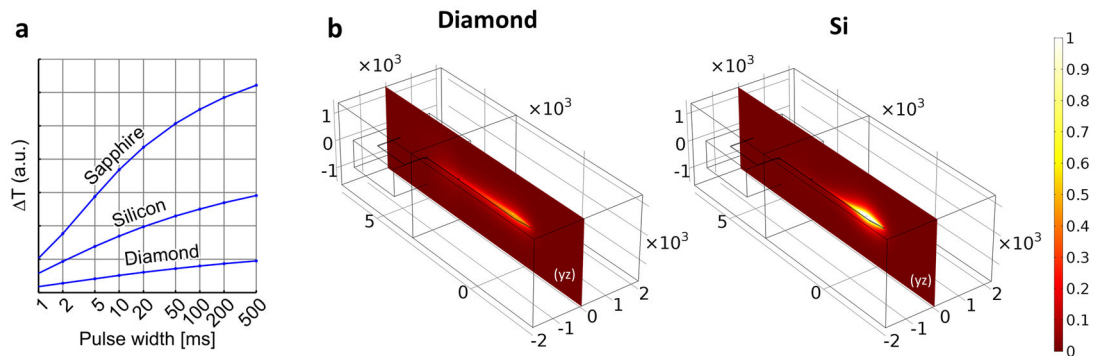


Figure 5.4 : Initial parametric studies highlight the benefits of diamond's superior thermal properties. The model is run for different probe materials, keeping all other parameters constant. **a)** Comparison of simulated peak temperature at LED surface (arbitrary units) during a single pulse at 20mW electrical power, for probes made of sapphire, silicon and diamond (from [23]). **b)** Comparison of simulated tissue heat profiles (yz plane) caused by LED pulsed at 15mW electrical power and 30% duty cycle (50ms pulses), for a silicon probe (right) and a diamond probe (left), adapted from [24].

Initial model runs suggested that a diamond-based optrode would exhibit markedly superior heat-sinking properties compared to similar probes made of GaN-compatible growing substrates such as sapphire or silicon (fig 5.4). The very high thermal conductivity of the diamond substrate is predicted to drive fast heat extraction along the probe shank, largely limiting heat buildup in tissue around the LED compared to a silicon device (fig 5.4.b).

These early semi-quantitative predictions informed probe design and development. The model was more extensively used after final devices were fabricated, in order to correlate and check model predictions against direct thermal measurements in air, and produce detailed predictions of the probes thermal behaviour in brain tissue. This detailed analysis is presented in section 5.3.1.

### 5.2.3 Contribution of radiative heating to tissue temperature increase

Until recently, radiative heating from light emitted in brain tissue has been understudied, and generally assumed to be negligible compared to conductive and convective heating in the case of embedded heat sources such as LEDs [25]. However Stujenske et al. demonstrated that high-intensity light delivered through optical fibres could lead to significant tissue heating and elevate local cell firing rates, irrespective of opsin expression

[26]. As an example, 532nm light emitted with an optical power of 5mW (irradiance 40mW.mm<sup>-2</sup> across a 200µm optic fibre) was experimentally found to cause a >1°C peak change in tissue temperature, possibly up to mm-depth levels below the fibre tip [26, Fig. 3E & suppl.]. Even higher temperature changes were predicted for blue (470nm) light due to its higher absorption by tissue hemoglobin.

The 50-µm diameter µLEDs used in this work are capable of high optical power densities (up to ~300 mW/mm<sup>2</sup>, section 3.4.4), warranting assessment of these effects for our design. Stujenske’s Matlab numerical model for heat diffusion in tissue, experimentally validated and made available in [26], was adapted to a LED Lambertian emitter and run with high reported absorption coefficients [15] to predict the “worst-case” radiative heating from the diamond optrode. Briefly, the optical power density distribution from a µLED emitting in brain tissue was first simulated using the Monte-Carlo algorithm presented in section 5.2.1. That distribution was then used as a heat source for the above mentioned Pennes equation modified to incorporate incident light :

$$\rho C \frac{\partial T}{\partial t} = \nabla k \nabla T + \rho_b c_b w_b (T_A - T) + q_m + \boldsymbol{\varphi} \boldsymbol{\mu}_a \quad (5.3)$$

where  $\boldsymbol{\varphi}(x,y,z)$  is the fluence rate and  $\boldsymbol{\mu}_a$  the tissue coefficient of absorption. To isolate the effect of radiative heating only, LED Joule heating was not considered (blood perfusion and metabolic heat production were taken into account as in the COMSOL model). The model was solved numerically to yield 3D time-varying tissue heat maps (fig 5.5.a).

Representative results of that simulation are shown in fig. 5.5. At an optical power of 0.3mW, corresponding to LED current of ~2mA and irradiance ~200mW.mm<sup>-2</sup>, highly absorbing tissue closest to the µLED is predicted to experience temperature peak changes of up to ~0.2°C. Tissue within a 100µm radius from µLED would experience >0.1°C change in CW mode. The temperature profile dynamics are dominated by passive heat conduction away from the LED [26], with a steady-state gradient established within a timescale of a few seconds. These “slow” heat diffusion dynamics contrast with ms-timescale modulation of LED radiation considered as an instantaneous, spatially spread heat source, and explain why peak temperatures reached during pulsed operation are close to those reached during CW mode (fig 5.5.b). Average light-induced temperature changes, however, are predicted to drop linearly with duty cycle.

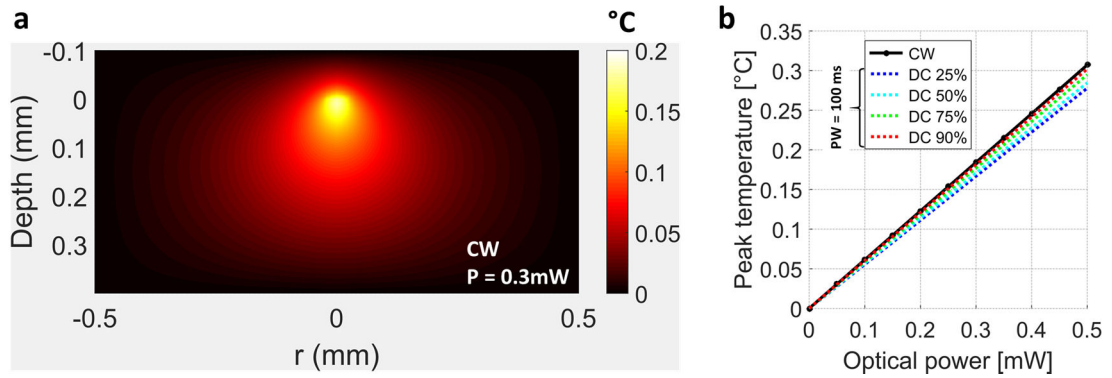


Figure 5.5 : Magnitude of tissue radiative heating by a 50 $\mu$ m-diameter  $\mu$ LED emitter at  $\lambda = 470$ nm. Model adapted from Stujenske et al. [26], and run with high reported absorption coefficient for cortical tissue ( $\mu_a = 1.06 \text{ mm}^{-1}$  [15]) as a “worst-case scenario”. **a)** Steady state heat map of tissue temperature change due to LED radiation during CW operation at 0.3mW optical power. LED is placed at  $(x,y) = (0,0)$  and steady state is conservatively taken at 60s of CW operation. The 0.1 $^{\circ}\text{C}$  isotherm range reaches  $\sim 95\%$  of that of steady state after  $\sim 5$ s operation. **b)** Simulated tissue peak temperature increase caused by radiative heating depending on  $\mu$ LED optical power, after 10s operation in CW (black line) or pulsed mode at various duty cycles (PW = 100ms, dotted lines). In CW operation, only  $\sim 0.6$ s operation are needed for the “hottest” regions close to the  $\mu$ LED to reach  $>95\%$  of their peak temperature. By contrast, the average temperature drops linearly with duty cycle [26].

These model predictions for  $\mu$ LEDs tend to complete those made for optical fibres by Stujenske et al. Peak temperature change coefficients in both cases can reach 0.6 $^{\circ}\text{C}/\text{mW}$  for a 50 $\mu$ m radius emitter at 470nm (fig 5.5.b for LED; simulation not shown for fibre case). Importantly however, the more diffuse emission profile of  $\mu$ LEDs (see 5.2.1) limits the concentration of “hot spots” to within  $\sim 1$  radius of the emitter, with a  $>$  twofold decrease in temperature at 100 $\mu$ m distance from the LED (fig 5.5.a). By contrast, the typical conical fibre emission profiles studied by Stujenske et al. yield cylindrical volumes of heated tissue with  $\sim$ mm decay lengths, with the concentrated heat only slowly spreading out by conduction. As such, the  $\mu$ LEDs Lambertian emission profile is highly beneficial in spreading the radiative heat load and allows “safe” operation of LED emitters at higher optical powers than similar fibre-based systems.

As a conclusion, radiative heating from the  $\mu$ LEDs used in this work is expected to contribute to increased tissue temperatures on an order of  $\sim 0.1^{\circ}\text{C} \pm 0.05^{\circ}\text{C}$  during optrode operation at relatively high power densities (100-200  $\text{mW}/\text{mm}^2$ ). This is still typically an order of magnitude less than Joule-heating induced temperature changes (see section 5.3.2), but might still bear significance in certain contexts. The small emitter size (compared to optical fibres) concentrates high irradiance levels close to the LED, which can sustain light-induced

temperature changes close to peak values e.g within a 50 $\mu$ m radius. Furthermore, the model might underestimate blue light-induced effect on tissue regions rich in hemoglobin (large absorption peak between 400 and 450 nm [27]). More generally, as  $\mu$ LEDs become more efficient, radiative heating effects will need to be routinely considered for sustained, high-intensity optogenetic stimulations *in vivo*.

## 5.3 Device characterisation

Precise assessment of the diamond optrode electrical, optical and thermal performance is essential for prototype validation, comparison with existing state-of-the-art and later use *in vivo*. A singulated double shank optrode (n°1E) from sample S4 was fully characterised after bonding to a PCB (all devices were previously characterised on-chip before probe separation). Thermal simulations were directly checked against measurements in air and used for detailed predictive modelling of probe operation in cortical tissue.

### 5.3.1 Electro-optical characterisation and expected output in tissue

- o *IV, LI and spectral characteristics*

On both shanks of the S4-1E device,  $\mu$ LEDs L1 and R1 (bottom-most on each shank) did not turn on, an issue directly attributable to parylene delamination at probe tip (see section 6.2.3).  $\mu$ LEDs (LR) 2, 3 and 4 turned on and were characterised. Micrographs of the  $\mu$ LEDs at low-voltage operation showed a uniform and homogeneous emission profile indicative of a good quality, undamaged current spreading layer, while low-footprint side bridge contacts were not significantly blocking upward light emission (fig 5.6.a).

For each LED, I-V and L-I curves were taken using a Yokogawa GS610, micro-manipulated probes contacting bondpads on the PCB, and a Thorlabs PM100A/S120C powermeter (Si photodiode, 9.7mm diameter) mounted at a distance of  $\sim$ 8mm above and parallel to the  $\mu$ LED. The limited solid angle subtended by the detector cannot cover all the light emitted by the Lambertian emitter and a correction factor of  $\sim$  3.62 had to be applied to the measured values of optical power (see annex A8 for additional values and details). This approximation was applied in previous work on comparable  $\mu$ LEDs emitters and found to agree within +/- 10% of accurate values measured with an integrating sphere [16].

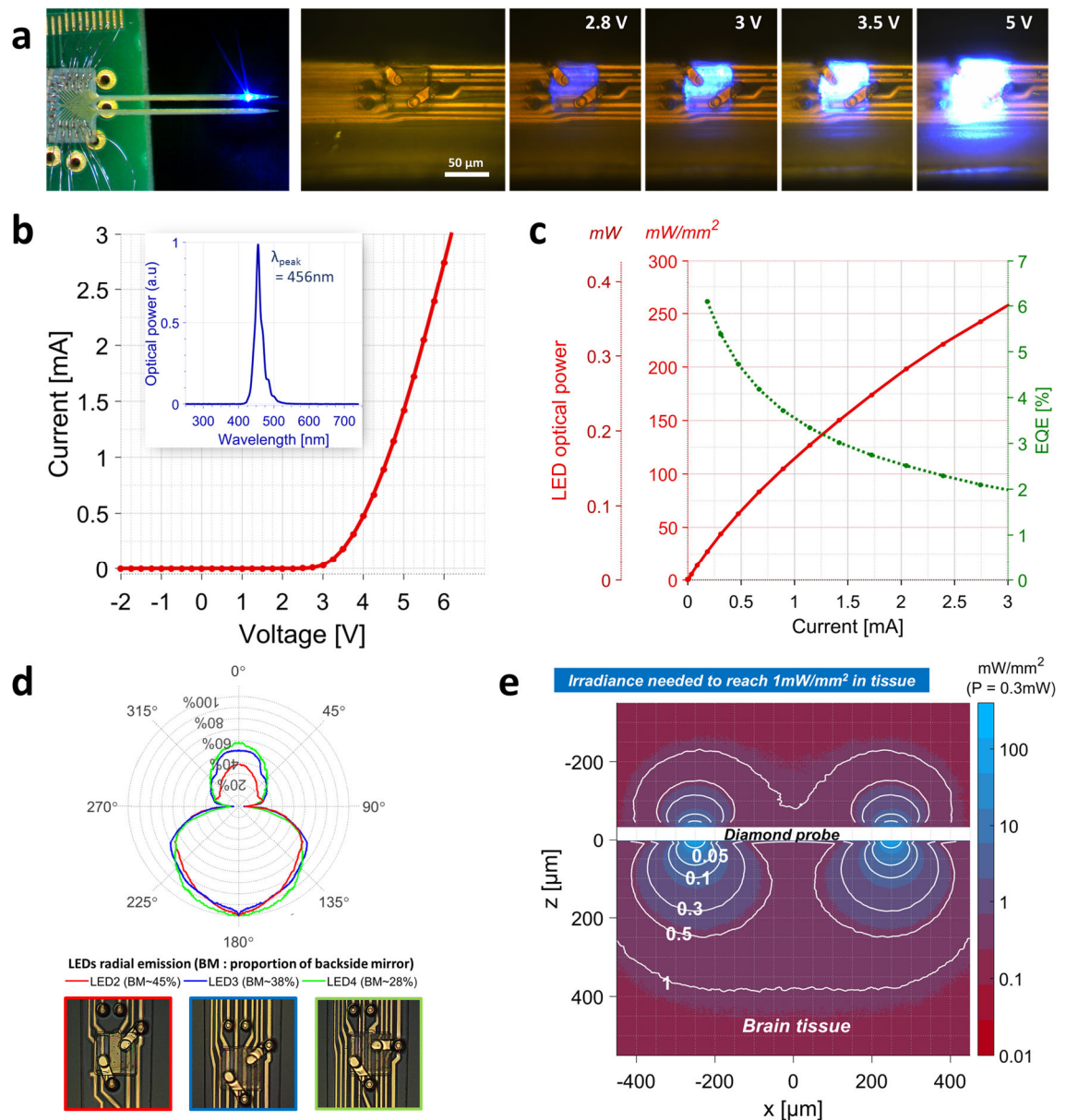


Figure 5.6 : Electrical and optical characterisation of a diamond probe (sample SC4, double-shank device). 6  $\mu$ LEDs out of 8 were functional due to parylene delamination at shank tip (see section 6.2.3). **a**) Full probe view with LED L4 lit (left) and micrographs of LED L3 operated at different voltages, showing uniform illumination across the current spreading layer (turn-on voltage  $\sim 3.6$ V). **b**) Representative  $\mu$ LED I-V curve (red) and spectral emission curve (inset), with an emission peak at 456nm. **c**) Representative  $\mu$ LED L-I curve (red) and external quantum efficiency (EQE, “plug efficiency”) curve (green). At 120mW.mm<sup>-2</sup> irradiance, EQE remains above 3.5%. **d**) Measured 360° radiation profile of downward-facing  $\mu$ LEDs in air (vertical plane intersecting LED), for  $\mu$ LEDs at different positions on shank, from second-bottom-most (LED L2, red curve) to topmost (LED L4, green curve). Through-probe emission decreases as the fill factor of reflective metal under  $\mu$ LEDs increases. **e**) Monte Carlo simulation of light propagation in cortical tissue, for 2 downward-facing  $\mu$ LEDs (500 $\mu$ m pitch) operated simultaneously with a radiation profile corresponding to  $\mu$ LED L3. Colour heatmap shows the irradiance profile obtained for an optical power of 0.3mW for each  $\mu$ LED. White contour lines reflect the reach of 1mW.mm<sup>-2</sup> irradiance for different optical powers, from 0.05mW to 1mW.

A previously developed LabVIEW program was used to simultaneously drive the LEDs and record IV and optical power values, typically with voltage (current) sweeps of -3V to +8V (0mA to 4mA) and a maximum current compliance set at 4mA. Representative I-V and L-I curves for  $\mu$ LEDs of singulated diamond optrode S4-1E are given in fig. 5.6.b and 5.6.c. The devices reach external quantum efficiencies (EQE) of up to 3% at  $\sim 160 \text{ mW}\cdot\text{mm}^{-2}$  irradiance (only light emitted upward is considered). The typical  $\mu$ LED emission spectrum is further given in fig. 5.6.b (inset, measurement with AvaSpec EVO spectrometer). The peak wavelength was measured at 456nm with a full-width at half maximum (FWHM) of  $\sim 30\text{nm}$ .

o *Radiative emission profile and simulated light output in tissue*

Because the diamond probe is a low-absorption medium with high-refractive index, it is expected to affect, but not totally suppress, “through-probe” light emission and as such characterising the radial emission profile of the probe is important. While photons are initially emitted from the device in roughly similar downwards and upwards Lambertian distributions, “mediumward”-emitted light can propagate in air or tissue unimpeded while “probeward”-emitted light will be partially reflected by the patterns of metal traces underlying the LED, and partially trapped into the diamond probe shank through total internal reflection (TIR). Monte-Carlo simulations estimate that TIR alone can reduce through-probe optical output by  $\sim 55\%$ .

The  $\mu$ LEDs radial emission profile was measured by fixing the powermeter (diaphragm-limited to  $\sim 1.5\text{mm}$  for higher angular resolution) on a rotation mount with the  $\mu$ LED (probe axis) as centre of rotation; the relative angular optical power emitted by a given  $\mu$ LED driven at a constant 2mA current was recorded for the full  $360^\circ$  range within the intersecting plane perpendicular to the probe. The averaged radial profiles are presented in fig. 5.6.d for LED L2 (second from shank bottom), LED L3 (third from bottom) and L4 (topmost). The backside mirror effect of reflective metal traces is apparent. LED L4 was printed on a pattern of very thin ( $\sim 2\mu\text{m}$ ) traces, which act as a backside mirror with a relatively low “fill factor” of  $\sim 28\%$  of the  $\mu$ LED area, leading to a probeward/mediumward emission ratio (PMER) of  $\sim 0.6$ . This value is close to, but higher than, that expected from Monte-Carlo modelling, which might be due e.g to the unmodelled contribution from mediumward obstructing bridge contacts. LED L2, with a higher specially patterned backside mirror of  $\sim 45\%$ , exhibits a PMER of  $\sim 0.4$ . These distributions can be approximated as a double Lambertian of different amplitudes. This asymmetric radiation profile was fed into the Monte-Carlo simulation presented in fig 5.6.e, where the light emitted from two  $\mu$ LEDs is propagated in brain tissue in both directions.

At an easily attainable optical power of 0.3mW, each LED can illuminate tissue with  $> 1\text{mW}\cdot\text{mm}^{-2}$  irradiance up to a radial distance of  $\sim 180\mu\text{m}$ . Variations of that reach for different optical powers are given by the white contour lines.

### 5.3.2 Thermal characterisation, simulation accuracy and predictions in tissue

It is well known that the peak temperatures increases reached by GaN-based  $\mu\text{LEDs}$  operated in air at  $>10\text{ mW}$  electrical power, with current densities above  $100\text{ A}\cdot\text{cm}^{-2}$ , can easily exceed  $50^\circ\text{C}$  in the active region even when considering “optimised” devices on thermally efficient substrates [28]. However, it is important to note that such high-irradiance  $\mu\text{LED}$  operation does not necessarily translate into harmful optogenetic protocols as corresponding heating levels of tissue surrounding LED-based implants are typically orders of magnitude lower [16], [19], [24], [29], [30]. This is rendered possible through 3 major reasons : *a)* the very high heat capacity of brain tissue (fig. 5.3.b; as an example, the volumetric heat capacity of brain tissue,  $V_{\text{hc}(\text{tissue})} \sim 3.65\text{ MJ}/\text{m}^3\cdot\text{K}$  is roughly 5000 times that of the air at 300K), *b)* the usual limitation of heating to local hotspots (the extent of these being dependent on intrinsic substrate thermal conductivity) and *c)* optimised implant designs including thermally insulating barriers and probe geometries limiting heat buildup. As a result, GaN-on-silicon  $\mu\text{LED}$  monolithic probes have been shown to operate well within  $1^\circ\text{C}$  tissue temperature increases thresholds, with a typical  $>$  ten-fold decrease between LED temperature measured in air and predicted tissue temperature change [16].

#### o *Infrared imaging and measurement calibration*

An FLIR SC7000 infrared (IR) camera was used to measure device heating during operation. In order to understand the thermal properties of the optrode and to compare them with model predictions, the temperature of the whole probe was monitored, including  $\mu\text{LEDs}$ , shanks and base. The video frame size was limiting by windowing to the probe area only, allowing imaging frame rates of 100Hz to 500Hz for a pixel size of  $\sim 20\mu\text{m}$ .

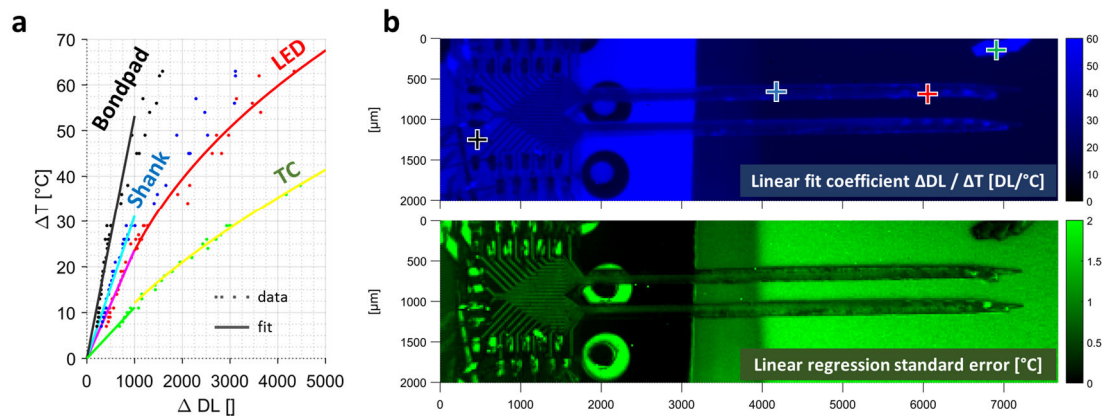


Figure 5.7 : Calibration of FLIRSC7000 IR measurements. **a)** Calibration curves for 4 pixels located in various probe regions, shown by cursors on top map of panel b. Emissivity varies across probe regions due to patterned layers of different materials and surface characteristics. As such a custom calibration curve, comprising a linear and non-linear part, must be determined for each image pixel (temperature change  $\Delta T$  vs sensor digital counts DL). These measurements are repeated 5 times and averaged for calibration fit. **b)** Calibration maps of the probe (and underlying PCB) showing distribution of  $\Delta DL/\Delta T$  coefficients (top) and standard error of the fit for the linear part of the calibration curves of pixels.

Specific calibration procedures were required as the multi-material, textured probe had no defined emissivity and the camera IR sensor exhibited nonlinear response for high counts values. Calibration curves relating temperature to IR detector counts (“digital levels”, DL) were determined for each pixel of the image. This was done by using a type E thermocouple (TC) placed within  $\sim 150\mu\text{m}$  of the probe. The probe and thermocouple were heated to a number of given temperatures by a heat gun and the IR image was recorded when the temperature stabilised for a given value. The process was repeated five times for a given thermocouple positions, and over 5 different thermocouple positions and 2 heat gun positions to average out discrepancies between TC and probe arising from e.g convection within the air volume considered. A two-part fit was applied to the data for each pixel (linear fit to 1000  $\Delta DL$ ; power fit from 1000 to 5000  $\Delta DL$ ) as shown on fig. 5.8.a for one measurement. Matlab programs were developed to carry out this analysis (and subsequent thermal measurement conversions and plots) automatically. Calibration uncertainty on the linear fits were assessed and, for temperature increases lower than  $20^\circ\text{C}$ , were found to average  $\sim 1^\circ\text{C}$  or less on the large majority of pixels considered (fig. 5.8.b).

- o *Measurement vs simulation of the  $\mu\text{LED}$  hotspot in air*

The thermal camera and calibration curves can then be used to record the  $\mu\text{LED}$  and probe temperature in air, under a variety of operating conditions. As explained above,  $\mu\text{LED}$



operation in air yields relatively large local temperature increases, which can be helpfully used to assess the numerical model's robustness.

Figure 5.9.a,b directly compares measured  $\mu$ LED temperature in air (red dots, maximum value of the LED 4 pixels) to simulation results (green curve). The  $\mu$ LED temperature increase is found to remain below  $90^{\circ}\text{C}$  for all currents below 3mA (5.6.a), in good agreement with the model predictions up to  $T \sim 75^{\circ}\text{C}$  (start of detector high nonlinearity). Importantly, the model adequately predicted pulsed operation behaviour (5.6.b), even if temperature falloff times were slightly overestimated. The predicted temperature increase of a  $\mu$ LED on a Silicon device (5.9.c) is about twice that of the diamond optrode, with a much longer cooloff time ( $\tau_{1/e} \sim 20\text{ms}$ ) in the same range as that measured experimentally in previous work on Silicon probes ([16], [19], [31]).

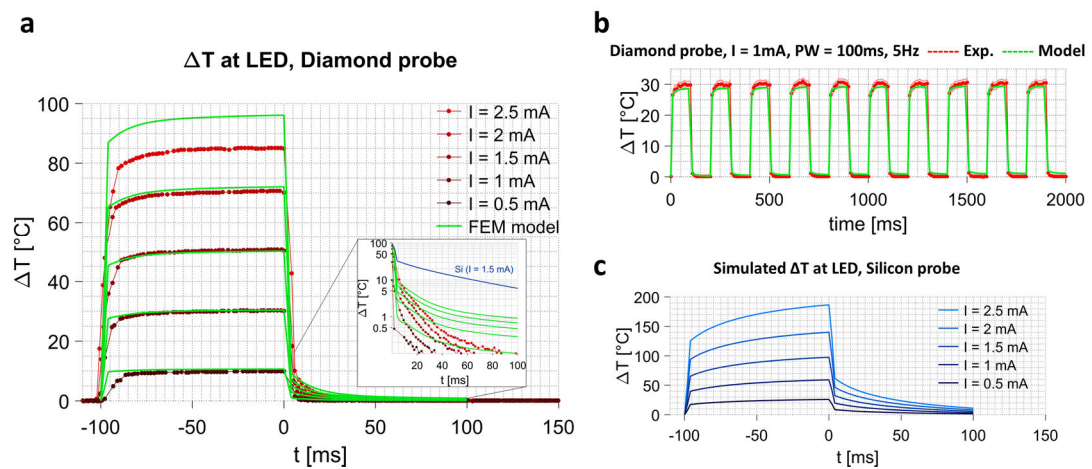


Figure 5.8 : Comparison between experimental and modelled values of temperature increase  $\Delta T_{\text{LED}}$  at  $\mu$ LED, in air, during operation. **a)** Measured (red curve, average over  $n > 20$  pulses) and simulated (green)  $\Delta T_{\text{LED}}$  during a single 100ms pulse at various currents (inset: close-up on decay period). The model accurately predicts LED peak temperature up to 2mA current but tends to overestimate heat buildup (measured  $\tau_{1/e} \sim 2\text{-}4\text{ms}$ ). Rise time discrepancies may be due in part to aliasing of the IR camera ( $\sim 3\text{ms}$  temporal resolution in the mode used). **b)** Measured and simulated  $\Delta T_{\text{LED}}$  during pulsed operation (1mA, 100ms, 5Hz). **c)** Simulated  $\Delta T_{\text{LED}}$  for a silicon probe, for comparison. Heat buildup is clear at higher currents,  $\tau_{1/e} \sim 20\text{ms}$ .

#### o Whole-probe measurements and relevance of simulation

The spatial spread and timescale of temperature change was also recorded to assess heat transfer dynamics. The whole probe was imaged at 500Hz during pulsed operation with varying currents ( $I = 0.5\text{mA}$  to  $3\text{mA}$  in  $0.5\text{mA}$  increment), pulse widths (1, 5, 10, 20, 50, 100, 200 ms) and frequencies (1, 5, 10, 20, 50, 100 Hz). The recorded movies were converted into temperature heatmaps using MATLAB programs developed for this purpose. A limited example of this dataset is given in figure 5.10, comparing the heat spread measured along

the optrode's right shank for 3 different driving conditions of  $\mu$ LED R2 ( $I = 2\text{mA}$ ) to the heatmaps obtained from their simulation in COMSOL.

This data clearly delineates three optrode regions : the operating  $\mu$ LED "hotspot" (temperatures  $>50^\circ\text{C}$  over an area of less than  $70 \times 70 \mu\text{m}^2$ ), the shank "heatspreader" with an exponential drop of temperature with distance away from the  $\mu$ LED, and the "cold" base acting as a heatsink, with a much lower temperature rise limited to  $\sim 1^\circ\text{C}$ . Importantly, the heat profile of the shank at the peak of pulsed stimulation (100ms, 50% duty cycle, panel c) is virtually unchanged from that of a single pulse peak (panel b), showing that the shank very efficiently conducts the heat away from the  $\mu$ LED with little to no heat buildup. This suggests that the exceptional thermal conductivity of diamond allows ms-timescale heat redistribution across the whole probe, with a large part of the heat absorbed in the base, the region of greatest heat capacity due to its larger volume. The probe base temperature is indeed slightly increased during pulsed operation (and at higher currents/duty cycles, the whole probe average temperature may be raised by up to  $3^\circ\text{C}$  for  $I=3\text{mA}$ , with visible heating of the second shank too).

The simulation agrees well with both  $\mu$ LED hotspot temperature and "cold" shank head and base, but tends to overestimate the temperature rise towards the shank tip. This might be due to an underestimation of the thermal conductivity of the diamond probe (value set at  $k_{\text{diamond}} = 2100 \text{ W}\cdot\text{m}^{-1}\cdot\text{K}^{-1}$ , given by single-crystal diamond provider), an overestimation of the thermally resistive effects of the  $\text{SiO}_2$  underlayer, or more complex considerations of heat transfer between the patterned layers of the actual device or even air convective cooling. Rather than overcomplicating or "tweaking" the simulation with possibly unrealistic material parameters, with a potential risk to model robustness, the model was left as is as a satisfactory representation of the probe thermal dynamics within specific limitations ( $I \leq 2\text{mA}$ ), which if anything tends to underestimate the probe thermal efficiency and as such may provide a slightly conservative estimate of the probe behaviour in brain tissue.

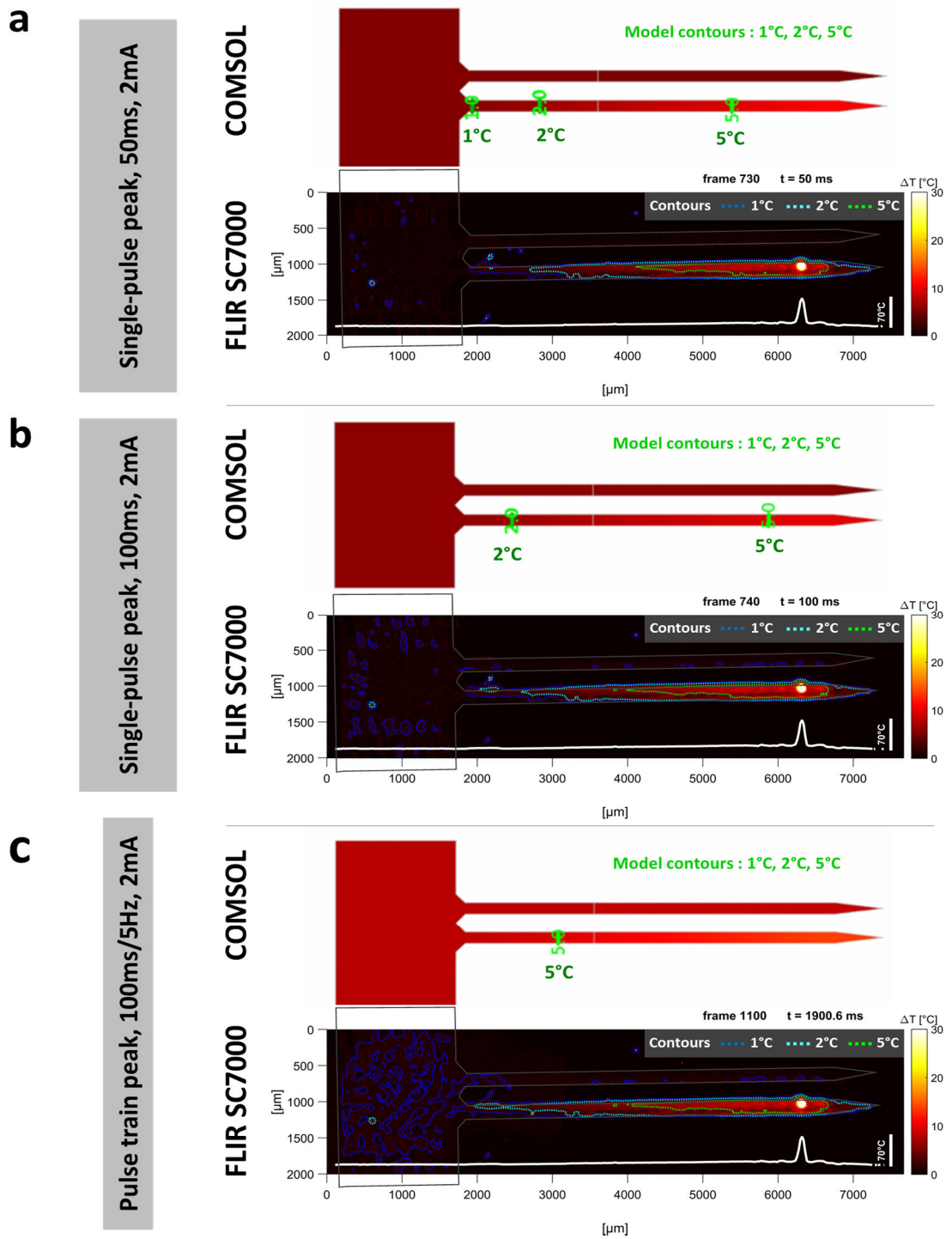


Figure 5.9 : Full-probe temperature maps during LED R2 operation at 2 mA (~11 mW electrical power), at the peak of **a**) a single 50ms pulse, **b**) a single 100ms pulse and **c**) a continuous pulsed stimulation (100ms, 5Hz; steady-state pulse peak). Top graph of each panel is the simulated probe temperature ( $\mu$ LED not shown) with 1°C/2°C/5°C contours in green. Bottom graph is the probe temperature measured by IR camera (similar heatmap colour), with same contours delineated and shank temperature profile in white bottom line. The model reasonably predicts the generic heat spread with 1°C and 2°C contours but tends to overestimate heat buildup in pulsed operation (panel c).

## 5.4 Prediction of optrode-induced heating in brain tissue

Once validated against experimental data, the COMSOL thermal model can be used to predict temperature changes in brain tissue surrounding a light-emitting diamond optrode. The probe medium was changed from modelled air to a “brain tissue” medium with parameters taken from the literature ([17], see table 5.1). Time-dependent simulations were run for a relevant range of pulse widths, frequencies and current as in air. Simulations were also run for silicon probe designs, to highlight the expected advantages of highly thermally efficient diamond optrodes over more standard silicon devices.

The simulated conditions of LED stimulation in the brain (optical power densities, pulse widths and frequency) were inspired by the requirements and specifications listed in table 1.1. In practical ChR2-based excitatory protocols, typical pulses of 1ms to 50ms are used, at sub-100Hz frequencies. Very local stimulation of neurons in the immediate implant vicinity may only require  $\mu\text{W}$ -levels of light [19], while circuit-level ChR2 stimulation may require irradiating thousands of neurons with  $>1\text{mW}\cdot\text{mm}^2$  optical power density [32], [33]. The latter translates as  $\sim\text{mW}$  light levels, or power densities well above  $100\text{mW}\cdot\text{mm}^2$  at the  $\mu\text{LED}$ . Optically-based inhibition initially often required long (second-scale) pulses likely to compound Joule heating concerns [25]. Although novel efficient inhibitory-type opsins allow to mitigate these, many optogenetic protocols focusing on inhibitory interneurons may still require pulse width in the range of hundreds of milliseconds [34]. These conditions inform the parameters of the simulations presented below, where the levels of heat generation in tissue are simulated for various combinations of these parameters and are given as time- and space- dependencies. In these and in line with previous work [19], [35], the contribution of the electrodes and tracks to heat increase has been taken as negligible compared to Joule heating of the  $\mu\text{LED}$  emitters.

Although neuronal activity can be affected by temperature changes exceeding  $\sim 1^\circ\text{C}$  [36], [37], thermal effects on brain function are difficult to interpret and there is currently no established temperature threshold for “safe” probe operation in brain tissue [17]. In practice, values of  $+0.5^\circ\text{C}$  or  $+1^\circ\text{C}$  are often loosely accepted as conservative limits of average tissue temperature rise for safe operation of implants *in vivo* eliciting no significant heat-induced

perturbation to cell electrical activity. In this work, the magnitude of predicted tissue heating was systematically compared to both thresholds for all thermal simulations in tissue.

The simulated spatial and temporal spread of tissue heating under these conditions is reported in figure 5.11 (values given for  $I = 1\text{mA}$  – see annex A9 for  $I = 2\text{mA}$ ). The expected temperature changes in tissue close to the  $\mu\text{LEDs}$  are an order of magnitude lower than the LED temperature, thanks both to the thermal insulation provided by the parylene layer and to the high specific heat of brain tissue. Post-pulse cool off for diamond is expected to be  $\sim 5$  times faster than for silicon probes (5.11.a), with heat diffusion away from the LED reduced by an order of magnitude (5.11.b). The compound effect is that diamond optrodes are expected to produce a minimal radial heating around the probe even during high-intensity stimulation such as 50% duty cycle 100ms pulses (below  $0.5^\circ\text{C}$  threshold within  $\sim 20\mu\text{m}$  from the LED in tissue), while silicon-based (Si) devices build up a considerable amount of heat over a few repeated pulses, with tissue regions above the  $0.5^\circ\text{C}$  threshold found up to  $\sim 210\mu\text{m}$  from the probe (5.11.c).

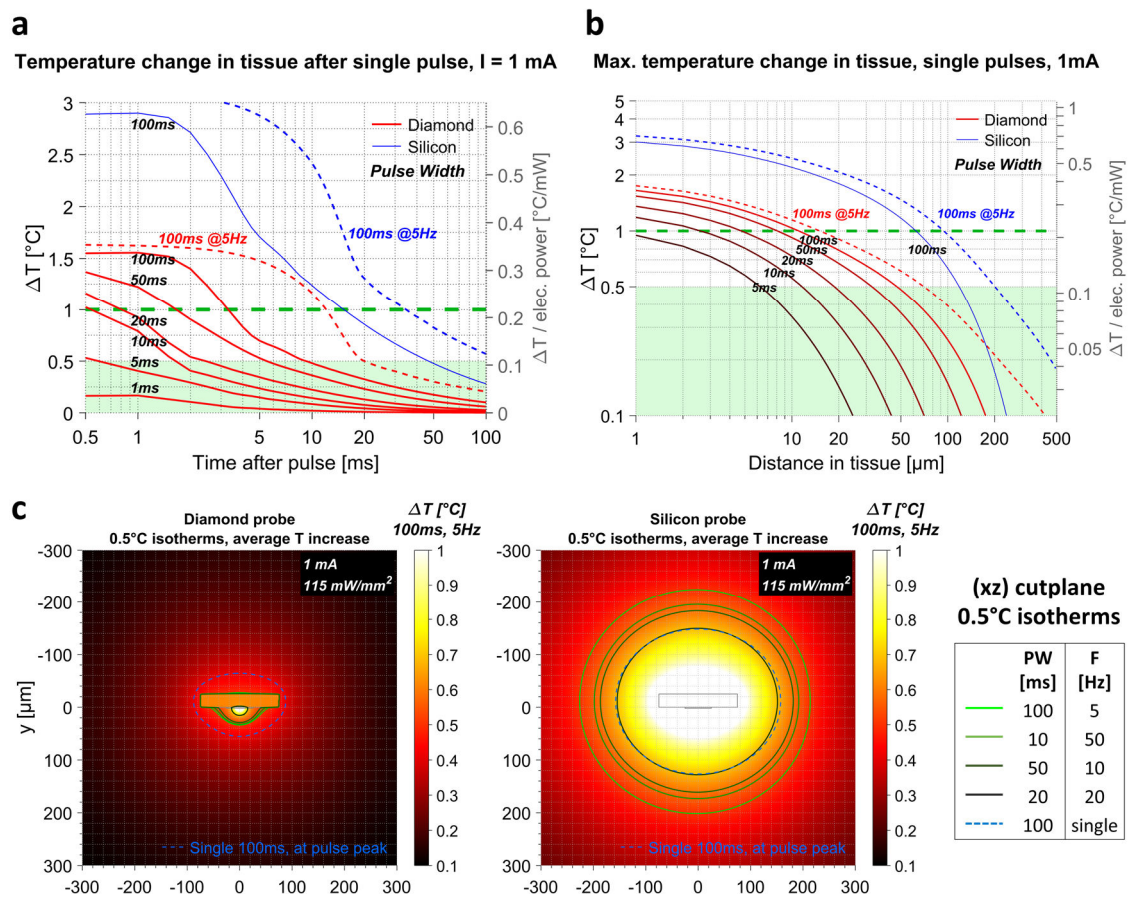


Figure 5.10 : Simulated spatial and temporal spread of temperature change in surrounding brain tissue during  $\mu\text{LED}$  pulsed operation at various pulse width and frequencies, given here for an LED current of  $I = 1 \text{ mA}$  ( $\sim 4.7 \text{ mW}$  electrical power,  $\sim 115 \text{ mW/mm}^2$  irradiance at LED). **a)** Decay with time of temperature change  $\Delta T = T - T_0$  in tissue directly below LED ( $1 \mu\text{m}$  from parylene boundary), following single pulses (full lines), for diamond (red) and silicon (blue) probes. The two dotted lines are extracted from simulation of pulsed operation (100ms pulse width, 5Hz) and represent the interpulse temperature decay for both probe materials. **b)** Maximum  $\Delta T$  recorded in tissue with increasing vertical distance from  $\mu\text{LED}$ , same colour code as in panel a). **c)** Average temperature changes within vertical ( $xz$ ) cutplanes across the probe intersecting a pulsed  $\mu\text{LED}$ , for a diamond (left) and silicon (right) probe. The heatmap represents the steady-state averaged  $\Delta T$  for a 100ms/5Hz pulsed operation. Full contour lines show the  $0.5^\circ\text{C}$  isotherms of average  $\Delta T$  for different pulse widths and frequencies. The blue dotted  $0.5^\circ\text{C}$  isotherm is taken at peak of a single 100ms pulse for contrast.

It is worth assessing the tissue volumes affected by potentially damaging or activity perturbing heating during optogenetic protocols against those targeted by the photostimulation. During stimulation by a  $\mu\text{LED}$ -based optrode, regions of the tissue surrounding the device may heat up, potentially leading to artificial cell activity, and partly overlapping (fig 5.12.c) with tissue regions irradiated over a certain threshold (e.g  $1 \text{ mW/mm}^2$  for ChR2 activation).

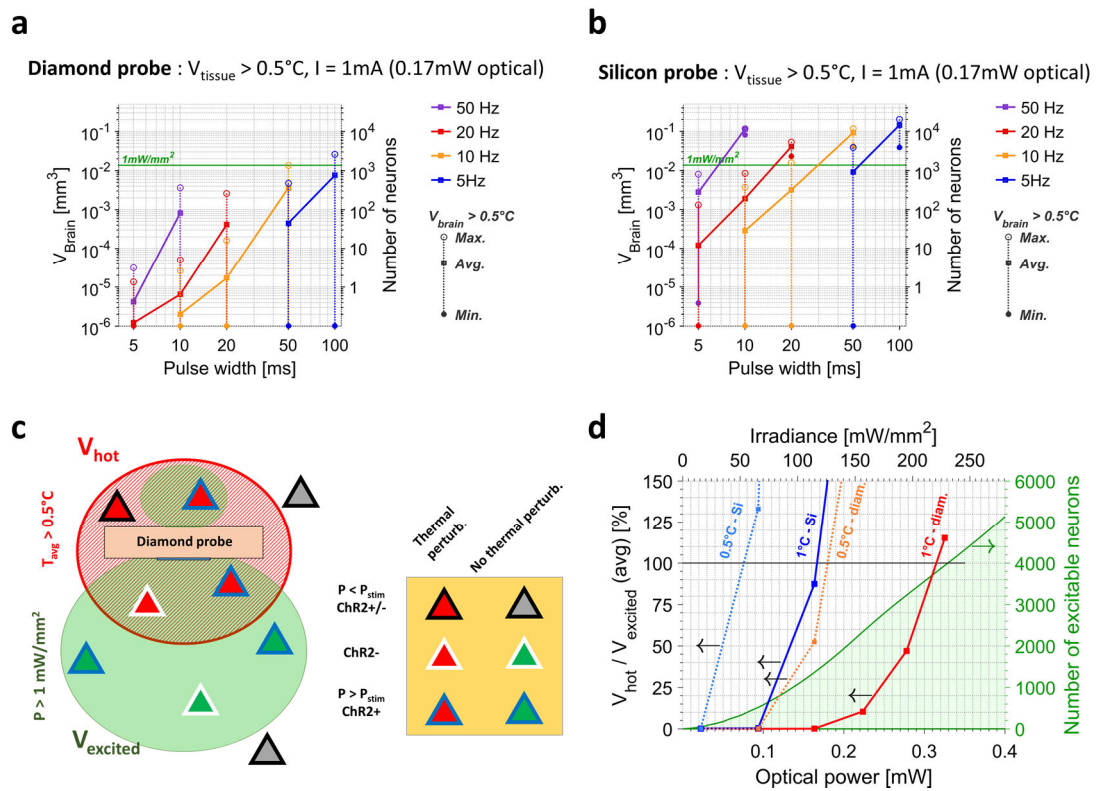


Figure 5.11 : Simulated LED operation allows comparison between tissue volume experiencing potentially detrimental heating and that irradiated above a given optogenetically relevant threshold. **a, b** Tissue volumes and corresponding number of neurons (assuming a cortical density of  $\sim 10^5 \cdot \text{mm}^{-3}$  [38]) experiencing "overheating" above  $0.5^{\circ}\text{C}$  during  $\mu\text{LED}$  operation at 1 mA ( $\sim 4.7\text{mW}$  electrical power) and various pulse widths and frequencies for **a**) a diamond probe and **b**) a geometrically identical silicon probe. The maximum, minimum and average spread of overheated volume (neuronal number) is given for each range of parameters and can be contrasted with the absolute volume irradiated by at least  $1\text{mW}/\text{mm}^2$  as the ChR2 optogenetic threshold, extracted from Monte Carlo simulations (section 5.2.1). **c**) Schematic representation of tissue regions significantly affected by  $\mu\text{LED}$  operation, through "overheating" ( $V_{\text{hot}} > 0.5^{\circ}\text{C}$ , red) and/or significant irradiation ( $V_{\text{excited}}$  receiving optical power  $> 1\text{mW}/\text{mm}^2$ , green). Thermal effects risk altering electrical activity of neurons within "overheated" regions (red-filled triangles), potentially creating false positives during optrode operation irrespective of channelrhodopsin expression. Only neurons exclusively located within  $V_{\text{excited}}$  (green-filled triangles) may be unequivocally optically-driven if expressing opsins. **d**) Ratio of average "overheated" volumes ( $>0.5^{\circ}\text{C}$  and  $>1^{\circ}\text{C}$ ) to the corresponding irradiated volumes  $V_{\text{excited}}$  for various  $\mu\text{LED}$  optical powers at high-intensity operation (100ms pulse width at 5Hz), for a silicon probe (cyan/blue curves) and a diamond probe (orange/red curves). The number of neurons irradiated by  $>1\text{mW}/\text{mm}^2$  (i.e. within  $V_{\text{excited}}$ ) is given by the shaded green slope (right axis).

The volumes and number of neurons involved are given in fig 5.12a,b for diamond and Si probes respectively. While the average temperature increase over a given volume is usually much lower than the peak, this difference abates at higher duty cycles and powers especially for Si devices, as heat cannot be extracted fast enough, neither by conduction in the brain nor by heatsinking of the probe. As a result diamond probes should be safely usable at a drive

current of 1 mA over a range of frequencies and pulsewidths, while Si probes will typically induce above-threshold temperatures in tissue for these (5.12.b).

As another example, the diamond optrode could be used at optical  $\mu$ LED powers of 0.2mW to irradiate a population of  $\sim 2000$  neurons above the optogenetic threshold of  $1\text{mW}\cdot\text{mm}^{-2}$ , while keeping the number of neurons heated above  $1^\circ\text{C}$  below  $\sim 200$  (5.12.d). At this power, a silicon probe would heat up an unacceptable  $> 7000$  neurons including all the photostimulated area. Only stimulations of much lower power (photostimulation of  $\sim 800$  neurons) would allow silicon devices to exhibit this same 1/10 ratio. As such the diamond probe proves able to directly extend the range of stimulation protocols available to neuroscientists.

## 5.5 Conclusion

This chapter covered the development of modelling tools used for analysis of the fabricated diamond optrode, the experimental characterisation of its electrical, optical and thermal performance in air, and its expected performance *in vivo* once inserted in tissue. The thermal COMSOL model was successfully validated against a range of experimental measurements. The optrode was able to reliably produce high optical power densities ( $> 250\text{mW}\cdot\text{mm}^{-2}$ ) while exhibiting superior heatsinking properties thanks to ms-timescale heat extraction along the probe shank, thus minimising heat buildup in the surrounding medium. Compared to silicon-based devices of similar geometry, this device is predicted to allow an order of magnitude increase in  $\mu$ LED power, pulse width and/or operation frequency while keeping tissue temperature increase under “safe” thresholds of e.g  $0.5^\circ\text{C}$ .

This chapter concludes the development and testing of the diamond-based optrodes integrated with GaN-based  $\mu$ LEDs. The next section will detail the remaining limitations and focus on future developments of these devices.



## 5.6 References

- [1] E. F. Schubert, *Light-emitting diodes*. Cambridge University Press, 2006.
- [2] E. Xie, "High performance microstructured light emitting diodes - mechanisms and processes," University of Strathclyde, 2013.
- [3] F. Bevilacqua, D. Piguet, P. Marquet, J. D. Gross, B. J. Tromberg, and C. Depeursinge, "In vivo local determination of tissue optical properties: applications to human brain," *Appl. Opt.*, vol. 38, no. 22, p. 4939, Aug. 1999.
- [4] L. V Wang and S. L. Jacques, "Source of error in calculation of optical diffuse reflectance from turbid media using diffusion theory," *Comput Methods Programs Biomed*, vol. 61, no. 3, pp. 163–170, 2000.
- [5] S. L. Jacques and L. Wang, "Monte Carlo Modeling of Light Transport in Tissues," *Opt. Response Laser-Irradiated Tissue*, vol. 2607, no. 713, pp. 73–100, 1995.
- [6] M. Azimipour, R. Baumgartner, Y. Liu, S. L. Jacques, K. Eliceiri, and R. Pashaie, "Extraction of optical properties and prediction of light distribution in rat brain tissue.," *J. Biomed. Opt.*, vol. 19, no. 7, p. 75001, 2014.
- [7] S. Song, Y. Kobayashi, and M. G. Fujie, "Monte-carlo simulation of light propagation considering characteristic of Near-infrared LED and evaluation on tissue phantom," *Procedia CIRP*, vol. 5, pp. 25–30, 2013.
- [8] S. A. Prahl, M. Keijzer, S. L. Jacques, and A. J. Welch, "A Monte Carlo Model of Light Propagation in Tissue," *Proc. SPIE vol. IS 5*, vol. I, no. 1989, pp. 102–111, 1989.
- [9] S. L. Jacques, "Modelling light propagation in tissues," no. 22416, pp. 21–32, 1996.
- [10] A. N. Yaroslavsky, I. V. Yaroslavsky, T. Goldbach, and H.-J. Schwarzmaier, "Influence of the Scattering Phase Function Approximation on the Optical Properties of Blood Determined from the Integrating Sphere Measurements," *J. Biomed. Opt.*, vol. 4, no. 1, p. 47, 1999.
- [11] S. L. Jacques, "Optical properties of biological tissues: a review," *Phys. Med. Biol.*, vol. 58, no. 11, pp. R37–R61, Jun. 2013.
- [12] J. D. Johansson, "Spectroscopic method for determination of the absorption coefficient in brain tissue," *J. Biomed. Opt.*, vol. 15, no. 5, p. 057005, 2010.
- [13] G. Yona, N. Meitav, I. Kahn, and S. Shoham, "Realistic Numerical and Analytical Modeling of Light Scattering in Brain Tissue for Optogenetic Applications," *Eneuro*, vol. 3, no. 1, pp. 1–9, 2015.
- [14] A. Yaroslavsky, "Optical properties of selected native and coagulated human brain tissues in vitro in the visible and near infrared spectral range," *Phys. Med. ...*, vol. 2059, 2002.
- [15] L. Acker, E. N. Pino, E. S. Boyden, and R. Desimone, "FEF inactivation with improved optogenetic methods.," *Proc. Natl. Acad. Sci. U. S. A.*, vol. 113, no. 46, pp. E7297–E7306, 2016.

- [16] R. Scharf, T. Tsunematsu, N. McAlinden, M. D. Dawson, S. Sakata, and K. Mathieson, "Depth-specific optogenetic control in vivo with a scalable, high-density  $\mu$ LED neural probe," *Sci. Rep.*, vol. 6, no. January, p. 28381, 2016.
- [17] M. M. Elwassif, Q. Kong, M. Vazquez, and M. Bikson, "Bio-heat transfer model of deep brain stimulation-induced temperature changes.," *J. Neural Eng.*, vol. 3, no. 4, pp. 306–315, 2006.
- [18] A. N. Smith, M. P. Christian, S. L. Firebaugh, G. W. Cooper, and B. G. Jamieson, "Predicting and managing heat dissipation from a neural probe," *Biomed. Microdevices*, vol. 17, p. 81, 2015.
- [19] F. Wu, E. Stark, P. C. Ku, K. D. Wise, G. Buzsáki, and E. Yoon, "Monolithically Integrated  $\mu$ LEDs on Silicon Neural Probes for High-Resolution Optogenetic Studies in Behaving Animals," *Neuron*, vol. 88, no. 6, pp. 1136–1148, 2015.
- [20] Y. Li, X. Shi, J. Song, C. Lü, T. Kim, J. G. McCall, M. R. Bruchas, J. a. Rogers, and Y. Huang, "Thermal analysis of injectable, cellular-scale optoelectronics with pulsed power," *Proc. R. Soc. A Math. Phys. Eng. Sci.*, vol. 469, no. 2156, p. 20130142, 2013.
- [21] H. H. Pennes, "Analysis of Tissue and Arterial Blood Temperatures in the Resting Human Forearm," *J. Appl. Physiol.*, vol. 1, no. 2, pp. 93–122, Aug. 1948.
- [22] Speciality Coating Systems, "Parylene Conformal Coating Specifications & Properties," pp. 1–12, 2013.
- [23] R. Scharf, A. Boudet, M. Dawson, S. Sakata, and K. Mathieson, "Next-generation high-density  $\mu$ LED probes for depth-specific stimulation," in *Optogen 2016*, 2016.
- [24] A. Boudet, R. Scharf, M. Dawson, and K. Mathieson, "A diamond-based, hybrid optrode for multisite optogenetics," in *Frontiers in Optics 2016*, 2016, p. FTh4D.5.
- [25] O. Yizhar, L. E. Fenno, T. J. Davidson, M. Mogri, and K. Deisseroth, "Optogenetics in Neural Systems," *Neuron*, vol. 71, no. 1, pp. 9–34, 2011.
- [26] J. M. Stujenske, T. Spellman, and J. A. Gordon, "Modeling the Spatiotemporal Dynamics of Light and Heat Propagation for In Vivo Optogenetics," *Cell Rep.*, vol. 12, no. 3, pp. 525–534, 2015.
- [27] E. Booth, C. Dukatz, J. Ausman, and M. Wider, "Cerebral and somatic venous oximetry in adults and infants," *Surg. Neurol. Int.*, vol. 1, no. 1, p. 75, 2010.
- [28] T. Il Kim, Y. H. Jung, J. Song, D. Kim, Y. Li, H. S. Kim, I. S. Song, J. J. Wierer, H. A. Pao, Y. Huang, and J. A. Rogers, "High-efficiency, microscale GaN light-emitting diodes and their thermal properties on unusual substrates," *Small*, vol. 8, no. 11, pp. 1643–1649, 2012.
- [29] T. Il Kim, J. G. McCall, Y. H. Jung, X. Huang, E. R. Siuda, Y. Li, J. Song, Y. M. Song, H. A. Pao, R. H. Kim, C. Lu, S. D. Lee, I. S. Song, G. Shin, R. Al-Hasani, S. Kim, M. P. Tan, Y. Huang, F. G. Omenetto, J. A. Rogers, and M. R. Bruchas, "Injectable, cellular-scale optoelectronics with applications for wireless optogenetics," *Science (80-. )*, vol. 340, no. 6129, pp. 211–216, 2013.
- [30] N. McAlinden, D. Massoubre, E. Richardson, E. Gu, S. Sakata, M. D. Dawson, and K. Mathieson, "Thermal and optical characterization of micro-LED probes for in vivo optogenetic neural

- stimulation.,” *Opt. Lett.*, vol. 38, no. 6, pp. 992–4, 2013.
- [31] K. Kim, D. English, S. Mckenzie, F. Wu, E. Stark, J. Seymour, P. Ku, K. Wise, G. Buzsaki, and E. Yoon, “GaN-on-Si  $\mu$  LED optoelectrodes for high-spatiotemporal-accuracy optogenetics in freely behaving animals,” *IEEE Int. Electron Devices Meet.*, pp. 643–646, 2016.
- [32] G. Buzsáki, E. Stark, A. Berényi, D. Khodagholy, D. R. Kipke, E. Yoon, and K. D. Wise, “Tools for probing local circuits: High-density silicon probes combined with optogenetics,” *Neuron*, vol. 86, no. 1, pp. 92–105, 2015.
- [33] K. L. Montgomery, A. J. Yeh, J. S. Ho, V. Tsao, S. Mohan Iyer, L. Grosenick, E. A. Ferenczi, Y. Tanabe, K. Deisseroth, S. L. Delp, and A. S. Y. Poon, “Wirelessly powered, fully internal optogenetics for brain, spinal and peripheral circuits in mice,” *Nat. Methods*, vol. 12, no. 10, pp. 969–974, 2015.
- [34] M. Häusser, “Optogenetics: the age of light,” *Nat. Methods*, vol. 11, no. 10, pp. 1012–1014, 2014.
- [35] R. Scharf, T. Tsunematsu, N. McAlinden, M. D. Dawson, S. Sakata, and K. Mathieson, “Depth-specific optogenetic control in vivo with a scalable, high-density  $\mu$ LED neural probe - SUPPLEMENTARY,” *Sci. Rep.*, vol. 6, 2016.
- [36] E. Moser, I. Mathiesen, and P. Andersen, “Association between brain temperature and dentate field potentials in exploring and swimming rats,” *Science (80-. )*, vol. 259, no. 5099, pp. 1324–1326, Feb. 1993.
- [37] P. Andersen and E. I. Moser, “Brain temperature and hippocampal function,” *Hippocampus*, vol. 5, no. 6, pp. 491–498, 1995.
- [38] A. Schüz and G. Palm, “Density of neurons and synapses in the cerebral cortex of the mouse,” *J. Comp. Neurol.*, vol. 286, no. 4, pp. 442–455, Aug. 1989.

# Chapter 6

## Discussion and future work

### 6.1 Introduction

The development of powerful, minimally invasive and adaptable tools for *in vivo* optogenetics and electrophysiology is important to advance our understanding of the brain. As shown in the previous chapters, microfabricated devices harnessing the robustness of semiconductor processing and the versatility of heterogeneous integration techniques open a very promising path.

The diamond optrodes developed in this work are at the forefront of technological development and show consistent advantages over current state-of-the-art devices. A few final adjustments will still be required before these devices can be reliably used *in vivo*, notably regarding the bio/electrical insulation layer. Other improvements, planned during device development, can be implemented directly at the next prototype iteration to further increase the device potential and are detailed in **section 6.3**.

In later stages of development, various additional features can be introduced which will again increase device usefulness to neuroscientists. **Section 6.4** considers these next steps including the use of the techniques developed in this work to enhance readily available commercial devices.

## 6.2 Diamond optrode outcome and adjustments

### 6.2.1 Versatile fabrication techniques and diamond optrodes

Resulting from an extensive development phase, the diamond optrodes produced in this work demonstrate the feasibility of thermally efficient  $\mu$ LED-based probes, inherently modular and integrated with electrode arrays within a low footprint structure.

These devices can finally allay the main concern over  $\mu$ LEDs probes, often reiterated when considering options for precise light delivery *in vivo* [1]–[4], that limits in power dissipation may preclude their use when upscaling to larger numbers of active light emitters on implanted devices. Furthermore, this work successfully demonstrated reliable integration of  $50 \times 50 \mu\text{m}^2$  TP- $\mu$ LEDs and patterned electrodes on a  $\sim 100 \mu\text{m}$  wide shank, approaching dimensions of more conventional silicon-based devices [2], [5], [6] and sensibly improving footprint compared to the large majority current hybrid devices, which are usually larger by a two- to five-fold factor [7]–[13], with the exception of the polymer-based device proposed by Kim et al. in 2013 [14].

Beside the necessary measures to counter the last failure mode analysed in section 6.2.3, a few improvements can still be suggested to directly improve the device properties and direct usefulness to neuroscientists as end users. A few examples are given below. Additionally, a certain number of features can be added to those probes at the next development stage, which would dramatically improve their output and performance *in vivo*. Some such features are discussed in detail later on in this chapter, in order to explore possibilities.

### 6.2.2 Parallel fabrication of silicon-based devices for experimental comparison

While modelling can give useful insights in comparing the experimental thermal behaviour of diamond optrodes to that expected of more conventional silicon-based devices, direct measurement of the latter would provide further quantitative evidence. With this purpose in mind, silicon optrodes were fabricated in this work using the exact same process as the diamond devices up to the probe separation stage (steps 0 to 11.3, see section 4.4). After probe contour patterning by thick protective resist (SPR200-7,  $8 \mu\text{m}$  thick),  $50 \mu\text{m}$ -deep trenches were deep-reactive ion etched (DRIE) in the silicon substrate by an external vendor (Stanford University). The devices at that stage are shown in Figure 6.1.a, with feature definition and alignment finer than on the diamond probe thanks to much easier handling of larger, robust silicon samples.

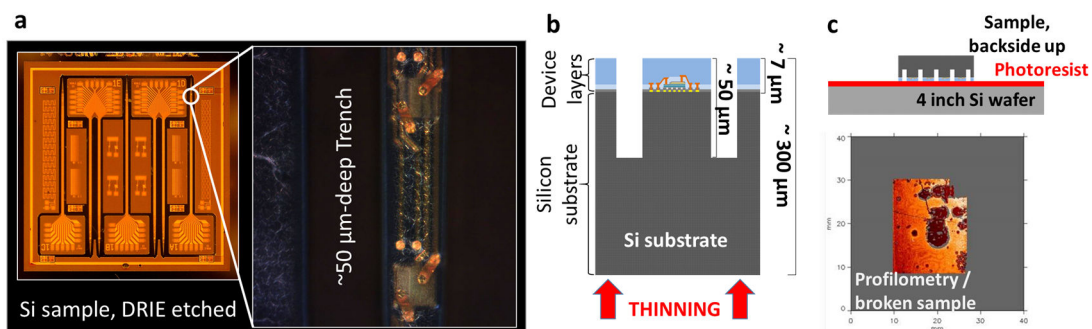


Figure 6.1 : Same geometry silicon-based probes were fabricated for direct comparison with diamond optrodes but samples were destroyed during externally sourced separation process. **a)** (left) View of silicon sample with fully functional probes separated by DRIE-etched trenches ( $\sim 50\mu\text{m}$  deep), with (right) close-up micrograph on the shank of probe 1A showing 2  $\mu\text{LEDs}$  and corresponding electrodes (“veined” structures are caused by photoresist residues after etch). **b)** Side-view schematic of the devices shown in a), showing the subsequent backside thinning step. **c)** (top) schematic of backside thinning configuration and (bottom) optical profilometry profile of the carrier rectangular wafer after the sample broke during thinning (DISCO GmbH, Germany). Dark red areas show uneven (thinner) photoresist adhesion layer.

After the DRIE step, the silicon sample was bonded upside down on a carrier wafer using a  $\sim 7\mu\text{m}$ -thick photoresist layer and sent to another external vendor (DISCO GmbH, Germany [15]) for backside thinning until probe separation (Figure 6.1.b,c). Unfortunately the samples broke in the polishing tool and no part could be retrieved. The time taken by these external processes did not allow for another fabrication run of these silicon-based probes within this project; however, their production process is now established and could be replicated at will, i.e to produce larger volumes of testbed integrated devices.

### 6.2.3 Improvement of bioinsulation layer

After etching through the diamond samples and cleaning, the state of the separated devices was assessed under the microscope and significant regional delamination of the parylene layers was observed on all devices. Parylene layers started to delaminate at the shank tip (most severe example given in Figure 6.2) and, for some probes, at the base corners, over lengths of up to  $\sim 600\mu\text{m}$ . This delamination did not progress during cleaning or dipping in deionized water. However, it was sufficient to damage contacts to the bottom-most  $\mu\text{LEDs}$  (positions L1/R1) on the shank, rendering them non-operational.

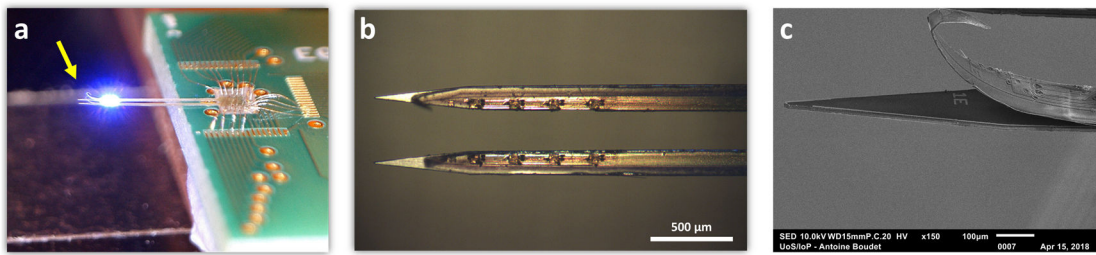


Figure 6.2 : Final devices exhibit significant parylene-C delamination at the probe shank tip. **a)** Visible curling of parylene layers during probe operation. **b)** Top micrograph of same probe showing delamination area (bottom-most  $\mu$ LEDs L1/R1 were non-operational as a result. **c)** SEM scan showing detail of the parylene curling, leaving the diamond/ $\text{SiO}_2$  exposed at the tip.

This failure mode was observed despite the precautions taken early on in the design and testing phase, and briefly described below. As was acknowledged during design, untreated parylene has a well-reported history of poor adhesion on metals and on some dielectrics [16]–[21], especially when devices are soaked in wet environments [19], [22]–[26]. As a chemically inert polymer deposited by low-energy CVD processes (section 2.2.3.2), parylene-C does not form bonds, nor is implanted into the deposited surface. Film adhesion instead relies on mostly physical adsorption processes and the weak van der Waals interaction [21]. However, surface treatments have been reported to improve long-term parylene-C adhesion notably through silanisation of the receiving surface directly before deposition [27]–[29]. Before prototype fabrication, a detailed investigation of parylene-on-glass adhesion within our laboratory conditions was carried out using the ASTM 3359 “cross-hatch” peel test for different applications of A-174 silane adhesion promoter. The results, corroborating previous work, are given in Table 6.1 (see also annex A4). Vapour silanisation of the samples immediately prior to deposition was found to promote the highest level of adhesion both before and after heat-cycling at  $140^\circ\text{C}$  for 3 hours (grades 5B and 3B respectively, test ASTM D3359-B).

Adhesion test for Parylene-C coated on 4" glass wafers : ASTM D3359 peel test								
		Average adhesion grade 5B (strongest adhesion) to 0B (very poor)						
Adhesion promoter	a/ No primer		b/ VPD Silane		c/ Immersion in Silane solution		# of arrays	Adhesion to steel (vendor)
	Directly after parylene coating							
1st peel : #810 tape	2B		5B		5B		n=5	250 N/m
2d peel : Kapton	1B		5B		5B		n=5	240 N/m
3d peel : Gorilla	0B		5B		5B		n=5	1240 N/m
Peel after bake	cut before	cut after	cut before	cut after	cut before	cut after	<- Cut after/before 140°C bake for 3hrs	
1st peel : #810 tape	-	0B*	2B-3B	2B	3B	0B-1B	n=4 (*n=3)	250 N/m

Table 6.1 : Collated results of Parylene-C adhesion tests (test protocol and details are given in annex A4). Adhesion values are given from ASTM D3359-B grading (% of film removed after peel tests on cross-hatch cut structure), from the highest adhesion grade 5B (0% film removed) to medium 3B (5%-15%) to the lowest 0B (>65%). Vapour phase deposition (VPD) of silane as an adhesion promoter gave the best adhesion strength of the film (no delamination observed even for very strong peel with “Gorilla” tape, limited delamination (3B) with scotch tape after a 3hr heat cycle).

Following this study, vapour phase silanisation was used for every parylene deposition during probe fabrication. Despite the succession of wet/dry processing steps and relatively high feature aspect ratio, no parylene delamination was observed on the devices at any stage (including probe contouring etch in parylene) before the very last step of diamond through-etch. This confirms good adhesion of the film during “standard” processing steps and points to a failure mode specific to the high-power ICP etching step. In this case, the most likely cause of parylene delamination is thermal stress related to a mismatch of coefficients of thermal expansion (CTE) between parylene layers and the underling probe/diamond, and induced by excessive heating of the sample during the hour-long etches. Although sample temperature could not be measured *in situ*, local temperature during long **DIA-ARO2** etches is thought to rise up to 100-120°C as the wax initially used to bond test samples fully melted and would bubble. The curling of the parylene layers observed in figure 6.1 is typical of a stressed film. Furthermore, no parylene delamination could be detected on same-design silicon probes



contoured by a non-heating deep-reactive ion etch (DRIE), which were also fabricated as part of the project (see section 6.2.2).

These observations point out parylene delamination as a specific failure mode of diamond optrodes due to long thermal cycling at the very last step of the fabrication process. As a tentative remedial measure, shorter, staggered diamond etch runs ( $\leq 15$  min) could be attempted to limit sample heating, but would increase fabrication time. Other diamond etch methods or laser cutting are likely to involve local heating due to the high energies needed to break carbon-carbon bonds. A more definitive solution may be to explore emerging alternative solutions to parylene insulation such as silicon carbide bioinsulation (see section 6.3.1).

## 6.3 Direct next steps : upcoming prototype iteration

### 6.3.1 Silicon carbide based insulation layer

As reported above, probe insulation by planar thin film parylene creates challenges which might eventually prove intractable for devices destined to be implanted in wet, corrosive biological environments. Other process-compatible materials may need to be explored. Traditional IC passivation layers such as low-temperature silicon oxide/nitride stacks are known to significantly degrade *in vivo* over time [30], [31]. A promising alternative could be silicon carbide (SiC), a material historically explored for sensor technology [32], with proven high biocompatibility [33]–[36], hermetic barrier properties [37], [38] and very low dissolution rates in saline compared to SiO<sub>2</sub>/SiN<sub>x</sub> layers [36], [39]. In a recent study, Diaz-Botia et al. extensively optimised CVD deposition parameters and demonstrated SiC electrode arrays with outstanding longevity in electrically-strained accelerated aging tests, far outperforming more commonly used insulators. These “low-complexity” devices are predicted to have a functional lifetime *in vivo* in the order of decades [40].

Such high-quality SiC films can be deposited at temperatures of  $\sim 350^\circ\text{C}$  and patterned using standard techniques, and thus could be seamlessly integrated into the optrode fabrication process in place of parylene deposition. A possible structure is schematised in fig. 6.3.a, with a thick layer of low-stress SiC ( $\sim 2\text{-}4\ \mu\text{m}$ ) fully encapsulating the TP- $\mu\text{LED}$  and a thinner upper layer of parylene added to reduce the refractive index mismatch between high-index SiC ( $n \sim 2.7$  at  $\lambda = 480\text{nm}$ ) and lower-index brain tissue ( $n \sim 1.4$ ). In order to ensure light propagation into tissue, the stack transmittance can be maximised at the desired wavelength(s) by adjusting layer thicknesses to tailor thin film interference properties, which can be accurately

determined by the transfer matrix method [41]. A Matlab program implementing this method was used (adapted from [42, p. 223]) to determine the maximum transmittance at  $\lambda = 480\text{nm}$  (close to ChR2 absorption peak) of the stack for a range of layer thicknesses, both at normal incidence (NI, figure 6.3.b) and at a  $30^\circ$  angle (fig 6.3.c). By tailoring both parylene and SiC thicknesses to adequate values (e.g. 1200nm, 3500nm respectively with an experimentally attainable film thickness accuracy of  $\pm 10\text{nm}$ ), the stack transmittance can exceed 95% for rays emitted within a cone angle of  $\theta \leq 30^\circ$ .

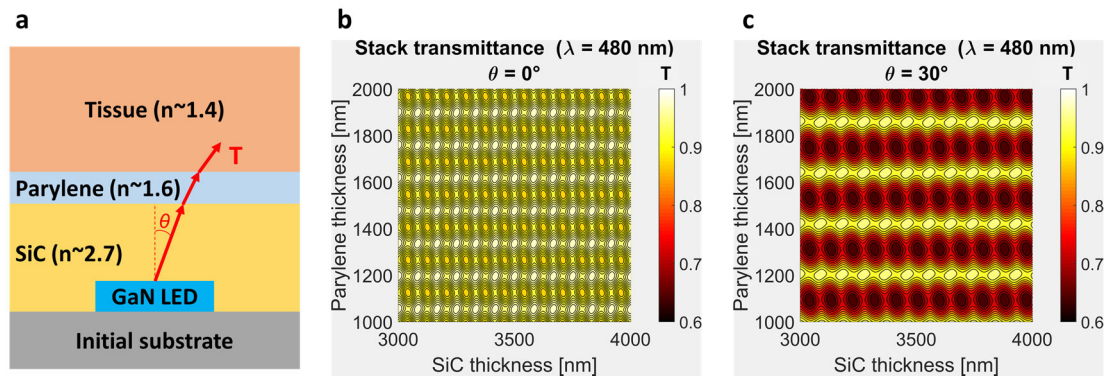


Figure 6.3 : Simulated optical transmittance into tissue of bioinsulating SiC-parylene stacks as a function of layer thicknesses. Data calculated using the transfer matrix method (TMM). **a)** Schematic of the example stack considered ( $\mu\text{LED}$  rays emitted upward at  $\lambda = 480\text{nm}$  and angle  $\theta$ ). **b)** Stack transmittance at normal incidence for a realistic range of SiC and parylene thicknesses. Transmittance range [87%-99%]. **c)** Stack transmittance at  $\theta = 30^\circ$  (s-polarised only). Transmittance range [64%-98%].

These simple considerations suggest that SiC insulation, could be relatively easily implemented onto the existing optrode design, at an affordable cost and without strongly impairing light extraction. Such a diamond-SiC optrode design, based on materials which essentially do not corrode *in vivo*, could present a very high potential gain for chronic applications requiring no or very limited device degradation over very long-term insertions.

### 6.3.2 Use of diamond optrode *in vivo*

The immediate next step in the use of the diamond optrodes is direct insertion *in vivo*, demonstrating device operation and performance in the mouse brain and using its specific capabilities for the study of neural networks.

Experiments will be carried out with neuroscientist colleagues at the University of Strathclyde's Institute for Pharmacological and Biological Sciences (SIPBS), using procedures already established for previous light-emitting probes produced at the Institute of Photonics [5], [43]. At the next iteration of the device with a new bioinsulation layer (above section), the electrodes will be platinised in solution after probe wirebonding. Devices can then be

inserted in the neocortex of anaesthetised mice, a six-layered structure with distant functional properties ideal for testing depth-dependent neuronal stimulation and readout. The initial experiments will be carried with probes patterned with in-built thermistors (section 6.3.3) to directly assess probe and tissue temperature during and after  $\mu$ LED operation, and verify simulation results. As a control experiment, the effect of LED joule heating can be assessed by recording the potential change in neural activity during  $\mu$ LED operation in a non-photosensitised tissue.

After experimental qualification of the probe performance and “safe” regime of operation in vivo, neuroscientifically relevant experiments can then be performed harnessing the particular capabilities of the diamond optrode. The optrodes could be implanted within mouse neocortical regions expressing ChR2 channelrhodopsin variants (e.g fast and sensitive Chronos [44]) following adeno-associated viral infection. While operation of the  $\mu$ LED at low power should excite only very local neuronal populations down to single-cell levels [6], high-power illumination afforded by the optrode design should be able to recruit a large number of cells within the whole cortical layer of implantation, triggering circuit-wide responses which should be recorded within upstream and downstream cortical layers by the corresponding electrodes.

### **6.3.3 *In vivo* temperature measurements**

Implanted devices with integrated  $\mu$ LEDs must always operate within strict limits of Joule heating of brain tissue. The modelling described in section 5.2.2 offers conservative guidelines. However, the progressing of such probes to medical application would likely require real-time monitoring of tissue/probe temperature, *a minima* during calibration phases. Such direct experimental feedback would also be beneficial for research as it would allow better detection of heat-induced effects in brain tissue and thus better determination of the safe operation regimes of LED-based optrodes.

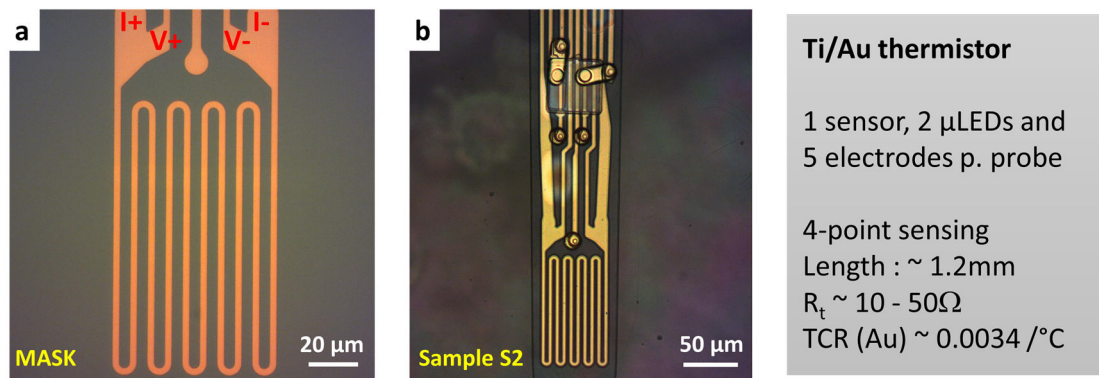


Figure 6.4 : Design and prototype of a resistive temperature sensor directly integrated on optrode. **a)** Mask design of the serpentine thermistor (trace width =  $3\mu\text{m}$ , thickness  $\sim 500\mu\text{m}$ ), with “load” and “sense” terminals for four-point voltage sensing indicated in red. **b)** (left) Micrograph of thermistor-integrated probe, showing  $\mu$ LED, electrodes and thermistor element, fabricated on diamond sample S2 (broken during process preventing actual  $\mu$ LED or thermistor operation) and (right) characteristic configuration of this probe design including expected thermistor resistance  $R_t$  (film thickness-dependent) and expected temperature coefficient of resistance (based on Au [45], [46]).

Commercial sensors often suffer from prohibitive footprints. While various probe-integrated sensing solutions exist including thermocouples [47], silicon diodes [48] or even reverse-biased GaN LEDs [10], the most popular technology is based on easily patternable metallic thin-film resistance temperature detectors (RTDs) [11], [14], [49]–[55]. Inspired by this approach, a thermistor element was integrated to some of the probe designs in this work, and shown on Figure 6.4. Located at the probe tip, the serpentine gold thermistor resistance could be accurately determined by 4-point measurement and calibration-correlated with surrounding tissue temperature.

Based on structure/material considerations and published experimental work on comparable devices [51], [55], this thermistor design is expected to show a sensitivity of  $\sim 0.5\text{ mV}/^\circ\text{C}$  (1mA lead current), with a response time in the order of  $\sim 100\text{ ms}$  and a typical accuracy of  $\pm 0.1^\circ\text{C}$ . As such the device will be able to measure the local average temperature rise *in vivo* (either on a probe shank heated by an operated  $\mu$ LED, or on a second shank in direct thermal equilibrium with surrounding tissue). Modelling results presented in section 5.4 may then give useful insights into the peak temperatures reached and help further refine operating protocols. The fabricated structure on a diamond optrode is shown in Figure 6.4 b, but could not be tested due to the fracture of diamond sample S2 which broke probe traces.

### 6.3.4 Multicolour diamond optrodes

While optogenetics was initially demonstrated with modified membrane proteins photosensitive to blue light, rapid development of biological constructs soon ensured the availability of opsins with red-shifted absorption spectra – some notably capable of neuronal suppression [56]. This opens the possibility of multi-channel optogenetics, where various emission wavelengths are used to simultaneously and independently activate or silence targeted neurons within a circuit, offering an unprecedented level of control over neuronal electrical signals.

Multicolour *in vivo* emission has already been achieved through invasive multi-optical fibre solutions [57] or more advanced waveguide-based devices [58], and could be done using colour-converting coatings (e.g quantum dots) on existing LED probes [59]. However, pick-and-placed  $\mu$ LED solutions are capable of providing multicolour stimulation in an exceptional multi-site, high-precision and adaptable fashion, as demonstrated on a polymer probe in a landmark work by Kim et al. [14]. Low-footprint red and green-shifted  $\mu$ LEDs suitable for pickup and release have already been demonstrated [60] but have not so far been integrated on minimally invasive probes. Furthermore, TP- $\mu$ LED-based emission may help address a recurrent issue of multicolour optogenetics, that created by the broad absorption spectra of many opsins, which may lead to spectral overlap during stimulation and complicate interpretation of results. Transfer-printing processes offer the possibility of ultra-local, wavelength-tuned emitters at the very sites of opsin expression, thus limiting potential interference.

Thanks to the development of advanced transfer-printing techniques, this work and its continuation are uniquely placed to integrate various colour  $\mu$ LEDs to diamond- or silicon-based devices with state-of-the-art capabilities. PA printing and the current contacting scheme could be directly applied to e.g GaAs-based red  $\mu$ LEDs, with innate modularity as LED type can be chosen *ad hoc* for each “slot”. Such devices, just one iteration away from the current diamond prototypes, could then be directly adapted to the request of neuroscientists for specific optogenetic protocols.

## 6.4 Future work

### 6.4.1 Upscaled fabrication process for mid-volume fabrication

Growth techniques of synthetic diamond have been quickly progressing in the last decade, making available cheaper, larger-scale material for an expanding market . Freestanding

ultrathin single-crystal (SC) diamond membranes still cannot currently be grown to large sample sizes ( $< 10\text{mm} \times 10\text{mm}$ , [61]). However, large-area ( $> 4$  inches) wafers of thin polycrystalline (PC, down to  $10\mu\text{m}$ ) diamond with thermal properties close to those of SC diamond have recently become available [62].

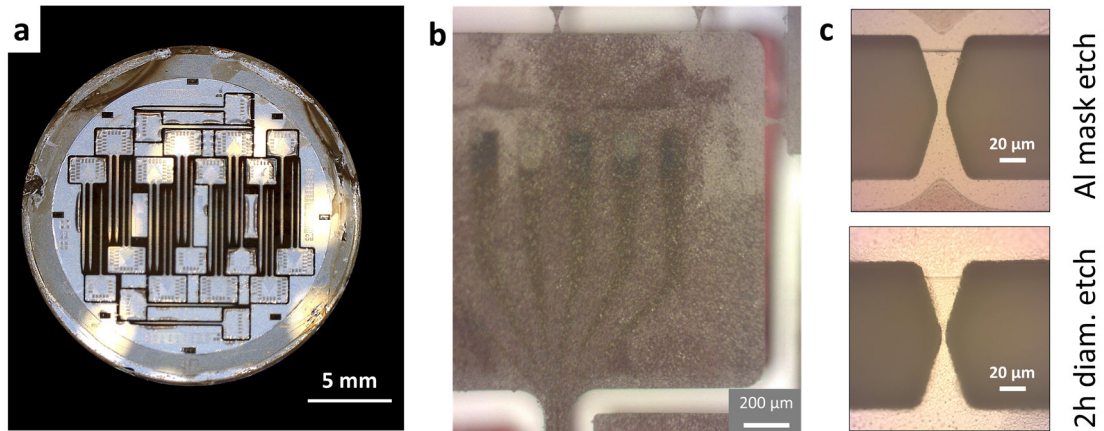


Figure 6.5 : Scalability is achievable through use of large-area polycrystalline (PC) diamond wafers. **a)** Fully through-etched 20mm-diameter PC membrane, showing all 20 probes separated. The centre area was unaffected by edge-bead and all probe structures were correctly defined. Parylene delamination was more severe at wafer edge than on smaller single-crystal samples and need to be addressed to yield functioning probes (section 6.2.3). **b)** Micrograph of the flipped probe base showing breakable anchors to the contour-etched structures and **c)** close-up of the anchor immediately after aluminium mask etching (notch width  $\sim 8\mu\text{m}$ ) and after two hours diamond etching from the topside (notch  $\sim 3\text{-}4\mu\text{m}$ ).

A 20mm-diameter PC wafer was used in this work to demonstrate scalability of diamond optrode production. The fully processed sample is shown on Figure 6.5.a, and contains a total of 20 probes of designs D100 and D50 (section 4.2.3). After diamond etching, each probe remains attached to the wafer base through specifically designed narrow anchors, which can be easily broken to release the given device. Singulated devices could not be tested as the PC sample suffered from parylene delamination more pronounced than on smaller SC samples, due to increased strain over its larger area. However, devices tested on the PC wafer during processing exhibited the same opto-electrical characteristics as those on SC diamond. As such there is high confidence that the deposition of an adequate, stress-free bioinsulation layer such as high-quality silicon carbide will enable the production of fully functional, low-cost, highly efficient polycrystalline diamond optrodes with properties matching or close to those of the single-crystal devices presented in this work.

### 6.4.2 Hybridisation of existing, commercially available devices

The processes developed in the frame of this project are versatile. TP- $\mu$ LED fabrication and picodroplet adhesive (PA) printing allow the transfer of tailor-made light emitters onto a very wide range of potential substrates. These capabilities could be harnessed to endow virtually any recording probe with light-emitting capabilities, using relatively minor adjustments to their fabrication process.

A first-step demonstrator of this potential application has been realised on a NeuroNexus commercial wafer (Figure 6.6). NeuroNexus probes are widely used for neuro-electrophysiology and provide a commercial standard of limited cost, high reliability and versatility thanks to a large device catalogue [63]. As a proof-of concept, 8 TP- $\mu$ LEDs were PA-printed on the 4 shanks of a “Buzsaki”-type probe on a 4” wafer (final stage before separation) sent by the company. The  $\mu$ LEDs reduced dimensions are compatible with the probe low footprint (Figure 6.6.c). PA printing resulted in a 100% transfer success at first try, with  $\pm 1\mu\text{m}$  precision. The total printing time added up to  $\sim 45$  minutes, but could be greatly reduced by automation.

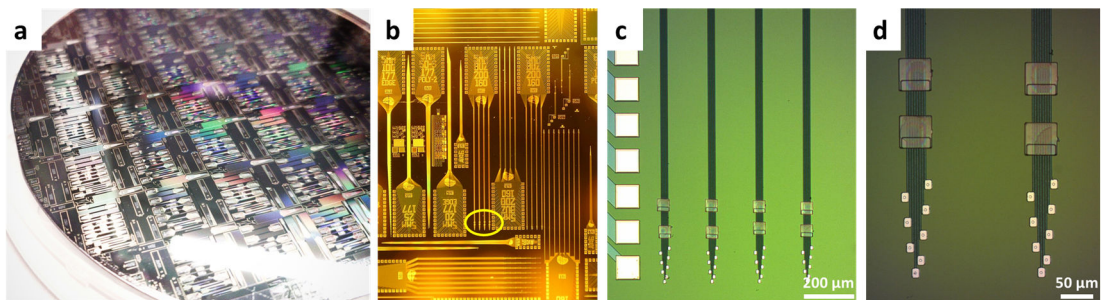


Figure 6.6 :  $50 \times 50 \mu\text{m}^2$   $\mu$ LEDs printed on a commercial NeuroNexus 4” wafer as a proof of concept for integration with existing medium-volume technology. **a)** Wafer as received from NeuroNexus ( $\sim 500$  probes/wafer). **b)** Wafer region chosen for printing (4-shank “Buzsaki 200” design). **c)** Micrograph of shank tip showing 8 printed  $\mu$ LEDs and **d)** close-up on two shanks showing detailed structure.

This demonstrates a directly feasible path to hybrid integration onto state-of-the-art devices, with only 2 more photolithography steps (and mask designs) to be added to the process (insulation and contact metallisation). Arrays of such TP- $\mu$ LEDs could also be embedded in this way onto high electrode count probes such as the CMOS-based Neuropixel devices [64] or other emerging high-density devices [65]–[70] providing both precise, tunable multisite optical stimulation and high-volume neuronal recording, a crucial feature for perturbative study of large neural networks [2]. Light-induced artifacts in the CMOS structure, potentially

detrimental to the operation of such probes [71], could be minimised by backside mirroring and adequate  $\mu$ LED operation parameters as described in section 3.4.

### 6.4.3 Wireless optrodes

Probes using wireless protocols for power and/or data transmission could be very useful for the neuroscience community as they can greatly facilitate experiments with freely behaving animals. Wirelessly powered systems have been proposed using batteries [72], photovoltaics [73], radio frequency transmission [14], [74]–[76], or inductive coupling [77], [78]. All these technologies could drive  $\mu$ LEDs at the electrical power used in this work, but must abide by stringent regulation on weight regulations (e.g normal total headweight < 3g for mice in UK). For wireless data transfer, transmission rates must be very high to accommodate the large datasets produced through electrophysiological recordings : at a sampling rate of 20kHz and a resolution of 12 bit, a high-density 100-channel interface needs to transmit at a rate of 24Mbps. This is not straightforward given the added constraints on antenna size and power. However, it could be achieved in a scalable approach by using visible light communication (“Li-Fi” technology [79]), creating an optical link comprising a transmitting red LED and a receiving photodiode. Rates exceeding 5Gb/s in free space have been demonstrated using this technology [80]. A miniaturised, low-weight prototype for data transfer has been developed at the Institute of Photonics specifically for neural probes [81].

### 6.4.4 Multifunctional devices and electronics on chip

The transfer-printing methods developed here for  $\mu$ LEDs can be extended to a wide range of releasable “inks”. Transfer-printing of optoelectronic components or CMOS-type ICs has been demonstrated at volume scale [82]–[85]. This opens a path for volume production of modular, multifunctional devices tailored for specific applications. As an example, rigid diamond- or silicon-carbide probes patterned with metal electrodes and temperature sensors could then be integrated with various  $\mu$ LED emitters, transfer-printable photodiodes for real-time *in vivo* photodetection, and printed ASICs for electrode readout (amplification and serialisation), enabling unparalleled capacities for multimodal interrogation of complex neural circuits. Such transfer-printing based integration could also help functionalise polymer-based, highly flexible recording devices capable of long-term scar-free neural



integration [86], [87], maximising their potential for experiments during long-term implantation.

On-probe integration of signal processing capabilities is sought after as a means of improving noise and artifact resistance through active filtering, reducing shank dimensions and scaling up recording sites by increasing routing density, and simplifying device connectivity and data transmission [64], [66], [67], [88], [89]. Volume-produced CMOS circuitry fabricated at a standard foundry as well as  $\mu$ LED current sources could be embedded directly on non-silicon probe substrates to facilitate ultra-parallel optogenetic stimulation and recording.

#### 6.4.5 Probe arrays and 3D stacking

Due to SC diamond dimensions and for prototype simplicity, only single- and dual-shank probe have been designed in this work. Further design iterations could easily extend to multi-shank devices for high-density photostimulation/recording, inspired by well-established designs offered commercially e.g by NeuroNexus [90], or by previous devices developed at the Institute of Photonics (6-shank, 96- $\mu$ LED probe by Scharf et al. [5]).

Furthermore, with chip stacking now an industry standard [91], such 2D arrays could be extended to produce 3D arrays densely mapping a small brain volume e.g through dual-sided fabrication [92]–[94] and/or stacking arrays on top of each other with dielectric spacers [69], [95], [96]. The probes could e.g be bonded onto arrays of thin (e.g 0.5mm) double-sided PCBs, and driven using multiplexing and adequate control hardware.

## 6.5 Conclusion

The development process described in chapters 3, 4 and 5 led to the realisation of the first diamond optrodes. The devices, now at the latest stages of prototype refinement, are very close to *in vivo* implantation. Incorporated in its design plan, various features and improvement are readily accessible for the next fabrication stage, including the move to a hermetic insulation layer such as silicon carbide, on-probe temperature sensing capabilities, and multicolour integration e.g using externally-sourced existing  $\mu$ LEDs. Other features are suggested for later stages in order to exploit the full potential of these hybrid devices, produce them on larger scales, and further increase their functionality.

## References

- [1] E. Segev, J. Reimer, L. C. Moreaux, T. M. Fowler, D. Chi, W. D. Sacher, M. Lo, K. Deisseroth, A. S. Tolia, A. Faraon, and M. L. Roukes, “Patterned photostimulation via visible-wavelength photonic probes for deep brain optogenetics,” *Neurophotonics*, vol. 4, no. 1, p. 011002, 2016.
- [2] M. T. Alt, E. Fiedler, L. Rudmann, J. S. Ordonez, P. Ruther, and T. Stieglitz, “Let There Be Light-Optoprobes for Neural Implants,” *Proc. IEEE*, vol. 105, no. 1, pp. 101–138, 2017.
- [3] B. Fan and W. Li, “Miniaturized optogenetic neural implants: a review.,” *Lab Chip*, vol. 15, no. 19, pp. 3838–55, 2015.
- [4] R. Pashaie, P. Anikeeva, J. H. Lee, R. Prakash, O. Yizhar, M. Prigge, D. Chander, T. J. Richner, and J. Williams, “Optogenetic brain interfaces,” *IEEE Rev. Biomed. Eng.*, vol. 7, pp. 3–30, 2014.
- [5] R. Scharf, T. Tsunematsu, N. McAlinden, M. D. Dawson, S. Sakata, and K. Mathieson, “Depth-specific optogenetic control in vivo with a scalable, high-density  $\mu$ LED neural probe,” *Sci. Rep.*, vol. 6, no. January, p. 28381, 2016.
- [6] F. Wu, E. Stark, P. C. Ku, K. D. Wise, G. Buzsáki, and E. Yoon, “Monolithically Integrated  $\mu$ LEDs on Silicon Neural Probes for High-Resolution Optogenetic Studies in Behaving Animals,” *Neuron*, vol. 88, no. 6, pp. 1136–1148, 2015.
- [7] C. Gößler, C. Bierbrauer, R. Moser, M. Kunzer, K. Holc, W. Pletschen, K. Köhler, J. Wagner, M. Schwaerzle, P. Ruther, O. Paul, J. Neef, D. Keppeler, G. Hoch, T. Moser, and U. T. Schwarz, “GaN-based micro-LED arrays on flexible substrates for optical cochlear implants,” *J. Phys. D. Appl. Phys.*, vol. 47, no. 20, p. 205401, May 2014.
- [8] S. Ayub, C. Gossler, M. Schwaerzle, E. Klein, O. Paul, U. T. Schwarz, and P. Ruther, “High-density probe with integrated thin-film micro light emitting diodes ( $\mu$ LEDs) for optogenetic applications,” in *2016 IEEE 29th International Conference on Micro Electro Mechanical Systems (MEMS)*, 2016, pp. 379–382.
- [9] S. Ayub, L. J. Gentet, R. Fiáth, M. Schwaerzle, M. Borel, F. David, P. Barthó, I. Ulbert, O. Paul, and P. Ruther, “Hybrid intracerebral probe with integrated bare LED chips for optogenetic studies,” *Biomed. Microdevices*, vol. 19, no. 3, pp. 1–12, 2017.
- [10] F. Dehkoda, A. Soltan, N. Ponon, A. Jackson, A. O’Neill, and P. Degenaar, “Self-sensing of temperature rises on light emitting diode based optrodes,” *J. Neural Eng.*, vol. 15, no. 2, 2018.
- [11] S. Goncalves, J. Palha, H. Fernandes, M. Souto, S. Pimenta, T. Dong, Z. Yang, J. Ribeiro, and J. Correia, “LED Optrode with Integrated Temperature Sensing for Optogenetics,” *Micromachines*, vol. 9, no. 9, p. 473, 2018.
- [12] L. Li, C. Liu, Y. Su, J. Bai, J. Wu, Y. Han, Y. Hou, S. Qi, Y. Zhao, H. Ding, Y. Yan, L. Yin, P. Wang, Y. Luo, and X. Sheng, “Heterogeneous Integration of Microscale GaN Light-Emitting Diodes and Their Electrical, Optical, and Thermal Characteristics on Flexible Substrates,” *Adv. Mater. Technol.*, vol. 1700239, p. 1700239, 2017.

- [13] B. Fan, K. Kwon, R. Rechenberg, A. Khomenko, M. Haq, M. F. Becker, A. J. Weber, and W. Li, "A polycrystalline diamond-based, hybrid neural interfacing probe for optogenetics," *2015 28th IEEE Int. Conf. Micro Electro Mech. Syst.*, pp. 616–619, 2015.
- [14] T. Il Kim, J. G. McCall, Y. H. Jung, X. Huang, E. R. Siuda, Y. Li, J. Song, Y. M. Song, H. A. Pao, R. H. Kim, C. Lu, S. D. Lee, I. S. Song, G. Shin, R. Al-Hasani, S. Kim, M. P. Tan, Y. Huang, F. G. Omenetto, J. A. Rogers, and M. R. Bruchas, "Injectable, cellular-scale optoelectronics with applications for wireless optogenetics," *Science (80-. )*, vol. 340, no. 6129, pp. 211–216, 2013.
- [15] DISCO Hi-Tec Europe GmbH, "Grinding / thinning services." [Online]. Available: <https://www.dicing-grinding.com/services/grinding/>.
- [16] R. K. Sathir, W. J. James, H. K. Yasuda, A. K. Sharma, M. F. Nichols, and A. W. Haln, "The adhesion of glow-discharge polymers, Silastic and Parylene to implantable platinum electrodes: results of tensile pull tests after exposure to isotonic sodium chloride," *Biomaterials*, vol. 2, no. 4, pp. 239–243, 1981.
- [17] K. S. Hwang and J. H. Park, "Effect of Atmospheric-Plasma Treatments for Enhancing Adhesion of Au on Parylene-c-Coated Protein Chips," *J. Korean Phys. Soc.*, vol. 44, no. 5, pp. 1168–1172, 2004.
- [18] P. N. Wahjudi, J. H. Oh, S. O. Salman, J. A. Seabold, D. C. Rodger, Y. C. Tai, and M. E. Thompson, "Improvement of metal and tissue adhesion on surface-modified parylene C," *J. Biomed. Mater. Res. - Part A*, vol. 89, no. 1, pp. 206–214, 2009.
- [19] J. P. Seymour, Y. M. Elkasabi, H. Y. Chen, J. Lahann, and D. R. Kipke, "The insulation performance of reactive parylene films in implantable electronic devices," *Biomaterials*, vol. 30, no. 31, pp. 6158–6167, 2009.
- [20] J.-M. Hsu, L. Rieth, S. Kammer, M. Orthner, and F. Solzbacher, "Effect of Thermal and Deposition Processes on the Surface Morphology, Crystallinity, and Adhesion of Parylene-C," *Sens. Mater*, vol. 20, no. 2008, pp. 87–102, 2008.
- [21] J. Ortigoza-Diaz, K. Scholten, C. Larson, A. Cobo, T. Hudson, J. Yoo, A. Baldwin, A. Weltman Hirschberg, and E. Meng, "Techniques and Considerations in the Microfabrication of Parylene C Microelectromechanical Systems," *Micromachines*, vol. 9, no. 9, p. 422, 2018.
- [22] W. Li, D. Rodger, P. Menon, and Y.-C. Tai, "Corrosion Behavior of Parylene-Metal-Parylene Thin Films in Saline," *ECS Trans.*, vol. 11, no. 18, pp. 1–6, 2008.
- [23] J. M. Hsu, L. Rieth, R. A. Normann, P. Tathireddy, and F. Solzbacher, "Encapsulation of an integrated neural interface device with parylene C," *IEEE Trans. Biomed. Eng.*, vol. 56, no. 1, pp. 23–29, 2009.
- [24] R. P. Von Metzen and T. Stieglitz, "The effects of annealing on mechanical, chemical, and physical properties and structural stability of Parylene C," *Biomed. Microdevices*, vol. 15, no. 5, pp. 727–735, 2013.
- [25] J. Charmet, J. Bitterli, O. Sereda, M. Liley, P. Renaud, and H. Keppner, "Optimizing parylene C

- adhesion for MEMS processes: Potassium hydroxide wet etching," *J. Microelectromechanical Syst.*, vol. 22, no. 4, pp. 855–864, 2013.
- [26] J. Ortigoza-diaz, K. Scholten, and E. Meng, "Characterization and Modification of Adhesion in Dry and Wet Environments in Thin-Film Parylene Systems," *J. Microelectromechanical Syst.*, vol. PP, pp. 1–12, 2018.
- [27] R. Huang and Y. C. Tai, "Parylene to silicon adhesion enhancement," in *TRANSDUCERS 2009 - 2009 International Solid-State Sensors, Actuators and Microsystems Conference*, 2009, pp. 1027–1030.
- [28] C. Hassler, R. P. Von Metzen, P. Ruther, and T. Stieglitz, "Characterization of parylene C as an encapsulation material for implanted neural prostheses," *J. Biomed. Mater. Res. - Part B Appl. Biomater.*, vol. 93, no. 1, pp. 266–274, 2010.
- [29] C. Pang, "Parylene Technology for Neural Probes Applications," vol. 2008, p. 191, 2008.
- [30] J. M. Maloney, S. A. Lipka, and S. P. Baldwin, "In Vivo Biostability of CVD Silicon Oxide and Silicon Nitride Films," *MRS Online Proc. Libr.*, vol. 872, p. null-null, 2005.
- [31] M. Jorfi, J. L. Skousen, C. Weder, and J. R. Capadona, "Progress towards biocompatible intracortical microelectrodes for neural interfacing applications," *J. Neural Eng.*, vol. 12, no. October, p. 011001, 2015.
- [32] R. Maboudian, C. Carraro, D. G. Senesky, and C. S. Roper, "Advances in silicon carbide science and technology at the micro- and nanoscales," *J. Vac. Sci. Technol. A Vacuum, Surfaces, Film.*, vol. 31, no. 5, p. 050805, 2013.
- [33] M. Amon, A. Bolz, and M. Schaldach, "Improvement of stenting therapy with a silicon carbide coated tantalum stent," *J. Mater. Sci. Mater. Med.*, vol. 7, no. 5, pp. 273–278, 1996.
- [34] A. Rzany and M. Schaldach, "Smart Material Silicon Carbide: Reduced Activation of Cells and Proteins on a-SiC:H-coated Stainless Steel," *Prog. Biomed. Res.*, vol. 6, no. 5, pp. 182–194, 2001.
- [35] G. Kotzar, M. Freas, P. Abel, A. Fleischman, S. Roy, C. Zorman, J. M. Moran, and J. Melzak, "Evaluation of MEMS materials of construction for implantable medical devices," *Biomaterials*, vol. 23, no. 13, pp. 2737–2750, 2002.
- [36] X. Lei, S. Kane, S. Cogan, H. Lorach, L. Galambos, P. Huie, K. Mathieson, T. Kamins, J. Harris, and D. Palanker, "SiC protective coating for photovoltaic retinal prosthesis," *J. Neural Eng.*, vol. 13, no. 4, p. 046016, 2016.
- [37] M. J. Loboda and K. W. Michael, "Silicon carbide metal diffusion barrier layer," 5818071, 1998.
- [38] S. Merchant, S. Misra, and P. Roy, "Silicon carbide barrier layers for porous low dielectric constant materials," 6100587, 2000.
- [39] S. F. Cogan, D. J. Edell, A. A. Guzelian, Y. P. Liu, and R. Edell, "Plasma-enhanced chemical vapor deposited silicon carbide as an implantable dielectric coating," *J. Biomed. Mater. Res. - Part A*, vol. 67, no. 3, pp. 856–867, 2003.

- [40] C. A. Diaz-Botia, L. E. Luna, R. M. Neely, M. Chamanzar, C. Carraro, J. M. Carmena, P. N. Sabes, R. Maboudian, and M. M. Maharbiz, "A silicon carbide array for electrocorticography and peripheral nerve recording," *J. Neural Eng.*, vol. 14, no. 5, p. 056006, Oct. 2017.
- [41] H. A. MacLeod, *Thin Film Optical Filters, 4th edition*. CRC Press, 2010.
- [42] J. Zhang, "Hyper-NA Optical Systems and Applications in Sample Measurement," University of Arizona, 2010.
- [43] N. McAlinden, E. Gu, M. D. Dawson, S. Sakata, and K. Mathieson, "Optogenetic activation of neocortical neurons in vivo with a sapphire-based micro-scale LED probe," *Front. Neural Circuits*, vol. 9, no. May, p. 25, 2015.
- [44] N. C. Klapoetke, Y. Murata, S. S. Kim, S. R. Pulver, A. Birdsey-Benson, Y. K. Cho, T. K. Morimoto, A. S. Chuong, E. J. Carpenter, Z. Tian, J. Wang, Y. Xie, Z. Yan, Y. Zhang, B. Y. Chow, B. Surek, M. Melkonian, V. Jayaraman, M. Constantine-Paton, G. K.-S. Wong, and E. S. Boyden, "Independent optical excitation of distinct neural populations.," *Nat. Methods*, vol. 11, no. 3, pp. 338–46, 2014.
- [45] R. B. Belsler and W. H. Hicklin, "Temperature Coefficients of Resistance of Metallic Films in the Temperature Range 25° to 600°C Temperature Coefficients of Resistance of Metallic Films\* in the Temperature Range 25° to 600°C," *J. Appl. Phys. J. Appl. Phys. J. Chem. Phys. J. Chem. Phys. J. Appl. Phys.*, vol. 30, no. 3, pp. 2658–751, 1959.
- [46] K. L. Zhang, S. K. Chou, and S. S. Ang, "Fabrication, modeling and testing of a thin film Au/Ti microheater," *Int. J. Therm. Sci.*, vol. 46, no. 6, pp. 580–588, 2007.
- [47] R. Shrestha, T. Y. Choi, W. Chang, and D. Kim, "A high-precision micropipette sensor for cellular-level real-time thermal characterization," *Sensors*, vol. 11, no. 9, pp. 8826–8835, 2011.
- [48] D. H. Kim, S. Wang, H. Keum, R. Ghaffari, Y. S. Kim, H. Tao, B. Panilaitis, M. Li, Z. Kang, F. Omenetto, Y. Huang, and J. A. Rogers, "Thin, flexible sensors and actuators as 'instrumented' surgical sutures for targeted wound monitoring and therapy," *Small*, vol. 8, no. 21, pp. 3263–3268, 2012.
- [49] J. Chen and K. D. Wise, "A silicon probe with integrated microheaters for thermal marking and monitoring of neural tissue," *IEEE Trans. Biomed. Eng.*, vol. 44, no. 8, pp. 770–774, 1997.
- [50] R. Gomez, N. Noguera, a. Ivorra, R. Villa, J. Aguilo, J. Millan, J. Lopez, L. Palacios, a. Sola, and G. Hotter, "Instrumentation system for in vivo organ studies," *2001 Int. Semicond. Conf. CAS 2001 Proc. (Cat. No.01TH8547)*, vol. 1, 2001.
- [51] Y. M. and M. A. M. Gijs, "Miniaturized Flexible Temperature Sensor," *J. Microelectromechanical Syst.*, vol. 16, no. 6, pp. 1349–1354, 2007.
- [52] M. F. P. Cruz, E. Fiedler, O. F. C. Monjarás, and T. Stieglitz, "Integration of temperature sensors in polyimide-based thin-film electrode arrays," *Curr. Dir. Biomed. Eng.*, vol. 1, no. 1, pp. 529–533, 2015.
- [53] A. Koh, S. R. Gutbrod, J. D. Meyers, C. Lu, R. C. Webb, G. Shin, Y. Li, S. K. Kang, Y. Huang, I. R.

- Efimov, and J. A. Rogers, “Ultrathin Injectable Sensors of Temperature, Thermal Conductivity, and Heat Capacity for Cardiac Ablation Monitoring,” *Adv. Healthc. Mater.*, vol. 5, no. 3, pp. 373–381, 2016.
- [54] Y. Zhang, R. C. Webb, H. Luo, Y. Xue, J. Kurniawan, N. H. Cho, S. Krishnan, Y. Li, Y. Huang, and J. A. Rogers, “Theoretical and Experimental Studies of Epidermal Heat Flux Sensors for Measurements of Core Body Temperature,” *Adv. Healthc. Mater.*, vol. 5, no. 1, pp. 119–127, 2016.
- [55] Z. Fekete, M. Csernai, K. Kocsis, Á. C. Horváth, A. Pongrácz, and P. Barthó, “Simultaneous in vivo recording of local brain temperature and electrophysiological signals with a novel neural probe,” *J. Neural Eng.*, vol. 14, no. 3, p. 034001, Jun. 2017.
- [56] O. Yizhar, L. E. Fenno, T. J. Davidson, M. Mogri, and K. Deisseroth, “Optogenetics in Neural Systems,” *Neuron*, vol. 71, no. 1, pp. 9–34, 2011.
- [57] E. Stark, T. Koos, and G. Buzsáki, “Diode probes for spatiotemporal optical control of multiple neurons in freely moving animals,” *J. Neurophysiol.*, vol. 108, no. 1, pp. 349–63, 2012.
- [58] K. Kampasi, E. Stark, J. Seymour, K. Na, H. G. Winful, G. Buzsáki, K. D. Wise, and E. Yoon, “Fiberless multicolor neural optoelectrode for in vivo circuit analysis,” *Sci. Rep.*, vol. 6, no. August, p. 30961, 2016.
- [59] R. Scharf, A. Boudet, M. Dawson, S. Sakata, and K. Mathieson, “Next-generation high-density  $\mu$ LED probes for depth-specific stimulation,” in *Optogen 2016*, 2016.
- [60] C. A. Bower, M. A. A. Meitl, B. Raymond, E. Radauscher, R. Cok, S. Bonafede, D. Gomez, T. Moore, C. Prevatte, B. Fisher, R. Rotzoll, G. A. Melnik, A. Fecioru, and A. J. Trindade, “Emissive displays with transfer-printed assemblies of  $8 \mu\text{m} \times 15 \mu\text{m}$  inorganic light-emitting diodes,” *Photonics Res.*, vol. 5, no. 2, pp. 23–29, 2017.
- [61] Excellent Diamond Products Japan, “Diamond membranes.” [Online]. Available: <http://www.d-edp.jp/en/products.html>. [Accessed: 05-Aug-2018].
- [62] Diamond Materials GmbH, “CVD Diamond wafers.” [Online]. Available: [http://www.diamond-materials.com/EN/products/disks\\_films\\_membranes/disks.htm](http://www.diamond-materials.com/EN/products/disks_films_membranes/disks.htm). [Accessed: 02-Aug-2018].
- [63] Neuronexus, “Neural Probes,” 2018. [Online]. Available: <http://neuronexus.com/products/neural-probes/>. [Accessed: 01-Sep-2018].
- [64] J. J. Jun, N. A. Steinmetz, J. H. Siegle, D. J. Denman, M. Bauza, B. Barbarits, A. K. Lee, C. A. Anastassiou, A. Andrei, Ç. Aydin, M. Barbic, T. J. Blanche, V. Bonin, J. Couto, B. Dutta, S. L. Gratiy, D. A. Gutnisky, M. Häusser, B. Karsh, P. Ledochowitsch, C. M. Lopez, C. Mitelut, S. Musa, M. Okun, M. Pachitariu, J. Putzeys, P. D. Rich, C. Rossant, W. L. Sun, K. Svoboda, M. Carandini, K. D. Harris, C. Koch, J. O’Keefe, and T. D. Harris, “Fully integrated silicon probes for high-density recording of neural activity,” *Nature*, vol. 551, no. 7679, pp. 232–236, 2017.
- [65] A. Berényi, Z. Somogyvári, A. J. Nagy, L. Roux, J. D. Long, S. Fujisawa, E. Stark, A. Leonardo, T. D. Harris, and G. Buzsáki, “Large-scale, high-density (up to 512 channels) recording of local

- circuits in behaving animals.,” *J. Neurophysiol.*, vol. 111, no. 5, pp. 1132–49, 2014.
- [66] G. Buzsáki, E. Stark, A. Berényi, D. Khodagholy, D. R. Kipke, E. Yoon, and K. D. Wise, “Tools for probing local circuits: High-density silicon probes combined with optogenetics,” *Neuron*, vol. 86, no. 1, pp. 92–105, 2015.
- [67] B. C. Raducanu, R. F. Yazicioglu, C. M. Lopez, M. Ballini, J. Putzeys, S. Wang, A. Andrei, V. Rochus, M. Welkenhuysen, N. van Helleputte, S. Musa, R. Puers, F. Kloosterman, C. van Hoof, R. Fiáth, I. Ulbert, and S. Mitra, “Time Multiplexed Active Neural Probe with 1356 Parallel Recording Sites,” *Sensors*, vol. 17, no. 10, p. 2388, Oct. 2017.
- [68] J. Scholvin, J. P. Kinney, J. G. Bernstein, C. Moore-Kochlacs, N. Kopell, C. G. Fonstad, and E. S. Boyden, “Close-packed silicon microelectrodes for scalable spatially oversampled neural recording,” *IEEE Trans. Biomed. Eng.*, vol. 63, no. 1, pp. 120–130, 2016.
- [69] G. Rios, E. V. Lubenov, D. Chi, M. L. Roukes, and A. G. Siapas, “Nanofabricated Neural Probes for Dense 3-D Recordings of Brain Activity,” *Nano Lett.*, vol. 16, no. 11, pp. 6857–6862, 2016.
- [70] J. L. Shobe, L. D. Claar, S. Parhami, K. I. Bakhurin, and S. C. Masmanidis, “Brain activity mapping at multiple scales with silicon microprobes containing 1,024 electrodes,” *J. Neurophysiol.*, vol. 114, no. 3, pp. 2043–2052, Sep. 2015.
- [71] N. A. Steinmetz, C. Koch, K. D. Harris, and M. Carandini, “Challenges and opportunities for large-scale electrophysiology with Neuropixels probes,” *Curr. Opin. Neurobiol.*, vol. 50, pp. 92–100, 2018.
- [72] Y. Iwai, S. Honda, H. Ozeki, M. Hashimoto, and H. Hirase, “A simple head-mountable LED device for chronic stimulation of optogenetic molecules in freely moving mice,” *Neurosci. Res.*, vol. 70, no. 1, pp. 124–127, 2011.
- [73] S. Il Park, G. Shin, A. Banks, J. G. McCall, E. R. Siuda, M. J. Schmidt, H. U. Chung, K. N. Noh, J. G.-H. Mun, J. Rhodes, M. R. Bruchas, and J. a Rogers, “Ultraminiaturized photovoltaic and radio frequency powered optoelectronic systems for wireless optogenetics,” *J. Neural Eng.*, vol. 12, no. 5, p. 056002, 2015.
- [74] K. L. Montgomery, A. J. Yeh, J. S. Ho, V. Tsao, S. Mohan Iyer, L. Grosenick, E. A. Ferenczi, Y. Tanabe, K. Deisseroth, S. L. Delp, and A. S. Y. Poon, “Wirelessly powered, fully internal optogenetics for brain, spinal and peripheral circuits in mice,” *Nat. Methods*, vol. 12, no. 10, pp. 969–974, 2015.
- [75] M. A. Rossi, V. Go, T. Murphy, Q. Fu, J. Morizio, and H. H. Yin, “A wirelessly controlled implantable LED system for deep brain optogenetic stimulation,” *Front. Integr. Neurosci.*, vol. 9, no. February, p. 8, 2015.
- [76] S. Il Park, D. S. Brenner, G. Shin, C. D. Morgan, B. A. Copits, H. U. Chung, M. Y. Pullen, K. N. Noh, S. Davidson, S. J. Oh, J. Yoon, K.-I. Jang, V. K. Samineni, M. Norman, J. G. Grajales-Reyes, S. K. Vogt, S. S. Sundaram, K. M. Wilson, J. S. Ha, R. Xu, T. Pan, T.-I. Kim, Y. Huang, M. C. Montana, J. P. Golden, M. R. Bruchas, R. W. Gereau, and J. A. Rogers, “Soft, stretchable, fully implantable

- miniaturized optoelectronic systems for wireless optogenetics.," *Nat. Biotechnol.*, vol. 33, no. 12, pp. 1280–1286, 2015.
- [77] K. Y. Kwon, H.-M. Lee, M. Ghovanloo, A. Weber, and W. Li, "Design, fabrication, and packaging of an integrated, wirelessly-powered optrode array for optogenetics application.," *Front. Syst. Neurosci.*, vol. 9, no. May, p. 69, 2015.
- [78] G. Shin, A. M. Gomez, R. Al-Hasani, Y. R. Jeong, J. Kim, Z. Xie, A. Banks, S. M. Lee, S. Y. Han, C. J. Yoo, J. L. Lee, S. H. Lee, J. Kurniawan, J. Tureb, Z. Guo, J. Yoon, S. Il Park, S. Y. Bang, Y. Nam, M. C. Walicki, V. K. Samineni, A. D. Mickle, K. Lee, S. Y. Heo, J. G. McCall, T. Pan, L. Wang, X. Feng, T. il Kim, J. K. Kim, Y. Li, Y. Huang, R. W. Gereau, J. S. Ha, M. R. Bruchas, and J. A. Rogers, "Flexible Near-Field Wireless Optoelectronics as Subdermal Implants for Broad Applications in Optogenetics," *Neuron*, vol. 93, no. 3, p. 509–521.e3, 2017.
- [79] D. Tsonev, H. Chun, S. Rajbhandari, J. J. D. McKendry, S. Videv, E. Gu, M. Haji, S. Watson, A. E. Kelly, G. Faulkner, M. D. Dawson, H. Haas, and D. O'Brien, "A 3-Gb/s Single-LED OFDM-Based Wireless VLC Link Using a Gallium Nitride  $\mu$ LED," *IEEE Photonics Technol. Lett.*, vol. 26, no. 7, pp. 637–640, Apr. 2014.
- [80] S. Rajbhandari, J. J. D. McKendry, J. Herrnsdorf, H. Chun, G. Faulkner, H. Haas, I. M. Watson, D. O'Brien, and M. D. Dawson, "A review of gallium nitride LEDs for multi-gigabit-per-second visible light data communications," *Semicond. Sci. Technol.*, vol. 32, no. 2, p. 023001, Feb. 2017.
- [81] G. Varkonyi, J. J. D. McKendry, N. McAlinden, M. D. Dawson, and K. Mathieson, "Data transmission for high-bandwidth neural interfacing using visible light communication," in *2016 IEEE Photonics Conference (IPC)*, 2016, pp. 41–42.
- [82] A. Carlson, A. M. Bowen, Y. Huang, R. G. Nuzzo, and J. A. Rogers, "Transfer printing techniques for materials assembly and micro/nanodevice fabrication," *Adv. Mater.*, vol. 24, no. 39, pp. 5284–5318, 2012.
- [83] J. Justice, C. Bower, M. Meitl, M. B. Mooney, M. A. Gubbins, and B. Corbett, "Wafer-scale integration of group III–V lasers on silicon using transfer printing of epitaxial layers," *Nat. Photonics*, vol. 6, no. 9, pp. 610–614, Sep. 2012.
- [84] X. Sheng, C. A. Bower, S. Bonafede, J. W. Wilson, B. Fisher, M. Meitl, H. Yuen, S. Wang, L. Shen, A. R. Banks, C. J. Corcoran, R. G. Nuzzo, S. Burroughs, and J. A. Rogers, "Printing-based assembly of quadruple-junction four-terminal microscale solar cells and their use in high-efficiency modules," *Nat. Mater.*, vol. 13, no. 6, pp. 593–598, Jun. 2014.
- [85] B. Corbett, R. Loi, W. Zhou, D. Liu, and Z. Ma, "Transfer print techniques for heterogeneous integration of photonic components," *Prog. Quantum Electron.*, vol. 52, pp. 1–17, Mar. 2017.
- [86] L. Luan, X. Wei, Z. Zhao, J. J. Siegel, O. Potnis, C. A. Tuppen, S. Lin, S. Kazmi, R. A. Fowler, S. Holloway, A. K. Dunn, R. A. Chitwood, and C. Xie, "Ultraflexible nanoelectronic probes form reliable, glial scar-free neural integration," *Sci. Adv.*, vol. 3, no. 2, p. e1601966, 2017.



- [87] J. W. Jeong, G. Shin, S. Il Park, K. J. Yu, L. Xu, and J. A. Rogers, "Soft materials in neuroengineering for hard problems in neuroscience," *Neuron*, vol. 86, no. 1, pp. 175–186, 2015.
- [88] J. Viventi, D.-H. Kim, L. Vigeland, E. S. Frechette, J. a Blanco, Y.-S. Kim, A. E. Avrin, V. R. Tiruvadi, S.-W. Hwang, A. C. Vanleer, D. F. Wulsin, K. Davis, C. E. Gelber, L. Palmer, J. Van der Spiegel, J. Wu, J. Xiao, Y. Huang, D. Contreras, J. a Rogers, and B. Litt, "Flexible, foldable, actively multiplexed, high-density electrode array for mapping brain activity in vivo.," *Nat. Neurosci.*, vol. 14, no. 12, pp. 1599–605, 2011.
- [89] A. H. Marblestone, B. M. Zamft, Y. G. Maguire, M. G. Shapiro, T. R. Cybulski, J. I. Glaser, D. Amodei, P. B. Stranges, R. Kalhor, D. A. Dalrymple, D. Seo, E. Alon, M. M. Maharbiz, J. M. Carmena, J. M. Rabaey, E. S. Boyden, G. M. Church, and K. P. Kording, "Physical principles for scalable neural recording," *Front. Comput. Neurosci.*, vol. 7, no. October, pp. 1–34, 2013.
- [90] Neuronexus, "Standard Probes - 'Buzsaki', 256 channels," 2018. [Online]. Available: <http://neuronexus.com/products/neural-probes/standard-probes/>. [Accessed: 01-Aug-2018].
- [91] Amkor Technology, "3D die stacking." [Online]. Available: <https://amkor.com/technology/3d-stacked-die/>.
- [92] F. Barz, T. Holzhammer, O. Paul, and P. Ruther, "Novel technology for the in-plane to out-of-plane transfer of multiple interconnection lines in 3D neural probes," *2013 Transducers Eurosensors XXVII 17th Int. Conf. Solid-State Sensors, Actuators Microsystems, TRANSDUCERS EUROSENSORS 2013*, no. June, pp. 884–887, 2013.
- [93] F. Barz, O. Paul, and P. Ruther, "Modular assembly concept for 3D neural probe prototypes offering high freedom of design and alignment precision," *Conf. Proc. ... Annu. Int. Conf. IEEE Eng. Med. Biol. Soc. IEEE Eng. Med. Biol. Soc. Annu. Conf.*, vol. 2014, pp. 3977–3980, 2014.
- [94] Y. T. Lee, D. Moser, T. Holzhammer, W. Fang, O. Paul, and P. Ruther, "Ultrathin, dual-sided silicon neural microprobes realized using BCB bonding and aluminum sacrificial etching," *Proc. IEEE Int. Conf. Micro Electro Mech. Syst.*, pp. 1021–1024, 2013.
- [95] J. Du, M. L. Roukes, and S. C. Masmanidis, "Dual-side and three-dimensional microelectrode arrays fabricated from ultra-thin silicon substrates," *J. Micromechanics Microengineering*, vol. 19, p. 075008, 2009.
- [96] A. N. Zorzos, J. Scholvin, E. S. Boyden, and C. G. Fonstad, "Three-dimensional multiwaveguide probe array for light delivery to distributed brain circuits.," *Opt. Lett.*, vol. 37, no. 23, pp. 4841–3, 2012.

# Conclusion

130 years after the discovery of the neuron, understanding the brain neural circuits and their functional mechanisms remains a major challenge, now tackled on a global scale. Optogenetics provides a powerful perturbative technique for circuit analysis by allowing genetically tagged optical control of neural cells with high spatial and temporal resolution. The fast development of various “electrically actuating” membrane proteins photosensitive to a wide range of wavelengths and low optical powers, as well as the broadening of targeting solutions, paved the way for new experimental paradigms. Neural engineering now needs to complement these biological breakthroughs to implement systematic mapping of circuits of brain regions. This can be achieved by minimally invasive, high-density recording probes capable of precise multisite photostimulation. Inspired by recent developments in the field, this work introduced novel diamond-based optrodes and their associated fabrication techniques.

With its superior thermal properties, excellent biocompatibility and increasing availability, diamond holds a strong potential for the next generation of hybrid bioimplants. In this work we designed, fabricated and characterised the first minimally invasive, thermally efficient single-crystal diamond optrode prototype integrated with 8 transfer-printed AlInGaN  $\mu$ LEDs and 16 electrodes over two shanks. Specific techniques were developed for processing ultrathin diamond membranes, manufacturing efficient transfer-printing LEDs and for their advanced transfer-printing with good thermal contact on highly textured substrates, including CMOS chips and other unconventional surfaces.

The probe dimensions (shank width  $\sim 100\ \mu\text{m}$ ) and large irradiance range (up to  $\sim 300\text{mW}/\text{mm}^2$  per LED) approached those of state-of-the-art monolithic silicon-based optrodes, while thermal performance was improved by more than an order of magnitude. Once implanted the probes should allow simultaneous excitation and recording of deep cortical structures at multiple sites, while enabling high-power and/or high duty cycle photostimulation. Process scalability was demonstrated on polycrystalline diamond membrane (commercially available as wafers up to 4") and a final passivation process was proposed to enable *in vivo* experiments, hopefully opening the way to novel, inexpensive diamond-based tools for neurophotonics and biomedical applications.

## Appendix A1 : Deposition & Etch recipes

### A1.1 Photoresists used in this work

Photoresist	Type	Developer	Thickness range [ $\mu\text{m}$ ]
<b>Microposit S-1805</b>	Positive	Diluted Microposit MF-300 series "MicroDev" : DI 1:1	0.4 – 0.6
<b>Microposit S-1818</b>			1.7 – 2.1
<b>Megaposit SPR 220-4.5</b>			3.5 – 5
<b>Megaposit SPR 220-7.0</b>			6.5 – 8.5
<b>MRT ma-N 440</b>	Negative	maD 533-S (pure)	3 - 5
<b>MRT ma-N 1410</b>			0.9 – 1.2
<b>MRT ma-N 1420</b>			1.9 – 2.3

### A1.2 Deposition recipes

#### A1.2.a Dielectrics deposition

- o *Silicon dioxide*

SiO <sub>2</sub> PECVD deposition (Oxford 80+ Plasmalab)		Comments
<b>Recipe name</b>	"oxide200.rec"	
<b>Deposition rate [nm/min]</b>	<b>33 +/-2</b>	32-34nm/min, stable etch rate
<b>Temperature</b>	<b>300°C</b>	
<b>Gases [sccm]</b>	SiH <sub>4</sub> (170) / N <sub>2</sub> O (710) / He (16)	
<b>Process pressure</b>	CM Gauge : 1 Torr	
<b>Power [W]</b>	HF forward : 70 / HF reflected : 0	NB power switch at 30W RF mode : continuous
<b>Notes</b>	<i>Always use test sample to determine actual thickness Initial surface must be clean (solvent or O<sub>2</sub> plasma strip)</i>	

- o *Parylene-C*

Parylene-C deposition (SCS Labcoter2)					
Adhesion rating w/o primer (ASTMD3359*)	Ratio dimer weight [g] to thickness [um]	Pressure** [mTorr]	Dimer weight (+/- 0.01) [g]	Dep. time** [min]	Corresponding thickness*** [nm]
No primer : 0B VPD silane : 5B Liquid silane : 5B	~1.33 (<1.5um) ~1.43 (>2um)	<25	0.7 1.5 3 4.5	45-60	540 1150 2080 3120
<p>* Adhesion to glass (see A4); adhesion is affected by long heating periods and structure size.</p> <p>** Deposition time depends on set coating pressure and dimer quantity (lower maximum coating pressure will limit deposition rate through feedback control)</p> <p>*** Thickness given +/- 100nm : variation with position within chamber (thicker on top of fixture) and chamber load (increased samples surface -&gt; decrease in coating thickness)</p>					

### A1.2.b Metal deposition

- o *DC sputtering*

Metal deposition by DC sputtering							
Metal	Pressure [Torr]	Voltage [V]	Current [A]	Dep. rate [nm/min]	Predep. [min]	Typical dep. Time [min]	Corresponding thickness [nm]
Ti	$5 \times 10^{-7}$	260	6	~16	3	3.25	50
Au	$5 \times 10^{-7}$	480	3.2	65 +/- 5	0.25	3	195 +/- 15
Al	$5 \times 10^{-7}$	260	6	20-28	3	20	480 +/- 40

- o *E-beam evaporation*

Metal deposition by electron beam evaporation			
Metal	Deposition pressure [mbar]	Electron gun current [mA]	Recommended deposition rate [nm/s]
Pd	$< 1.5 \times 10^{-5}$	25-40	< 0.05
Ni	$< 1.5 \times 10^{-5}$	80-140	< 0.05
Au	$< 1 \times 10^{-5}$	50-90	< 0.05

## A1.3 Annealing recipes – Rapid thermal annealer

### A1.3.a Ni/Au annealing

	<b>Program 3 (RTA)</b>				
<b>Primary purpose</b>	<b>Annealing of evaporated Ni/Au film (LED spreading layer)</b>				
<b>Main annealing step</b>	510 °C – 180s - Air (50 sccm)				
<b>Detailed process steps</b>	Step #	Target T [°C]	Duration [s]	Gas [sccm]	Gas flow
	1	0	0	Air (50)	ON
	2	90	30	Air (50)	ON
	3	350	30	Air (50)	ON
	4	510	30	Air (50)	ON
	5	510	180	Air (50)	ON
	6	250	60	Air (50)	ON
	7	0	15	Air	OFF
<i>Notes</i>	<i>Unannealed Ni/Au (10nm/20nm) is highly transparent. After annealing, film shows slightly more opacity, roughness and a few dark inclusions.</i>				

### A1.3.b Pd annealing

	<b>Program 5 (RTA)</b>				
<b>Primary purpose</b>	<b>Annealing of evaporated Pd film (LED spreading layer)</b>				
<b>Main annealing step</b>	305 °C – 180s - N <sub>2</sub> (50sccm)				
<b>Detailed process steps</b>	Step #	Target T [°C]	Duration [s]	Gas [sccm]	Gas flow
	1	0	30	N <sub>2</sub>	OFF
	2	95	30	N <sub>2</sub> (50)	ON
	3	305	40	N <sub>2</sub> (50)	ON
	4	305	180	N <sub>2</sub> (50)	ON
	5	95	40	N <sub>2</sub> (50)	ON
	6	0	60	N <sub>2</sub> (50)	ON
<i>Notes</i>	<i>After annealing, Pd films appears much shinier (&gt;50nm thickness) and/or more opaque (&lt;50nm)</i>				

## A1.4 Wet etch recipes

### A1.4.a Table – wet etch rates

Measured / referenced etch rates of materials used in this work [nm/min]					
Wet etchant	HCl (pure) 21°C	Base piranha (RCA1) H <sub>2</sub> O:NH <sub>4</sub> OH:H <sub>2</sub> O <sub>2</sub> 5:1:1, 75°C	Acid piranha H <sub>2</sub> SO <sub>4</sub> :H <sub>2</sub> O <sub>2</sub> 3:1, 100°C	BOE 40%NH <sub>4</sub> F: 49%HF 7:1, 21°C	Hot KOH 40% w/w, 80°C
<b>Primary target material</b>	Oxide clean	Full organic clean (removes metal + oxide residues)	Full organic clean (+ metal residues)	Oxide strip SiO <sub>2</sub>	Si (100)
<b>PR (S1800 series)</b>	<20 (1)	high	>9200 (3)	0 (3)	>15000 (3)
<b>Si (100)</b>	0 (2)	0 (2)	0 (3)	0 (3)	>600 (4)
<b>SiO<sub>2</sub> PECVD</b>	Very slow		0 (3)	400-500	10-15
<b>Pd annealed (ebeam)</b>		high	3 (3)	~0 (delamination risk for >60s dips in BOE)	0 (3)
<b>Ni/Au annealed (ebeam)</b>		high	Ni : 380 (3)	~0 (delamination risk for >60s dips in BOE)	Ni : 0 (3) Au : NA
<b>Ti* (sputtered)</b>		high	240 (3)	>500 (3)	Soft material left (3)
<b>Au (sputtered)</b>		high	0 (3, given for Au evap)	0 (3, given for Au evap)	0 (3, Au evap)
<b>Al (sputtered)</b>	>500 (1)	high	>5000 (3)	> 100 (3)	>10000 (3)
<b>GaN</b>	NA			Slow	Anisotropic - plane etch attack
<b>Parylene C</b>	low	high	2.6 (3)	<5 (3)	0.42 (3)
<b>Diamond</b>	0	0	0	0	0

\* 50nm adhesion layer

**Gold-coloured cells: values directly measured by the author for etches done in the IoP cleanroom.**

**Referenced values [1]–[4] taken from :**

[1] E. Chen, "Harvard Applied Physics Course 298r - Fabrication techniques III : etching." 2004.

[2] W. Kern, "The Evolution of Silicon Wafer Cleaning Technology," *J. Electrochem. Soc.*, vol. 137, no. 6, p. 1887, Jun. 1990.

[3] K. R. Williams, K. Gupta, and M. Wasilik, "Etch rates for micromachining processing - Part II," *J. Microelectromechanical Syst.*, vol. 12, no. 6, pp. 761–778, 2003.

[4] M. Shikida, K. Sato, K. Tokoro, and D. Uchikawa, "Comparison of anisotropic etching properties between KOH and TMAH solutions," in *Technical Digest. IEEE International MEMS 99 Conference. Twelfth IEEE International Conference on Micro Electro Mechanical Systems (Cat. No.99CH36291)*, 1999, pp. 315–320.

#### A1.4.b Protocol for base piranha clean (RCA-1/SC1)

**H<sub>2</sub>O: Ammonium Hydroxide (NH<sub>4</sub>OH, 30% w/w) : Hydrogen Peroxide (H<sub>2</sub>O<sub>2</sub>, 30% w/w)  
(5:1:1)**

**Caution – dangerous etch: the etch must be performed with caution in a reserved extract bench with sash kept in down position, using adequate PPE (nitrile gloves + acid gauntlets, polypropylene apron, covering facemask). A glass thermometer must be used to monitor solution temperature at all times and all beakers generously rinsed in water after etch end.**

1. Start heating **325mL (100mL)** DI water in a Pyrex dish (*beaker*)
2. Gently add **65mL (20mL)** Ammonium Hydroxide FIRST
3. Heat to 70 +/- 5°C on hot plate, with constant thermometer check and gentle stirring
4. Temporarily removing from hot plate, slowly add **65mL (20mL)** H<sub>2</sub>O<sub>2</sub> SECOND; solution will bubble vigorously after 1-2min, indicating it is ready for use. Keep temperature within bounds of 70+/- 5°C
5. Soak the wafer or samples in solution for 15 to 30 minutes
6. Remove wafer/samples and rinse the wafer generously in DI water
7. After 10min cooling, dispose of solution down the drain with cold tap water to flush

#### A1.4.c Protocol for anisotropic etching of silicon in hot KOH etch

**KOH solution 40% w/w, 80°C**

**Caution – relatively dangerous etch: the etch must be performed with caution in a reserved extract bench with sash kept in down position, using adequate PPE (nitrile gloves + acid gauntlets, polypropylene apron, covering facemask). All beakers must be generously rinsed in water after etch end.**

1. Prepare a water bath by heating a large amount of DI water in a crystallising dish on hot plate (T=80 °C with feedback control)
2. In PTFE beaker with magnetic bottom, put magnetic spinner and pour precisely 40mL (*60mL*) DI water. Put beaker in water bath and ensure its stability and suitable bath height to evenly heat solution
3. Weigh 26.6g (*40g*) KOH pellets in plastic boat or beaker and rapidly add into PTFE beaker to avoid reaction with water vapour in air. Briefly set magnetic spinner at high speed (~800rpm) to fully dissolve pellets then set back to ~400rpm
4. Place sample holder in beaker; reaction will start and produce bubbling. Adjust stirring speed and cover beaker to stop evaporation and prevent photoelectric effects
5. After set etch time, retrieve samples from solution (NB: gentle handling whenever working with suspended 3D structures) and rinse generously in DI water
6. After 10min cooling, dispose of solution down the drain with cold tap water to flush



## A1.5 Dry etch recipes

### A1.5.a Inductively coupled plasma RIE etching - ICPs

#### o GaN etching

Recipe name	mLED3 (ICP#2)	KHSGaN4 (ICP#1)	Comments
Primary purpose	GaN etching	GaN etching	
Etch rates [nm/min]	GaN : ~390 SiO <sub>2</sub> : ~40 PR (S1805) : NA PR (maN-1410) : <500	GaN : ~450 SiO <sub>2</sub> : ~50 PR (S1805) : NA PR (maN-1410) : <500	Selectivity 10:1 to SiO <sub>2</sub>
Lithography	maN1410 OK S1800 series not tested	maN1410 OK S1800 series not tested	maN1410 withstands 1min40s etch but needs immediate matrix clean, 10min @ 250°C
Gases [sccm]	Ar (10) Cl <sub>2</sub> (30)	Ar (10) Cl <sub>2</sub> (30)	
Process pressure	5 mTorr	5 mTorr	
Power [W]	Coil : 400 Platen : 200	Coil : 400 Platen : 200	DC bias : 700-750V Peak-to-peak voltage : 1700-1800V
Notes	<i>Typical etch from p-GaN down to n-GaN (Plessey wafers) : 1min40s Etch down through whole GaN to Si substrate : typically 8min30s in ICP#2</i>		

#### o Aluminium etching

Recipe name	AlRobert (ICP#1)	Comments
Primary purpose	Aluminium or Titanium/Aluminium etching	
Etch rates [nm/min]	Ti/Al : >200 (after initial oxide etch) S1818 : ~60 <i>Non-linear etch rate (induction period)</i> <i>Directionality :</i> <i>Al lateral etching ~125nm/min</i>	3min30s a priori sufficient to etch ~500nm Ti (50)/Al(450) Etch rate dependent on thickness of native oxide Al <sub>2</sub> O <sub>3</sub> layer
Lithography	S1805 OK	Better feature definition after hard bake (2min @ 115°C)
Gases [sccm]	Cl <sub>2</sub> (4) BCl <sub>3</sub> (16)	Highly chemical etch
Process pressure	20mTorr	
Power [W]	Platen : 50W	DC bias : 210-240V Peak-to-peak voltage : 740-790V
Notes	<i>Strong etch isotropy on Aluminium leads to thinning of patterned lines Etch endpoint visible by change of sample colour when all Al etched</i>	

o *Diamond etching (Ar/Cl<sub>2</sub> chemistry)*

	<b>Diamond Ar/Cl<sub>2</sub> (ICP#2)</b>	Comments
<b>Primary purpose</b>	<b>Diamond slow etch</b>	Smooths diamond surface
<b>Etch rates [nm/min]</b>	<b>Diamond : ~60 (~ 3.6um/hour) SiO<sub>2</sub> : &gt;120 (TBC)</b>	1:2 etch rates diamond:SiO <sub>2</sub>
Lithography	SiO <sub>2</sub> hard mask	
Gases [sccm]	Ar (25) Cl <sub>2</sub> (40)	
Process pressure	10 mTorr	
Power [W]	Coil : 400 Platen : 300	T = 40°C

o *Diamond etching (Ar/O<sub>2</sub> chemistry)*

	<b>Diamond Ar/O<sub>2</sub> (ICP#2)</b>	<b>DIA_ARO<sub>2</sub> (ICP#1)</b>	Comments
<b>Primary purpose</b>	<b>Diamond fast etch</b>		Very strong roughening and grassing of the diamond surface. Used for full through-membrane etch
<b>Etch rates [nm/min]</b>	<b>Diamond : ~100 -200 SiO<sub>2</sub> : 12-18 Si : 11-12 Al : 2.5-6</b>	<b>Diamond : ~100 - 220 SiO<sub>2</sub> : 12-18 Si : 11-12 Al : 2.5-6</b>	See Al mask tests for selectivity to Al
Lithography	Al or SiO <sub>2</sub> mask	Al or SiO <sub>2</sub> mask	PR not suitable (very fast etch rate and burns)
Gases [sccm]	Ar (15) O <sub>2</sub> (40)	Ar (15) O <sub>2</sub> (40)	
Process pressure	5 mTorr	5 mTorr	
Power [W]	Coil : 800 Platen : 300	Coil : 800 Platen : 300	DC bias : 430-470V Peak-to-peak : 1050-1150V
<i>Notes</i>	<i>Start with conditioning run and end with chamber clean: Ar/Cl<sub>2</sub> chemistry for 20min+. 1-hour long etch warms up chamber lid to ~80°C. Sample temperature probably exceeds 100°C during etch.</i>		

### A1.5.b Reactive Ion Etching – RIE#1 (SiO<sub>2</sub>, polymers)

#### o SiO<sub>2</sub> etching

	<b>mlesio2.rec (RIE#1)</b>	<b>lopsio2.rec (RIE#1)</b>	Comments
<b>Primary purpose</b>	<b>SiO<sub>2</sub> etching, low power (slow etch / no resist burning)</b>	<b>SiO<sub>2</sub> etching, high power (fast etch / resist damage)</b>	
<b>Etch rates [nm/min]</b>	<b>SiO<sub>2</sub> : ~23-25 Al : &lt;20 Au : &lt;20 Pd : &lt;10 PR (S1805) : &lt;10 PR (maN-1410)</b>	<b>SiO<sub>2</sub> : ~ 39</b>	Typically used with up to 50% overetch depending on application
Lithography	S1805 adapted	S1805 adapted	S1805 resist allows good feature definition (<2µm)
Gases [sccm]	CHF <sub>3</sub> (5) Ar (15)	CHF <sub>3</sub> (5) Ar (15)	
Process pressure	0.03 Torr	0.03 Torr	
Power [W]	RF forward : 120 RF reflected : 0 DC bias : ~410V	RF forward : RF reflected : 0 DC bias : ~620V	
Notes	<i>When using the higher power recipe, S1818 resist burns/carbonises and proves very difficult / impossible to remove</i>		

#### o Parylene-C etching

	<b>paryl-rs.rec (RIE#1)</b>	Comments
<b>Primary purpose</b>	<b>Parylene etching</b>	
<b>Etch rates [nm/min]</b>	<b>Parylene C : ~310-390 (DC bias 430 to 520V) S1818, S1828, SPR220-4.5 : ~340-420 (same DC bias)  <b>Directionality :</b> <b>Parylene lateral etching ~200nm/min</b></b>	Etch rate highly dependent on DC bias Fractioned etch needed to avoid parylene burning – proceed by succession of 3min long etches
Lithography	Positive/negative PR OK; No parylene/PR adhesion issue	Selectivity less than 1:1 to PR
Gases [sccm]	O <sub>2</sub> (50)	
Process pressure	0.080 Torr	
Power [W]	RF forward : 200 RF reflected : 0	DC bias : 430V to 520V
Notes	<i>A very thin residual layer may remain after etch for t&gt;2µm, to be removed by generous overetch (40%+).</i>	

### A1.5.c Reactive Ion Etching – RIE#2 (Metals, Si)

#### o Silicon etching

	<b>Sietch2.rec (RIE#2)</b>	Comments
<b>Primary purpose</b>	<b>Silicon etching</b>	
<b>Etch rates [nm/min]</b>	<b>Si : ~530 SiO<sub>2</sub> : ~140 S1805 : NA (very fast/carbonises resist)</b>	Aggressive high power etch, relatively low selectivity with SiO <sub>2</sub> hard mask
Lithography	SiO <sub>2</sub> hard mask needed*	
Gases [sccm]	Ar (10) O <sub>2</sub> (10) SF <sub>6</sub> (60)	
Process pressure	0.05 Torr	
Power [W]	RF forward : 300 RF reflected : <2	DC bias : 440 V

#### o Gold etching

	<b>auetch.rec (RIE#2)</b>	Comments
<b>Primary purpose</b>	<b>Gold etching</b>	
<b>Etch rates [nm/min]</b>	<b>Au : &gt;40 (after undetermined induction period) SiO<sub>2</sub> : ~25</b>	
Lithography	Hard mask needed* (SiO <sub>2</sub> adapted) (Strip PR before etching)	PR masking not adapted – will carbonise, very difficult strip
Gases [sccm]	Ar (40)	
Process pressure	0.045 Torr	
Power [W]	RF forward : 300 RF reflected : <2	DC bias : 625V
Notes	<i>Purely physical etch, high power: good precision and fidelity (anisotropic) but will etch all materials indiscriminately. No metal redep. observed.</i>	

#### o Titanium etching

	<b>tietch.rec (RIE#2)</b>	Comments
<b>Primary purpose</b>	<b>Titanium etching</b>	
<b>Etch rates [nm/min]</b>	<b>Ti : &gt;25 SiO<sub>2</sub> : ~25</b>	Typically 2-3min following auetch.rec to etch 50nm Ti
Lithography	Hard mask needed* (SiO <sub>2</sub> works well) (Strip PR before etching)	PR masking not adapted – will carbonise, very difficult strip
Gases [sccm]	Ar (40) SF <sub>6</sub> (10)	
Process pressure	0.045 Torr	
Power [W]	RF forward : 200 RF reflected : <1	DC bias : 440V
Notes	<i>Mostly physical etch at high power : good precision and fidelity (anisotropic) but will etch all materials quite fast -&gt; hard mask needed</i>	

## o Palladium etching

	pdetch.rec (RIE#2)	Comments
<b>Primary purpose</b>	<b>Etching of non-annealed Palladium</b>	
<b>Etch rates [nm/min]</b>	<b>Pd : &gt;20</b> <b>Pd (annealed) : &lt;&lt;30</b> <b>SiO<sub>2</sub> : ~5-8</b>	
Lithography	S1805, S1818 OK for short etches* (<4min) <i>SiO<sub>2</sub> hard mask not suitable for thin Pd layers : seems to affect film quality**</i>	Immediate PR strip needed after etch
Gases [sccm]	Ar (20)	
Process pressure		
Power [W]	RF forward : 300 RF reflected : <2	DC bias : 600-670V Process pressure : 0.035 Torr
Notes	<i>Physical etch, minimise etch time to allay PR damage. Typically 3min needed to etch 50nm Pd.</i>	

## o Etching of Ni/Au bilayer

	niautest.rec (RIE#2)	Comments
<b>Primary purpose</b>	<b>Etching of non-annealed Ni/Au bilayer</b>	
<b>Etch rates [nm/min]</b>	<b>Ni/Au : &gt;15</b> <b>Ni/Au (annealed) : NA</b> <b>SiO<sub>2</sub> : &lt;7</b>	
Lithography	S1805 OK for short etches* (~2min) S1818 possible (hard to remove) <i>SiO<sub>2</sub> hard mask not recommended (seems to affect film quality**)</i>	Thin PR preferred for post-etch removal. Immediate PR strip needed after etch.
Gases [sccm]	Ar (40) O <sub>2</sub> (4)	
Process pressure	0.045 Torr	
Power [W]	RF forward : 300 RF reflected : <2	DC bias : 635V
Notes	<i>Partly physical etch, minimised etch times important for easy PR removal. Typically 2min15s sufficient to etch Ni(11nm)/Au(22nm) bilayer</i>	

\* High-power sputtering etches, especially Argon ion bombardment at low pressures, rapidly cause photoresist degradation by roughening and carbonisation/reticulation [5], [6]. Carbonised PR may prove extremely difficult to strip except by very aggressive methods such as acid "piranha" etch, which will damage or remove metal layers in the process. Hence only oxide hard masks are used for thick (>50nm) metal etches in this work. Hard-baked, thin PR films with low solvent content have experimentally been found to withstand short Ar etches (<2-3 min) without substantial carbonisation and can thus be used as making layers for thin metal films (<30nm).

\*\* SiO<sub>2</sub>-patterning of thin (<30nm) spreading layers yielded poor opto-electrical characteristics of final devices (2 samples with Ni/Au SL, 2 samples with Pd SL). This effect might be due to temperature-induced effects during deposition and/or interfacial chemical reactions with PECVD precursor gases.

## A1.6 Plasma ashing – plasma cleaning recipes

### A1.6.a Matrix cleaning

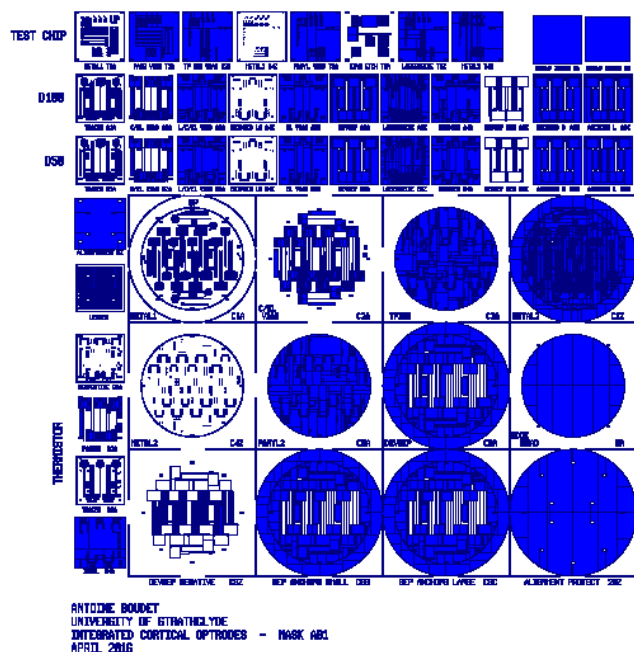
	<b>Recipe 1 – 150°C (Matrix stripper M102)</b>	<b>Recipe 2 – 250°C (Matrix stripper M102)</b>
<b>Primary purpose</b>	<b>Photoresist/organics ashing</b>	
<b>PR etch rate [nm/min]</b>	<b>&gt; 500</b>	<b>&gt; 500</b>
<b>Temperature</b>	<b>150°C</b>	<b>250°C</b>
Process pressure	3.75 Torr	3.75 Torr
Power [W]	RF : 500W	RF : 500W
	MFC 1 = 35%, MFC 2 = 0%, MFC 3 = 0% EP Level = 995	MFC 1 = 35%, MFC 2 = 0%, MFC 3 = 0% EP Level = 995
<i>Notes</i>	<i>Use : quick descum or thin PR strip while minimising risk to sample</i>	<i>Use : removal of burnt/cross-linked PR on non-fragile samples</i>

### A1.6.b Diener barrel Asher

	<b>Oxygen plasma (Diener barrel asher)</b>	Comments
<b>Primary purpose</b>	<b>Ashing of photoresist/organics residues</b>	Much gentler process than the Matrix asher.
<b>PR etch rate [nm/min]</b>	<b>@ 200W : &gt; 100</b>	Quick PR descum : 80W used
<b>Temperature</b>	<b>Room temperature (&lt;50 °C)</b>	
Process pressure	0.3 mbar	
Max. power [W]	200	Power range 10W-200W
<i>Notes</i>	<i>Typically used in complement to solvent clean to remove residual PR layers.</i>	

## Appendix A2 : Photomasks

a) Mask AB1



b) Mask AB2

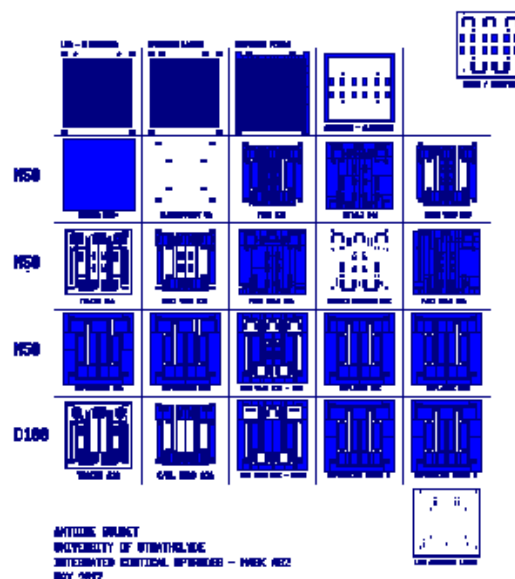


Figure A2.1 : Photomasks designed and used by the author for the fabrication of diamond probes and  $50 \times 50 \mu\text{m}^2$   $\mu\text{LEDs}$  for transfer-printing. **a) Mask AB1** (5"), with arrays of patterns for various test structures ("test chip"), initial probe designs (SC diamond,  $8\text{mm} \times 8\text{mm}$  : "D100", "D50"), layers for polycrystalline diamond wafers (20mm circular patterns). **b) Mask AB2** (4", not shown on same scale), with patterns for  $\mu\text{LED}$  fabrication (top left), refined probe designs for SC diamond samples ("N50" rows, including thermistor designs) and patterns for PR-assisted bonding.

c) Mask uTP (designed by Benoit Guilhabert)

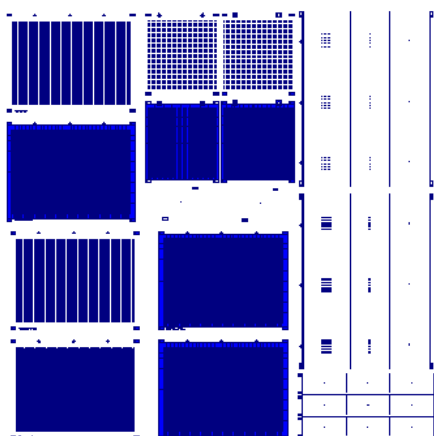


Figure A2.2 : Photomask used for fabrication of  $\mu\text{TP}$  stamp and  $100 \times 100 \mu\text{m}^2$   $\mu\text{LEDs}$ . (Design by Dr. Benoit Guilhabert)

## Appendix A3: $\mu$ TP stamp fabrication

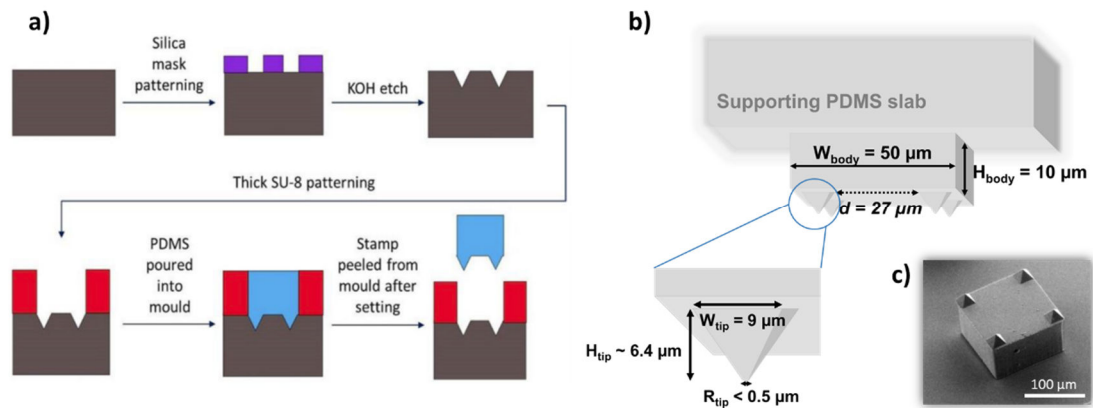


Figure A3.1 : Fabrication of transfer-printing PDMS stamps. a) Schematic fabrication process, b) Dimensions of the  $50 \times 50 \mu\text{m}^2$  structured stamps used in this work, c) SEM scan of a larger  $100 \times 100 \mu\text{m}^2$  specimen. Panels a),c) adapted from [7].

The fabrication of  $50 \times 50 \mu\text{m}^2$  PDMS stamps with pyramids was directly adapted from previous work ( $90 \times 90 \mu\text{m}^2$  stamps [8]), by homothetic downscaling. The fabrication process is schematised in figure A3.1. Briefly, a 300nm layer of  $\text{SiO}_2$  is first deposited by PECVD on a (100)-oriented silicon wafer. Alignment marks and a set of four square vias ( $9 \times 9 \mu\text{m}^2$ ) are patterned using maN-1410 photoresist, the  $\text{SiO}_2$  is etched in RIE#1 (recipe “mlesio2.rec” for 25min) and the PR is stripped by Matrix ashing (8min,  $150^\circ\text{C}$ ). The samples are then etched in hot KOH (40% w/w,  $80^\circ\text{C}$ , 600rpm magnetic stirring) for 10 minutes, with the etch progressing along the (111) planes and yielding self-closed pyramidal recesses with a sidewall angle of  $54.7^\circ$  in place of the vias (see chapter 2, section 2.3.2 and figure 2.7). After full stripping of the damaged  $\text{SiO}_2$  layer in buffered oxide etch (BOE 7:1, 1min30s, followed by DI rinse), a 100nm layer of new  $\text{SiO}_2$  is PECVD-deposited on the sample to smoothen surfaces and help the final PDMS delamination. The stamp body mould is realised in SU8 photoresist : a  $10 \mu\text{m}$  layer of SU8 GM1070 resist is spun, patterned and adequately baked and cured post-exposure (see annex A1) to create rectangular openings encompassing the pyramids.

To form PDMS, a liquid mix of siloxane B and curing agent A is poured in the mould (A:B mix ratio 1:8, producing a relatively rigid PDMS stamp with fast relaxation time ([9], [10], see also chapter 2.5), left to degas in air or vacuum, and cured by baking for 60min at  $80^\circ\text{C}$  on a hot plate. Individual stamps are cut out of the mould, and permanently bonded to a clean  $20 \times 20 \text{mm}^2$  glass coverslip by  $\text{O}_2$  plasma activation [11], [12] in the Diener barrel asher ( $\text{O}_2$  plasma, 120W for 6s), followed by a 1h30 oven bake at  $80^\circ\text{C}$ . The coverslips are fixed to a metal holder and mounted at will on the NLP2000 transfer-printing tool used in this work.



# Appendix A4: Parylene-C adhesion tests

## A4.1 Test protocol: adhesion of parylene on glass substrates

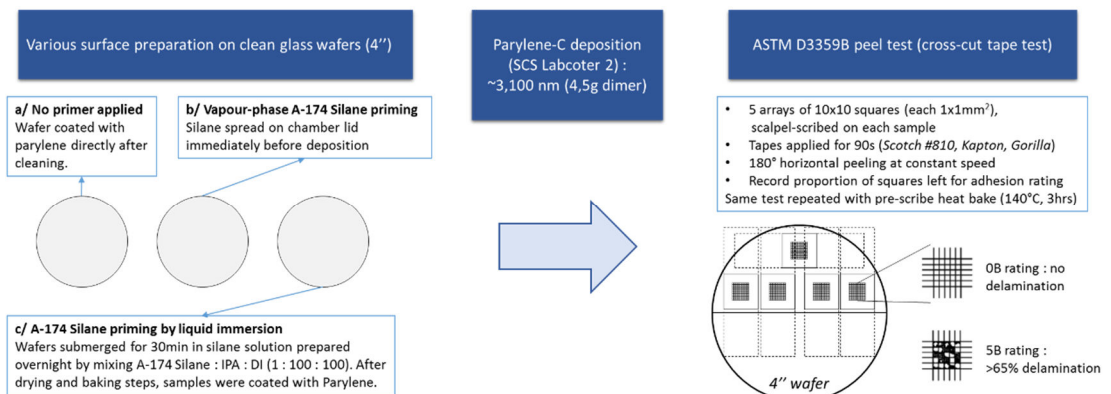


Figure A4.1 : Protocol used to test adhesion of parylene-C to clean glass wafers (ASTMD3359B peel test). Five peel tests were done on each of the three wafers with three different priming conditions, with the results given in table A4.3.

## A4.2 Adhesion test results

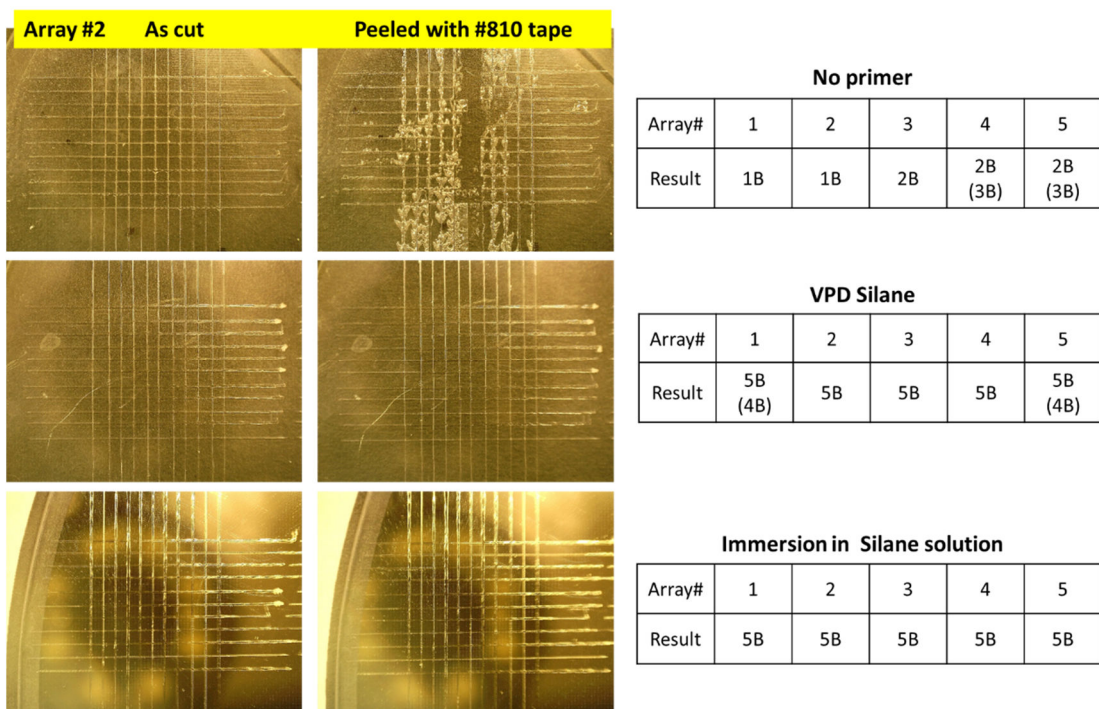


Figure A4.2 : (left) results obtained on array #2 (photograph before/after first peel test) and (right) results of the first peel test on all arrays (#810 "scotch" tape), for all three wafers.

Adhesion test for Parylene C coated on 4" glass wafers : ASTM D3359 peel test								
Average adhesion grade 5B (strongest adhesion) to 0B (very poor)								
Adhesion promoter	a/ No primer		b/ VPD Silane		c/ Immersion in Silane solution		Number of arrays	Adhesion to steel (vendor)
Directly after parylene coating								
1st peel : #810 tape	2B		5B		5B		n=5	250 N/m
2d peel : Kapton	1B		5B		5B		n=5	240 N/m
3d peel : Gorilla	0B		5B		5B		n=5	1240 N/m
Peel after bake	cut before	cut after	cut before	cut after	cut before	cut after	<- Cut after/before 140°C bake for 3hrs	
1st peel : #810 tape	-	0B*	2B-3B	2B	3B	0B-1B	n=4 (*n=3)	250 N/m

Table A4.3: Collated results of all adhesion tests, including bake cycles, for all arrays and wafers. Grades are defined in the ASTM D3359 standard and range from 5B (no delamination visible) to 0B (>65% delamination). A rating of 3B corresponds to 5-15% of the array area removed.

## Appendix A5: comparison of integrated $\mu$ LED performance

Comparison of $\mu$ LED performance to previous work (GaN LEDs for transfer-printing only)					
	Area [ $\mu\text{m}^2$ ]	Turn-on Voltage $V_T$	Leak. current @ $V_T/2$	EQE [%] @ 2mA	Optical power [mW] @ 2mA
Kim et al. 2012 [13] GaN/Sapph*, LLO***	100x100	~4.1 V	0.1-0.2 mA	~6 %	~ 0.5
Kim et al. 2013 [14] GaN/Sapph, LLO + uTP	40x40	~3.5 V	NA	8 %	0.2
Goßler et al. 2014 [15] GaN/Sapph, LLO + WB	50x50	~3.1 V	NA	@1 mA: ~ 1.7 %	@1 mA: 0.015
Ayub et al. 2016 [16] GaN/Sapph, LLO + WB#	112x112	~6 V	NA	~0.1 %	0.015
Ayub et al. 2017 [17] Commercial LED chips (50 $\mu\text{m}$ thick)	270x220	~2.8 V	NA	2 %	0.12
Soltan et al. 2017 [18] GaN/Sapph, ball bond.	100x100	3.6-4.5 V	NA (>0.1 mA)	< 0.7%	< 0.04
Li et al. 2018 [19] GaN/Sapph, LLO + WB	180x125	~2.6 V	NA	3-8 %	Not given
IoP work					
Prev. IoP work : GaN/Si, monolithic [20]	25 $\mu\text{m}$ diameter	~4.5 V	<10 nA	1.3 %	0.12
Prev. IoP work (uTP, GaN/Si**) - [21]–[23]	150x150 [21] 100x100 [22], [23]	~3.5 V 4.5-6 V	NA Up to ~0.5 mA	< 0.4 % 0.1-1 %	~ 0.05 0.007 to 0.15
This work GaN/Si, uTP, Pd (8nm)	50x50				
This work GaN/Si, uTP, Ni/Au	50x50	~ 3.9 V	< 10 nA	2.5%	0.28
*GaN/Sapph : GaN-on-sapphire; **GaN/Si : GaN-on-Si; ***LLO : laser liftoff; #WB : wafer bonding					

### A5 – Table references

- [1] E. Chen, "Harvard Applied Physics Course 298r - Fabrication techniques III : etching." 2004.
- [2] W. Kern, "The Evolution of Silicon Wafer Cleaning Technology," *J. Electrochem. Soc.*, vol. 137, no. 6, p. 1887, Jun. 1990.
- [3] K. R. Williams, K. Gupta, and M. Wasilik, "Etch rates for micromachining processing - Part II," *J. Microelectromechanical Syst.*, vol. 12, no. 6, pp. 761–778, 2003.
- [4] M. Shikida, K. Sato, K. Tokoro, and D. Uchikawa, "Comparison of anisotropic etching properties between KOH and TMAH solutions," in *Technical Digest. IEEE International MEMS 99 Conference. Twelfth IEEE International Conference on Micro Electro Mechanical Systems (Cat. No.99CH36291)*, 1999, pp. 315–320.
- [5] S. Franssila, *Introduction to microfabrication*. John Wiley & Sons, 2010.
- [6] A. R. Pal, R. L. Bruce, F. Weilmboeck, S. Engelmann, T. Lin, M.-S. Kuo, R. Phaneuf, and G. S. Oehrlein, "Real-time studies of surface roughness development and reticulation mechanism of advanced photoresist materials during plasma processing," *J. Appl. Phys.*, vol. 105, no. 1, p. 013311, Jan. 2009.

- [7] K. Rae, "Micro-transfer printing for visible light communications applications," University of Strathclyde, 2017.
- [8] A. J. Trindade, "Transfer printing of nitride based light emitting diodes," 2015.
- [9] J. Friend and L. Yeo, "Fabrication of microfluidic devices using polydimethylsiloxane," *Biomicrofluidics*, vol. 4, no. 2, p. 026502, Jun. 2010.
- [10] Y. Y. Huang, W. Zhou, K. J. Hsia, E. Menard, J. U. Park, J. A. Rogers, and A. G. Alleyne, "Stamp collapse in soft lithography," *Langmuir*, vol. 21, no. 17, pp. 8058–8068, 2005.
- [11] K. Chau, B. Millare, A. Lin, S. Upadhyayula, V. Nuñez, H. Xu, and V. I. Vullev, "Dependence of the quality of adhesion between poly(dimethylsiloxane) and glass surfaces on the composition of the oxidizing plasma," *Microfluid. Nanofluidics*, vol. 10, no. 4, pp. 907–917, Apr. 2011.
- [12] L. Xiong, P. Chen, and Q. Zhou, "Adhesion promotion between PDMS and glass by oxygen plasma pre-treatment," *J. Adhes. Sci. Technol.*, vol. 28, no. 11, pp. 1046–1054, Jun. 2014.
- [13] T. Il Kim, Y. H. Jung, J. Song, D. Kim, Y. Li, H. S. Kim, I. S. Song, J. J. Wierer, H. A. Pao, Y. Huang, and J. A. Rogers, "High-efficiency, microscale GaN light-emitting diodes and their thermal properties on unusual substrates," *Small*, vol. 8, no. 11, pp. 1643–1649, 2012.
- [14] T. Il Kim, J. G. McCall, Y. H. Jung, X. Huang, E. R. Siuda, Y. Li, J. Song, Y. M. Song, H. A. Pao, R. H. Kim, C. Lu, S. D. Lee, I. S. Song, G. Shin, R. Al-Hasani, S. Kim, M. P. Tan, Y. Huang, F. G. Omenetto, J. A. Rogers, and M. R. Bruchas, "Injectable, cellular-scale optoelectronics with applications for wireless optogenetics," *Science (80-. )*, vol. 340, no. 6129, pp. 211–216, 2013.
- [15] C. Goßler, C. Bierbrauer, R. Moser, M. Kunzer, K. Holc, W. Pletschen, K. Köhler, J. Wagner, M. Schwaerzle, P. Ruther, O. Paul, J. Neef, D. Keppeler, G. Hoch, T. Moser, and U. T. Schwarz, "GaN-based micro-LED arrays on flexible substrates for optical cochlear implants," *J. Phys. D. Appl. Phys.*, vol. 47, p. 205401, 2014.
- [16] S. Ayub, C. Gossler, M. Schwaerzle, E. Klein, O. Paul, U. T. Schwarz, and P. Ruther, "High-density probe with integrated thin-film micro light emitting diodes ( $\mu$ LEDs) for optogenetic applications," *Proc. IEEE Int. Conf. Micro Electro Mech. Syst.*, vol. 2016–Febru, no. January, pp. 379–382, 2016.
- [17] S. Ayub, L. J. Gentet, R. Fiáth, M. Schwaerzle, M. Borel, F. David, P. Barthó, I. Ulbert, O. Paul, and P. Ruther, "Hybrid intracerebral probe with integrated bare LED chips for optogenetic studies," *Biomed. Microdevices*, vol. 19, no. 3, pp. 1–12, 2017.
- [18] A. Soltan, B. McGovern, E. Drakakis, M. Neil, P. Maaskant, M. Akhter, J. S. Lee, and P. Degenaar, "High Density, High Radiance  $\mu$ LED Matrix for Optogenetic Retinal Prostheses and Planar Neural Stimulation," *IEEE Trans. Biomed. Circuits Syst.*, vol. 11, no. 2, pp. 347–359, Apr. 2017.
- [19] L. Li, C. Liu, Y. Su, J. Bai, J. Wu, Y. Han, Y. Hou, S. Qi, Y. Zhao, H. Ding, Y. Yan, L. Yin, P. Wang, Y. Luo, and X. Sheng, "Heterogeneous Integration of Microscale GaN Light-Emitting Diodes and Their Electrical, Optical, and Thermal Characteristics on Flexible Substrates," *Adv. Mater. Technol.*, vol. 1700239, p. 1700239, 2017.
- [20] R. Scharf, T. Tsunematsu, N. McAlinden, M. D. Dawson, S. Sakata, and K. Mathieson, "Depth-specific optogenetic control in vivo with a scalable, high-density  $\mu$ LED neural probe - SUPPLEMENTARY," *Sci. Rep.*, vol. 6, 2016.
- [21] A. J. Trindade, B. Guilhabert, D. Massoubre, D. Zhu, N. Laurand, E. Gu, I. M. Watson, C. J. Humphreys, and M. D. Dawson, "Nanoscale-accuracy transfer printing of ultra-thin AlInGaN light-emitting diodes onto mechanically flexible substrates," *Appl. Phys. Lett.*, vol. 103, no. 25, 2013.
- [22] a. J. Trindade, B. Guilhabert, E. Y. Xie, R. Ferreira, J. J. D. McKendry, D. Zhu, N. Laurand, E. Gu, D. J. Wallis, I. M. Watson, C. J. Humphreys, and M. D. Dawson, "Heterogeneous integration of gallium nitride light-emitting diodes on diamond and silica by transfer printing," *Opt. Express*, vol. 23, no. 7, p. 9329, 2015.
- [23] K. Rae, C. Foucher, B. Guilhabert, N. Laurand, D. Zhu, C. J. Humphreys, D. J. Wallis, and M. D. Dawson, "InGaN micro-LEDs integrated onto an ultra-thin , colloidal quantum dot functionalized glass platform," *Opt. Express*, vol. 25, no. 16, pp. 19179–19184, 2017.

## Appendix A6: Estimation of $\mu$ LED curvature from monocolour micrographs based on Newton Rings analysis

A schematic description of the program is given in figure A6.1. The curvature analysis is done on the base of user-selected dark and bright interference rings. These correspond respectively to destructive and constructive interference of path length  $2t$ , where  $t$  is the elevation of the membrane at the  $m^{\text{th}}$  ring and given by the simple formula:

$$\text{(dark ring)} \quad t = \frac{m\lambda}{2} \quad \text{Eq. (A6.1)}$$

$$\text{(bright ring)} \quad t = \frac{\left(m + \frac{1}{2}\right)\lambda}{2} \quad \text{Eq. (A6.2)}$$

where the ring number  $m \in \mathbb{N}$  and  $\lambda$  is the wavelength of light striking the membrane at normal incidence.

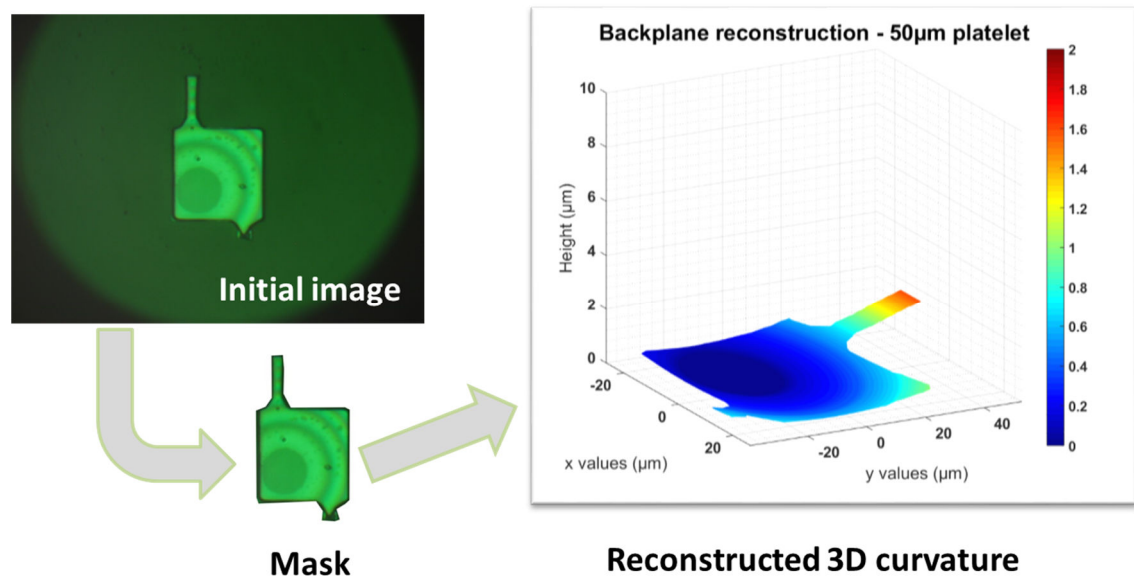


Figure A6.1: After applying a mask, the Matlab program reconstructs the ( $\sim$ spherical) curvature of a membrane from the Newton rings observed at a given observation wavelength. The resulting reconstruction provides a rough estimate of the radii of curvature of various membranes.

## A6.1 Matlab codes

### A6.1.a Generic calling routine

```

%% NewtonRingsAB_v4
%% MATLAB SCRIPT FOR CURVATURE ANALYSIS OF THIN MATERIALS USING NEWTON RINGS
%%
% *****
% Usage and limitations:
% -> Curvature is assumed to be spherical or close to spherical: elliptic
% rings will not yield correct results
% -> Curvature is assumed to be positive on whole sample, with no inversion
% of curvature at any point (and only 1 contact point between sample and
% substrate)
% -> This program is not intended for extracting absolute height values but
% a "rough curvature profile". Allow at least +/- 5% error and double-check
% with other profiling methods if accurate measurements needed.
%
% 2 possible types of INPUTS:
%   - 1 image of the ringed part of the sample, cropped to known
% dimensions (no mask required)
%   - or 1 image of the full sample (can include surroundings), with 1
% mask image added to allow Matlab to select right portion for ring analysis
%
% The program will ask the user to identify the rings manually by clicking.
% The user must also define the mesh resolution, ETC -> see parameters
% section.
%
% The main output of the program is a 3D reconstruction of the backplane of
% the sample
% through interpolation based on ring heights. Matrices storing ring
% heights, etc. are also stored for further analysis.
% This program is intended as a "rough tool" for checking the curvature of a
% sample (typically a transfer-printed membrane platelet).
% Values should be taken with at least +/-5% error (more if rings are
% elliptic). If precise absolute values are needed, it is best to
% cross-check the obtained reconstruction with data obtained by
% profilometry (e.g WYKO optical profilometer).
%
% *****
% *****
% Created 2015-2017 by Antoine BOUDET / antoine.boudet@strath.ac.uk
% University of Strathclyde - Institute of Photonics
% *****
% *****

%% Parameters for generic function NRAB (curved membrane reconstruction
based on NewtonRings micrographs)
im=('Raw_50.JPG');
mask=imread('Raw_50_mask.JPG');
UseMask='Y'; % if want to use mask for final rendering. UseMask is 'Y' 'N';
lambda = 0.530; % wavelength used for imaging, in microns
t_offset = 2; % thickness of membrane, in um; must be positive (>0) to
avoid calculation errors
xsize=232; % x (horizontal) size of full image, in microns - will serve in
creation of polar map
ninterp = 500; % number of interpolation points across x or y direction

```

```

interptype='cubic'; % options : 'linear','natural','cubic'
Rcurvheightmin = lambda/8;

%% 1. Read and store image
originalimage=imread(im);
grayimage=rgb2gray(originalimage);
[mrow,ncol] = size(grayimage);
BWmask = ones(size(grayimage)); % pass all by default, modify to mask if
activated
if UseMask == 'Y'
    graymask=imcomplement(rgb2gray(mask));
    BWmask=double(logical(graymask)); BWmask(~BWmask)=nan; % creates actual
mask matrix
end

%% 2. MANUALLY SELECT RINGS : function Newton2clickrings
% Asks user to click first on 1st dark ring centre, then on each dark ring,
then on each bright ring.
disp('----- Manually select rings -----');
[x1,y1,xd,yd,xb,yb] = Newton2clickrings(originalimage);
% stores the x and y values of the clicks in ad hoc arrays xd,yd (dark) and
xb,yb (bright)
close all;

%% 3. Calculations and interpolation to reconstruct backplane : function
NRAB
[rhomap,rhodarklines,rhobrightlines,Allrings,RingHeights,xq,yq,Backplane,Bac
kplane_m,CurvRadius,CurvRadius_m] =
NRAB(grayimage,BWmask,lambda,t_offset,xsize,ninterp,interptype,Rcurvheightmi
n,x1,y1,xd,yd,xb,yb);

% clearvars x1 y1 xd yd xb yb

%% 4. Plots

% 1. Plot rings superimposed on original image for verification (3D plot
% viewed from above)
hfig1 = figure(1); hold on;
xImage = [0 ncol; 0 ncol]; % x data for the image corners
yImage = [0 0; mrow mrow]; % y data for the image corners
zImage = [0 0; 0 0]; % z data for the image corners
surf(xImage,yImage,zImage,'CData',originalimage,'FaceColor','texturemap','Fa
ceAlpha',0.75); % show image on z=0 axis
view(0,90); axis equal; axis tight; grid off; hold on;
mesh(Allrings,'Marker','+','MarkerSize',0.75);
title('Identified ring regions superimposed on image');
xlabel('x'); ylabel('y'); axis off;

% 2. Simple mesh, reconstructed backplane
% NB : LATERAL SCALE NOT SET.
hfig2 = figure(2); hold on;
mesh(yq,xq,Backplane_m); view(45,45); grid on; grid minor;
title('Reconstructed backplane');
xlabel('x'); ylabel('y'); zlabel('z [um]'); zlim([0 4*max(Backplane_m(:))]);

```

## A6.1.b Click ring selection

```

% NEWTON RINGS
% 2. Get circles : ask user to click first on 1st dark ring centre, then on
% each dark ring, then on each bright ring.

function [x1,y1,xd,yd,xb,yb] = Newton2clickrings(originalimage)

% Get wanted values by clicking
disp('Click on centre of first ring, hit return when finished');
pause;
imshow(originalimage);
title('Click on centre of first ring, hit return when finished');
set(gcf, 'units','normalized','outerposition',[0 0 1 1]);
[x1,y1]=ginput;
close all;
x1=round(x1); y1=round(y1);

disp('Click on mean radii of dark rings, from edge of base ring to last, hit
return when finished');
pause;
% figb=figure('name','Final output','units','normalized','outerposition',[0
0 1 1]);
imshow(originalimage);
title('Click on mean radii of dark rings, from edge of base ring to last,
hit return when finished');
set(gcf, 'units','normalized','outerposition',[0 0 1 1]);
hold on
viscircles([x1 y1],size(originalimage,1)/2,'LineStyle','--');
hold on
plot(x1,y1,'r*');

[xd,yd]=ginput;
close all;
xd=round(xd); yd=round(yd);

disp('Click on center of bright rings, from 1st bright ring to last, hit
return when finished');
pause;
imshow(originalimage);
title('Click on mean radii of bright rings, hit return when finished');
set(gcf, 'units','normalized','outerposition',[0 0 1 1]);
hold on
viscircles([x1 y1],size(originalimage,1)/2,'LineStyle','--');
hold on
plot(x1,y1,'r*');

[xb,yb]=ginput;
close all;
xb=round(xb); yb=round(yb);

end

```



### A6.1.c NRAB function – curvature analysis

```

%% NewtonRingsAB_v4
%% MATLAB SCRIPT FOR CURVATURE ANALYSIS OF THIN MATERIALS USING NEWTON RINGS
%%
% *****
% Usage and limitations:
% -> Curvature is assumed to be spherical or close to spherical : elliptic
% rings will not yield correct results
% -> Curvature is assumed to be positive on whole sample, with no inversion
% of curvature at any point (and only 1 contact point between sample and
% substrate)
%
% 2 possible types of INPUTS :
%   - 1 image of the ringed part of the sample, cropped to known
dimensions (no mask required)
%   - or 1 image of the full sample (can include surroundings), with 1
mask image added to allow matlab to select right portion for ring analysis
%
% The program will ask the user to identify the rings manually by clicking.
% The user must also define the mesh resolution, ETC.
%
% 3 main OUTPUTS are given as figures :
%   - 2D plots of the x=X/2, y=Y/2 and diagonal profiles of the
interpolated curvature of the sample
%   - a calculation/interpolation of the radius of curvature of the sample
%   - a 3D reconstruction of the backplane of the sample.
% *****
% *****
% Created 2016 by Antoine BOUDET / antoine.boudet@strath.ac.uk
% University of Strathclyde - Institute of Photonics
% *****
% *****

function
[Irhomap,Irhodarklines,Irhobrightlines,Allrings_nans,Heights,xq,yq,vq,BWvq,R
ad,BWRad] =
NRAB(grayimage,BWmask,lambda,t_offset,xsize,ninterp,interpype,Rcurvheightmi
n,xl,y1,xd,yd,xb,yb);

[mrow,ncol] = size(grayimage);
ysize=xsize*(mrow/ncol); % y dimensions of image in microns, here assuming
square pixels
xpixelsize = xsize/ncol; ypixelsize = ysize/mrow; % pixel size in um
% plateletxsize=50; plateletysize=50; % in um, for a square sample
% plateletarea=plateletxsize*plateletysize;

%% 3. CREATE POLAR MAP OF COORDINATES
disp('- Starting time count -');
tic; % start time count
disp('----- Creating polar map -----');

% Create polar maps in pixels
ixcart = linspace(-xl(1),ncol-xl(1),ncol); % shift cartesian map of indices
to centre it on centre of first dark ring
iycart = linspace(-y1(1),mrow-y1(1),mrow); % CAREFUL : x is read from left
to right, y from top to bottom (ie y increases as we go down the y axis)

```

```

[Ixcart,Iycart]=meshgrid(ixcart,iycart); % pixel grid needed for the polar
map creation
[Ithetamap,Irhomap] = cart2pol(Ixcart,Iycart); % polar coordinates maps in
units of pixels, centred on centre of 1st dark ring
Irhomap = floor(Irhomap); % round down to get only integer values of pixel
distances

% Retrieve radii of the rings, in pixels - (coordinates from user click
input)
Irhodark = diag(Irhomap(yd,xd)); % NB yd is here the row index, xd is the
column index
Irhobright = diag(Irhomap(yb,xb));
clearvars ixcart iycart yd xd xl yl yb xb;
toc;

%% 4. CREATE MATRICES OF NUMBERED DARK AND BRIGHT LINES AT CLICK LOCATIONS
% Dark and bright lines will act as pixel-thin rings needed for good
% interpolation (no "plateau" caused by ring finite width)
disp('----- Creating matrices of numbered rings -----');

Irhodarklines = zeros(size(Irhomap));
Irhodarklines = Irhodarklines+(Irhomap<Irhodark(1)); % for definition of
first circle
for i=2:numel(Irhodark)
    % Irhodarklines = Irhodarklines+(Irhomap>Irhodark(i)-linewidth &
Irhomap<Irhodark(i)+linewidth)*i; % filter out all elements with radii not
comprised btw given values
    Irhodarklines = Irhodarklines + (Irhomap == Irhodark(i))*i; % no notion
of ring linewidth here, only rounded to pixel size
end
% Output is matrix in double format storing dark ring number at
corresponding ring position

Irhobrightlines=zeros(size(Irhomap));
for i=1:numel(Irhobright)
    % Irhobrightlines=Irhobrightlines+((Irhomap>Irhobright(i)-linewidth &
Irhomap<Irhobright(i)+linewidth))*i; % filter out all elements with radii
not comprised btw given values
    Irhobrightlines = Irhobrightlines + (Irhomap == Irhobright(i))*i; % no
notion of ring linewidth here, only rounded to pixel size
end
% Output is matrix in double format storing bright ring number at
corresponding ring position

% Also create binary matrix storing just the position of all rings (not
numbered)
% Matrix in double format with 1s at position of all rings, NaN otherwise
Allrings_nans = logical(Irnodarklines)+logical(Irhobrightlines);
Allrings_nans(Allrings_nans==0)=NaN; % double matrix with NaN for plotting
toc;

%% 5. FROM NEWTON RINGS FORMULA, CALCULATE CORRESPONDING HEIGHTS OF LINE
RINGS (in microns)
% Height = mring*lambda/2 for dark rings,
% Height = (mring+1/2)*lambda/2 for bright rings
% mring = 0,1,2,...,n
% An initial t_offset is used to account for membrane thickness
disp('----- Calculating heights (Newton Rings formula) -----');
% Matrix storing height of dark rings [µm]

```

```

hdarkline=logical(Irhodarklines).*((Irhodarklines-1)*(lambda/2)+t_offset); %
-1 in ring number because m starts at 0; set base altitude at 2 (platelet
thickness)
% Matrix storing height of bright rings [µm]
hbrightline=logical(Irhobrightlines).*((Irhobrightlines-
1+1/2)*(lambda/2)+t_offset);
% Final heights matrix : contains rings with their respective heights
Heights=hdarkline+hbrightline;
clearvars hdarkline hbrightline;
toc;

%% 6.1 INTERPOLATE HEIGHTS FOR FULL BACKPLANE RECONSTRUCTION
% Interpolation through method defined by variable "interptype"
disp('----- Interpolate btw lines for full backplane reconstruction ---
-----');
[xi,yi,zi]=find(Heights); % find indices x,y and values of non-zero elements
in Heights
% [xq,yq] = meshgrid(linspace(0,ncol,ninterp), linspace(0,mrow,ninterp));
[xq,yq] = meshgrid(linspace(0,ncol,ninterp),
linspace(0,mrow,round(ninterp*mrow/ncol))); % keep aspect ratio
vq = griddata(xi,yi,zi,xq,yq,interptype); % create interpolated surface
toc;

%% 6.2 INTERPOLATE MASK to same size
disp('----- Interpolate mask -----');
BWmask_interp = imresize(BWmask, [round(ninterp*mrow/ncol)
ninterp],'nearest'); % interpolate image
BWvq = vq.*BWmask_interp-t_offset; % apply mask and remove offset
toc;

%% 7.1 CALCULATE RADIUS OF CURVATURE AT EACH INTERPOLATION POINT - GENERIC
FORMULA
% 7.1 Calculate real mean radius of curvature at each surface point using
% differentiation (generic equations)
% OUTPUT IS SURFACE MATRIX Rad
disp('----- Calculate radius of curvature for each interpolation point
-----');
disp('--- 1) Using surfature function (generic) ---');
Rvq = vq; Rvq(Rvq<min(Rvq(:))+ Rcurvheightmin) = nan; % Remove minimum
values corresponding to flat surface (infinite R)
[Curv_gaussian,Curv_mean,Curv_principall,Curv_principal2] =
AB_surfature(xq,yq,Rvq); % Extract surface curvatures with function
AB_surfature
Rad = 1./abs(Curv_mean);
% Remove outliers (artifacts) : keep only values within mean +/- std
Radmiddle = Rad(:,round(size(Rad,2)/2));
Radmean = mean(Radmiddle(~isnan(Radmiddle)));
Radstd = std(Radmiddle(~isnan(Radmiddle)));
Rad=Rad.*(Rad>(Radmean-Radstd) & Rad<(Radmean+Radstd));
BWRad = Rad.*BWmask_interp; % apply mask
% imagesc(Rad); colorbar; caxis([0 max(Rad(:))/5]);
clearvars Radmiddle Radmean Radstd Rvq
toc;

end

```

## Appendix A7 : INTAN RHS2116 chip

The INTAN RHS2116 digital stimulator & amplifier chip used in this work (chapter 3.3) is one of the first commercial, compact system capable of fully bidirectional electrophysiology. Each of its 16 channels can be independently used to either sample electrical signals (up to  $\sim 45\text{kHz}$ , with input-referred noise as low as  $\sim 2.4\mu\text{V}_{\text{RMS}}$ ) with selective bandwidth amplification, or to drive a constant-current stimulation with programmable amplitude. The chip circuitry comprises low- and high-gain amplifiers, analog and digital filters; a multiplexed 16-bit analog-to-digital converter (ADC) allows a single digitised output data stream to be read through serial peripheral interface protocols (SPI).

### A7.1 Chip characteristics

Some chip characteristics and circuitry relevant to this work are given below.

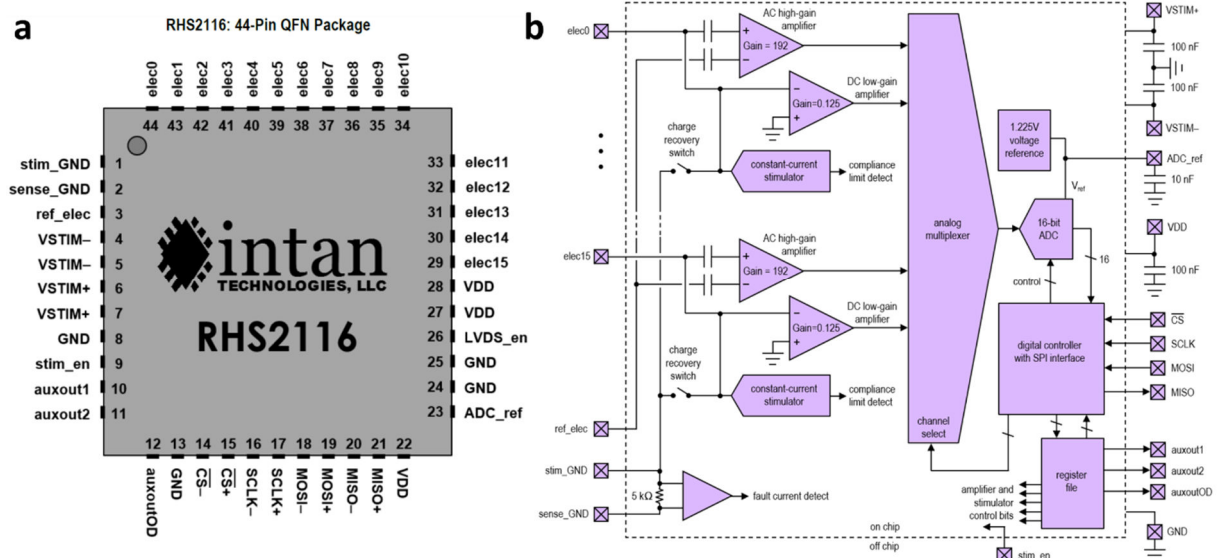


Figure A7.1: **RHS2116 chip diagrams.** **a)** Pin diagram. In this work, all electrode channels (elec0 to elec15), VDD, GND, VSTIM, MISO and CLK channels were wirebonded for use. **b)** Simplified circuit diagram. Each stim/amp channel includes two amplifiers for sensing electrode voltages: an AC-coupled high gain amplifier, for small variations such as extracellular action potentials ( $\mu\text{V}$  to  $\text{mV}$ ) and a DC-coupled low-gain amplifier for larger swing monitoring ( $10\text{mV}$  to several volts). Each channel also includes an independent stimulator module capable of maintaining constant current output over a wide range of electrode voltages. Importantly, **each channel has a built-in charge recovery switch** capable of briefly connecting it to ground, a crucial feature to bleed off built-up charge at the electrode e.g after stimulation pulses.

Characteristics	Value range	Comments
RHS2116 die dimensions : W x L x thickness	4.94 mm x 4.74 mm x 0.20 mm	Handling on carrier sample
Supply voltage VDD	3.2-3.6 V	Set at 3.3V during operation
Stimulation voltage swing VSTIM+ - VSTIM-	Max. stimulator voltage is +/-9V	Not used in these experiments (potential short between VSTIM+ and VSTIM- due to imperfect manufacturing)
Stimulation current	10nA to 2.55mA	
Stim. current step size	10nA to 10 $\mu$ A (8 bit)	
AC high-gain amplifier differential gain	x 192 (>45 dB)	No DC gain – sensitivity to the $\mu$ V range
Sampling frequency	Up to 714 kHz	Each of the 16 channels can be sampled up to ~45kSamples/s each

Table A7.1 : Some characteristics of the INTAN RHS2116 CMOS chip.

## A7.2 Shorting of bondpads during processing

During experiments, a short between a VSTIM channel and the chip ground was discovered, preventing chip operation in stimulation mode. Microscope analysis of the chip sides revealed golden flakes at a few places on the chip sidewall, touching some of the bonding wires (fig A7.2). These are attributed to insufficient protection of the chip sidewalls during either metallisation 1 or 2, leading to shorts. Some of these residues were successfully scraped off and this issue could be further mitigated by shaping the wirebond in arching bonds departing vertically from the bondpads rather than the straight, horizontal bonding used.

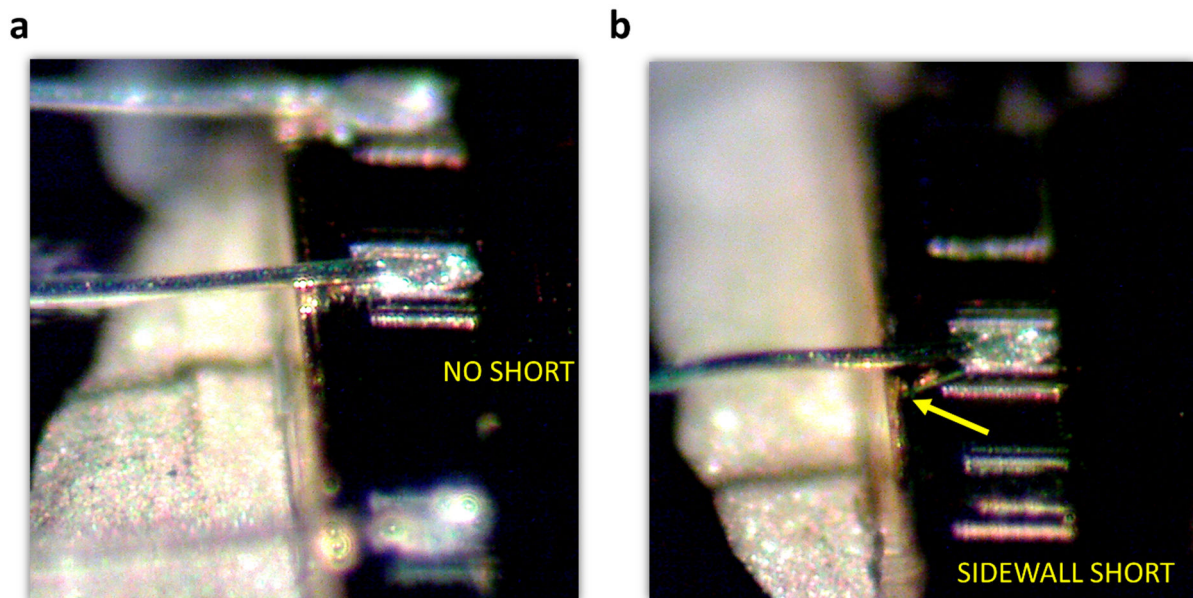


Figure A7.2: Side view of wirebonds on INTAN chip showing bonding wires, chip bondpads and sidewalls. **a)** Correct bonding, functioning channel. **b)** Unwanted sidewall metal (Ti/Au) residues such as indicated by arrow, led to shorting of VSTIM channels to the chip ground, preventing stimulator operation.

## Appendix A8: Photodetector correction factor

A Matlab code was written to determine the proportion of light output received by a photodiode placed at a finite distance and a given angle of the  $\mu$ LED emitter. The calculations are based on simple geometry and an LED lambertian emission profile. Any parallel photodetector placed at  $>1\text{mm}$  will not intercept fully the emission cone of the LED and a significant portion of the light will thus not be detected, meaning a correction factor needs to be apply to estimate the actual optical power of the LED based on photodiode output.

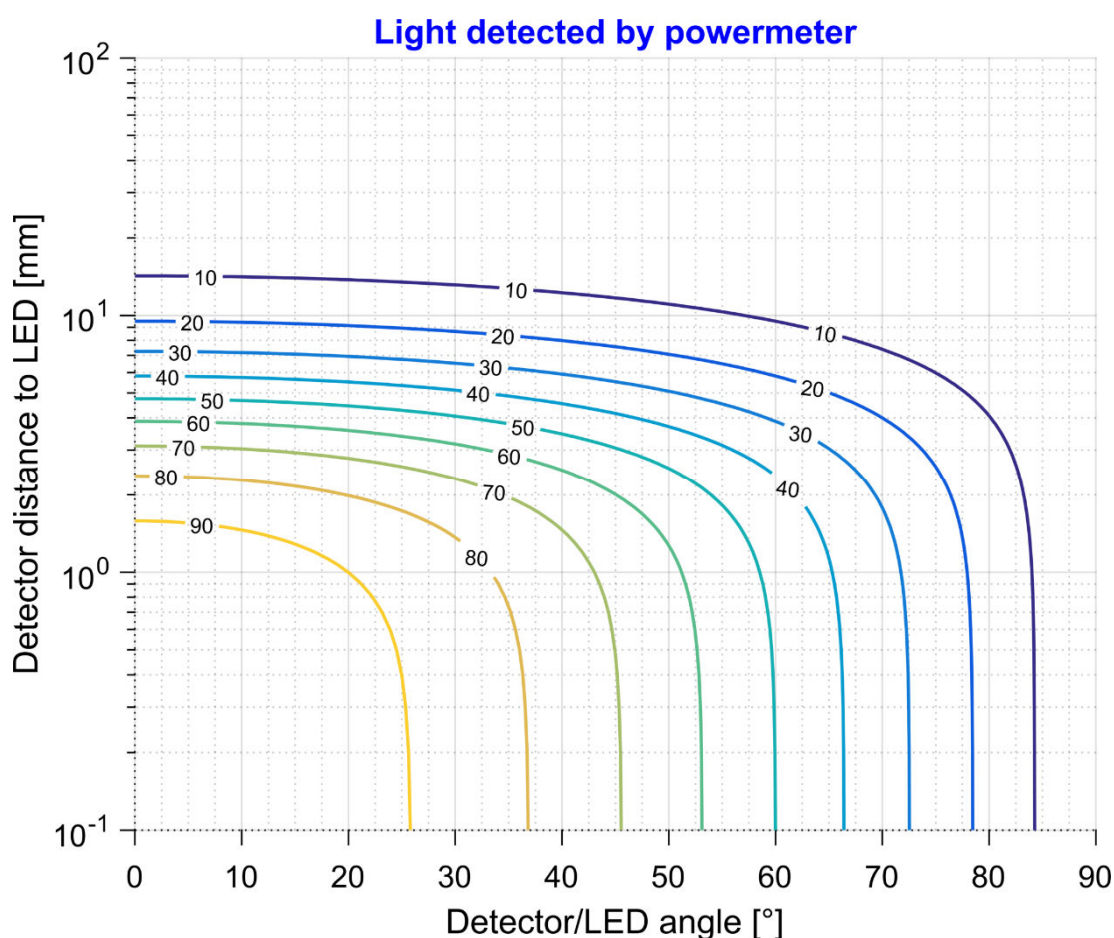


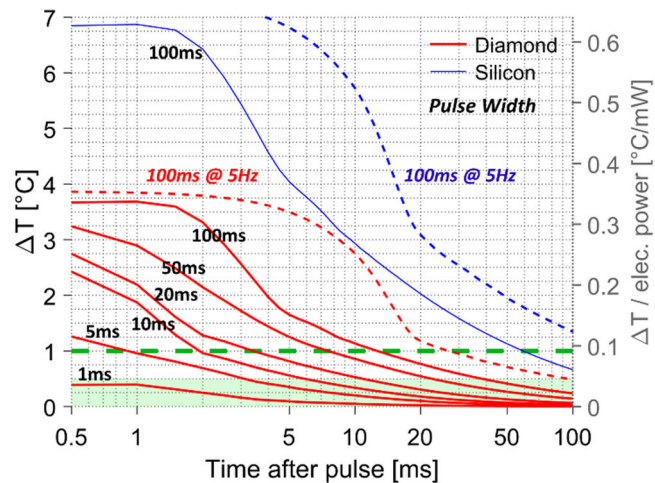
Figure A8. 1: Calculation of the light output received at the photodiode from a  $\mu$ LED operated at a distance  $y$  and an angle  $x$  to the detector. Values are given in percentage. A lambertian light distribution is assumed. This model was used to determine the approximate correction factor to extract PI curve for the  $\mu$ LEDs (chapter 5).

## Appendix A9: Modelled tissue $\Delta T$ , $I = 2\text{mA}$

Below are given counterpart figures to figure 5.11, modelling the thermal changes induced in tissue by  $\mu\text{LED}$  operation as a function of time and distance.

**a**

Temperature change in tissue after single pulse,  $I = 2\text{ mA}$



**b**

Max. temperature change in tissue, single pulses,  $2\text{mA}$

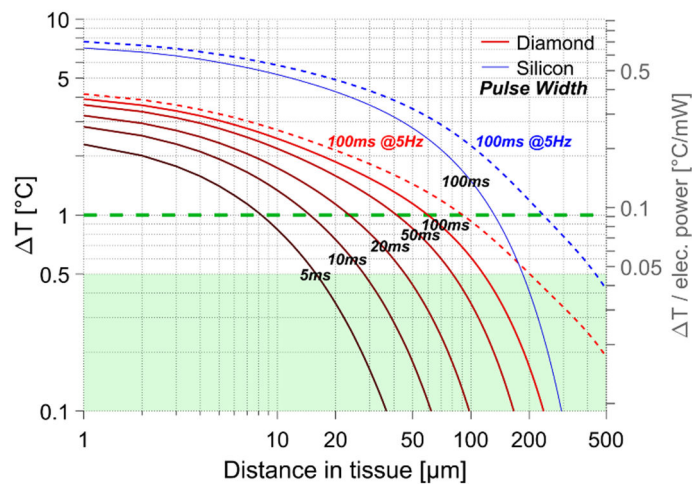


Figure A9.1: Simulated spatial and temporal spread of temperature change in surrounding brain tissue during  $\mu\text{LED}$  pulsed operation at various pulse width and frequencies, given here for an LED current of  $I = 2\text{mA}$  ( $1\text{mA}$  curves given in fig. 5.11). **a)** Decay with time of temperature change in tissue directly below LED and **b)** Maximum temperature change in tissue with increasing vertical distance from  $\mu\text{LED}$ . (See fig. 5.11 for details).

# Acknowledgements

I acknowledge and thank Prof. Keith Mathieson who has supervised this work.

I also acknowledge and thank Dr. Niall McAlinden, Dr. Enyuan Xie, Dr. Debbie Gunning, and Dr. Robert Scharf, as well as past and present fellow PhD students in the Neuro-Photonics group: Dr. Filippo Pisano, Dr. Douglas Young, Dr. Gabor Varkonyi, Dr. Yunzhou Cheng, and Ruaridh Winstanley.

I thank Prof. Martin Dawson and his team for their expertise in  $\mu$ LEDs, and Prof. Erdan Gu and Dr. Hangyu Liu for their expertise in diamond processing.

With them, I thank all members of the Institute of Photonics and Paul Hynd.

I want to extend particular thanks to Dr. Pengfei Tian for training me in the microfabrication of micro-sized LEDs, Dr. Benoit Guilhabert and Dr. Katie Rae for helping me to learn the transfer-printing process and valuable discussions, Dr. Yunzhou Cheng for his precious help and time spent on challenging wirebonding, and Ruaridh Winstanley for all the work done together on a LED-printed CMOS chip.

Heartfelt thanks to Jim Sweeney for his amazing work in the Institute's cleanroom.

Merci à Bruno Latour, René Girard et quelques autres pour leur pensée éclairante. Merci à Solenn pour sa patience, et pour tout le reste.



# Contributions

## Journal publications

A thermally efficient, ultrathin diamond-based  $\mu$ LED neural probe for versatile optogenetic protocols *in vivo*. A. Boudet et al. – in preparation

## Conference publications

A. Boudet, R. Scharf, M. Dawson, and K. Mathieson, “A diamond-based, hybrid optrode for multisite optogenetics,” in *Frontiers in Optics 2016*, 2016, p. FTh4D.5.

## Conference presentations and posters (presenter highlighted in bold)

**A. Boudet**, B. Guilhabert, E. Gu, M. Dawson, and K. Mathieson, “Thermally efficient, ultrathin, diamond-based  $\mu$ LED neural probes for versatile optogenetic protocols *in vivo*”, SU2P symposium 2018, Glasgow

**A. Boudet**, R. Scharf, M. Dawson, and K. Mathieson, “Silicon and diamond hybrid optrodes for multisite optogenetics”, oral presentation at *Frontiers in Optics 2016*, Rochester, NY, US

**R. Scharf**, A. Boudet, M. Dawson, S. Sakata, and K. Mathieson, “Next-generation high-density  $\mu$ LED probes for depth-specific stimulation,” in *Optogen 2016*, 2016

**A. Boudet** and K. Mathieson, “Enhanced optogenetics : micro-LED probes for specific and multi-depth stimulations”, 4<sup>th</sup> EPS Young Minds meeting, ICFO Barcelona, Spain 2015